

Kynurenic acid and its analog SZR104 exhibit strong antiinflammatory effects and alter the intracellular distribution and methylation patterns of H3 histones in immunochallenged microglia-enriched cultures of newborn rat brains

**Noémi Lajkó Biróné**

Theoretical Medical Doctoral School

**PhD Thesis**

Department of Cell Biology and Molecular Medicine  
Albert Szent-Györgyi Medical School – Faculty of Science and Informatics  
University of Szeged, Hungary



Thesis advisor: Professor Karoly Gulya, PhD, DSc

Szeged, 2022

## LIST OF PUBLICATIONS

*(MTMT2 IDENTIFIER: 10073718)*

### *PUBLICATIONS DIRECTLY RELATED TO THE THESIS*

I) **Lajkó N**, Kata D, Szabó M, Mátyás A, Dulka K, Földesi I, Fülöp F, Gulya K, Vécsei L, Mihály A (2020) Sensitivity of rodent microglia to kynurenines in models of epilepsy and inflammation in vivo and in vitro: Microglia activation is inhibited by kynurenic acid and the synthetic analogue SZR104. **Int J Mol Sci.** 21(23):9333. doi: 10.3390/ijms21239333. **(IF: 5.924)** (Q1)

II) Dulka K, Nacska K, **Lajkó N**, Gulya K (2021) Quantitative morphometric and cell-type-specific population analysis of microglia-enriched cultures subcloned to high purity from newborn rat brains. **IBRO Neurosci Rep.** 10:119-129. doi: 10.1016/j.ibneur.2021.01.007. **(IF: -)**

III) Szabo\* M, **Lajkó\*** N, Dulka K, Szatmári I, Fülöp F, Mihály A, Vécsei L, Gulya K (2022) Kynurenic acid and its analog SZR104 exhibit strong antiinflammatory effects and alter the intracellular distribution and methylation patterns of H3 histones in immunochallenged microglia-enriched cultures of newborn rat brains. **Int J Mol Sci.** 23(1079) doi: 10.3390/ijms23031079. **(IF 5,924)** (Q1) *(\*These authors contributed equally to this work and should be considered joint first authors.)*

### *PUBLICATIONS NOT DIRECTLY RELATED TO THE THESIS*

I) Dulka K, Szabo M, **Lajkó N**, Beleczi I, Hoyk Z, Gulya K (2021) Epigenetic consequences of in utero exposure to rosuvastatin: Alteration of histone methylation patterns in newborn rat brains. **Int J Mol Sci.** 22(7):3412. doi: 10.3390/ijms22073412. **(IF: 5.924)** (Q1)

***Number of full publications: 4***

***Cumulative impact factor: 17.772***

*POSTERS DIRECTLY RELATED TO THE THESIS*

I) Dulka K, Nacsa K, **Lajkó N**, Gulya K (2018) Nagy tisztaságú mikroglia kultúra készítése primer és szekunder tenyészetekből. **Magyar Élettani Társaság Vándorgyűlése**, Szeged, Hungary, 2018.06.27-30. (P1.56)

II) Szabo M, **Lajkó N**, Dulka K, Mihály A, Vécsei L, Gulya K (2020) Kynurenic acid and its analog SZR104 exhibit strong anti-inflammatory effects in microglia-enriched newborn rat cerebral cultures. **12<sup>th</sup> FENS 2020 Virtual Forum of Neuroscience**, 2020.07.11-15. (e-poster)

*POSTERS NOT DIRECTLY RELATED TO THE THESIS*

I) Dulka K, Szabo M, **Lajkó N**, Beleczi I, Hoyk Z, Gulya K (2020) Prenatal exposure to rosvastatin changes histone methylation patterns in the newborn rat brain. **12<sup>th</sup> FENS 2020 Virtual Forum of Neuroscience**, 2020.07.11-15. (e-poster)

II) Légrádi Á, Szabeni G J, Yaqub M, Dulka K, **Lajkó N**, Szabó M, Monostori É, Gulya K (2020) Galectin-1 expression correlates with the microglial activation state in primary and secondary cultures of newborn rat cortical tissue. **12<sup>th</sup> FENS 2020 Virtual Forum of Neuroscience**, 2020.07.11-15. (e-poster)

TABLE OF CONTENTS	page
Abbreviations	4
Summary	6
1. Introductions	8
1.1. Kynurenic acid (KYNA) and immunomodulation	8
1.2. Microglial cells and inflammation	10
1.3. Epigenetics and histone methylation	11
2. Specific aims	14
3. Materials and methods	14
3.1. Animal handling	14
3.2. Reagents and antibodies	15
3.3. Cell culture	15
3.4. Immunocytochemistry	19
3.5. <i>In vitro</i> phagocytosis assay	20
3.6. Western blot analysis	20
3.7. Image analysis and statistics	21
4. Results	22
4.1. KYNA and SZR104 downregulate LPS-induced CXCL10 levels while differentially altering CCR1 levels	22
4.2. KYNA and SZR104 inhibit microglial phagocytosis	25
4.3. KYNA and SZR104 alter the intracellular histone H3 distribution and H3 lys methylation patterns	31
5. Discussion	34
6. The main findings of the study	44
7. Acknowledgements	44
8. References	45
9. Co-Authors' statement	54
10. Appendix	55

## ABBREVIATIONS

3-HAO	3-hydroxyanthranilic acid oxygenase (EC 1.12.11.6)
$\alpha$ 7nAChR	$\alpha$ 7 nicotinic acetylcholine receptor
Ac	acetylation
AHR	aryl hydrocarbon receptor
ANOVA	one-way analysis of variance
CCR1	C-C motif chemokine receptor 1 (also known as chemokine receptor 1)
CD11b/c	cluster of differentiation 11b/c
CNS	central nervous system
CNPase	2',3'-cyclic nucleotide 3'-phosphodiesterase (EC 3.1.4.37)
CSF	cerebrospinal fluid
CTCF	corrected total cell fluorescence, an area-dependent value
CXCL10	C-X-C motif chemokine ligand 10 (also known as interferon-inducible cytokine IP-10)
DAPI	2-[4-(aminoiminomethyl)phenyl]-1H-indole-6-carboximidamide hydrochloride
DIV	day(s) <i>in vitro</i>
DMEM	Dulbecco's Modified Eagle's Medium
DNA	deoxyribonucleic acid
FBS	fetal bovine serum
FITC	fluorescein isothiocyanate
GAPDH	glyceraldehyde 3-phosphate dehydrogenase (EC 1.2.1.12)
GFAP	glial fibrillary acidic protein
GPR35	G-protein-coupled receptor 35
H	histone
H3K9me2	histone H3 (dimethyl K9)
H3K9me3	histone H3 (trimethyl K9)
H3K36me2	histone H3 (dimethyl K36)
Iba1	ionized calcium-binding adaptor molecule 1
ICC	immunocytochemistry
IDO	indolamine 2,3-dioxygenase (EC 1.13.11.52)
IFN- $\gamma$	interferon- $\gamma$
K	lysine amino acid
KAT	kynurenine aminotransferase (EC 2.6.1.64)
KMO	kynurenine 3-monooxygenase (EC 1.14.13.9)
KP	kynurenine pathway
KYN	kynurenine
KYNA	kynurenic acid
LPS	lipopolysaccharide
Me, me	methylation
mRNA	messenger ribonucleic acid
N	N-terminal tail
NMDA	<i>N</i> -methyl-D-aspartate receptor
P	phosphorylation (only in Figure 3)
P	primary culture (only in Figure 4)
PBS	phosphate-buffered saline
PTMs	posttranslational modifications
QUIN	quinolinic acid
rpm	revolutions per minute

RT	room temperature
S1; S2	secondary culture, 1 <sup>st</sup> shake; secondary culture, 2 <sup>nd</sup> shake
SEM	standard error of the mean
subDIV	subcloned day(s) <i>in vitro</i>
SZR72	2-(2-N,N-dimethylaminoethylamine-1-carbonyl)-1H-quinolin-4-one hydrochloride
SZR104	N-(2-(dimethylamino)ethyl)-3-(morpholinomethyl)-4-hydroxyquinoline-2-carboxamide
T1, T2	tertiary culture, 1 <sup>st</sup> shake; tertiary culture, 2 <sup>nd</sup> shake
TBS	Tris-buffered saline
TDO	tryptophan 2,3-dioxygenase (EC 1.13.11.52)
TLR4	Toll-like receptor4
TNF- $\alpha$	tumor necrosis factor-alpha
TRPA1, 4	transient receptor potential ankyrin 1 and 4 receptors
TSG-6	tumor necrosis factor-stimulated gene-6
U	ubiquitination
WB	western blot

## SUMMARY

Experimental and clinical studies found that endogenous tryptophan metabolites, including kynurenic acid (KYNA), are involved in several neurophysiological and neuropathophysiological mechanisms, and could beneficially regulate immune responses. However, since KYNA does not pass the blood–brain barrier, researchers are attempting to synthesize KYNA analogs (such as N-(2-(dimethylamino)ethyl)-3-(morpholinomethyl)-4-hydroxyquinoline-2-carboxamide; SZR104) that can penetrate this barrier and hence to provide possible treatments for neurodegenerative or neuroinflammatory disorders.

Microglial cells are the intrinsic immune cells of the central nervous system, and possess complex cellular and molecular mechanisms that detect deviations from homeostasis. They also release inflammatory cytokines and other potentially cytotoxic substances that can amplify inflammatory responses by activating and recruiting other cells to a lesion or infection.

DNA in the nucleus is wrapped around proteins known as histones, which form the chromatin structure. The capability of eukaryotic cells to maintain their diverse phenotypes is ensured by the chemical modifications of the DNA molecule, the activities of chromatin-associated proteins, and numerous posttranslational modifications (PTMs) of the histone proteins (acetylations, methylations, phosphorylations, ubiquitinations, etc.). Although histones are typically located inside the nucleus, where they regulate transcription, they are known to have a wide range of functions in various cytoplasmic and extracellular locations as well. Alterations in histone PTMs are viewed as an important process by which several cellular functions, including transcription, gene silencing, and immunity, are regulated.

To demonstrate whether KYNA and SZR104, a brain-penetrable KYNA analog, could alter 1) microglial functions such as phagocytosis, 2) inflammatory mechanisms that give rise to epigenetic changes *via* histone methylations or 3) induce distribution/localization change of unmethylated as well as methylated histones, newborn rat microglial cell cultures were treated with lipopolysaccharide (LPS), KYNA and SZR104, either alone, or in combination. The following six culture types were used: (a) control (unchallenged and untreated) cultures, (b) LPS-stimulated cultures, (c) KYNA-treated cultures, (d) SZR104-treated cultures, (e) LPS-challenged + KYNA-treated cultures, and (f) LPS-challenged + SZR104-treated cultures. The secondary cultures were assessed using immunocytochemical and western blot techniques employing antibodies against a microglia-specific protein (CD11b/c), two inflammation markers (CXCL10 and CCR1), one unmodified core histone (H3) and two specific histone H3 modifications at lysine (lys (K)) sites (H3K9me3 and H3K36me2). The fluid-phase

phagocytotic capacity of the microglial cells was determined *via* the uptake of fluorescent microspheres.

In this study, we demonstrated that KYNA and SZR104 downregulate LPS-induced CXCL10 levels while differentially altering CCR1 levels in microglial cultures. SZR104 and KYNA significantly decreased microglial phagocytosis *in vitro* as well. Furthermore, KYNA and SZR104 reduced the H3K9me3 and H3K36me2 levels after LPS treatment. Unexpectedly, we also found a cytoplasmic translocation of methylated H3K9 proteins from the nucleus after the LPS challenge; this translocation could be ameliorated or inhibited by KYNA and SZR104. Differential effects of KYNA and SZR104 on the cytoplasmic H3 localization were also noted: LPS + KYNA increased, while LPS + SZR104 returned cytoplasmic H3 levels to control values.

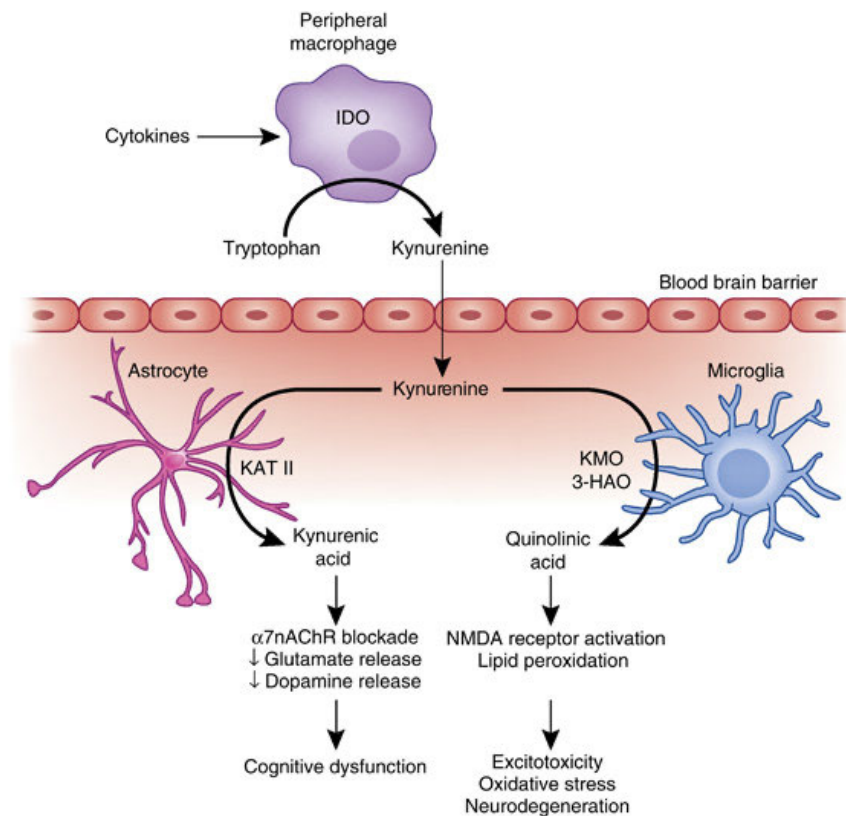
In summary, methylations of the histone H3 lys sites seem to be essential epigenetic marks for inflammation. Our data suggest that KYNA and its analog SZR104 potentially ameliorate neuroinflammation through the facilitation of antiinflammatory actions. Our findings corroborate previous studies on the antiinflammatory properties of endogenous KYNA and raise the possibility that some of the newly designed KYNA analogs that can penetrate the blood–brain barrier may alter gene expression epigenetically to activate antiinflammatory mechanisms. Hence, our findings may lead to the development of antiinflammatory medications targeting the central nervous system.

## 1. INTRODUCTION

### 1.1. Kynurenic acid (KYNA) and immunomodulation

Several recent experimental and clinical studies have found that endogenous tryptophan metabolites, including kynurenic acid (KYNA), are involved in several neurophysiological and neuropathophysiological mechanisms (Vazirinejad et al., 2014; Vécsei et al., 2013; Wirthgen et al., 2017) and plays a crucial role in the regulation of the immune response (Wirthgen et al., 2015). In the central nervous system (CNS), the kynurenine pathway (KP) starts by the catabolism of tryptophan into kynurenine by indoleamine 2,3-dioxygenase 1 (IDO1), IDO2, or tryptophan 2,3-dioxygenase (TDO) (**Figure 1**); this is a rate-limiting step in KYNA synthesis (Takikawa, 2005). In peripheral immune cells (e.g., macrophages, dendritic cells) or cells in the brain (e.g., microglia, astrocytes, and neuron) converted to KYNA by kynurenine aminotransferase II (KAT II) (Erhardt et al., 2017; Pedraz-Petrozzi et al., 2020) in astrocytes or quinolinic acid by kynurenine 3-monooxygenase (KMO) and 3-hydroxy-anthranilic acid oxygenase (3-HAO) in microglia or infiltrating macrophages (Haroon et al., 2011; Guillemin et al., 2005; Guillemin et al., 2007). KYNA can reduce glutamate release and the release of dopamine *via* blockade of the  $\alpha 7$ nAChR, both of which can lead to cognitive dysfunction. In contrast, quinolinic acid (QUIN) through activation of the NMDA receptor can increase glutamate release as well as contribute to lipid peroxidation, so contributing to excitotoxicity, oxidative stress, and neurodegeneration (Haroon et al., 2011). The biological significance of the kynurenine pathway; KYNA synthesis, degradation, and excretion; and the kynurenine pathway's immunomodulatory properties in vertebrates are all well-established (Vécsei et al., 2013; Wirthgen et al., 2017; Routy et al., 2016). KYNA exerts modulatory effects on the immune system through the regulation of T cells, natural killer cells (Routy et al., 2016), and microglial cells (Lajkó et al., 2020). The neuroprotective role of KYNA in different inflammatory/neurodegenerative CNS disorders is of particular interest. KP activation depends on the production of biologically active metabolites such as kynurenine (KYN), KYNA, QUIN, or anthranilic acid mediating various immuno- and neuromodulatory functions. IDO1 and 2 are upregulated by inflammatory stimuli such as interferon- $\gamma$  (IFN- $\gamma$ ) (Mándi et al., 2012). In addition, dysregulation of KP, resulting in alterations of the balance between KYNA and QUIN, has been described in many neurological disorders (Moroni et al., 2012). KYNA alterations are also documented in several inflammatory-related states (e.g., sepsis, inflammatory bowel disease), and described as a potential cancer marker (Gkotsos et al., 2017). Overactive microglia and elevated KYNA levels in the cerebrospinal fluid (CSF) were seen in bipolar disorders (Fries et al., 2019; Wang et al., 2018). In depression, decreased KYNA, QUIN, and kynurenine levels

correlated with pro-inflammatory cytokines (Ogyu et al., 2018). In summary, it is generally accepted that KYNA mediates immunosuppressive effects (Moroni et al., 2012), notably by targeting the G-protein-coupled receptor 35 (GPR35)- or aryl hydrocarbon receptor (AHR)-associated signaling pathways (Wirthgen et al., 2015; Wang et al., 2006).

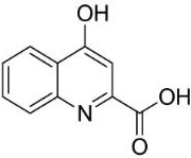
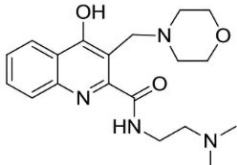


**Figure 1. Tryptophan metabolism in inflammation-induced CNS pathology.** The kynurenine pathway starts by the catabolism of tryptophan into kynurenine by indoleamine 2,3-dioxygenase 1 (IDO1), IDO2, or tryptophan 2,3-dioxygenase (TDO); this is a rate-limiting step in KYNA synthesis. In peripheral immune cells (e.g., macrophages, dendritic cells) or cells in the brain (e.g., microglia, astrocytes, and neurons) kynurenine is converted to kynurenic acid (KYNA) by kynurenine aminotransferase II (KAT II) (Erhardt et al., 2017), while to quinolinic acid by kynurenine 3-monooxygenase (KMO) and 3-hydroxy-anthranilic acid oxygenase (3-HAO) in microglia or infiltrating macrophages (Haroon et al., 2011; Guillemin et al., 2007).  $\alpha 7$ nAChR:  $\alpha 7$  nicotinic acetylcholine receptor; NMDA: N-methyl-D-aspartate receptor. (Adapted from Haroon et al., 2011).

However, since KYNA does not pass the blood–brain barrier, researchers are attempting to synthesize KYNA analogs that can penetrate this barrier (Molnár et al., 2021) and hence to provide possible treatments for neurodegenerative or neuroinflammatory disorders (Biernacki et al., 2020; Mándi et al., 2019). One such analog, N-(2-(dimethylamino)ethyl)-3-(morpholinomethyl)-4-hydroxyquinoline-2-carboxamide (SZR104; **Table 1**), was recently synthesized (Fülöp et al., 2009; Fülöp et al., 2012) and applied successfully against

pentylenetetrazole-induced seizures, and in doing so significantly it decreased the seizure-evoked field potentials (Demeter et al., 2012).

**Table 1.** Molecular structure, chemical name, empirical formula, and molecular weight of KYNA and its analog SZR104.

Abbreviation	Molecular structure	Chemical name	Empirical formula and molecular weight
KYNA		4-hydroxyquinolin-2-carboxylic acid	C <sub>10</sub> H <sub>7</sub> NO <sub>3</sub> 189.17
SZR104		N-(2-(dimethylamino)ethyl)-3-(morpholinomethyl)-4-hydroxyquinoline-2-carboxamide	C <sub>19</sub> H <sub>26</sub> N <sub>4</sub> O <sub>3</sub> 358.43

## 1.2. Microglial cells and inflammation

Microglial cells are the intrinsic immune cells of the CNS, and they possess complex cellular and molecular mechanisms that detect deviations from homeostasis in nervous tissue. Under physiological conditions, microglia are mostly ramified and survey the parenchymal integrity of the CNS (Ginhoux et al., 2014). At the site of damage or inflammation, activated microglia change their morphology, express increased levels of major histocompatibility antigens, and become phagocytic (Kettenmann et al., 2011). They also release inflammatory cytokines and other potentially cytotoxic substances that can amplify inflammatory responses by activating and recruiting other cells to a lesion or infection (Kreutzberg, 1996; Ubogu et al., 2006). For example, inflammation can be exacerbated by the secretion of the C–X–C motif chemokine ligand 10 (CXCL10) from microglia (Cheeran et al., 2003; Nakamichi et al., 2005) or other cell types (Dyer et al., 2009; Lo et al., 2010; Wilson et al., 2008). CXCL10 induces chemotaxis, apoptosis, the inhibition of cell growth, and angiostasis (Liu et al., 2011). Both CXCL10 and its receptor (the C–X–C motif chemokine receptor 3) are crucial for leukocyte trafficking and homing to inflamed tissues, as well as for the perpetuation of inflammation that leads to tissue damage (Klein, 2004). Previous studies have reported that CXCL10 is involved in the pathophysiology of multiple sclerosis (Vazirinejad et al., 2014; Tomioka et al., 2014). Similarly, the C–C motif chemokine receptor 1 (CCR1) and its ligands may play a role in the pathogenesis of multiple sclerosis (Szczuciński et al., 2007).

The experimental investigation of the pharmacology of microglial phagocytosis *in vivo* is hindered by technical difficulties (Diaz-Aparicio et al., 2016), but could be studied easily *in vitro*; therefore, we performed *in vitro* experiments using microglia-enriched forebrain cell cultures (Kata et al., 2016; Szabó et al., 2013). Our previous experiments proved that microglial cell cultures are suitable for the evaluation of the effects of pro- and antiinflammatory compounds (Szabó et al., 2013; Kata et al., 2016, 2017).

### **1.3. Epigenetics and histone methylation**

DNA in the nucleus is wrapped around proteins known as histones, which form the chromatin structure. The capability of eukaryotic cells to maintain their diverse phenotypes is ensured by the chemical modifications of the DNA molecule, the activities of chromatin-associated proteins, and numerous PTMs of the histone proteins (Kouzarides, 2007; Lawrence et al., 2016; Zlatanova et al., 1990). Although histones are typically located inside the nucleus (**Figure 2**), where they regulate transcription, they have a wide range of functions in various cellular and extracellular locations as well (Kouzarides, 2007; Lawrence et al., 2016; Zlatanova et al., 1990). When they are in the extracellular milieu, they become damage-associated molecular patterns that promote inflammation, cytotoxicity, coagulation, and apoptosis (Parseghian et al., 2006; Chen et al., 2014; Ekaney et al., 2014; Frydman et al., 2020). Cytoplasmic functions of histone proteins include participation in cell signaling pathways related to the mediation of innate immunity (Parseghian et al., 2006). The cytoplasmic accumulation of histones and nucleosomes precedes the externalization of phagocytosis signals on the outer membrane surface of apoptotically dying lymphoblasts (Gabler et al., 2003b; Gabler et al., 2004). For instance, the translocation of a specific histone H1 subtype from the nucleus into the cytoplasm triggers the release of cytochrome C from the mitochondria and thus leads to apoptosis (Konishi et al., 2003).

Histone modifications (acetylations, methylations, phosphorylations, ubiquitinations, etc.) (**Figure 3**) are PTMs made in the nucleus by the appropriate enzymes (Kouzarides, 2007; Gabler et al., 2004; Venkatesh et al., 2015). Consequently, transcription often becomes altered because modified histones and the DNA will interact differently. The cytoplasmic accumulation of such modified histones might indicate that they were released/transported from the nucleus, perhaps because of distress (Chen et al., 2014; Ekaney et al., 2014; Frydman et al., 2020). Histone modifications are key epigenetic regulatory features that govern many cellular functions. Specific histone PTMs can direct site-specific activation or silencing of transcription (Venkatesh et al., 2015); hence, they are the principal players that regulate gene expression.

Histone methylations at lysine (lys (K)) and arginine residues are relatively stable and considered potential marks for carrying the epigenetic information present in specific regions of the genome. For example, several monomethylations (i.e., H3K9me1, H3K27me1, and H3K79me1) and some dimethylations of histone H3 proteins (H3K36me2) are linked to active transcription, while other dimethylations (H3K9me2) and most trimethylations of this core histone (i.e., H3K9me3, H3K27me3, and H3K79me3) are linked to gene repression (Barski et al., 2007; Hyun et al., 2017).

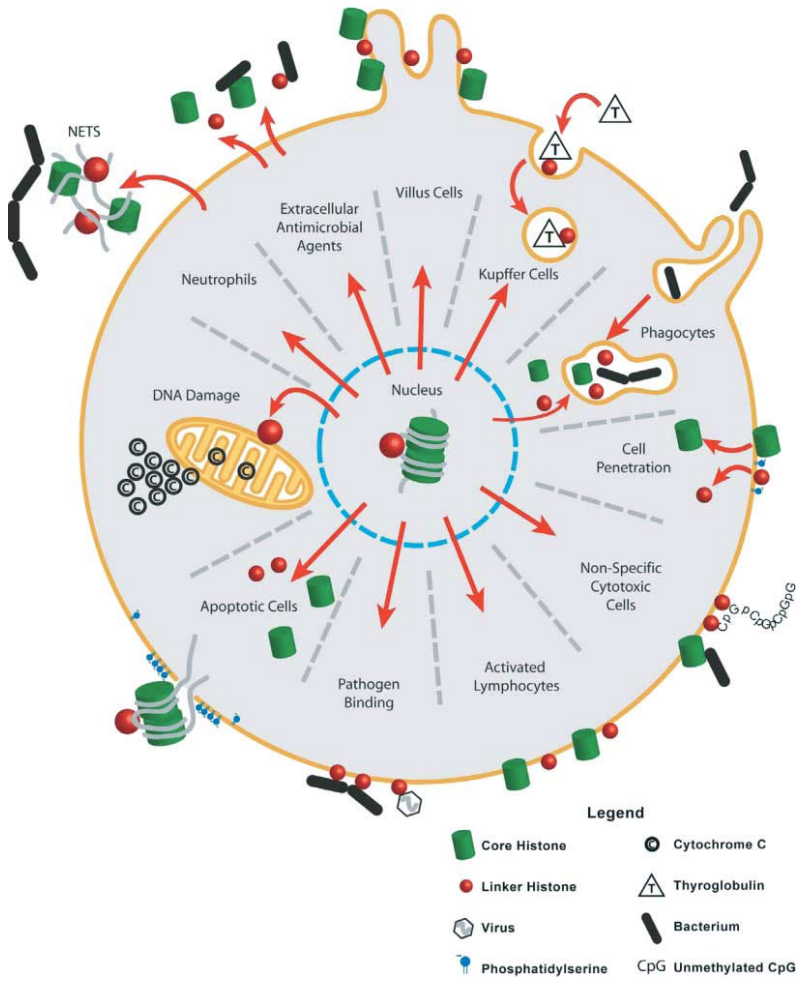


**Figure 2. Intracellular localization of histone proteins.** Histones have a wide range of functions in various cellular and extracellular locations. NETS: neutrophil extracellular traps. (Adapted from Parseghian et al., 2006.)

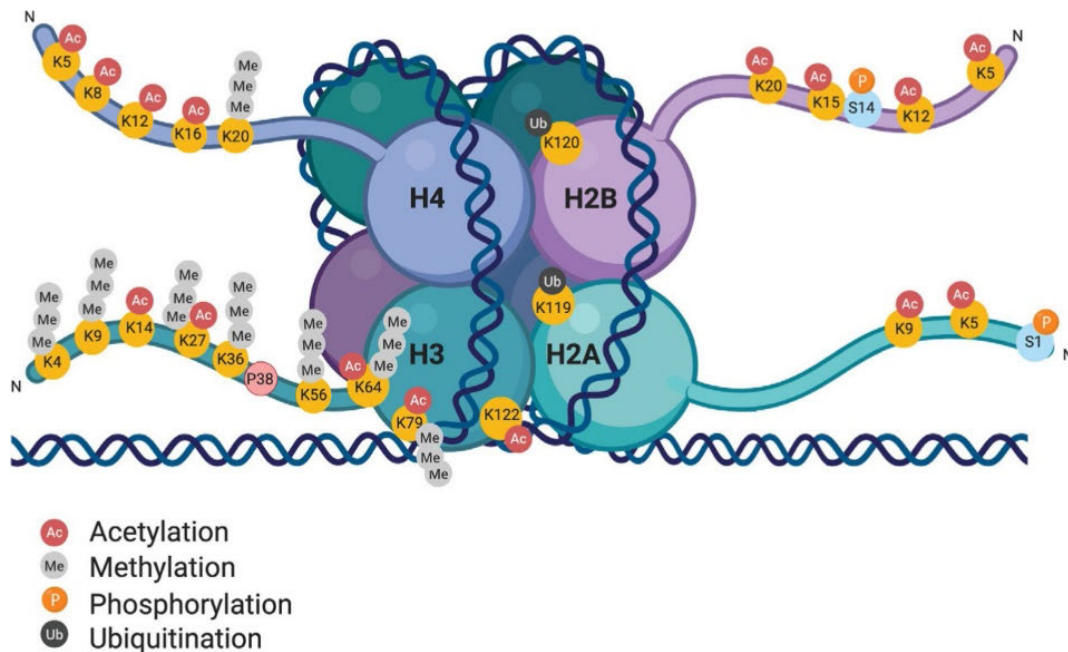


**Figure 3. Histone PTMs.** Histone modifications (acetylations, methylations, phosphorylations, ubiquitinations, etc.) are PTMs made in the nucleus by the appropriate enzymes. Me: methylation; Ac: acetylation; P: phosphorylation; Ub: ubiquitination; K: lysine amino acid; S: serine amino acid; N: N-terminal tail; H: histone. (Adapted from Klein and Hainer, 2020.)

In this study, we investigated the relationships among (a) KYNA and its analog SZR104, (b) the change in phagocytotic activity of the microglial cells, (c) the inflammatory mechanisms that give rise to epigenetic changes *via* histone methylations, and (d) the intracellular distribution/localization of unmethylated and methylated histones in microglial cells. Besides the inflammatory markers CXCL10 and CCR1, we quantitatively analyzed the levels of unmodified core histone H3 and histone H3 lys methylations at the H3K9me3 and H3K36me2 sites (**Table 2**), marks that are considered contrary in regulating gene expression (Barski et al., 2007; Hyun et al., 2017) and also involved in immunomodulation (Honma et al., 2020; Jain et al., 2018; Zhuang et al., 2018; Saccani et al., 2002), using western blots and multicolor light microscopic immunofluorescence. As far as we know, our approach for studying KYNA and its brain-penetrable analog SZR104, with regard to epigenetics and neuroinflammation, is unique in the literature. Our results shed light on the indicator roles that these histones, translocated to the cytoplasm, might play in neuroinflammation; furthermore, our findings highlight the beneficial role that the endogenous kynurenine system could play in antiinflammatory mechanisms.

## 2. SPECIFIC AIMS

In the CNS, the kynurenine pathway is involved in several neurophysiological and neuropathophysiological mechanism (Vazirinejad et al., 2014; Vécsei et al., 2013; Wirthgen et al., 2017) and its immunomodulatory properties in vertebrates are all well-established (Vécsei et al., 2013; Wirthgen et al., 2017; Routy et al., 2016). As KYNA was shown to mediate immunosuppressive effects (Monori et al., 2012), we felt it was important to study inflammatory mechanism and microglia function using an analog that could penetrate the blood-brain barrier (Molnár et al., 2021). These analogs have the potential to provide possible treatments for neurodegenerative or neuroinflammatory disorders (Biernacki et al., 2020; Mándi et al., 2019).

Microglial cells possess complex cellular and molecular mechanisms that detect deviations from homeostasis in nervous tissue. In activated state, they release inflammatory cytokines and other potentially cytotoxic substances, such as CXCL10 or CCR1 and its ligands, that can amplify inflammatory responses by activating and recruiting other cells to a lesion or infection (Kreutzberg, 1996; Ubogu et al., 2006). Histone modifications are key epigenetic regulatory features that govern many cellular functions (for example, inflammation, coagulation, apoptosis) (Barski et al., 2007; Parsheghian et al., 2006).

In this study, our specific aims were:

- 1) to determine whether KYNA and its analog SZR104 alter microglial function (e.g., phagocytotic activity);
- 2) to determine whether KYNA and SZR104 induce the inflammatory mechanisms that give rise to epigenetic changes *via* histone methylations in microglial cells;
- 3) to determine whether KYNA and SZR104 induce changes in intracellular distribution/localization of unmethylated as well as methylated histones in microglial cells.

## 3. MATERIALS AND METHODS

### 3.1. Animal handling

The animal experiments were conducted in strict compliance with the European Council Directive (86/609/EEC) and EC regulations (O.J. of EC No. L 358/1, 18/12/1986), related to the care and use of laboratory animals for experimental procedures, and the relevant Hungarian and local legislation requirements were followed. Experimental protocols were approved by the Institutional Animal Welfare Committee of the University of Szeged (II./1131/2018; date of approval: 30 May 2018). The pregnant Sprague–Dawley rats (190–210 g) used in this study

were maintained under standard housing conditions and fed *ad libitum*. A total of five breeding runs (with 5–7 pregnant rats each) provided the litters (6–12 pups from each mother), from which independent culturing experiments were performed.

### 3.2. Reagents and antibodies

KYNA (mol. weight: 189.17 g) was purchased from Sigma-Aldrich (Budapest, Hungary), and SZR104 (mol. weight: 358.43 g; **Table 1**) was synthesized in-house as described in previous studies by our laboratories (Fülöp et al., 2009; Fülöp et al., 2012; Fülöp et al., 2021). KYNA and SZR104 were dissolved in Dulbecco's Modified Eagle's Medium (DMEM; Invitrogen, Carlsbad, CA, USA) and added at the appropriate concentration to the cultures. Bacterial lipopolysaccharide (LPS; Sigma Aldrich) was used to elicit immunochallenge. The primary and secondary antibodies used in our study are listed in **Table 2**. For the characterization of microglial cells, we used an antibody against the cluster of differentiation 11b/c protein (CD11b/c, clone OX-42; Szabo et al., 2013). We also used antibodies against the secreted ligand CXCL10 and the receptor CCR1 as inflammation markers (Liu et al., 2011; Neote et al., 1993). In addition, we used antibodies against the unmodified core histone H3 protein and its PTMs at lys sites, H3K9me3, and H3K36me2, to detect the cytoplasmic and nuclear localizations of these proteins. An anti-glyceraldehyde 3-phosphate dehydrogenase (GAPDH) antibody was used as an internal control in western blot experiments (Dulka et al., 2021a).

### 3.3. Cell culture

Forebrain tissue samples taken from newborn Sprague–Dawley rats of both sexes were removed, cleared from the meninges, minced with scissors, and homogenized for 10 min at 37°C in DMEM containing 1 g/L D-glucose, 110 mg/L Na-pyruvate, 4 mM L-glutamine, 3.7 g/L NaHCO<sub>3</sub>, 10,000 U/mL penicillin G, 10 mg/mL streptomycin sulfate, and 25 µg/mL amphotericin B supplemented with 0.25% trypsin (Invitrogen). After centrifugation at 1000 g and room temperature (RT) for 10 min, the pellet was resuspended, washed in 10 mL of DMEM containing 10% heat-inactivated fetal bovine serum (FBS; Invitrogen), and again centrifuged for 10 min at 1000 g and RT. The final pellet was filtered through a sterile filter (100 µm pore size; Greiner Bio-One Hungary Kft., Mosonmagyaróvár, Hungary) to eliminate tissue fragments that had resisted dissociation. The cells were resuspended in 2 mL of the same solution and then seeded on poly-L-lysine-coated culture flasks (75 cm<sup>2</sup>; 10<sup>7</sup> cells/flask) and cultured at 37 °C in a humidified air atmosphere supplemented with 5% CO<sub>2</sub>. The medium was changed the next day and then every 3 days. After 7 days of culture, microglial cells in the

primary cultures were shaken off using a platform shaker (120 rpm for 20 min) at 37 °C as we described earlier (Dulka et al., 2021a) (**Figure 4**).

**Table 2.** Primary and secondary antibodies used in western blot (WB) and immunocytochemistry (ICC).

Primary antibody, abbreviated name	Primary antibody, full name	Final dilution (for ICC or WB)	Company	Secondary antibody with fluorochrome, full name	Final dilution (for ICC or WB)	Company
CD11b/c	mouse anti-CD11b+CD11c ab.	1/500 (ICC)	Abcam, Cambridge, England	Alexa Fluor 568 goat anti-mouse (ICC)	1/1000 (ICC)	Invitrogen, Thermo Fisher Scientific Carlsbad, CA, USA
CXCL10	rabbit anti- C-X- C motif chemokine ligand 10 polycl. ab.	1/200 (ICC)	Biorbyt, Cambridge, England	Alexa Fluor 488 goat anti-rabbit (ICC)	1/1000 (ICC)	Invitrogen, Thermo Fisher Scientific Carlsbad, CA, USA
CCR1	rabbit anti-CCR1 polycl. ab.	1/200 (ICC); 1/250 (WB)	Novus, Centennial, CO, USA	Alexa Fluor 488 goat anti-rabbit (ICC); horseradish peroxidase goat anti-rabbit ab. (WB)	1/1000 (ICC); 1/2000 (WB)	Invitrogen, Thermo Fisher Scientific Carlsbad, CA, USA (ICC); Sigma-Aldrich, Budapest, Hungary (WB)
H3	rabbit anti-Histone H3 polycl. ab.	1/500 (ICC); 1/1500 (WB)	Abcam, Cambridge, England	Alexa Fluor 488 goat anti-rabbit (ICC); horseradish peroxidase goat anti-rabbit ab. (WB)	1/1500 (ICC); 1/2000 (WB)	Invitrogen, Thermo Fisher Scientific Carlsbad, CA, USA (ICC); Sigma-Aldrich, Budapest, Hungary (WB)
H3K9me3	rabbit anti-Histone H3 (trimethyl K9) polycl. ab.	1/500 (ICC)	Abcam, Cambridge, England	Alexa Fluor 488 goat anti-rabbit (ICC)	1/1000 (ICC)	Invitrogen, Thermo Fisher Scientific Carlsbad, CA, USA
H3K36me2	rabbit anti-Histone H3 (dimethyl K36) monoclonal ab.	1/500 (ICC)	Abcam, Cambridge, England	Alexa Fluor 488 goat anti-rabbit (ICC)	1/1000 (ICC)	Invitrogen, Thermo Fisher Scientific Carlsbad, CA, USA
GAPDH	mouse anti-glyceraldehyde 3-phosphate dehydrogenase ab.	1/20000 (WB)	Sigma-Aldrich, Budapest, Hungary	Horseradish peroxidase rabbit anti-mouse (WB)	1/2000 (WB)	Sigma-Aldrich, Budapest, Hungary

Microglia were collected from the supernatant by centrifugation (3000 g for 8 min at RT), resuspended in 4 mL of DMEM/10% FBS, and seeded in the same medium either on poly-L-lysine-coated coverslips (15 × 15 mm; 2 × 10<sup>5</sup> cells/coverslip) for immunocytochemistry or in poly-L-lysine-coated Petri dishes (10<sup>6</sup> cells/Petri dish) for western blot analysis. The number of cells collected was determined in a Bürker chamber after trypan blue staining. DMEM/10% FBS was replaced the next day and then on the third and sixth days of subcloning (subDIV6).

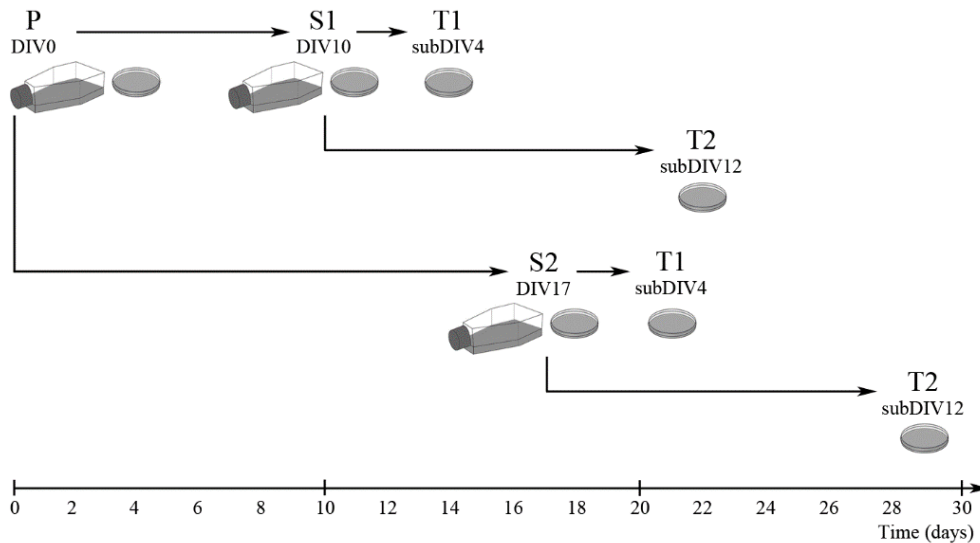


**Figure 4. Preparation of microglia-enriched secondary and tertiary cultures from mixed primary cultures.** Mixed primary cultures (P, DIV0) were prepared as described in the experimental procedures. The composition of the secondary (S1, S2) and tertiary (T1, T2) cultures was then analyzed *via* quantitative immunocytochemistry using cell-specific markers.

These cultures were used in previous studies (Lajkó et al., 2020; Dulka et al., 2021b), and 73.3% ± 17.8% purity was routinely achieved for microglia in secondary cultures (Dulka et al., 2021a) (**Figure 5 and 6**). We demonstrated that the main contaminating cell types were glial fibrillary acidic protein (GFAP)-immunoreactive astrocytes (19.0% ± 2.7%), β-tubulin III-positive neurons (3.1% ± 0.4%), and 2',3'-cyclic nucleotide 3'-phosphodiesterase- (CNPase)-positive oligodendrocytes (0.2% ± 0.1%). In the present study, only samples of harvested cultures from different breeding runs with the highest microglia purity (typically around 98%) were selected through immunocytochemical validation as reported earlier (Dulka et al., 2021a).

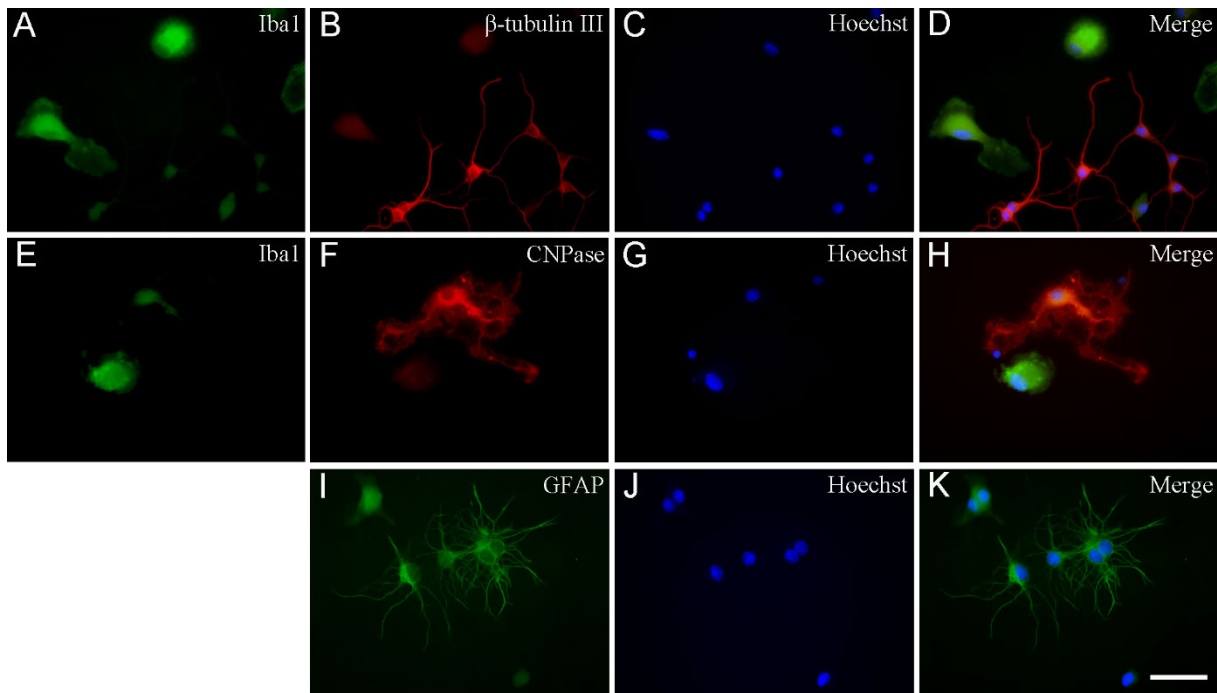


**Figure 5. Immunocytochemical localization of microglia, neurons, astrocytes, and oligodendrocytes in secondary cell cultures.** Different cell types were labeled by the corresponding marker proteins. An anti-Iba1 antibody was used to detect microglia (green in (A) and (E)), an anti- $\beta$  tubulin III antibody was used to detect neurons (red (B)), an anti-CNPase antibody was used to detect oligodendrocytes (red (F)) and an anti-GFAP antibody was used to detect astrocytes (green (I)). These primary antibodies were recognized by Alexa Fluor or FITC (fluorescein isothiocyanate)-conjugated secondary antibodies. The cell nuclei were stained with Hoechst 33258 (blue (C), (G), (J)). Merged images are also shown ((D), (H), (K)). Scale bar: 50  $\mu$ m.

On subDIV6, the expanded microglia-enriched secondary cultures were treated for 24 h with LPS alone (20 ng/mL final conc., dissolved in DMEM; Sigma-Aldrich), KYNA alone (1  $\mu$ M final conc., dissolved in DMEM), SZR104 alone (1  $\mu$ M final conc., dissolved in DMEM), or with a combination LPS + KYNA or LPS + SZR104. LPS treatment served as an immunochallenge. The following six culture types were used: (a) control (unchallenged and untreated) cultures, (b) 20 ng/mL LPS-stimulated cultures, (c) 1  $\mu$ M KYNA-treated cultures, (d) 1  $\mu$ M SZR104- treated cultures, (e) LPS-challenged + KYNA-treated cultures (at indicated doses), and (f) LPS-challenged + SZR104-treated cultures (at indicated doses).

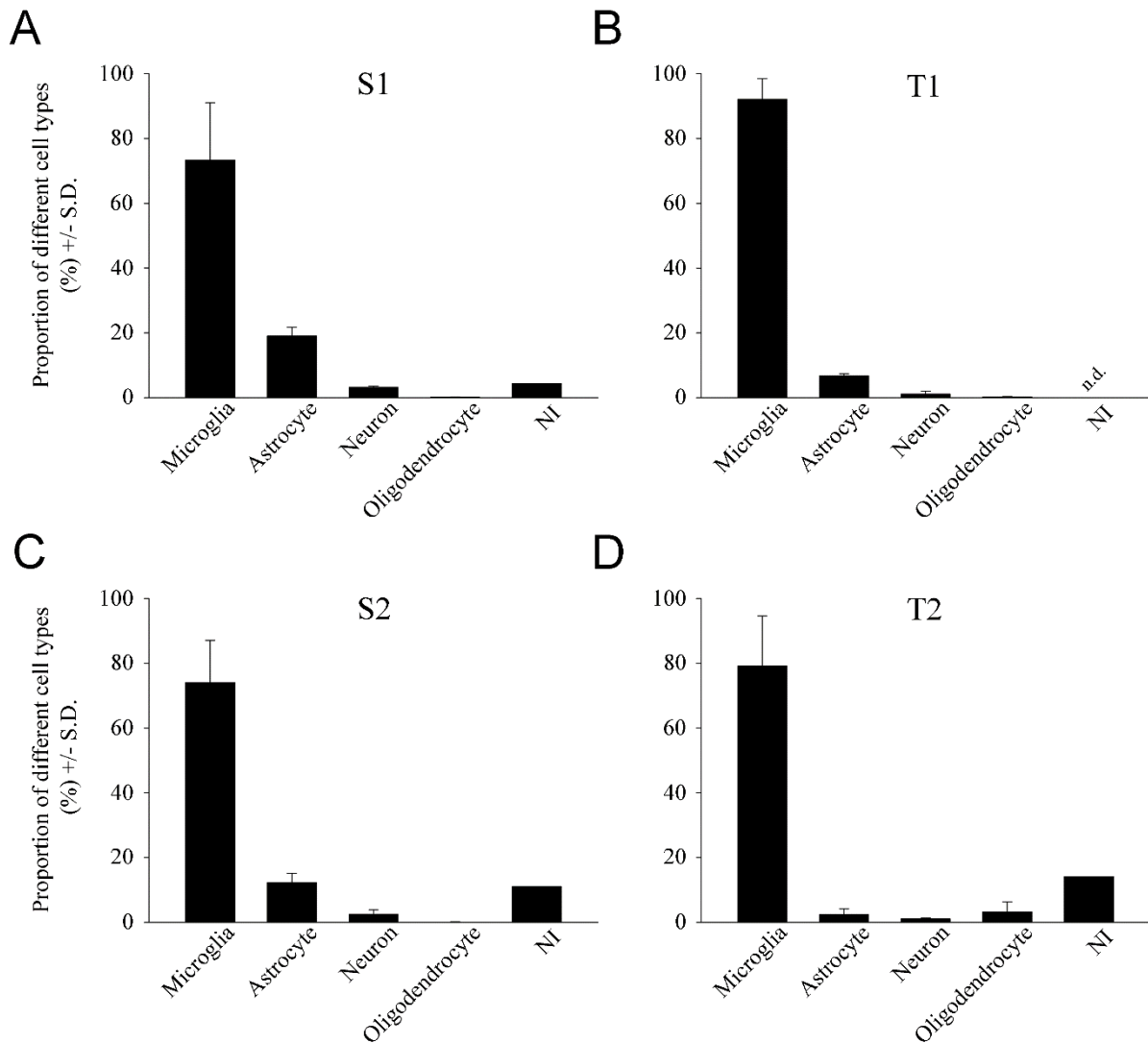


**Figure 6. Quantitative analysis of the distribution of different cell types in secondary (S1, S2) and tertiary (T1, T2) cultures.** Microglia-enriched cultures were obtained after the shaking of the primary cultures (S1 = 73.3%, S2 = 74.1%; (A) and (C), respectively). Shaking of the secondary cultures led to tertiary cultures with higher purities (T1 = 93.1%, T2 = 79.3%; (B) and (D), respectively). The number of astrocytes and neurons progressively decreased throughout culturing. Occasionally, a few cells that were not identified (NI) immunocytochemically in this study were also observed in secondary cultures; such cells were exceptionally rare in T1 but were somewhat more numerous in T2 cultures. n.d.: not detected.

### 3.4. Immunocytochemistry

The microglia-enriched secondary cultures were assessed using antibodies against a microglia-specific antigen, two inflammation markers, an unmodified core histone H3, and two antigens that recognize specific histone H3 lys modifications (Table 2). Immunocytochemistry was performed according to our previously used protocols (Lajkó et al., 2020; Dulka et al., 2021a). Briefly, the cells were fixed in 4% formaldehyde in 0.05 M phosphate-buffered saline (PBS; pH 7.4) at RT for 5 min and then rinsed in 0.05 M PBS for 3 × 5 min. After permeabilization

and blocking of the nonspecific sites for 30 min at 37 °C in 0.05 M PBS containing 5% normal goat serum and 0.3% Triton X-100, the cells on the coverslips were incubated overnight at 4 °C with the appropriate primary antibody diluted in 0.05% PBS containing 1% bovine serum albumin and 0.3% Triton X-100 solution. The cells were then washed in 0.05 M PBS for 3 × 5 min at RT before being incubated without Triton X-100 but with the appropriate Alexa Fluor fluorochrome-conjugated secondary antibody in the dark for 2 h at RT. Afterwards, the cells were washed in 0.05 M PBS for 3 × 5 min and then in distilled water once for 5 min at RT. Lastly, the prepared coverslips were mounted on microscope slides in Prolong Diamond Antifade with 4',6-diamidino-2-phenylindole dye (DAPI; Thermo Fisher, Waltham, MA, USA). To confirm the specificity of the secondary antibodies, omission control experiments (i.e., staining without the primary antibody) were also carried out. In these experiments, immunocytochemical signals were not observed (data not shown).

### **3.5. *In vitro* phagocytosis assay**

The fluid-phase phagocytotic capacity of the microglial cells was determined *via* the uptake of fluorescent microspheres (2 µm diameter; Sigma-Aldrich, St. Louis, MO, USA). The cells were plated on coverslips in Petri dishes at a density of 200,000 cells/coverslip in 2 mL DMEM containing 10% heat-inactivated bovine serum and cultured for 7 days (subDIV7); then, 2 µL 2.5% aqueous suspension of fluorescent microspheres was added and the secondary culture was incubated for 60 min at 37 °C. The cells were washed five times in 0.05 M PBS, fixed in 0.05 M PBS containing 4% formaldehyde, and CD11b/c-immunocytochemistry was performed. The coverslips were mounted in Prolong Diamond Antifade with DAPI (Thermo Fisher).

### **3.6. Western blot analysis**

Cultured secondary cells were collected with a rubber policeman; homogenized in 50 mM Tris-HCl (pH 7.5) containing 150 mM NaCl, 0.1% Nonidet P40, 0.1% cholic acid, 2 µg/mL leupeptin, 1 µg/mL pepstatin, 2 mM phenylmethylsulfonyl fluoride, and 2 mM ethylenediaminetetraacetic acid, and then centrifuged at 10,000 g for 10 min. The pellet was discarded, and the protein concentration of the supernatant was determined (Lowry et al., 1951). Due to the high purity and low yield of the cultures, the protein concentration was typically low (about 0.5 µg/µL). Western blot analysis was performed as previously described (Dulka et al., 2021b) apart from the occasional use of large, five-well combs to make wells with 50 µL capacity (Mini-Protean Tetra Cell module; Bio-Rad Hungary Ltd., Budapest, Hungary) to accommodate larger volumes to compensate for lower protein content; consequently, such

sample sets (control and 5 treatments) were often run in two gels. Briefly, equal amounts of proteins in the linear range of detection were loaded onto a polyacrylamide gel. For the quantitative assessment of protein expression on western blots, 10 µg of protein was denatured at 100 °C for 5 min, loaded into wells, and separated on 12% sodium dodecyl sulfate–polyacrylamide gel before being transferred onto a Hybond-ECL nitrocellulose membrane (Amersham Biosciences, Little Chalfont, Buckinghamshire, England), blocked for 1 h in 5% nonfat dry milk in 0.1 M Tris-buffered saline (TBS) containing 0.1% Tween 20, and finally incubated overnight with the appropriate antibody (**Table 2**). Nonspecifically bound or excess antibody was removed with 5 × 5 min rinses in 0.1 M TBS containing 0.1% Tween 20. The membranes were then incubated for 1 h with the appropriate peroxidase-conjugated secondary antibody. The enhanced chemiluminescence method (Amersham Biosciences) was used according to the manufacturer’s instructions to reveal immunoreactive bands. Proper dilutions and exposure times for each antibody were tested before performing the actual experiments. GAPDH detection was used as a control for equal protein load.

Grayscale digital images of the blots were acquired by scanning the autoradiographic films with a desktop scanner (Epson Perfection V750 Pro; Seiko Epson Corp., Nagano, Japan). Images were scanned and processed at identical settings to allow comparisons to be made of the blot results obtained from different samples. The densities of immunoreactive lanes equally loaded with protein aliquots were quantified, and data values were presented as a percentage of the control. For statistical comparisons, a one-way analysis of variance (ANOVA) or Mann–Whitney rank sum test was used and a p value of < 0.05 was considered significant. Values are presented as the mean ± standard error of the mean (SEM) from at least five immunoblots, one from each independent experiment.

### **3.7. Image analysis and statistics**

Digital images were captured using a Leica DMLB epifluorescence microscope equipped with a Leica DFC7000 T CCD camera (Leica Microsystems CMS GmbH, Wetzlar, Germany) and *via* the LAS X Application Suite X (Leica). For the intracellular (nuclear and cytoplasmic) localization and quantitative analyses of the levels of unmodified core histone H3 and the methylated histone H3 proteins H3K9me3 and H3K36me2, the DAPI-labeled cell nuclei of anti-CD11b/c-labeled cells were identified on coverslip-cultured samples.

For the quantitation of immunofluorescent images, 65–180 randomly selected CD11b/c-positive microglia were analyzed from three separate experiments. A quantitative microscopic analysis of cell specific and histone immunofluorescence was conducted in ImageJ (version

1.47; originally developed by W. Rasband at the U.S. National Institutes of Health, Bethesda, MD, USA) (Schneider et al., 2012), available at <https://imagej.net/Downloads>, accessed on 10 July 2013). Briefly, the densities of the whole cell and nuclei (mean gray values), the areas, and their integrated optical densities (fluorescence per area) were calculated. The corrected total cell fluorescence (CTCF) values ( $CTCF_{\text{whole cell}}$  and  $CTCF_{\text{nucleus}}$ ) were then computed as described in the method developed by L. Hammond (Queensland Brain Institute, The University of Queensland, Australia), available at <https://theolb.readthedocs.io/en/latest/imaging/measuring-cell-fluorescence-using-imagej.html>, accessed on 30 October 2020, as follows:  $CTCF = \text{integrated density} - (\text{area of selected cell} \times \text{mean fluorescence of background readings})$ . Lastly, cytoplasmic CTCF values were calculated using the following formula:  $CTCF_{\text{cytoplasm}} = CTCF_{\text{whole cell}} - CTCF_{\text{nucleus}}$ . Identical microscopic and software parameter settings were then applied for each color channel. The color correction of images was occasionally performed when photomicrographs were prepared for publication. Statistical comparisons were made using SigmaPlot (v. 12.3, Systat Software Inc., Chicago, IL, USA), and the data values were analyzed using Kruskal–Wallis one-way ANOVA on ranks followed by Dunn’s method for pairwise multiple comparisons of differences between groups; the significance was set at  $p < 0.05$ . Data values are presented as the mean  $\pm$  SEM.

The fluorescent microbeads were counted under the microscope with 20 $\times$  and 40 $\times$  objectives; 100 random fields with a total of 1690 bead-labeled cells were counted and the number of phagocytosed microbeads (mean  $\pm$  SEM) was quantitatively analyzed. Statistical comparisons were made using SigmaPlot and data were analyzed with a Kruskal–Wallis one-way analysis of variance on ranks, followed by Dunn’s method for pairwise multiple comparison procedures for statistically significant differences between the experimental groups.

## 4. RESULTS

### 4.1. KYNA and SZR104 downregulate LPS-induced CXCL10 levels while differentially altering CCR1 levels

In CD11b/c-labeled microglial cells taken from unchallenged (control) and treated microglia-enriched secondary cell cultures (subDIV7), there was a robust increase in the amount of immunoreactivity of the inflammation marker CXCL10 in LPS-treated microglia (**Figure 7**). Following an LPS immunochallenge, typical amoeboid morphology was observed (**Figure 7F**) with CXCL10 immunoreactivity localized in the cytoplasm (**Figure 7G**). Treatments with

KYNA or SZR104 (a brain-penetrable KYNA analog), either alone or in combination with LPS, reduced CXCL10 immunoreactivity to unchallenged levels (**Figure 7K,O,S,W**). Moreover, quantitative light microscopic microdensitometric analysis of CXCL10 protein expression revealed that LPS challenge significantly elevated CXCL10 immunoreactivity (approximately fourfold) in microglial cells, whereas KYNA alone, SZR104 alone, or either combined with LPS significantly depleted the CXCL10 immunoreactive signal to control (unchallenged) levels (**Figure 8**). A similar but weaker response was recorded when the immunoreactivity of CCR1, another inflammation marker, was tested in control and treated cells. A localization analysis in CD11b/c-labeled microglial cells revealed slightly increased CCR1 immunoreactivity in LPS-challenged cultures (**Figure 9G**) relative to that observed in the control (**Figure 9C**). A quantitative light microscopic microdensitometric analysis of the cellular CCR1 levels of the cultures showed that an LPS challenge significantly elevated CCR1 immunoreactivity by 48%, whereas KYNA or SZR104 alone, or the combined treatment with LPS + KYNA, proved ineffective (**Figure 10A**). Interestingly, the combined treatment of LPS + SZR104 significantly lowered CCR1 immunoreactivity as compared to LPS-treated cultures, and it reverted to a level observed in unchallenged (control) cultures. A quantitative western blot analysis revealed that cytoplasmic CCR1 immunoreactivity was significantly increased after LPS treatment (**Figure 10B**). KYNA or SZR104, either alone or in combination with LPS, did not noticeably affect CCR1 levels.

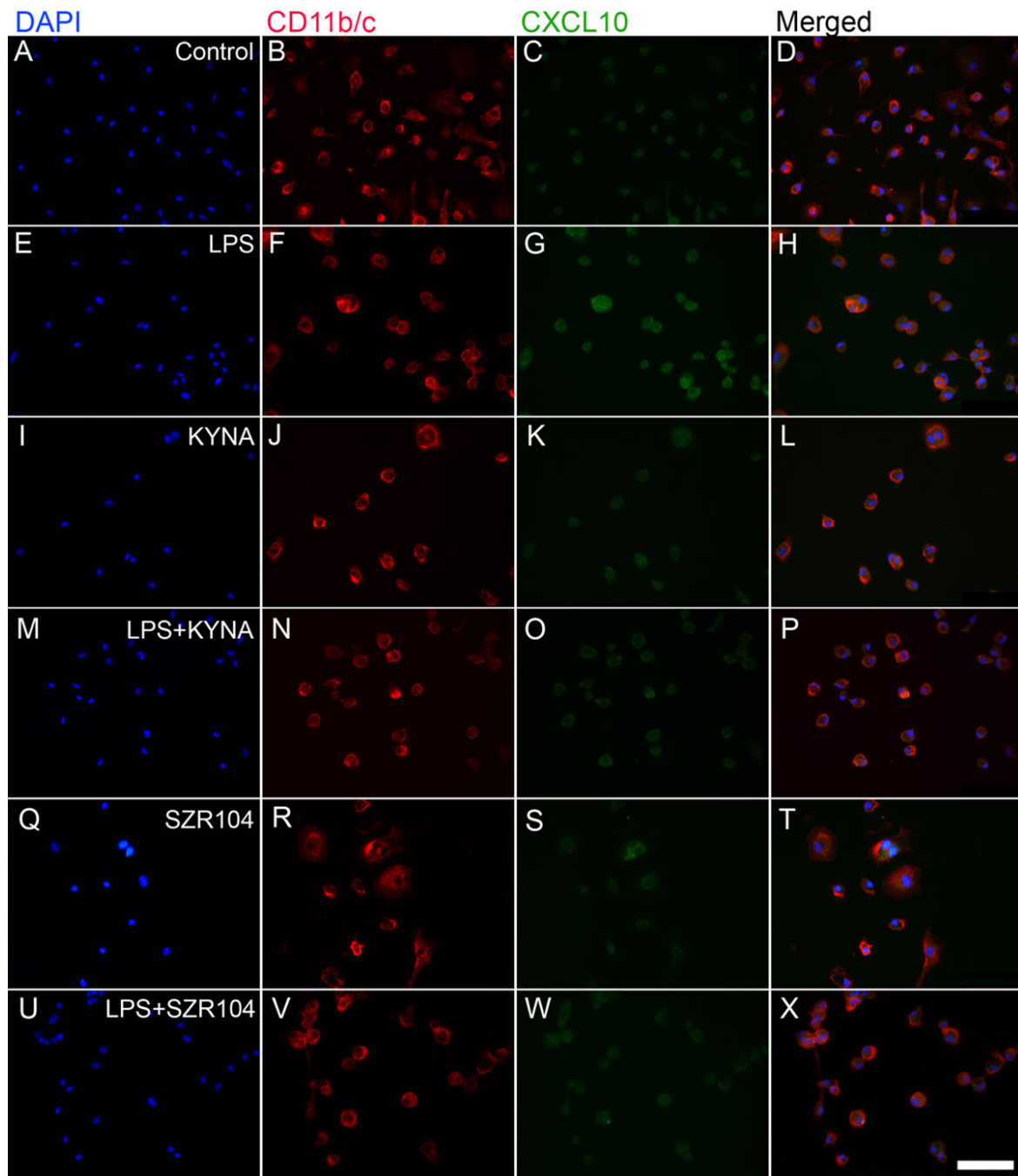


**Figure 7. Localization of CXCL10 immunoreactivity in CD11b/c-labeled microglia in unchallenged and treated microglia-enriched cultures.** The distribution of CD11b/c (red) and CXCL10 (green) immunoreactivities and their colocalizations is shown. The anti-CD11b/c antibody was used to highlight microglial cells. Note the very high purity of the microglial cultures (DAPI vs. CD11b/c labels). The following cultures (subDIV7) were used: (A–D) unstimulated (control), (E–H) LPS-challenged, (I–L) KYNA-treated, (M–P) LPS + KYNA-treated, (Q–T) SZR104-treated, and (U–X) LPS + SZR104-treated cultures. Cell nuclei are labeled with DAPI (blue). CXCL10 immunoreactivity was more intensive after LPS treatment in microglia; KYNA and SZR104 decreased the amount of CXCL10 in these cells. No visible cell loss was observed after the treatments were applied. This agrees with the findings of Steiner et al. (2014), who found there was no effect on cell viability when microglial cells were treated with KYNA. LPS: 20 ng/mL; KYNA: 1  $\mu$ M; and SZR104: 1  $\mu$ M. Scale bar: 75  $\mu$ m.

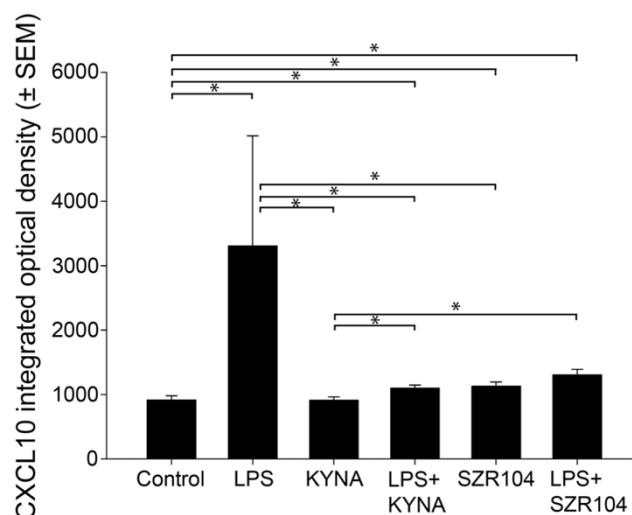


**Figure 8. Quantitative light microscopic microdensitometric analysis of CXCL10 protein expression in unchallenged and treated microglia-enriched cultures.** The LPS challenge significantly elevated cytoplasmic CXCL10 immunoreactivity (approximately fourfold) in microglial cells, whereas KYNA alone, SZR104 alone, or the combined treatments significantly weakened the CXCL10 immunoreactive signal to levels observed in unchallenged (control) cells. LPS: 20 ng/mL; KYNA: 1  $\mu$ M; and SZR104: 1  $\mu$ M. Data (presented as means  $\pm$  SEMs) were analyzed using Kruskal–Wallis one-way ANOVA on ranks: \*  $p < 0.05$ .

#### 4.2. KYNA and SZR104 inhibit microglial phagocytosis

The treatment of the secondary microglial cultures with LPS increased the phagocytotic activity of the microglia cells significantly (**Figures 11 and 12**). The unstimulated cultured microglia cells display a basal phagocytotic activity: the number of microbeads in a single cell is regularly two (**Figures 11 and 12**). Following the LPS challenge, this number rises sharply up to nine per single cell (**Figures 11 and 12**). Treatment of the cell culture with KYNA and SZR104 before the LPS challenge prevented the increase in the number of phagocytosed microbeads; the phagocytotic activity of the microglia in these cases remained at the control level (**Figures 11 and 12**). The inhibitory effects of KYNA and SZR104 were statistically significant (**Figure 12**). Furthermore, quantitative western blot analysis of Iba1 expression demonstrated that the Iba1 content of the secondary cultures did not change significantly following the different pharmacological (LPS, KYNA and SZR104) treatments (**Figure 13**).

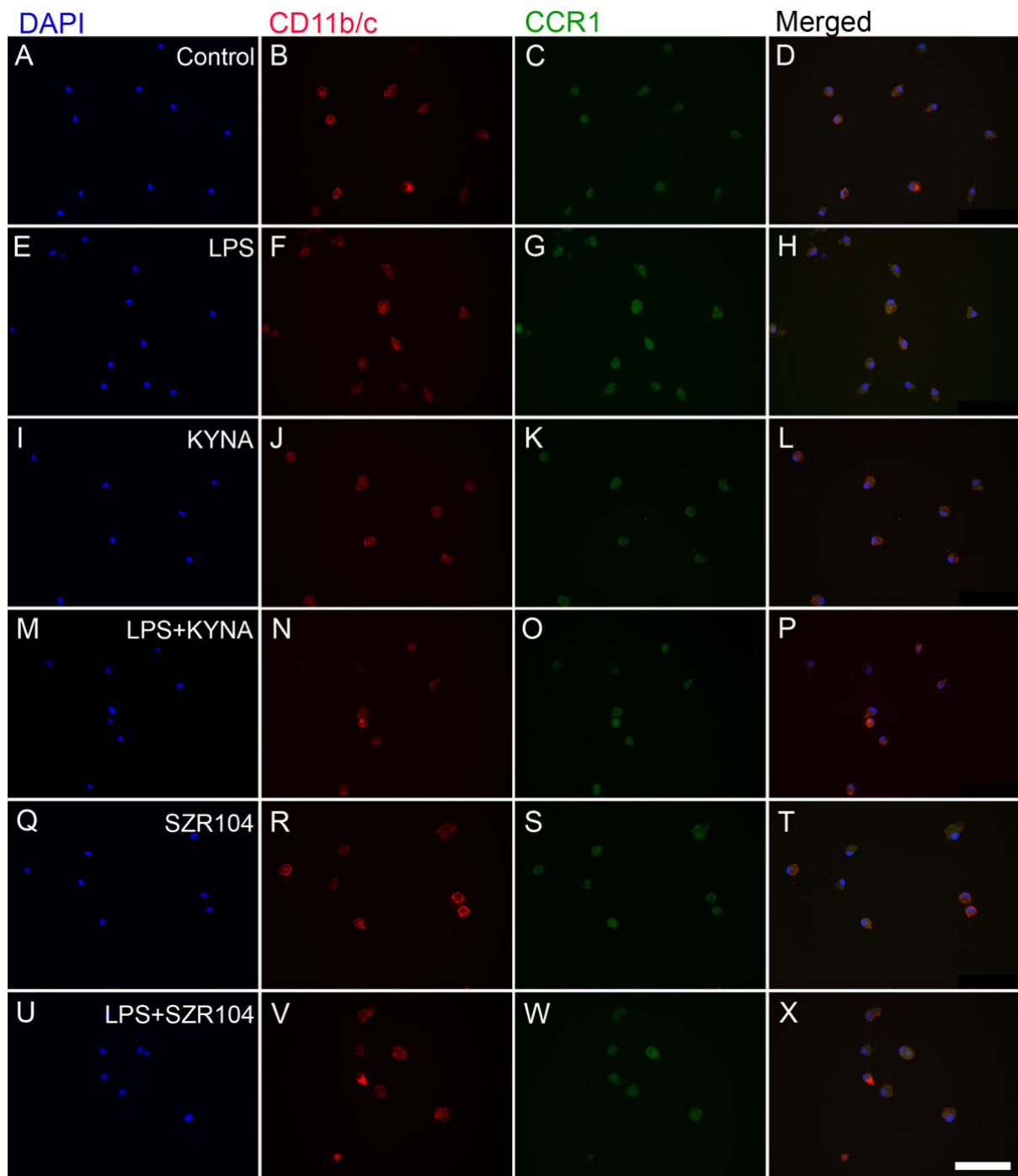


**Figure 9. Localization of CCR1 immunoreactivity in CD11b/c-labeled microglia in unchallenged and treated microglia-enriched cultures.** The distribution of CD11b/c (red) and CCR1 (green) immunoreactivities, as well as their colocalizations, is shown. The anti-CD11b/c antibody was used to highlight microglial cells. Cell nuclei are labeled with DAPI (blue). Note the very high purity of the microglial cultures (DAPI vs. CD11b/c labels). The following cultures (subDIV7) were used: (A–D) unstimulated (control), (E–H) LPS-challenged, (I–L) KYNA-treated, (M–P) LPS + KYNA-treated, (Q–T) SZR104-treated, and (U–X) LPS + SZR104-treated cultures. Representative immunocytochemical images confirm that the LPS challenge (G) slightly increased CCR1 immunoreactivity in microglial cells compared with that in unchallenged (control) cells (C), but the level of the immunoreactive signal returned to control levels with KYNA (K), SZR104 (S), or combined treatments (O, W). LPS: 20 ng/mL; KYNA: 1  $\mu$ M; and SZR104: 1  $\mu$ M. Scale bar: 75  $\mu$ m.

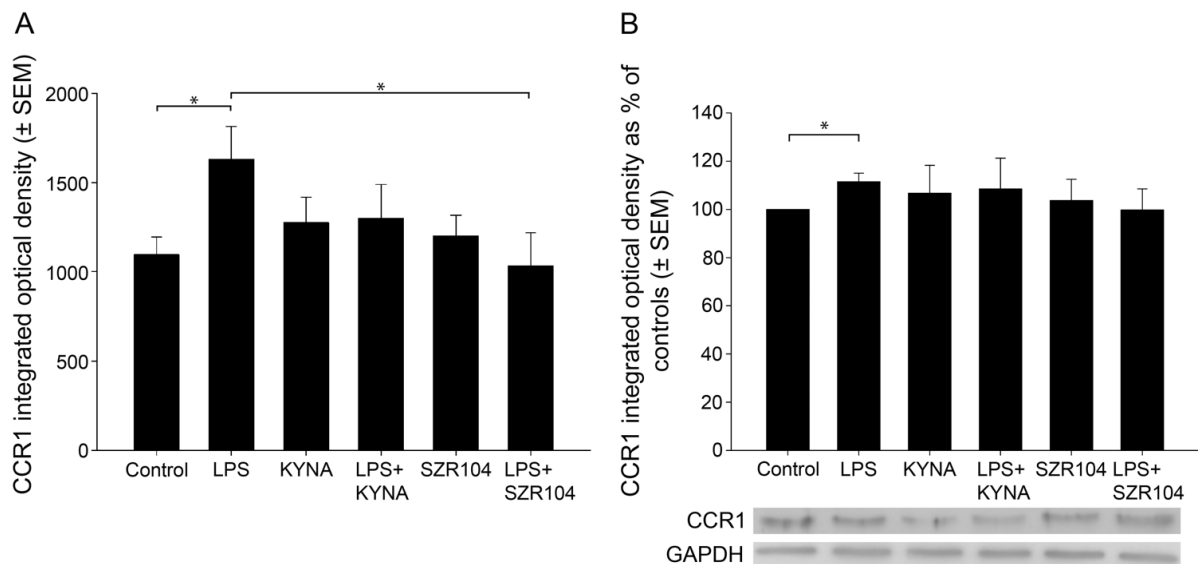


**Figure 10. Quantitative analysis of CCR1 protein expression in unchallenged and treated microglia-enriched cultures.** (A) A quantitative light microscopic microdensitometric analysis of CCR1 protein expression. The LPS challenge significantly elevated CCR1 immunoreactivity to approximately 148% of the control value in microglial cells, whereas KYNA or SZR104 alone, or the combined treatment of LPS + KYNA, did not significantly alter the amount of CCR1 immunoreactive signal compared to controls. However, LPS + SZR104-treated cultures displayed significantly lowered CCR1 levels compared to LPS-treated cultures, and they returned to levels seen in unchallenged (control) cells. Data (presented as means  $\pm$  SEMs) were analyzed with the Mann–Whitney rank sum test: \*  $p < 0.05$ . (B) A quantitative western blot analysis of cytoplasmic CCR1 immunoreactivity. Representative images of western blots are shown below the graph, together with the GAPDH immunoreactive bands that served as protein load control. Protein samples were collected from at least five separate cultures, electrophoresed, and then quantitatively analyzed, as described in the Materials and Methods section. CCR1 immunoreactivity significantly increased after the LPS treatment. It did not change when the cultures were treated with LPS + KYNA or LPS + SZR104. Error bars indicate integrated optical density values with the data values for each group expressed as a percentage of the control values. LPS: 20 ng/mL; KYNA: 1  $\mu$ M; and SZR104: 1  $\mu$ M. Integrated optical density data (presented as means  $\pm$  SEMs) were analyzed with the Mann–Whitney rank sum test: \*  $p < 0.02$ .

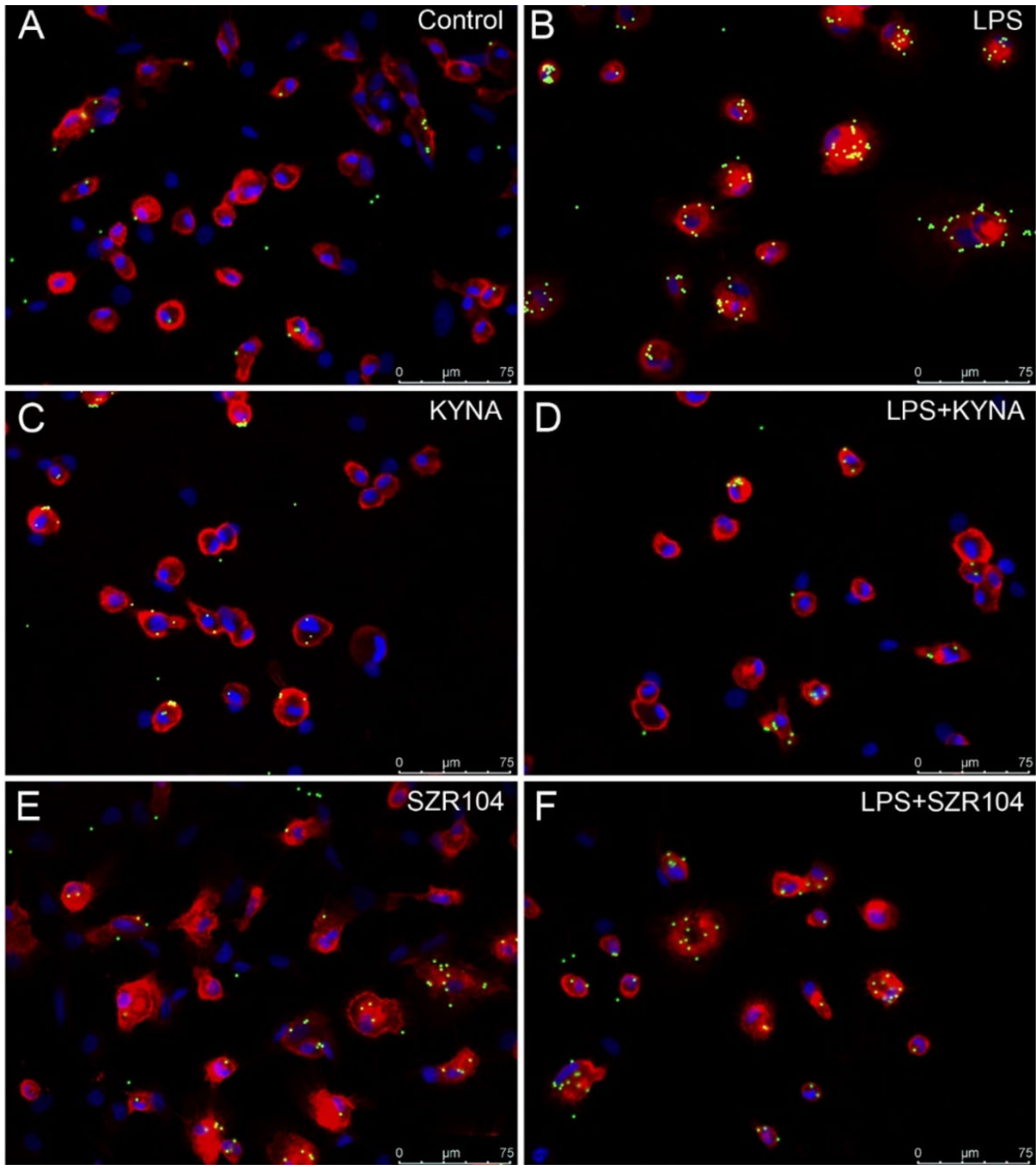


**Figure 11. Effects of KYNA and SZR104 on the phagocytic activity of microglial cells in cultures.** Pictures showing CD11b/c-immunostained microglia in red, microbeads in green and cell nuclei in blue. (A) Unstimulated and untreated control; (B) lipopolysaccharide (LPS)-challenged cells; (C) KYNA-treated; (D) LPS + KYNA-treated; (E) SZR104-treated; (F) LPS + SZR104-treated. Microglia displayed different phagocytotic activity, as evidenced by the number of phagocytosed microbeads. Scale bar: 75 μm.

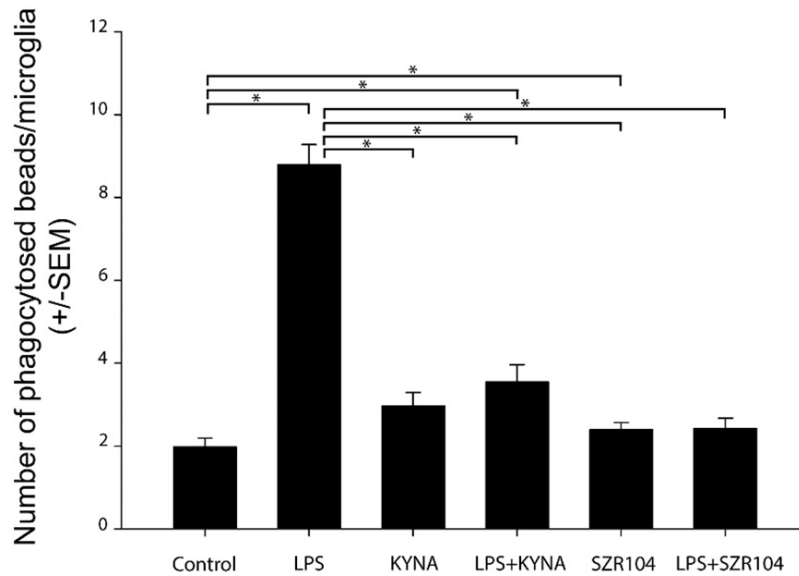


**Figure 12. Quantitative analysis of the number of phagocytosed microbeads after the pharmacological treatments demonstrated that KYNA and SZR104 significantly inhibited microglial phagocytosis.** The number of phagocytosed beads (n = 240; mean ± SEM) was counted in three separate culturing procedures. Data were analyzed with Kruskal–Wallis one-way analysis of variance on ranks. \* p < 0.05.

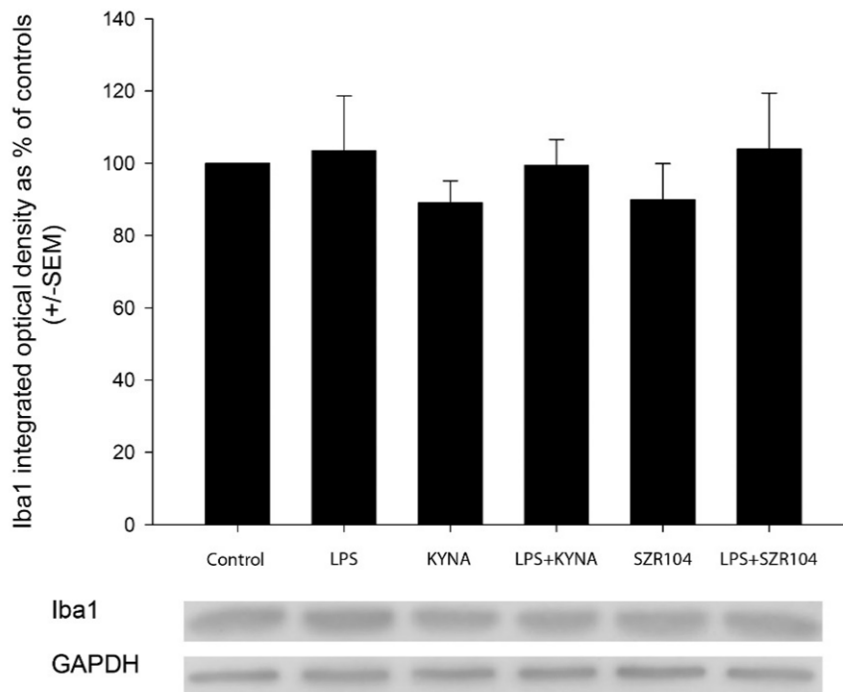


**Figure 13. Quantitative Western blot analysis of Iba1 and glyceraldehyde-3-phosphate dehydrogenase (GAPDH) immunoreactivities in microglia cell cultures.** Error bars indicate integrated optical density values as percent of controls (n = 4; mean ± SEM). Representative Western blot images are shown below the graphs. Data were analyzed with a one-way ANOVA. No statistically significant differences were found.

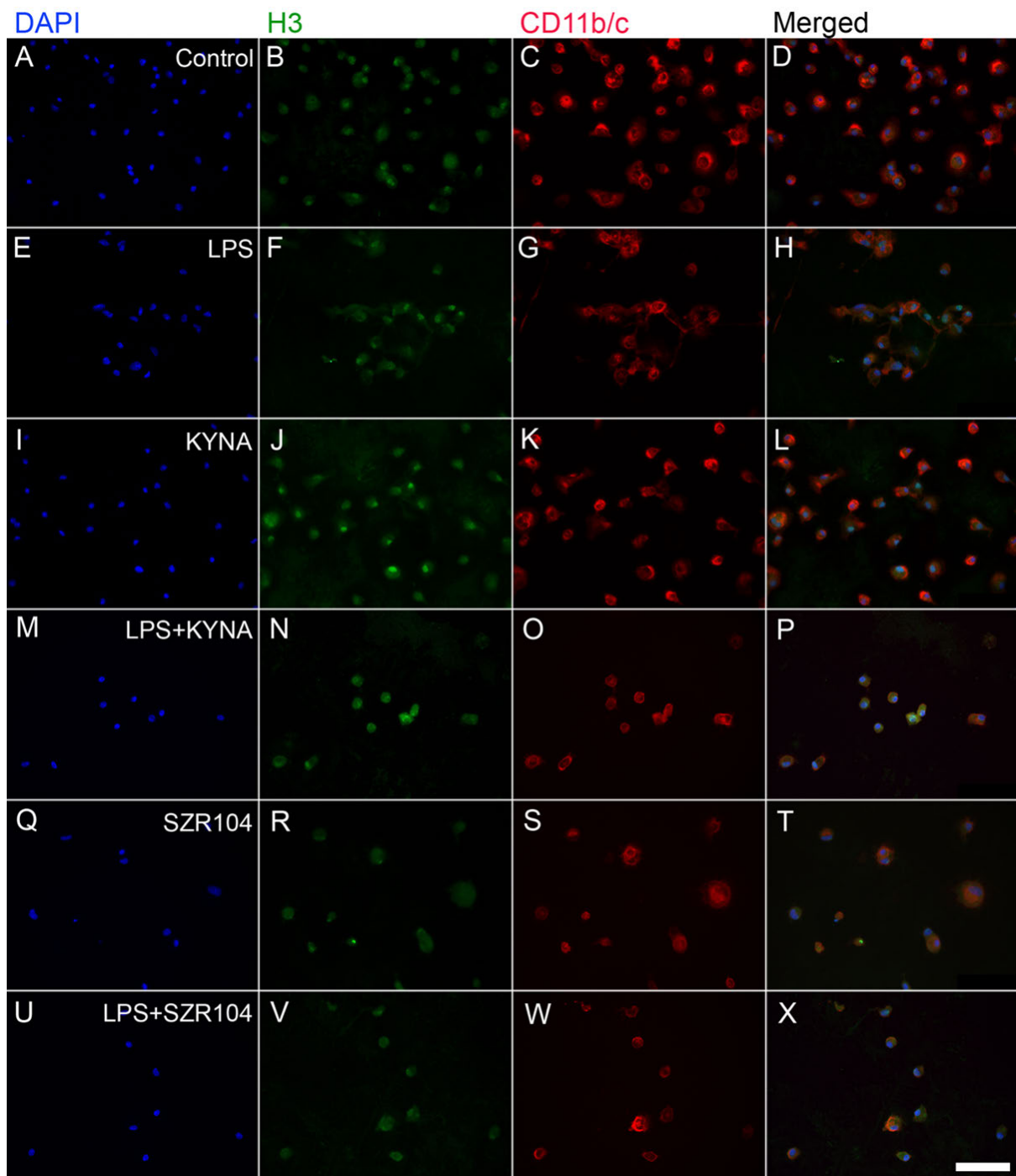


**Figure 14. Localization of histone H3 protein immunoreactivity in unchallenged and treated microglia enriched cultures.** Representative immunocytochemical images demonstrate the intracellular distribution of histone H3 protein immunopositivity (green) in unstimulated (control) (A–D), LPS-challenged (E–H), KYNA-treated (I–L), LPS + KYNA-treated (M–P), SZR104-treated (Q–T), and LPS + SZR104-treated (U–X) CD11b/c-immunopositive microglial cells (red). The anti-CD11b/c antibody was used to highlight microglial cells. Note the very high purity of the microglial cultures (DAPI vs. CD11b/c labels). Histone H3 was detected in both the nucleus and cytoplasm of microglia. Cell nuclei are labeled with DAPI (blue). LPS: 20 ng/mL; KYNA: 1  $\mu$ M; and SZR104: 1  $\mu$ M. Scale bar: 75  $\mu$ m.

### 4.3. KYNA and SZR104 alter the intracellular histone H3 distribution and H3 lys methylation patterns

Unmodified histone H3 levels were monitored because they form a pool for further PTMs. H3 immunoreactivity was detected in both the cytoplasm and the nucleus of unchallenged microglia; that is, after nuclear import, histone H3 mostly accumulated in the nucleus (**Figure 14A–D**). We did not detect extracellular histone signals in these studies. Interestingly, most of the experimental manipulations of the cells, except for the LPS + SZR104 treatments, resulted in the increased accumulation of histone H3 in both the nuclear and the cytoplasmic compartments, indicating that both compounds elevated *de novo* synthesis and increased nuclear import (**Figures 14E–X**). Of these treatments, KYNA produced the strongest nuclear accumulation of unmodified H3 immunoreactivity (**Figure 14J**). When LPS and SZR104 treatments were combined, however, neither the nuclear nor the cytoplasmic H3 immunoreactivities were different from the controls (**Figure 15**). Quantitative densitometry of H3 immunosignals on cultured microglia corroborated these findings (**Figure 16A**). The CTCF values for nuclear localization increased significantly only after LPS or KYNA treatments, compared to controls, but decreased significantly after the combined treatments of LPS + KYNA and LPS + SZR104, as compared to LPS-challenged cultures (**Figure 16A**). In contrast, CTCF values for cytoplasmic localization were higher in all experimental groups except for the LPS + SZR104 treatment case (**Figure 16B**). Moreover, cytoplasmic H3 levels were affected differently by the combined treatments, i.e., LPS + KYNA increased, while LPS + SZR104 returned cytoplasmic H3 levels to controls (**Figures 15J and 16B**). The nuclear and cytoplasmic histone H3 distributions elicited by the LPS + SZR104 treatment were rather like those of unchallenged microglia.

However, when the amount of unmodified cytoplasmic histone H3 was quantitatively analyzed *via* western blots, only the LPS + KYNA treatment showed a significant increase (**Figure 17**). This might be due to denaturing conditions in detecting histone H3 proteins in westerns that concealed the changes observed in multicolor immunocytochemistry when individually identified microglia were analyzed. Our analysis of the intracellular localization of H3K9me3 immunoreactivity in CD11b/c labeled microglia in unchallenged (control) and variably treated microglia-enriched secondary cell cultures (subDIV7) demonstrated that LPS challenge (**Figures 18E–H and 19F**) increased H3K9me3 immunopositivity relative to that observed in the unchallenged control (**Figures 18A–D and 19B**) or other treatments (**Figure 18I–X**).

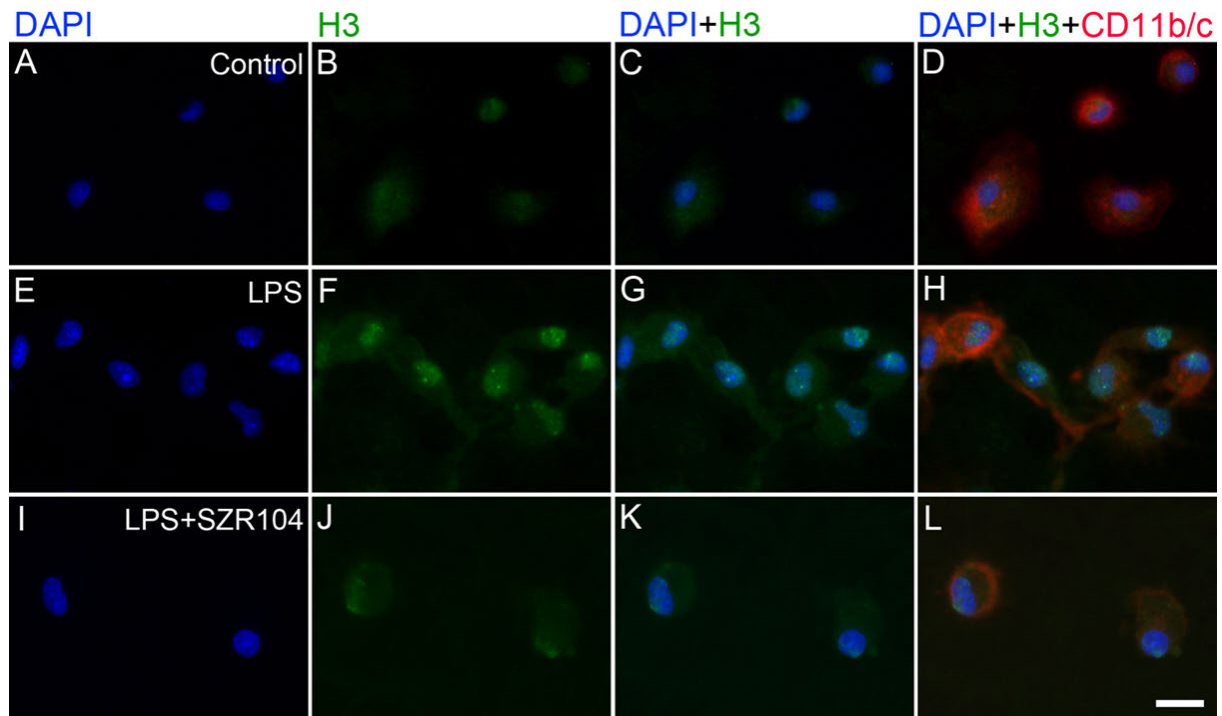


**Figure 15. Intracellular localization of histone H3 protein immunoreactivity in unchallenged and treated microglia-enriched cultures.** Representative enlarged immunocytochemical images showing a subset of microglial cells from Figure 14 demonstrate the intracellular distribution of histone H3 immunopositivity (green) in unstimulated (control) (A–D), LPS-challenged (E–H), and LPS + SZR104- treated (I–L) CD11b/c-immunopositive microglial cells (red). The anti-CD11b/c antibody was used to highlight microglial cells. After LPS treatment (F), unmodified histone H3 was detected in both the nucleus and cytoplasm of microglia. LPS + SZR104 treatments lowered both nuclear and cytoplasmic H3 immunosignal. Cell nuclei are labeled with DAPI (blue). Scale bar: 15  $\mu$ m.

Strong histone H3K9me3 immunoreactivity was detected in both the nucleus and cytoplasm after the LPS challenge (Figures 18F and 19F) but decreased when LPS treatment was combined with KYNA or SZR104 (Figure 19J). Quantitative fluorescent microdensitometry revealed that the nuclear accumulation of H3K9me3 protein increased significantly after LPS treatment but that the LPS + KYNA or LPS + SZR104 treatments reduced this accumulation (Figures 19J and 20A). However, the effect of KYNA alone did not differ significantly from that of the control. By contrast, SZR104 had a greater inhibiting effect on the extranuclear translocation of H3K9me3. Similar values and tendencies were noted when cytoplasmic H3K9me3 was analyzed (Figure 20B): KYNA or SZR104, either alone or in combination with LPS, was able to recover LPS-induced cytoplasmic accumulation of H3K9me3 protein. Furthermore, SZR104 was found to be more potent than KYNA in inhibiting H3K9me3 translocation to the cytoplasm (Figure 20B).

When the intracellular distribution of H3K36me2 immunoreactivity in CD11b/c labeled microglia was measured, a marked increase, relative to unchallenged control levels (**Figure 21A–D**), was seen exclusively within the nuclei of the microglia after LPS challenge (**Figures 21E–H and 22F**). By contrast, the other treatments did not affect H3K36me2 immunoreactivity appreciably (**Figure 21I–X**). For example, LPS + SZR104 treatments returned the nuclear levels of H3K36me2 to the control levels (**Figure 22J**). A quantitative microdensitometric analysis of H3K36me2-immunopositive signals revealed that LPS treatment dramatically increased the amount of H3K36me2 signal in the nuclei of CD11b/c labeled microglial cells, whereas the other treatments had only a minor effect. Moreover, KYNA or SZR104 alone, or the combination treatments, had significantly lower H3K36me2 signals compared to LPS-challenged levels (**Figure 23**).

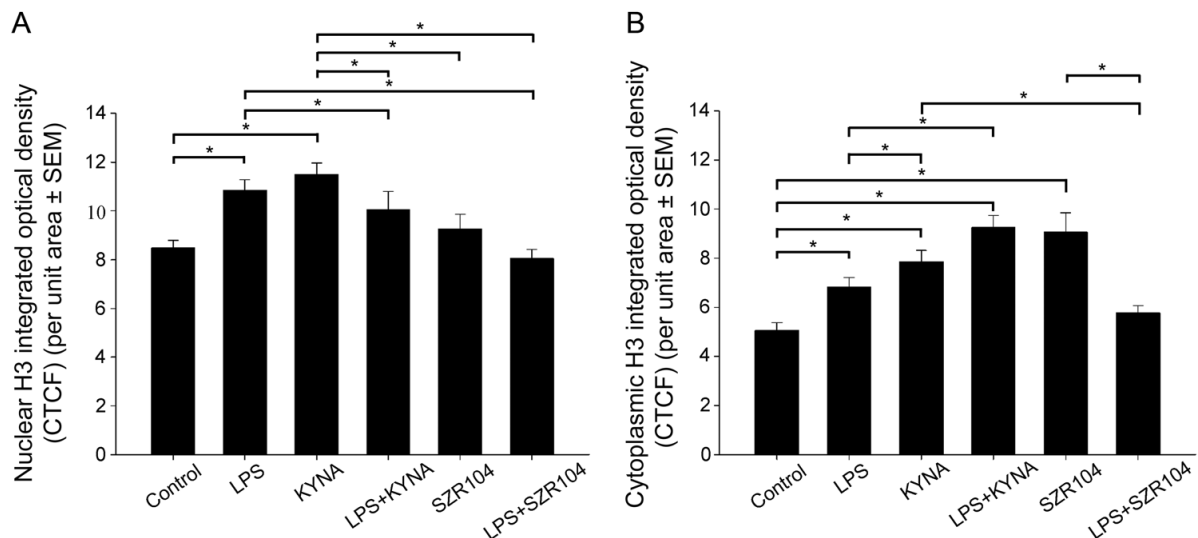


**Figure 16. Intracellular distribution of unmodified histone H3 protein immunoreactivity in the nucleus and cytoplasm of microglia in unchallenged and treated microglia-enriched cultures.** Corrected total cell fluorescence (CTCF) values for the whole cell, nucleus, and cytoplasm were calculated as described in the Materials and Methods section. **(A)** The amount of H3 immunoreactivity rose significantly in the nucleus of LPS- and KYNA-treated microglia. SZR104 effectively decreased the amount of histone H3 after LPS treatment. **(B)** Except for the LPS + SZR104 treatment, all the treatments increased the amount of unmodified cytoplasmic histone H3. LPS: 20 ng/mL; KYNA: 1  $\mu$ M; and SZR104: 1  $\mu$ M. Data (presented as means  $\pm$  SEMs) were analyzed with Kruskal–Wallis one-way ANOVA on ranks: \*  $p < 0.05$ .

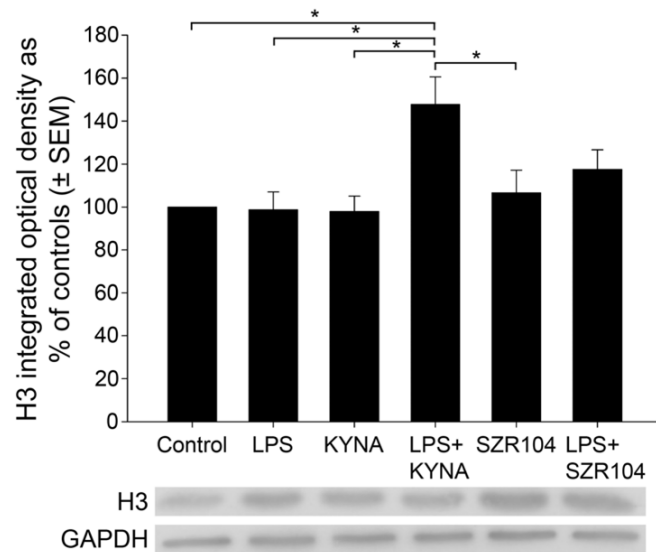


**Figure 17. Quantitative western blot analysis of the cytoplasmic histone H3 protein level in microglia enriched cultures.** Representative images of western blots are shown below the graph, together with the GAPDH immunoreactive bands that served as inner standards. Protein samples were collected from at least five separate cultures (subDIV7), electrophoresed, and quantitatively analyzed as described in the Materials and Methods section. The combined LPS + KYNA treatment induced a significant increase in histone H3 immunoreactivity when compared with that in control (unchallenged) and other treated cultures. The error bars indicate integrated optical density values with data expressed as a percentage of the control values. LPS: 20 ng/mL; KYNA: 1  $\mu$ M; and SZR104: 1  $\mu$ M. Data values (presented as means  $\pm$  SEMs) were analyzed using ANOVA followed by pairwise multiple comparisons (Holm–Sidak method): \*  $p < 0.05$ .

## 5. DISCUSSION

The endogenous kynurenine system is implicated in the functioning of the immune system. Recent studies showed that the amounts of several inflammation-related marker proteins decreased after treatments with KYNA or its analogs. For example, it was demonstrated by Mándi et al. (2019) and Lajkó et al. (2020) that KYNA and several KYNA analogs, including SZR104, interfered with immune functions *in vivo* and *in vitro*. KYNA and SZR104 attenuated tumor necrosis factor- $\alpha$  (TNF- $\alpha$ ) production and increased tumor necrosis factor-stimulated gene-6 (TSG-6) mRNA expression in U-937 cells stimulated with heat-inactivated *Staphylococcus aureus* (Mándi et al., 2019). Another potent proinflammatory cytokine, interleukin-1 $\beta$ , was elevated in sepsis but was ameliorated by KYNA and its synthetic analogues SZR72 (2-(2-N,N-dimethylaminoethylamine-1-carbonyl)-1H-quinolin-4-one hydrochloride) and SZR104 (Poles et al., 2021). Furthermore, SZR72 inhibited the production of several inflammatory mediators in blood cultures of rheumatoid arthritis patients (Balog et al., 2021).

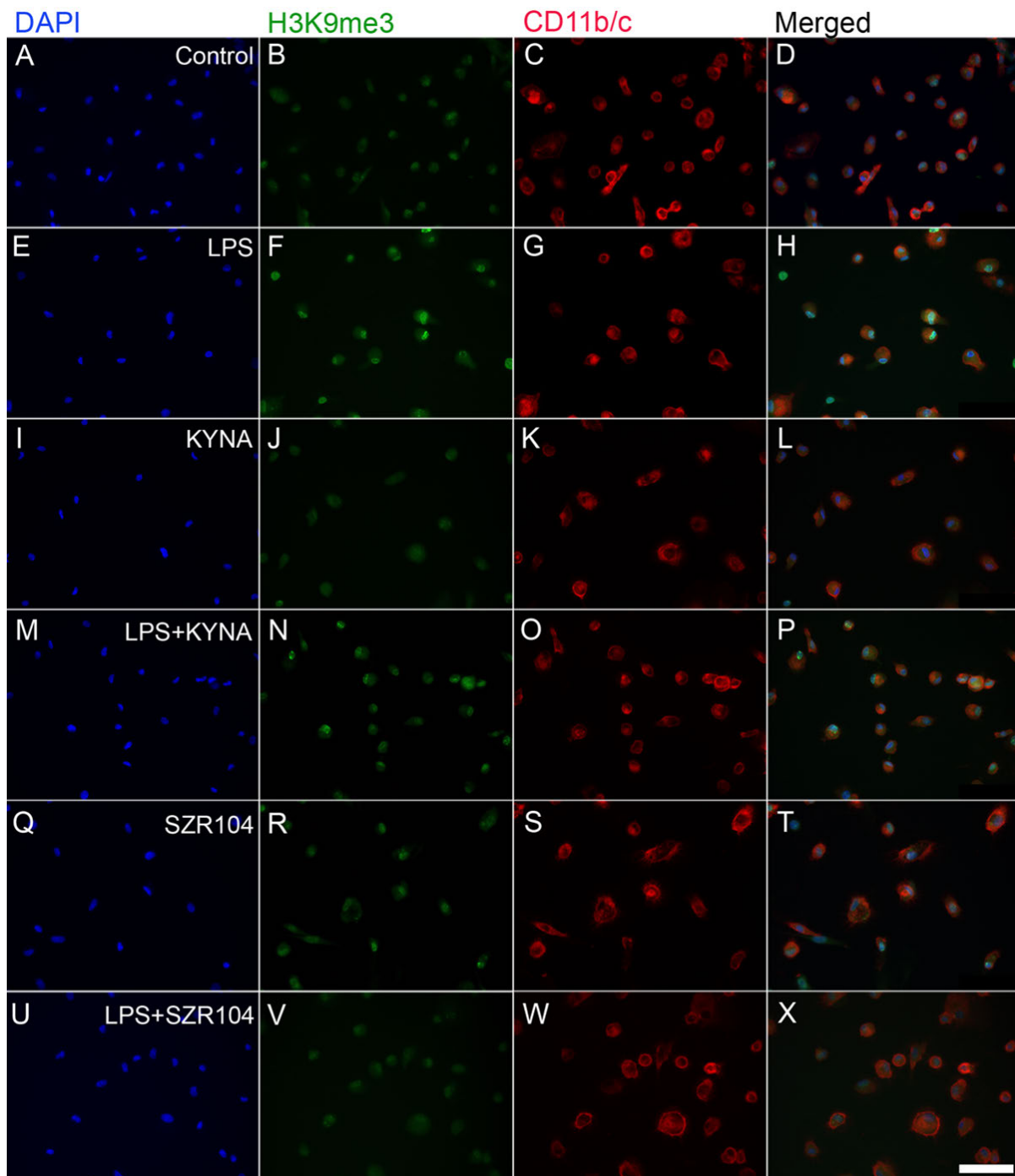


**Figure 18. Localization of H3K9me3 immunoreactivity in CD11b/c-labeled microglia in unchallenged and treated microglia-enriched cultures.** Representative immunocytochemical images showing the intracellular distribution of histone H3K9me3 protein immunopositivity (green) in unstimulated (control) (A–D), LPS-challenged (E–H), KYNA-treated (I–L), LPS + KYNA-treated (M–P), SZR104- treated (Q–T), and LPS + SZR104-treated (U–X) CD11b/c-immunopositive microglial cells (red). The anti-CD11b/c antibody was used to highlight microglial cells. The very high purity of the microglial cultures is evident (DAPI (blue) vs. CD11b/c label (red)). Note that LPS challenge (F) increased the H3K9me3 immunopositivity relative to that in unchallenged controls (B) or other treatments. Histone H3K9me3 was detected in both the nucleus and cytoplasm. LPS: 20 ng/mL; KYNA: 1  $\mu$ M; and SZR104: 1  $\mu$ M. Scale bar: 75  $\mu$ m.

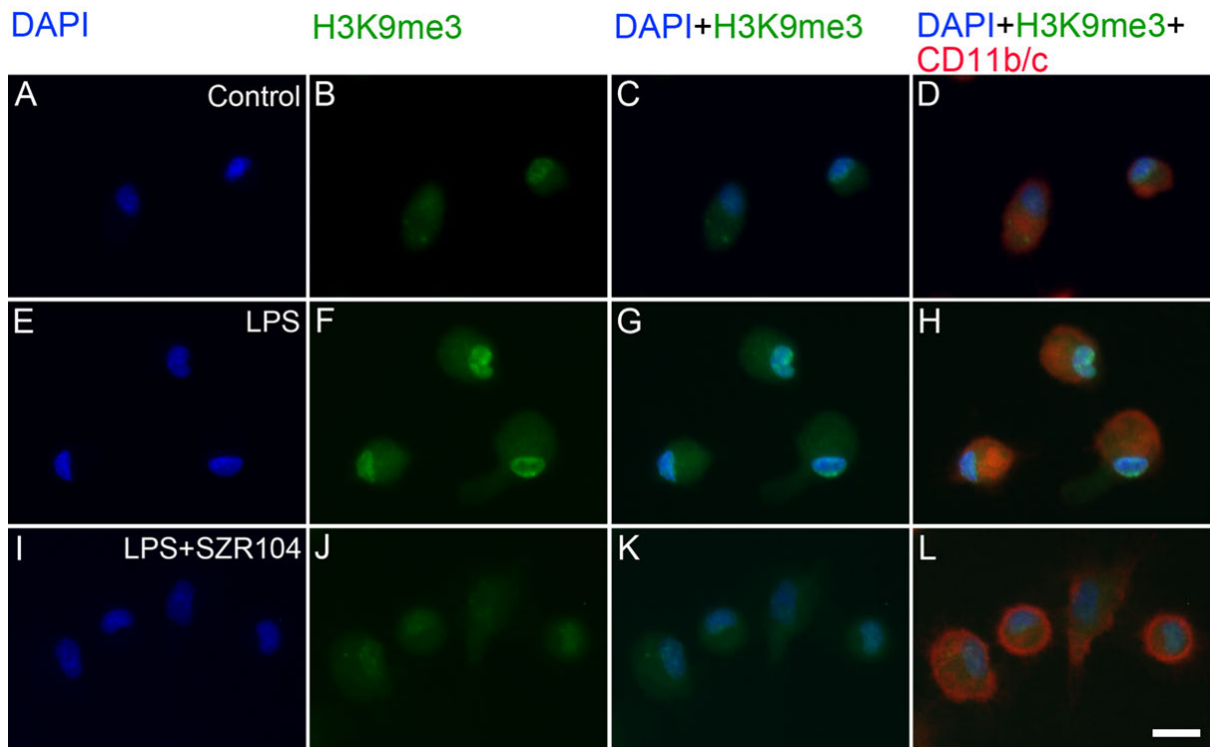


**Figure 19. Intracellular localization of H3K9me3 immunoreactivity in CD11b/c-labeled microglia in unchallenged and treated microglia-enriched cultures.** Representative enlarged immunocytochemical images showing a subset of microglial cells from Figure 18 demonstrate the intracellular distribution of histone H3K9me3 immunopositivity (green) in unstimulated (control) (A–D), LPS-challenged (E–H), and LPS + SZR104-treated (I–L) CD11b/c-immunopositive microglial cells (red). The anti-CD11b/c antibody was used to highlight microglial cells. After LPS treatment (F), increased amounts of H3K9me3 immunolabel were detected in both the nucleus and cytoplasm of microglia, although the nuclear component was more pronounced. LPS + SZR104 treatments lowered the amounts of both nuclear and cytoplasmic H3K9me3 immunosignal. Cell nuclei are labeled with DAPI (blue). Scale bar: 15  $\mu$ m.

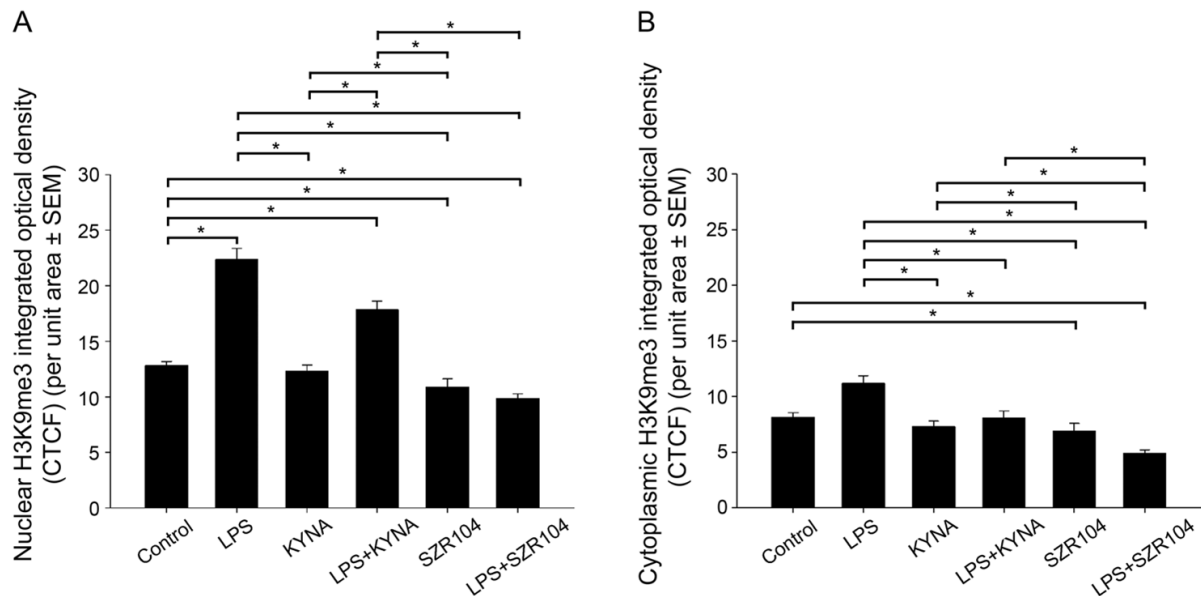


**Figure 20. Intracellular distribution of histone H3K9me3 protein immunoreactivity in the nucleus and cytoplasm of microglia in unchallenged and treated microglia-enriched cultures.** A quantitative microdensitometric analysis of H3K9me3-immunopositive signals in the nucleus (**A**) and cytoplasm (**B**) was performed, as described in the Materials and Methods section. (**A**) LPS treatment increased the amount of H3K9me3 signal in the nucleus, whereas KYNA and SZR104 treatment did not alter the signal compared to the control level. (**B**) Cytoplasmic H3K9me3 was reduced uniformly when cells were treated with KYNA, SZR104, or with a combination of treatments. LPS: 20 ng/mL; KYNA: 1  $\mu$ M; and SZR104: 1  $\mu$ M. Integrated density data values (presented as means  $\pm$  SEMs) were analyzed with Kruskal–Wallis one-way ANOVA: \*  $p < 0.05$ .

Interestingly, a possible role for IDO, a key kynurenine pathway enzyme, in immunity has recently emerged (Boros et al., 2019), further emphasizing the crucial role this system plays in immunomodulatory functions. As KYNA is a metabolite of the endogenous kynurenine system with proven antiinflammatory properties, we wanted to know whether its effect went beyond conventional targets in the intermediary metabolic or intracellular signaling pathways and perhaps had effects on phenomena such as epigenetics elicited through histone metabolism and/or intracellular transport. We sought to investigate (a) how KYNA and SZR104, a brain-penetrable analog of KYNA, behaves in our systems; (b) how phagocytic activity change in microglia cells; (c) how inflammatory signals affect histone methylations and, consequently, epigenetic changes; and (d) how the intracellular localization of unmodified and methylated histones change during inflammation or amelioration of inflammation.

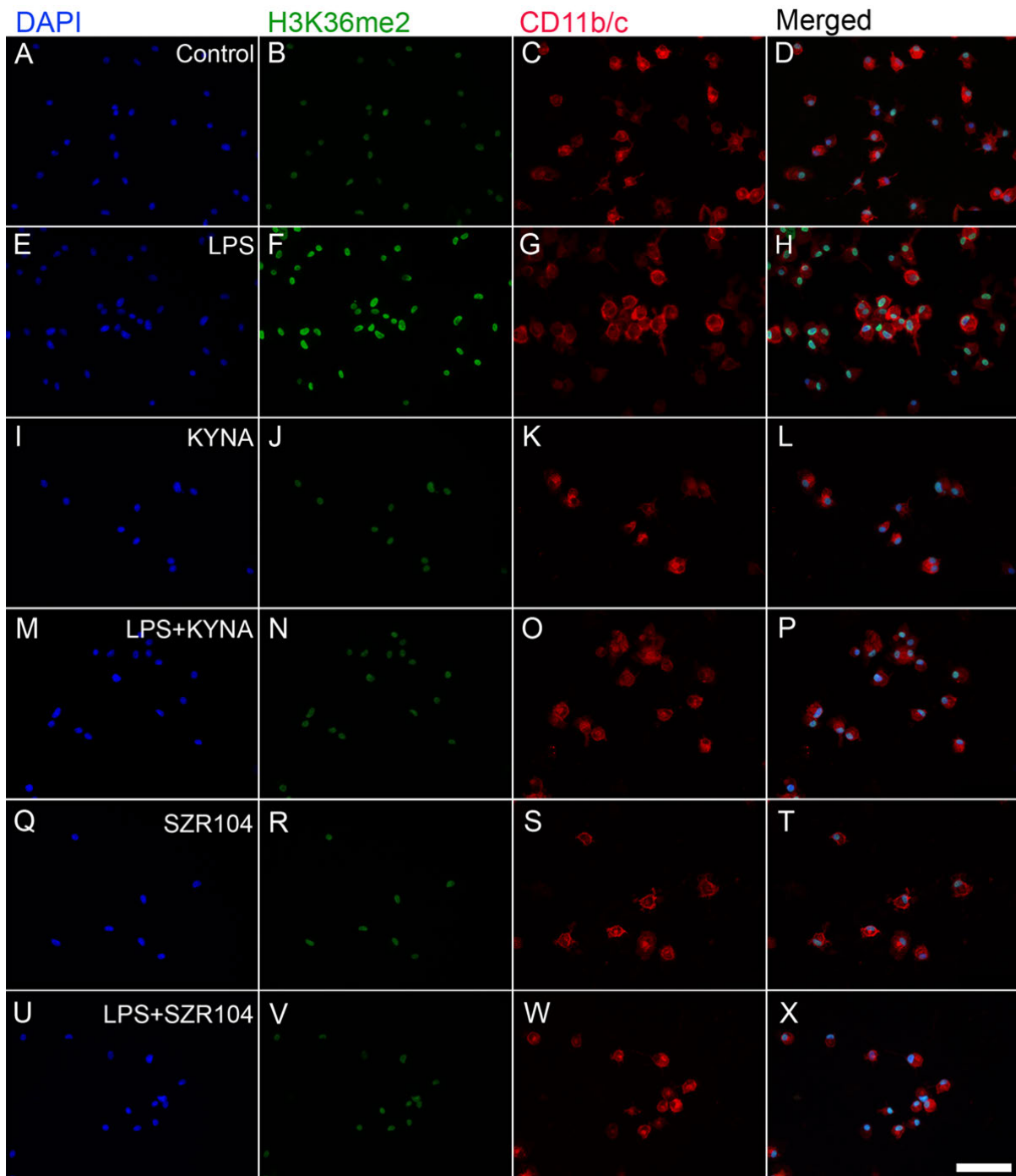


**Figure 21. Localization of H3K36me2 immunoreactivity in CD11b/c-labeled microglia in unchallenged and treated microglia-enriched cultures.** Representative immunocytochemical images showing the intracellular distribution of histone H3K36me2 protein immunopositivity (green) in unstimulated (control) (A–D), LPS-challenged (E–H), KYNA-treated (I–L), LPS + KYNA-treated (M–P), SZR104-treated (Q–T), and LPS + SZR104-treated (U–X) CD11b/c-immunopositive microglial cells (red). The anti-CD11b/c antibody was used to highlight microglial cells. The very high purity of the microglial cultures is evident (DAPI (blue) vs. CD11b/c labels). Note that the LPS challenge (E–H) markedly increased H3K36me2 immunopositivity relative to that of the unchallenged control (A–D) or any other treatment (I–X). Histone H3K36me2 was detected in the nucleus. LPS: 20 ng/mL; KYNA: 1  $\mu$ M; and SZR104: 1  $\mu$ M. Scale bar: 75  $\mu$ m.

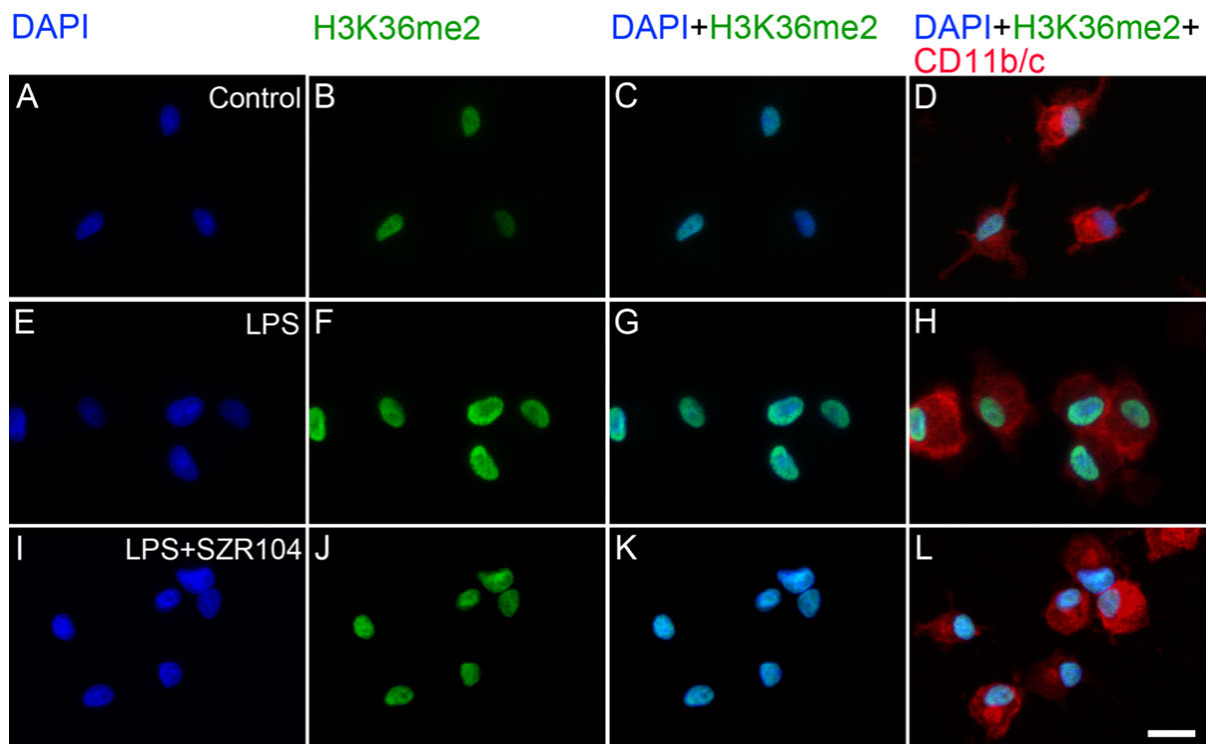


**Figure 22. Intracellular localization of H3K36me2 immunoreactivity in CD11b/c-labeled microglia in unchallenged and treated microglia-enriched cultures.** Representative enlarged immunocytochemical images showing a subset of microglial cells from Figure 21 demonstrate the intracellular distribution of histone H3K36me2 immunopositivity (green) in unstimulated (control) (A–D), LPS-challenged (E–H), and LPS + SZR104-treated (I–L) CD11b/c-immunopositive microglial cells (red). The anti-CD11b/c antibody was used to highlight microglial cells. After LPS treatment (F), increased amounts of H3K36me2 immunolabel were detected in the nucleus of microglia. There was no signal in the cytoplasm. LPS + SZR104 treatments lowered the amounts of nuclear H3K36me2 immunosignal (J). Cell nuclei are labeled with DAPI (blue). Scale bar: 15  $\mu$ m.

For the first time in the present study, KYNA and SZR104 were shown to exhibit strong antiinflammatory properties, as demonstrated by their effective amelioration of LPS-challenged CXCL10 and CCR1 production in microglial cultures. Our results agree with those of other studies that found similar CXCL10 reduction in activated microglia after treatment with antiinflammatory drugs (Hankittichai et al., 2020; Liu et al., 2019). We previously reported a similar downregulation of CCR1 after aspirin treatment in LPS-challenged microglial-enriched cultures (Kata et al., 2017). While KYNA and SZR104 were both effective in ameliorating the LPS-induced elevation of CXCL10 immunoreactivity, only the combined treatment with LPS + SZR104 was effective in significantly inhibiting CCR1 immunoreactivity in these tests. Structural differences between KYNA and SZR104 might be the reason these compounds produced somewhat different responses in immunocytochemical and western blot analyses. As

we used high-purity microglia, this was also the first time that we could identify microglia-specific immune responses to these compounds.

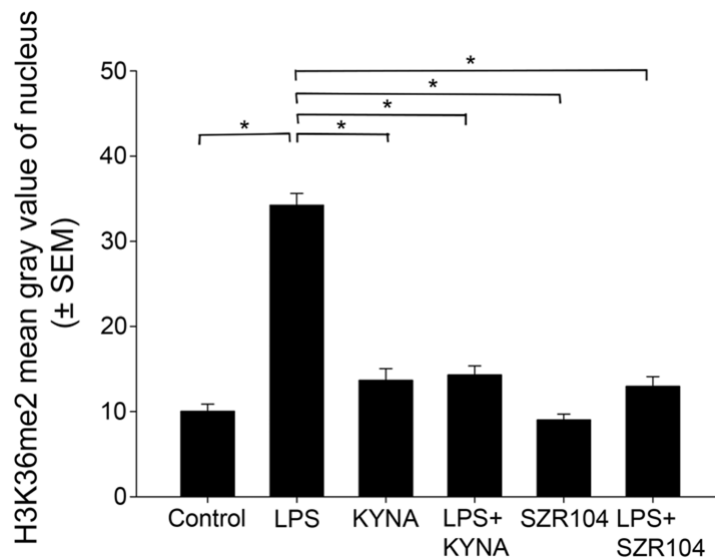


**Figure 23. Intracellular distribution of histone H3K36me2 protein immunoreactivity in the nucleus of microglia in unchallenged and treated microglia-enriched cultures.** A quantitative microdensitometric analysis of H3K36me2-immunopositive signals in the nucleus was performed as described in the Materials and Methods section. The LPS treatment dramatically increased the amount of the H3K36me2 signal in the nucleus, whereas KYNA, SZR104, or a combination of treatments decreased it toward the unchallenged control levels. LPS: 20 ng/mL; KYNA: 1  $\mu$ M; and SZR104: 1  $\mu$ M. The integrated density data values (presented as means  $\pm$  SEMs) were analyzed with Kruskal–Wallis one-way ANOVA on ranks: \*  $p < 0.05$ .

Previous data from our laboratory showed that cultured microglia cells stimulated with LPS displayed a large increase in phagocytosis of fluorescent microbeads (Kata et al., 2016; Szabó et al., 2013; Kata et al., 2017). The number of internalized microbeads increased more than four-fold in the LPS-stimulated cells probably due to stimulation through Toll-like receptor 4 (TLR4) and transient receptor potential ankyrin 1, 4 receptors (TRPA1, TRPA4) (Startek et al., 2018). These receptors mediated those membrane and cytoplasmic processes which lead to phagocytosis; they increase  $Ca^{++}$  permeability of the membrane and increase the cytoplasmic cation concentrations (TRPA effects), and exert regulatory effects on gene expression (TLR4 effect). Treatments of the cells with KYNA and SZR104 prevented the increase in phagocytotic activity elicited by LPS. We speculate that during *in vitro* exposure, KYNA and SZR104 prevented the actions of LPS mainly through the repression of TLR4 by the deregulation of inflammation-related genes, consequently preventing phagocytosis (Wirthgen et al., 2017; Mándi et al., 2019). Furthermore, KYNA and SZR104 directly facilitated the expression of anti-inflammatory TSG-6 and, at the same time, attenuated the

TNF- $\alpha$  production in monocytic cell cultures (Mándi et al., 2019). These actions are probably mediated through the cytoplasmic AHR (Wirthgen et al., 2017; Mándi et al., 2019) as experimental evidence suggests that KYNA is an endogenous ligand of AHR (Wirthgen et al., 2015; Routy et al., 2016; Larigot et al., 2018; Juricek et al., 2018; Mulero-Navarro et al., 2016) and inhibited phagocytosis in myeloid cells through AHR signaling (Kondrikov et al., 2020).

The strong antiinflammatory action of KYNA and SZR104 on inflammatory marker proteins was accompanied by a similarly favorable regulation of histone methylation marks in microglia-enriched cultures. We demonstrated that KYNA and SZR104 reverted the H3K9me3 and H3K36me2 immunoreactivities toward levels observed in the control, i.e., unchallenged values, after immunochallenge by LPS treatment. Our findings also indicated that the cytoplasmic translocation of methylated H3K9 proteins from the nucleus after the LPS challenge was a cellular response to immunological distress. Cytoplasmic translocation from the nucleus of these methylated histones could be ameliorated or inhibited by KYNA and SZR104, which confirms the antiinflammatory nature of these drugs in our experimental setup. We also observed differential effects of KYNA and SZR104 on the cytoplasmic H3 localization; that is, LPS + KYNA increased, while LPS + SZR104 returned cytoplasmic H3 levels to control values. The detailed mechanisms behind these differential effects of KYNA and SZR104 are not yet understood.

Histones are essential structural and functional components of the chromatin. These proteins are typically located in the nucleus, but they have functions at extranuclear or even extracellular sites. For instance, extracellular histones released in response to a bacterial challenge contribute to endothelial dysfunction, renal failure, and death during sepsis (Xu et al., 2009). Patients with sepsis have increased levels of extracellular histones that are correlated with a poor prognosis and the development of sepsis-related consequences such as end-organ damage. These histones originate in megakaryocytes that contain cytoplasmic histones and transfer the proteins to their platelet progeny (Frydman et al., 2020). Observations on cytoplasmic accumulation of histones have been made in certain pathologic states. For example, altered and differential intracellular histone distribution were detected by Wu et al. (2002) who demonstrated that not all cell lines released histones from nucleosomes during DNA fragmentation and apoptosis, while Gabler et al. (2004) demonstrated that the cytoplasmic accumulation of histones and nucleosomes in physiological cells was a precursor to apoptosis, occurring in parallel with the initial phagocytosis signals. During microglia activation by LPS, DNA damage and genome instability were observed (Jaiswal et al., 2009; Kovalchuk et al., 2013). Unmodified H2B in the cytoplasm could act as a sensor that detects double-stranded

DNA fragments derived from infectious agents or damaged cells and, consequently, could activate innate and acquired immune responses in various cell types (Kobiyama et al., 2010; Kobiyama et al., 2013). Therefore, the cytoplasmic localization of histones is also of pathophysiological importance. For example, the translocation of nuclear histone H1 to the cytoplasm in cultured pulmonary arterial smooth muscle cells is associated with pathologic states such as idiopathic pulmonary hypertension (Talati et al., 2012). The cytoplasmic accumulation of the unmodified nucleosomal histones H1, H2A, H2B, H3, and H4 in cell lysates was observed very early on in the process of apoptosis (Gabler et al., 2003a; Gabler et al., 2004). When the effects of doxorubicin, an anthracycline widely used in anticancer therapy, were tested on the aggregation and intracellular distribution of both partners of the H2A-H2B dimer, marked differences between the two histones were found (Nánási et al., 2020). For H2A, aggregation retention was observed; for H2B, a massive accumulation in the cytoplasm of Jurkat leukemia cells was observed concomitant with its disappearance from the nuclei.

Alterations in histone PTMs are viewed as an important process by which various cellular functions, including transcription (Kouzarides, 2007; Tran et al., 2017), gene silencing (Wiles et al., 2017), and immunity (Meng et al., 2019), are regulated. For example, methylation sites can influence the binding of epigenetic factors to histone tails, which alters the extent to which DNA is wrapped around histone proteins and the availability of genes in the DNA to be activated (Hyun et al., 2017; Kumar et al., 2019; Zhao et al., 2016). In neuronal cultures, Hayakawa et al. (Hayakawa et al., 2019) found three metabolites (kynurenine, 3-OH-kynurenine, and anthranilate) from the tryptophan pathways that increase H3K4 trimethylation, resulting in upregulated gene expression at hippocampal linked loci (except those encoding pan-neural markers). Dimethylated and trimethylated H3K9 sites, i.e., transcriptionally repressive marks, are both found more often at silenced genes (Barski et al., 2007) and are typical of heterochromatic regions (Rosenfeld et al., 2009). For instance, H3K9me2 is important in the regulation of inflammatory responses because it suppresses interferon and interferon-inducible antiviral gene expression (Fang et al., 2012) and epigenetically attenuates target gene-induction by inflammatory signaling in vascular smooth muscle cells (Harman et al., 2019). H3K9me3 has been implicated in the opening of chromatin on inflammatory gene promoters, and it is seen at significantly increased levels in treatment-resistant tumors (Torrano et al., 2019). Additionally, macrophages cultured in high-glucose conditions display increased expressions of cytokine genes and decreased H3K9me3 levels when compared with cells incubated in a normal glucose culture (Li et al., 2016). Methylation of H3K36 has also been found to be related to inflammatory functions and transcription of proinflammatory genes

(Honma et al., 2020; Jain et al., 2018; Zhuang et al., 2018). Our data suggest that while the expressions of unmodified histone H3 proteins and inflammatory marker proteins such as CXCL10 and CCR1 are probably regulated independently from each other by pro- and antiinflammatory agents, the subcellular localization of this protein and its methylated forms could be affected by both pro- and antiinflammatory agents through yet unidentified mechanisms.

Our results could be corroborated by previous studies from the literature as follows:

1) The antiinflammatory response by KYNA and SZR104 could attenuate TNF- $\alpha$  production and increase TSG-6 expression while elevate the interleukin-1 $\beta$  in sepsis. Interestingly, a possible role for IDO, a key kynurenine pathway enzyme, in immunity has recently emerged (Boros et al., 2019), further emphasizing the crucial role this system plays in immunomodulatory functions.

2) The inhibition of microglia phagocytosis by SZR104 and KYNA could also utilize AHR pathways, causing the decrease in TLR-4 expression on the cell surface (Larigot et al., 2018), the induction of cytoskeletal changes (Zhao et al., 2020) or the deregulation of the nuclear factor kappa-light-chain-enhancer of activated B cell pathway (Larigot et al., 2018).

3) The alterations in histone methylation modifications could be viewed as important processes in the regulation of inflammatory responses because they suppress inflammatory protein synthesis. Cytoplasmic accumulation of histones was observed in certain pathologic states (as a precursor of apoptosis, occurring in parallel with the initial phagocytosis signals). For example, DNA damage and genome instability were observed during microglia activation by LPS (Jaiswal et al., 2009; Kovalchuk et al., 2013).

In summary, methylations of the histone H3 lys sites seem to be essential epigenetic marks for inflammation. KYNA and its analog SZR104 might act on KYNA signaling pathways that potentially ameliorate neuroinflammation through the facilitation of antiinflammatory actions. Our findings corroborate previous studies on the antiinflammatory properties of endogenous KYNA and raise the possibility that some of the newly designed KYNA analogs that can penetrate the blood–brain barrier may alter gene expression epigenetically to activate antiinflammatory mechanisms. Hence, our findings may lead to the development of antiinflammatory medications targeting the CNS.

## 6. THE MAIN FINDINGS OF THE STUDY

1) KYNA and the KYNA analog SZR104 exhibited strong antiinflammatory properties, as demonstrated by their effective amelioration of LPS-challenged CXCL10 and CCR1 production in microglia-enriched cultures. While KYNA and SZR104 were both effective in ameliorating the LPS-induced elevation of CXCL10 immunoreactivity, only the combined treatment with LPS + SZR104 was effective in significantly inhibiting CCR1 immunoreactivity in these tests.

2) KYNA and SZR104 displayed further antiinflammatory effects as they inhibited the LPS-induced phagocytotic activity of microglia cells *in vitro*.

3) KYNA and SZR104 reverted the H3K9me3 and H3K36me2 immunoreactivities toward levels observed in the control, unchallenged cultures, after immunochallenge by LPS treatment.

4) Cellular response to LPS challenge resulted in a cytoplasmic translocation of methylated H3K9 proteins from the nucleus; this could be ameliorated or inhibited by KYNA and SZR104.

5) KYNA and SZR104 exerted differential effects on the cytoplasmic H3 localization: LPS + KYNA increased, while LPS + SZR104 returned cytoplasmic H3 levels to control values.

## 7. ACKNOWLEDGEMENTS

First and foremost, I would like to thank my PhD mentor Professor Karoly Gulya for his personal guidance, professional advice, and continuous support of my research work.

I wish to extend my heartfelt gratitude towards all members of the Department of Cell Biology and Molecular Medicine for the stimulating scientific discussions. I would like to express my gratitude to my colleges for the fruitful conversations, their encouragement and support. I would like to thank Dr. Karolina Fábíán-Dulka and Dr. Melinda Szabó for their ongoing support, suggestions, and encouragements.

I would like to express my deepest gratitude to my family for their emotional support, unconditional love and for always being there for me.

This study was supported by grants from the Ministry of National Resources (GINOP 2.3.2-15-2016-00030 and 2.3.2-15-2016-00034) through the European Union Cohesion Fund. At the time of the experiments, I was partly supported by the Theoretical Medicine Doctoral School, Albert Szent-Györgyi Medical School, University of Szeged. The funders were not involved in the design of the study, data collection and analysis, decision to publish or and preparation of the thesis.

## 8. REFERENCES

- Balog A, Varga B, Fülöp F, Lantos I, Toldi G, Vécsei L, Mándi Y (2021) Kynurenic acid analog attenuates the production of tumor necrosis factor- $\alpha$ , calgranulins (S100A 8/9 and S100A 12), and the secretion of HNP1-3 and stimulates the production of tumor necrosis factor-stimulated gene-6 in whole blood cultures of patients with rheumatoid arthritis. *Front Immunol.* 12:632513.
- Barski A, Cuddapah S, Cui K, Roh TY, Schonnes DE, Wang Z, Wei G, Chepelev I, Zhao K (2007) High-resolution profiling of histone methylations in the human genome. *Cell.* 129:823–837.
- Biernacki T, Sandi D, Bencsik K, Vecsei L (2020) Kynurenines in the pathogenesis of multiple sclerosis: Therapeutic perspectives. *Cells.* 9:1564.
- Boros FA, Vécsei L (2019) Immunomodulatory effects of genetic alterations affecting the kynurenine pathway. *Front Immunol.* 10:2570.
- Cheeran MCJ, Hu S, Sheng WS, Peterson PK, Lokensgard JR (2003) CXCL10 production from cytomegalovirus-stimulated microglia is regulated by both human and viral interleukin-10. *J Virol.* 7:4502–4515.
- Chen R, Kang R, Fan XG, Tang D (2014) Release and activity of histone in diseases. *Cell Death Dis.* 5:e1370.
- Demeter I, Nagy K, Gellért L, Vécsei L, Fülöp F, Toldi J (2012) A novel kynurenic acid analog (SZR104) inhibits pentylenetetrazole induced epileptiform seizures. An electrophysiological study. *J Neural Transm.* 119:151–154.
- Diaz-Aparicio I, Beccari S, Abiega O, Sierra A (2016) Clearing the corpses: Regulatory mechanisms, novel tool, and therapeutic potential of harnessing microglial phagocytosis in the diseased brain. *Neural Regen Res.* 11:1533–1539.
- Dulka K, Nacsa K, Lajkó N, Gulya K (2021a) Quantitative morphometric and cell-type-specific population analysis of microglia-enriched cultures subcloned to high purity from newborn rat brains. *IBRO Neurosci Rep.* 10:119–129.
- Dulka K, Szabo M, Lajkó N, Beleczi I, Hoyk Z, Gulya K (2021b) Epigenetic consequences of in utero exposure to rosuvastatin: Alteration of histone methylation patterns in newborn rat brains. *Int J Mol Sci.* 22:3412.
- Dyer KD, Percopo CM, Fischer ER, Gabryszewski SJ, Rosenberg HF (2009) Pneumoviruses infect eosinophils and elicit MyD88-dependent release of chemoattractant cytokines and interleukin-6. *Blood.* 114:2649–2656.

- Ekanev ML, Otto GP, Sossdorf M, Sponholz C, Boehringer M, Loesche W, Rittirsch D, Wilharm A, Kurzai O, Bauer M, et al (2014) Impact of plasma histones in human sepsis and their contribution to cellular injury and inflammation. *Crit Care*. 18:543.
- Erhardt S, Schwieler L, Imbeault S, Engberg G (2017) The kynurenine pathway in schizophrenia and bipolar disorder. *Neuropharmacology*. 112:297–306.
- Fang TC, Schaefer U, Mecklenbrauker I, Stienen A, Dewell S, Chen MS, Rioja I, Parravicini V, Prinjha RK, Chandwani R, et al (2012) Histone H3 lysine 9 di-methylation as an epigenetic signature of the interferon response. *J Exp Med*. 209:661–669.
- Fries GR, Walss-Bass C, Bauer ME, Teixeira AL (2019) Revisiting inflammation in bipolar disorder. *Pharmacol Biochem Behav*. 177:12–9.
- Frydman GH, Tessier SN, Wong KHK, Vanderburg CR, Fox JG, Toner M, Tompkins RG, Irimia D (2020) Megakaryocytes contain extranuclear histones and may be a source of platelet-associated histones during sepsis. *Sci Rep*. 10:4621.
- Fülöp F, Szatmári I, Toldi J, Vécsei L (2012) Modifications on the carboxylic function of kynurenic acid. *J Neural Transm*. 119:109–114.
- Fülöp F, Szatmári I, Toldi J, Vécsei L (2021) Novel Types of *c*-3 Substituted Kinurenic Acid Derivatives with Improved Neuroprotective Activity. Patent No: WO2017149333A1, 8 September 2017. Available online: <https://patents.google.com/patent/WO2017149333A1/en> (accessed on 2 June 2021).
- Fülöp F, Szatmári I, Vámos E, Zádori D, Toldi J, Vécsei L (2009) Syntheses, transformations and pharmaceutical applications of kynurenic acid derivatives. *Curr Med Chem*. 16:4828–4842.
- Gabler C, Blank N, Winkler S, Kalden JR, Lorenz HM (2003a) Accumulation of histones in cell lysates precedes expression of apoptosis-related phagocytosis signals in human lymphoblasts. *Ann NY Acad Sci*. 1010:221–224.
- Gabler C, Blank N, Hieronymus T, Schiller M, Berden JHM, Kalden JR, Lorenz HM (2004) Extranuclear detection of histones and nucleosomes in activated human lymphoblasts as an early event in apoptosis. *Ann Rheum Dis*. 63:1135–1144.
- Gabler C, Kalden JR, Lorenz HM (2003b) The putative role of apoptosis-modified histones for the induction of autoimmunity in systemic lupus erythematosus. *Biochem Pharmacol*. 66:1441–1446.
- Ginhoux F, Jung S (2014) Monocytes and macrophages: Developmental pathways and tissue homeostasis. *Nat Rev Immunol*. 14:392–404.

- Gkotsos G, Virgiliou C, Lagoudaki I, Sardeli C, Raikos N, Theodoridis G, et al. (2017) The role of sarcosine, uracil, and kynurenic acid metabolism in urine for diagnosis and progression monitoring of prostate cancer. *Metabolites*. 7(1):9.
- Guillemin GJ, Cullen KM, Lim CK, Smythe GA, Garner B, Kapoor V, et al. (2007) Characterization of the kynurenine pathway in human neurons. *J Neurosci*. 27(47):12884–92.
- Guillemin GJ, Smythe G, Takikawa O, Brew BJ (2005) Expression of indoleamine 2,3-dioxygenase and production of quinolinic acid by human microglia, astrocytes, and neurons. *Glia*. 49(1):15–23.
- Hankittichai P, Lou HJ, Wikan N, Smith DR, Potikanond S, Nimlamool W (2020) Oxyresveratrol inhibits IL-1 $\beta$ -induced inflammation via suppressing AKT and ERK1/2 activation in human microglia, HMC3. *Int J Mol Sci*. 21: 6054.
- Harman JL, Dobnikar L, Chappell J, Stokell BG, Dalby A, Foote K, Finigan A, Freire-Pritchett P, Taylor AL, Worssam MD, Madsen RR, Loche E, Uryga A, Bennett MR, Jørgensen HF (2019) Epigenetic regulation of vascular smooth muscle cells by histone H3 lysine 9 dimethylation attenuates target gene-induction by inflammatory signaling. *Arterioscler Thromb Vasc Biol*. 39:2289–2302.
- Haroon E, Raison CL, Miller AH (2011) Psychoneuroimmunology meets neuropsychopharmacology: translational implications of the impact of inflammation in behavior. *Neuropsychophar*. 1-26.
- Hayakawa K, Nishitani K, Tanaka S (2019) Kynurenine, 3-OH-kynurenine, and anthranilate are nutrient metabolites that alter H3K4 trimethylation and H2AS40 O-GlcNAcylation at hypothalamus-related loci. *Sci Rep*. 9:19768.
- Honma K, Machida C, Mochizuki K, Goda T (2020) Glucose and TNF enhance expression of TNF and IL1B, and histone H3 acetylation and K4/K36 methylation, in juvenile macrophage cells. *Gene*. 763S, 100034.
- Hyun K, Jeon J, Park K, Kim J (2017) Writing, erasing and reading histone lysine methylations. *Exp Mol Med*. 49:e324.
- Jain N, Vogel V (2018) Spatial confinement downsizes the inflammatory response of macrophages. *Nat Mater*. 17:1134–1144.
- Jaiswal YK, Jaiswal MK, Agrawal V, Chaturvedi MM (2009) Bacterial endotoxin (LPS)-induced DNA damage in preimplanting embryonic and uterine cells inhibits implantation. *Fertil Steril*. 91 (Suppl. 5), 2095–2103.

- Juricek L, Coumoul X (2018) The aryl hydrocarbon receptor and the nervous system. *Int J Mol. Sci.* 19:2504.
- Kata D, Földesi I, Feher LZ, Hackler L Jr, Puskás LG, Gulya K (2016) Rosuvastatin enhances anti-inflammatory and inhibits pro-inflammatory functions in cultured microglial cells. *Neuroscience.* 314:47–63.
- Kata D, Földesi I, Feher LZ, Hackler L Jr, Puskas LG, Gulya K (2017) A novel pleiotropic effect of aspirin: Beneficial regulation of pro- and anti-inflammatory mechanisms in microglial cells. *Brain Res Bull.* 132:61–74.
- Kettenmann H, Hanisch UK, Noda M, Verkhratsky A (2011) Physiology of microglia. *Physiol Rev.* 91:461–553.
- Klein DC, Hainer SJ (2020) Chromatin regulation and dynamics in stem cells. *Curr Top Dev Biol.* 138: 1–71.
- Klein RS (2004) Regulation of neuroinflammation: The role of CXCL10 in lymphocyte infiltration during autoimmune encephalomyelitis. *J Cell Biochem.* 92:213–222.
- Kobiyama K, Kawashima A, Jounai N, Takeshita F, Ishii KJ, Ito T, Suzuki K (2013) Role of extrachromosomal histone H2B on recognition of DNA viruses and cell damage. *Front Genet.* 4:91.
- Kobiyama K, Takeshita F, Jounai N, Sakaue-Sawano A, Miyawaki A, Ishii KJ, Kawai T, Sasaki S, Hirano H, Ishii N, et al (2010) Extrachromosomal histone H2B mediates innate antiviral immune responses induced by intracellular double-stranded DNA. *J Virol.* 84:822–832.
- Kondrikov D, Elmansi A, Bragg RT, Mobley T, Barrett T, Eisa N, Kondrikova G, Schoeinlein P, Aguilar-Perez A, Shi X-M, et al (2020) Kynurenine inhibits autophagy and promotes senescence in aged bone marrow mesenchymal stem cells through the arylhydrocarbon receptor pathway. *Exp Gerontol.* 130:110805.
- Konishi A, Shimizu S, Hirota J, Takao T, Fan Y, Matsuoka Y, Zhang L, Yoneda Y, Fujii Y, Skoultchi AI et al (2003) Involvement of histone H1.2 in apoptosis induced by DNA double-strand breaks. *Cell.* 114:673–688.
- Kouzarides T (2007) Chromatin modifications and their function. *Cell.* 128:693–705.
- Kovalchuk I, Walz P, Thomas J, Kovalchuk O (2013) Genomic instability in liver cells caused by an LPS-induced bystander-like effect. *PLoS ONE.* 8:e67342.
- Kreutzberg GW (1996) Microglia: A sensor for pathological events in the CNS. *Trends Neurosci.* 19:312–318.
- Kumar A, Kumari N, Sharma U, Ram S, Singh SK, Kakkar N, Kaushal K, Prasad R (2019) Reduction in H3K4me patterns due to aberrant expression of methyltransferases and

- demethylases in renal cell carcinoma: Prognostic and therapeutic implications. *Sci Rep.* 9:8189.
- Lajkó N, Kata D, Szabó M, Mátyás A, Dulka K, Földesi I, Fülöp F, Gulya K, Vécsei L, Mihály A (2020) Sensitivity of rodent microglia to kynurenines in models of epilepsy and inflammation in vivo and in vitro: Microglia activation is inhibited by kynurenic acid and the synthetic analogue SZR104. *Int J Mol Sci.* 21:9333.
- Larigot L, Juricek L, Dairou J, Coumoul X (2018) AhR signaling pathways and regulatory functions. *Biochim Open.* 7:1–9.
- Lawrence M, Daujat S, Schneider R (2016) Lateral thinking: How histone modifications regulate gene expression. *Trends Genet.* 32:42–56.
- Li MF, Zhang R, Li TT, Chen MY, Li LX, Lu JX, Jia WP (2016) High glucose increases the expression of inflammatory cytokine genes in macrophages through H3K9 methyltransferase mechanism. *J Interferon Cytokine Res.* 36:48–61.
- Liu M, Guo S, Hibbert JM, Jain V, Singh N, Wilson NO, Stiles JK (2011) CXCL10/IP-10 in infectious diseases pathogenesis and potential therapeutic implications. *Cytokine Growth Factor Rev.* 22:121–130.
- Liu W, Ye J, Yan H (2019) Investigation of key genes and pathways in inhibition of oxycodone on vincristine-induced microglia activation by using bioinformatics analysis. *Dis Markers.* 2019:3521746.
- Lo BKK, Yu M, Zloty D, Cowan B, Shapiro J, McElwee KJ (2010) CXCR3/ligands are significantly involved in the tumorigenesis of basal cell carcinomas. *Am J Pathol.* 176:2435–2446.
- Lowry OH, Rosebrough NJ, Farr AL, Randall RJ (1951) Protein measurement with the Folin phenol reagent. *J Biol Chem.* 193:265–275.
- Mándi Y, Endrész V, Mosolygó T, Burián K, Lantos I, Fülöp F, Szatmári I, Lőrinczi B, Balog A, Vécsei L (2019) The opposite effects of kynurenic acid and different kynurenic acid analogs on tumor necrosis factor- $\alpha$  (TNF- $\alpha$ ) production and tumor necrosis factor-stimulated gene-6 (TSG-6) expression. *Front Immunol.* 10:1406.
- Mándi Y, Vécsei L (2012) The kynurenine system and immunoregulation. *J Neural Transm.* 119(2):197–209.
- Meng M, Liu H, Chen S, Zhao H, Gao X, Zhang J, Chen D (2019) Methylation of H3K27 and H3K4 in key gene promoter regions of thymus in RA mice is involved in the abnormal development and differentiation of iNKT cells. *Immunogenetics.* 71:489–499.

- Molnár K, Lőrinczi B, Fazakas C, Szatmári I, Fülöp F, Kmetykó N, Berkecz R, Ilisz I, Krizbai IA, Wilhelm I, et al. (2021) SZR-104, a Novel Kynurenic Acid Analogue with High Permeability through the Blood-Brain Barrier. *Pharmaceutics*. 13:61.
- Moroni F, Cozzi A, Sili M, Mannaioni G (2012) Kynurenic acid: a metabolite with multiple actions and multiple targets in brain and periphery. *J Neural Transm*. 119(2):133–9.
- Mulero-Navarro S, Fernandez-Salguero PM (2016) New trends in aryl hydrocarbon receptor biology. *Front Cell Dev Biol*. 4:1–13.
- Nakamichi K, Saiki M, Sawada M, Takayama-Ito M, Yamamuro Y, Morimoto K, Kurane I (2005) Rabies virus-induced activation of mitogen-activated protein kinase and NF-kappaB signaling pathways regulates expression of CXC and CC chemokine ligands in microglia. *J Virol*. 79:11801–11812.
- Nánási P Jr, Imre L, Firouzi Niaki E, Bosire R, Mocsár G, Türk-Mázló A, Ausio J, Szabó G (2020) Doxorubicin induces large-scale and differential H2A and H2B redistribution in live cells. *PLoS ONE*. 15:e0231223.
- Neote K, DiGregorio D, Mak JY, Horuk R, Schall TJ (1993) Molecular cloning, functional expression, and signaling characteristics of a C-C chemokine receptor. *Cell*. 72:415–425.
- Ogyu K, Kubo K, Noda Y, Iwata Y, Tsugawa S, Omura Y, et al. (2018) Kynurenine pathway in depression: a systematic review and meta-analysis. *Neurosci Biobehav Rev*. 90:16–25.
- Parseghian MH, Luhrs KA (2006) Beyond the walls of the nucleus: The role of histones in cellular signaling and innate immunity. *Biochem Cell Biol*. 84:589–604.
- Pedraz-Petrozzi B, Elyamany O, Rummel C, Mulert C (2020) Effects of inflammation on the kynurenine pathway in schizophrenia – a systematic review. *J Neuroinfl*. 17:56.
- Poles MZ, Nászai A, Gulácsi L, Czakó BL, Gál KG, Glenz RJ, Dookhun D, Rutai A, Tallósy SP, Szabó A, Lőrinczi B, Szatmári I, Fülöp F, Vécsei L, Boros M, Juhász L, Kaszaki J (2021) Kynurenic acid and its synthetic derivatives protect against sepsis-associated neutrophil activation and brain mitochondrial dysfunction in rats. *Front Immunol*. 12:717157.
- Rosenfeld JA, Wang Z, Schones DE, Zhao K, DeSalle R, Zhang MQ (2009) Determination of enriched histone modifications in non-genic portions of the human genome. *BMC Genom*. 10:143.
- Routy JP, Routy B, Graziani GM, Mehraj V (2016) The kynurenine pathway is a double-edged sword in immune-privileged sites and in cancer: Implications for immunotherapy. *Int J Tryptophan Res*. 9:67–77.

- Saccani S, Natoli G (2002) Dynamic changes in histone H3 Lys 9 methylation occurring at tightly regulated inducible inflammatory genes. *Genes Dev.* 16:2219–2224.
- Schneider CA, Rasband WS, Eliceiri KW (2012) NIH Image to ImageJ: 25 years of image analysis. *Nat Methods.* 9:671–675.
- Startek JB, Talavera K, Voets T, Alpizar YA (2018) Differential interactions of bacterial lipopolysaccharides with lipid membranes: Implications for TRPA1-mediated chemosensation. *Nat Sci Rep.* 8:12010.
- Steiner L, Gold M, Mengel D, Dodel R, Bach JP (2014) The endogenous  $\alpha 7$  nicotinic acetylcholine receptor antagonist kynurenic acid modulates amyloid- $\beta$ -induced inflammation in BV-2 microglial cells. *J Neurol Sci.* 344:94–99.
- Szabo M, Gulya K (2013) Development of the microglial phenotype in culture. *Neuroscience.* 241:280–295.
- Szczuciński A, Losy J (2007) Chemokines and chemokine receptors in multiple sclerosis. Potential targets for new therapies. *Acta Neurol Scand.* 115:137–146.
- Takikawa O (2005) Biochemical and medical aspects of the indoleamine 2, 3-dioxygenase-initiated l-tryptophan metabolism. *Biochem Biophys Res Commun.* 338(1):12–9.
- Talati M, Seeley E, Ihida-Stansbury K, Delisser H, McDonald H, Ye F, Zhang X, Shyr Y, Caprioli R, Meyrick B (2012) Altered expression of nuclear and cytoplasmic histone H1 in pulmonary artery and pulmonary artery smooth muscle cells in patients with IPAH. *Pulm Circ.* 2:340–351.
- Tomioka R, Matsui M (2014) Biomarkers for multiple sclerosis. *Intern Med.* 53:361–365.
- Torrano J, Al Emran A, Hammerlindl H, Schaidler H (2019) Emerging roles of H3K9me3, SETDB1 and SETDB2 in therapy-induced cellular reprogramming. *Clin Epigenetics.* 11:43.
- Tran TQ, Lowman XH, Kong M (2017) Molecular Pathways: Metabolic control of histone methylation and gene expression in cancer. *Clin Cancer Res.* 23:4004–4009.
- Ubogu EE, Cossoy MB, Ransohoff RM (2006) The expression and function of chemokines involved in CNS inflammation. *Trends Pharmacol Sci.* 27:48–55.
- Vazirinejad R, Ahmadi Z, Kazemi Arababadi M, Hassanshahi G, Kennedy D (2014) The biological functions, structure and sources of CXCL10 and its outstanding part in the pathophysiology of multiple sclerosis. *Neuroimmunomodulation.* 21:322–330.
- Vécsei L, Szalárdy L, Fülöp F, Toldi J (2013) Kynurenines in the CNS: Recent advances and new questions. *Nat Rev Drug Discov.* 12:64–82.

- Venkatesh S, Workman JL (2015) Histone exchange, chromatin structure and the regulation of transcription. *Nat Rev Mol Cell Biol.* 16:178–189.
- Wang AK, Miller BJ (2018) Meta-analysis of cerebrospinal fluid cytokine and tryptophan catabolite alterations in psychiatric patients: comparisons between schizophrenia, bipolar disorder, and depression. *Schizophr Bull.* 44(1):75–83.
- Wang J, Simonavicius N, Wu X, Swaminath G, Reagan J, Tian H, et al. (2006) Kynurenic acid as a ligand for orphan G protein-coupled receptor GPR35. *J Biol Chem.* 281(31):22021–8.
- Wiles ET, Selker EU (2017) H3K27 methylation: A promiscuous repressive chromatin mark. *Curr Opin Genet Dev.* 43:31–37.
- Wilson NO, Huang MB, Anderson W, Bond V, Powell M, Thompson WE, Armah HB, Adjei AA, Gyasi R, Tettey Y, et al (2008) Soluble factors from *Plasmodium falciparum*-infected erythrocytes induce apoptosis in human brain vascular endothelial and neuroglia cells. *Mol Biochem Parasitol.* 162:172–176.
- Wirthgen E, Hoeflich A (2015) Endotoxin-induced tryptophan degradation along the kynurenine pathway: the role of indolamine 2, 3-dioxygenase and aryl hydrocarbon receptor-mediated immunosuppressive effects in endotoxin tolerance and cancer and its implications for immunoparalysis. *J Amino Acids.* 2015:973548.
- Wirthgen E, Hoeflich A, Rebl A, Günther J (2017) Kynurenic acid: The Janus-faced role of an immunomodulatory tryptophan metabolite and its link to pathological conditions. *Front Immunol.* 8:1957.
- Wu D, Ingram A, Lahti JH, Mazza B, Grenet J, Kapoor A, Liu L, Kidd VJ, Tang D (2002) Apoptotic release of histones from nucleosomes. *J Biol Chem.* 277:12001–12008.
- Xu J, Zhang X, Pelayo R, Monestier M, Ammollo CT, Semeraro F, Taylor FB, Esmon NL, Lupu F, Esmon CT (2009) Extracellular histones are major mediators of death in sepsis. *Nat Med.* 15:1318–1321.
- Zhao L, Shu Q, Sun H, Ma Y, Kang D, Zhao Y, Lu J, Gong P, Yang F, Wan F (2020) 1'H-indole-3'-carbonyl-thiazole-4-carboxylic acid methyl ester blocked human glioma cell invasion via aryl hydrocarbon receptors' regulation of cytoskeletal contraction. *Biomed Res Int.* 2020:2616930.
- Zhao Q, Zhang J, Chen R, Wang L, Li B, Cheng H, Duan X, Zhu H, Wei W, Li J, Wu Q, Han J-D J, Yu W, Gao S, Li G, Wong J (2016) Dissecting the precise role of H3K9 methylation in crosstalk with DNA maintenance methylation in mammals. *Nat Commun.* 7:12464.

- Zhuang L, Jang Y, Park YK, Lee JE, Jain S, Froimchuk E, Broun A, Liu C, Gavrilova O, Ge K (2018) Depletion of Nsd2-mediated histone H3K36 methylation impairs adipose tissue development and function. *Nat Commun.* 9:1796.
- Zlatanova JS, Srebrevna LN, Banchev TB, Tasheva BT, Tsanev RG (1990) Cytoplasmic pool of histone H1 in mammalian cells. *J Cell Sci.* 96 Pt 3:461–468.

## 9. CO-AUTHORS' STATEMENT

We, the Co-Authors, hereby state that data presented in this Thesis from the journal article specified below\* is largely the work of the Author of this PhD Thesis, and none of the Co-Authors have used or will ever use those data to obtain a PhD degree.

\*Dulka K, Nacsa K, Lajkó N, Gulya K (2021) Quantitative morphometric and cell-type-specific population analysis of microglia-enriched cultures subcloned to high purity from newborn rat brains. *IBRO Neurosci Rep.* 10:119-129. doi: 10.1016/j.ibneur.2021.01.007.

Szeged, June 15, 2022



Dr. Karolina Dulka, Co-Author



Dr. Kálmán Nacsa, Co-Author



Dr. Karoly Gulya, Co-Author

## 10. APPENDIX

I) **Lajkó N**, Kata D, Szabó M, Mátyás A, Dulka K, Földesi I, Fülöp F, Gulya K, Vécsei L, Mihály A (2020) Sensitivity of rodent microglia to kynurenines in models of epilepsy and inflammation in vivo and in vitro: Microglia activation is inhibited by kynurenic acid and the synthetic analogue SZR104. **Int J Mol Sci.** 21(23):9333. doi: 10.3390/ijms21239333. (IF: **5.923**) (Q1)

II) Dulka K, Nacsa K, **Lajkó N**, Gulya K (2021) Quantitative morphometric and cell-type-specific population analysis of microglia-enriched cultures subcloned to high purity from newborn rat brains. **IBRO Neurosci Rep.** 10:119-129. doi: 10.1016/j.ibneur.2021.01.007.

III) Szabo\* M, **Lajkó\* N**, Dulka K, Szatmári I, Fülöp F, Mihály A, Vécsei L, Gulya K (2022) Kynurenic acid and its analog SZR104 exhibit strong antiinflammatory effects and alter the intracellular distribution and methylation patterns of H3 histones in immunochallenged microglia-enriched cultures of newborn rat brains. **Int. J. Mol. Sci.** 23(1079) doi: 10.3390/ijms23031079. (IF **5.923**) (Q1) (*\*These authors contributed equally to this work and should be considered joint first authors.*)

# I)

**Lajkó N, Kata D, Szabó M, Mátyás A, Dulka K, Földesi I, Fülöp F, Gulya K, Vécsei L, Mihály A (2020)** Sensitivity of rodent microglia to kynurenines in models of epilepsy and inflammation in vivo and in vitro: Microglia activation is inhibited by kynurenic acid and the synthetic analogue SZR104. **Int J Mol Sci.** 21(23):9333. doi: 10.3390/ijms21239333 (**IF: 5.923**) (Q1)

Open Access (freely available online):

<https://www.mdpi.com/1422-0067/21/23/9333/htm>



Article

# Sensitivity of Rodent Microglia to Kynurenines in Models of Epilepsy and Inflammation In Vivo and In Vitro: Microglia Activation Is Inhibited by Kynurenic Acid and the Synthetic Analogue SZR104

Noémi Lajkó<sup>1</sup>, Diana Kata<sup>2</sup> , Melinda Szabó<sup>1</sup>, Adrienne Mátyás<sup>3</sup>, Karolina Dulka<sup>1</sup>, Imre Földesi<sup>2</sup>, Ferenc Fülöp<sup>4</sup> , Karoly Gulya<sup>1</sup> , László Vecsei<sup>5,6</sup> and András Mihály<sup>3,7,\*</sup>

<sup>1</sup> Department of Cell Biology and Molecular Medicine, University of Szeged, 6720 Szeged, Hungary; lajko.noemi@med.u-szeged.hu (N.L.); szabo.melinda.1@med.u-szeged.hu (M.S.); dulka.karolina@med.u-szeged.hu (K.D.); gulyak@bio.u-szeged.hu (K.G.)

<sup>2</sup> Department of Laboratory Medicine, University of Szeged, 6720 Szeged, Hungary; kata.diana@med.u-szeged.hu (D.K.); foldesi.imre@med.u-szeged.hu (I.F.)

<sup>3</sup> Department of Anatomy, University of Szeged, 6720 Szeged, Hungary; matyas.adrienne@med.u-szeged.hu

<sup>4</sup> Institute of Pharmaceutical Chemistry and Research Group for Stereochemistry, Hungarian Academy of Sciences, University of Szeged, 6720 Szeged, Hungary; fulop@pharm.u-szeged.hu

<sup>5</sup> Department of Neurology, University of Szeged, 6720 Szeged, Hungary; vecsei.laszlo@med.u-szeged.hu

<sup>6</sup> Department of Neurology, Interdisciplinary Excellence Centre, University of Szeged, 6720 Szeged, Hungary

<sup>7</sup> Department of Anatomy, Faculty of Medicine and Health Sciences, Carl von Ossietzky University Oldenburg, 26129 Oldenburg, Germany

\* Correspondence: mihaly.andras@med.u-szeged.hu

Received: 9 November 2020; Accepted: 4 December 2020; Published: 7 December 2020



**Abstract:** Kynurenic acid is an endogenous modulator of ionotropic glutamate receptors and a suppressor of the immune system. Since glutamate and microglia are important in the pathogenesis of epilepsy, we investigated the possible action of the synthetic kynurenic acid analogue, SZR104, in epileptic mice and the action of kynurenic acid and SZR104 on the phagocytotic activity of cultured microglia cells. Pilocarpine epilepsy was used to test the effects of SZR104 on morphological microglia transformation, as evaluated through ionized calcium-binding adaptor molecule 1 (Iba1) immunohistochemistry. Microglia-enriched rat secondary cultures were used to investigate phagocytosis of fluorescent microbeads and Iba1 protein synthesis in control and lipopolysaccharide-challenged cultures. SZR104 inhibited microglia transformation following status epilepticus. Kynurenic acid and SZR104 inhibited lipopolysaccharide-stimulated phagocytotic activity of microglia cells. Although kynurenic acid and its analogues proved to be glutamate receptor antagonists, their immunosuppressive action was dominant in epilepsy. The inhibition of phagocytosis in vitro raised the possibility of the inhibition of genes encoding inflammatory cytokines in microglial cells.

**Keywords:** epilepsy; inflammation; kynurenic acid; lipopolysaccharide; microglia; pilocarpine; secondary culture; SZR104

## 1. Introduction

Pharmacological experiments proved that endogenous kynurenic acid (4-hydroxyquinolin-2-carboxylic acid, C<sub>10</sub>H<sub>7</sub>NO<sub>3</sub>; KYNA) exerted a neuroprotective role in different inflammatory/neurodegenerative central nervous system (CNS) disorders [1,2]. KYNA is an endogenous antagonist of the N-methyl-D-aspartic acid (NMDA) receptor, and therefore, it may protect cells against the cytotoxic

actions of glutamic acid [1,2]. However, exogenous KYNA is not able to cross the blood–brain barrier (BBB); therefore, efforts are being made to synthesize KYNA analogues which penetrate the BBB, enter the brain and, supposedly, can be used in the pharmacological treatment of some neurodegenerative disorders [3]. One of these KYNA analogues, C<sub>19</sub>H<sub>26</sub>N<sub>4</sub>O<sub>3</sub> or N-(2-(dimethylamino)ethyl)-3-(morpholinomethyl)-4-hydroxyquinoline-2-carboxamide (SZR104), has been applied successfully in pentylenetetrazol (PTZ) seizures and significantly decreased the seizure-evoked field potentials [4]. These experiments were performed on rats in urethane anesthesia and investigated the electrophysiological effects of SZR104 pretreatment on PTZ convulsions [4]. In the present experiments, we aimed to study the pharmacological effects of SZR104 in the non-anesthetized, epileptic brain. Generalized epilepsy was induced in mice with pilocarpine (PILO), since our previous experiments proved that acute, generalized convulsive seizures significantly increase the brain extracellular concentration of glutamic acid [5]. It was also proven that the awake epilepsy model was useful for the pharmacological evaluation of some antiepileptic drugs [6].

KYNA also affects the immune system through the regulation and modulation of the cell cycle of effector immune cells [7,8]. Microglial cells are the effector immune cells of the brain, participating in every neuropathological event [9–11]. Microglia are activated and transformed by neurotransmitters (e.g., glutamate acting on microglial NMDA receptors [12]), damage-associated stress signals, cytokines, colony-stimulating factors and free radicals [13–15]. In neuropathology, this disease-associated phenotype is called reactive microglia [9,10,13]. Reactive microglia cells display significant morphological transformations: they increase in size and develop a large number of cytoplasmic processes which help migration and phagocytosis [9,16]. Disease-associated microglia not only protects but also damages and kills neurons [11,13]. Therefore, we evaluated the microglia effects of SZR104 in PILO-induced mouse epilepsy. We evaluated the proliferation tendency (number) and the size of hippocampal microglia cells with the help of ionized calcium-binding adaptor molecule 1 (Iba1) immunohistochemistry [17]. The receptors and signaling mechanisms of microglia cells regulate the expression of their genome and help their adaptation to pathogenic environmental stimuli through the secretion of cytokines [13,18]. We measured the blood levels of the cytokine interleukin-6 (IL-6) in order to track the functional alterations of the microglia, *in vivo* [18].

The experimental investigation of the pharmacology of microglial phagocytosis *in vivo* is very difficult [19]; therefore, we performed *in vitro* experiments using microglia-enriched forebrain cell cultures [20,21]. Our previous experiments proved that microglial cell cultures are suitable for the evaluation of the effects of anti-inflammatory compounds, and the *in vitro* lipopolysaccharide (LPS) challenge can be successfully used [21,22] in experimental pharmacological investigations [20,22]. In the present experiments, we evaluated the *in vitro* microglial phagocytosis induced by LPS and tested the pharmacological effects of SZR104 and KYNA by counting the number of internalized fluorescent microbeads [21,22]. The Iba1 expression of the microglia cells has been measured with Western blotting.

We observed that the concentration of IL-6 increased significantly in the venous blood of the epileptic mice. The KYNA analogue SZR104 significantly inhibited the *in vivo* transformation of hippocampal microglia cells from the resting into the activated/reactive forms. SZR104 also decreased the blood IL-6 level. However, the SZR104 pretreatment failed to reduce the motor hyperactivity and the status epilepticus in mice. We found that both KYNA and SZR104 significantly inhibited the *in vitro* phagocytosis of fluorescent microbeads in microglia cells induced by LPS treatment.

## 2. Results

### 2.1. Seizure Symptoms

PILO-treated mice displayed motor hyperactivity beginning 10–15 min after the intraperitoneal (i.p.) injections. The first symptoms were tremor of the limbs, movement automatisms and wild running. Then, the animal fell on its side, displaying frequent limb flexions and trunk extension

(tonic-clonic seizure). After a transient (6–8 min) recovery, the motor symptoms were repeated—often for 80–120 min. Not every animal displayed generalized tonic-clonic seizure; 35% of the mice were displaying only tremor, automatisms and wild running episodes lasting for 60–90 min. The animals which were pretreated with SZR104 (SZR104 and PILO-treated animals) presented similar symptoms; the latency of the motor symptoms and tonic-clonic convulsions was not delayed nor prevented by the KYNA analogue SZR104. The convulsing animals injected only with PILO suffered a 30% mortality rate. The combined treatment with 380 mg/kg SZR104 and 190 mg/kg PILO did not decrease the mortality rate; on the contrary, this animal group had a mortality rate of 40%. The solvent of pilocarpine (0.9% NaCl) and the 380 mg/kg SZR104 injected alone did not cause symptoms and did not cause mortality. Animals were further investigated after 24 h, following the treatments (Table 1).

**Table 1.** Animals used in pharmacological-immunohistochemical experiments and blood sampling for interleukin-6 (IL-6) ELISA measurement. The differences in surviving animal numbers reflected the increased mortality of the SZR104 + PILO-treated animals (see Results).

Pharmacological Treatment	Number of Surviving Animals	Experimental Procedures
Control animals: 0.9% NaCl i.p. injection	12	Blood samples (8 animals). Immunohistochemistry (4 animals).
Pilocarpine-treated: 190 mg/kg PILO, i.p. injection	21	Blood samples (18 animals). Immunohistochemistry (4 animals).
SZR104 solution i.p. (358 mg/kg)	12	Blood samples (8 animals). Immunohistochemistry (4 animals).
SZR104 (358 mg/kg) and PILO (190 mg/kg) i.p. injections	8	Blood samples (4 animals). Immunohistochemistry (4 animals).

## 2.2. IL-6 Levels in Blood

Significantly increased IL-6 levels were detected in the PILO-treated mice (Figure 1). In the venous blood taken 24 h after the pharmacological treatments, SZR104 pretreatment decreased the elevated IL-6 level, but the decrease (the effect of SZR104) was not significant. The levels of IL-6 were also slightly higher in SZR104 + PILO-treated mice than those in the controls; however, none of the alterations were significant (Figure 1). SZR104 alone did not cause any alterations; the IL-6 values were similar to the physiological saline-injected controls (Figure 1).

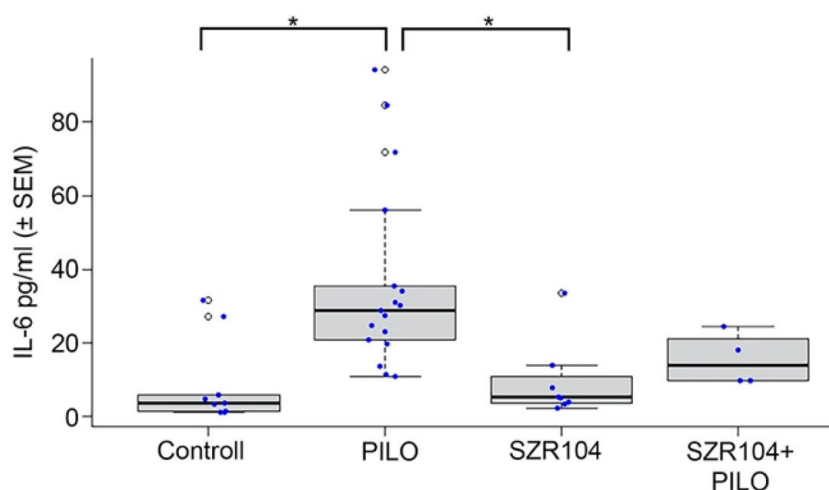


**Figure 1.** Interleukin-6 (IL-6) concentration (mean  $\pm$  SEM) in the blood 24 h after pharmacological treatments. Statistically significant differences were detected between controls and PILO-treated and between pilocarpine(PILO)-treated and SZR104-treated animals ( $* p \leq 0.05$ ). SZR104-pretreated epileptic animals (SZR104 + PILO) displayed decreased IL-6 level, but the decrease was not statistically significant (blood IL-6 concentrations in pg/mL; blue dots display the number of measurements/blood samples).

### 2.3. Iba1 Immunohistochemistry

Control mice displayed normal microglia cells; Iba1-stained cells were evenly distributed in the hippocampus, their shape and distribution were similar to those of the resting microglia, the diameter of the cell body was approx. 6–7  $\mu\text{m}$  and their ramified processes were thin and relatively short. The cells possessed 4–5 slender, 5–10- $\mu\text{m}$  long processes (Figure 2). The PILO treatment induced a significant increase in the number of cells when counted after 24 h. The number of Iba1-positive cells in a 1- $\text{mm}^2$  hippocampal area increased to 1700 per  $\text{mm}^2$  or above compared to the controls, in which we counted 500 cells or less in 1  $\text{mm}^2$ .

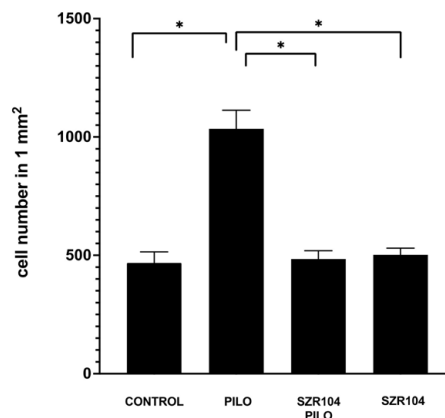


**Figure 2.** Analysis of ionized calcium-binding adaptor molecule 1 (Iba1)-positive cell counts in the entire area of the hippocampal formation of epileptic and control mice ( $n = 16$ ; mean  $\pm$  SEM). Statistical differences were detected between control, pilocarpine (PILO)-treated, SZR104 + PILO-treated and SZR104-treated animals ( $* p \leq 0.05$ ).

The size of the Iba1-stained cells was larger in PILO-treated mice; cell body diameters were 8–12  $\mu\text{m}$ , and the cytoplasmic processes were thicker compared to resting microglia cells (Figure 3). The measured surface area of the cells increased significantly compared to the controls (Figure 3). While the control, untreated microglia cell areas were in the  $\leq 500 \mu\text{m}^2$  range, the cells from epileptic animals were significantly larger ( $\leq 1500 \mu\text{m}^2$ ).

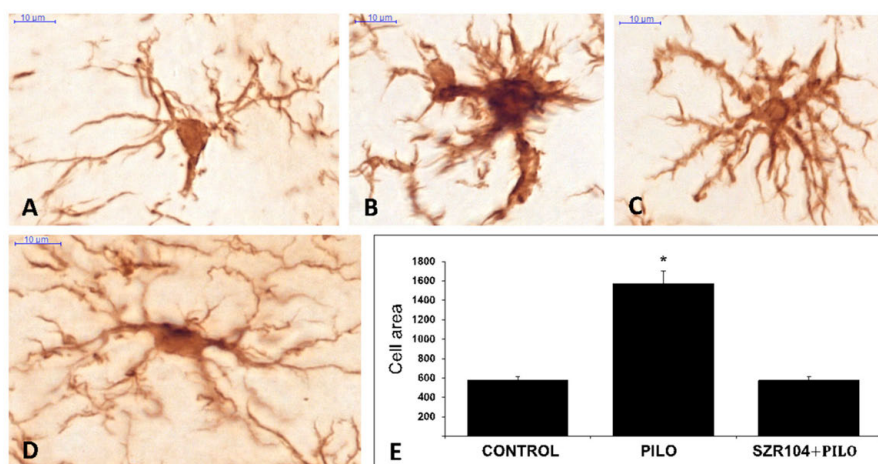


**Figure 3.** (A–D): ionized calcium-binding adaptor molecule 1 (Iba1)-stained microglia cells from control (A), pilocarpine(PILO)-treated (B,C) and SZR104 + PILO-treated (D) animals. Scale bars: 10  $\mu\text{m}$ . (E): The average microglia cell areas (cell body and processes) in  $\mu\text{m}^2$  values on the y-axis ( $n = 10$ ; mean  $\pm$  SEM) in control, PILO-treated and SZR104 + PILO-treated animals ( $* p \leq 0.05$ ).

The SZR104 pretreatment of epileptic animals prevented the seizure-caused microglial alterations. Both the number of Iba1-positive cells and the surface area of the single cells remained close to the control values (Figure 3). When compared to the PILO-treated hippocampi, the microglia-inhibiting effects of SZR104 proved to be significant (Figure 2). The shape, size and ramification were similar to controls (Figure 3). SZR104 given alone did not cause alterations in the number and morphology of microglia cells—these cells were similar to the control cells (Figure 3).

#### 2.4. Effect of KYNA and SZR104 on Microglia Phagocytosis and Iba1 Immunoreactivity

The treatment of the secondary microglial cultures with LPS increased the phagocytotic activity of the microglia cells significantly (Figures 4 and 5). The unstimulated cultured microglia cells display a basal phagocytotic activity: the number of microbeads in a single cell is regularly two (Figures 4 and 5). Following the LPS challenge, this number rises sharply up to nine per single cell (Figures 4 and 5). Treatment of the cell culture with KYNA and SZR104 before the LPS challenge prevented the increase in the number of phagocytosed microbeads; the phagocytotic activity of the microglia in the presence of KYNA and SZR104 remained at the control level (Figures 4 and 5). This pharmacological effect of the KYNA and SZR104 was significant (Figure 5). Quantitative Western blot analysis of Iba1 expression demonstrated that the Iba1 content of the secondary cultures did not change significantly following the different pharmacological (LPS, KYNA and SZR104) treatments (Figure 6).

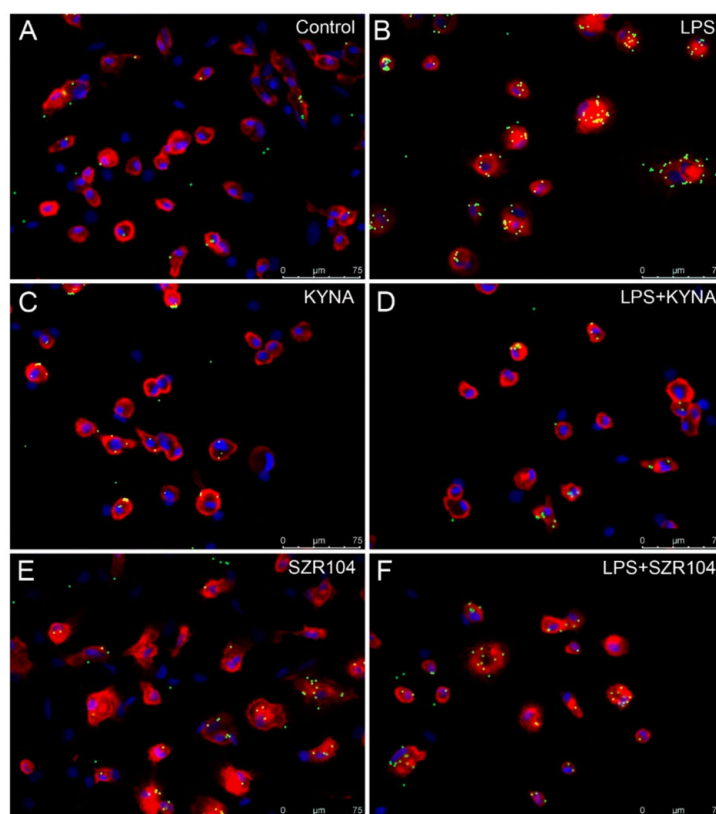


**Figure 4.** Effects of kynurenic acid (KYNA) and SZR104 on the phagocytic activity of microglial cells in cultures. Pictures showing CD11b/c-immunostained microglia in red, microbeads in green and cell nuclei in blue. (A) Unstimulated and untreated control; (B) lipopolysaccharide (LPS)-challenged cells; (C) KYNA-treated; (D) LPS + KYNA-treated; (E) SZR104-treated; (F) LPS + SZR104-treated. Microglia displayed different phagocytotic activity, as evidenced by the number of phagocytosed microbeads. Scale bar: 75  $\mu\text{m}$ .

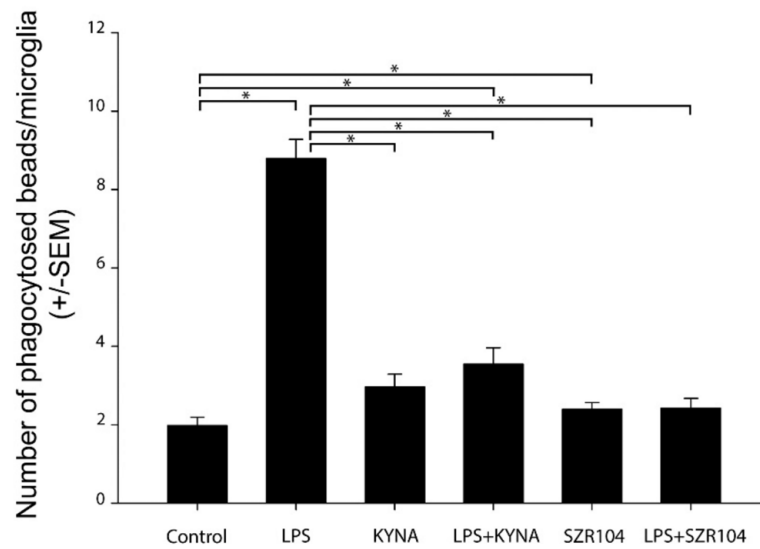


**Figure 5.** Quantitative analysis of the number of phagocytosed microbeads after the pharmacological treatments demonstrated that kynurenic acid (KYNA) and SZR104 significantly inhibited microglial phagocytosis. The number of phagocytosed beads ( $n = 240$ ; mean  $\pm$  SEM) was counted in three separate culturing procedures. Data were analyzed with Kruskal–Wallis one-way analysis of variance on ranks. \*  $p < 0.05$ .

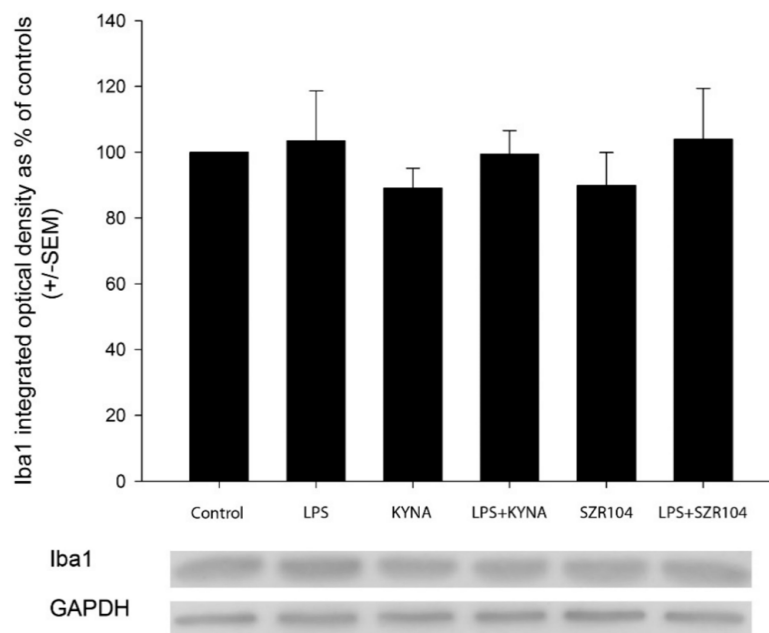


**Figure 6.** Quantitative Western blot analysis of Iba1 and glyceraldehyde-3-phosphate dehydrogenase (GAPDH) immunoreactivities in microglia cell cultures. Error bars indicate integrated optical density values as percent of controls ( $n = 4$ ; mean  $\pm$  SEM). Representative Western blot images are shown below the graphs. Data were analyzed with a one-way ANOVA. No statistically significant differences were found.

### 3. Discussion

The main findings of the experiments are as follows. (1) The KYNA analogue SZR104 did not prevent the symptoms of motor convulsions. At the same time, SZR104 injected before the PILO treatment did not improve the mortality rate of the epileptic animals. (2) The KYNA analogue SZR104

decreased the postepileptic elevated blood IL-6 levels, although the decrease was not significant. (3) The KYNA analogue SZR104 prevented the post-epileptic proliferation of microglia cells in the hippocampus. This effect was statistically significant. (4) The KYNA analogue SZR104 significantly prevented the post-epileptic in vivo reactive morphological transformation of hippocampal microglia. (5) KYNA and the KYNA analogue SZR104 prevented the LPS-induced increase in phagocytotic activity of microglia cells, in vitro. This pharmacological effect was statistically significant. (6) KYNA and SZR104 did not cause alteration of the Iba1 protein expression of in vitro microglia cells.

### 3.1. KYNA is an Endogenous Regulator in the CNS

Tryptophan metabolism is an important process in the central nervous system (CNS) because it is the source of serotonin and melatonin through the methoxyindole pathway [2,7,23]. The other direction of the tryptophan metabolism is the kynurenine pathway (KP), which accounts for more than 90% of tryptophan transformation in the CNS [2,7,23]. One of the key molecules of the KP is L-kynurenine, which results in the formation of other, pharmacologically active compounds, such as KYNA and quinolinic acid (QUIN). KYNA is antagonistic on ionotropic glutamate receptors (iGluRs), especially NMDA- and  $\alpha$ -amino-3-hydroxy-5-methyl-4-isoxazole (AMPA)/kainate receptors in micromolar concentrations [2,23], whilst QUIN is neurotoxic because it stimulates the synaptic release of glutamate [1,2,23].

Our previous experiments with iGluR antagonists (dizocilpine, ketamine, amantadine and GYKI52466) proved that iGluR antagonists prevented motor convulsions and decreased epilepsy-related mortality in the experimental animals significantly [6,24]. These effects were not detected in our animal experiments following the SZR104 pretreatment; therefore, we think that SZR104 did not exert its pharmacological effects on iGluRs. These measured microglia effects of KYNA and SZR104 are probably the consequences of the downregulation of inflammation-related genes in microglia cells [25].

### 3.2. Blood IL-6 Level Alterations in Seizure

Post-epileptic elevation of IL-6 in peripheral blood is described in the literature [18]. This elevation of IL-6 1–3 days post-seizure was also measured with RT-PCR and flow cytometry in mice treated with PILO [18]. Blood IL-6 certainly originated from the immune system in these epileptic animals, and some of the IL-6 elevation was certainly due to the secretion of IL-6 by brain microglia [12,18]. SZR104 alone did not cause any alteration in IL-6 blood level and microglia morphology. We think, therefore, that SZR104 acted indirectly in epileptic animals. The animals treated with SZR104 prior to PILO treatment did show some decrease in IL-6 levels. Although this decrease was not significant, we think that the non-significant decrease in IL-6 levels reflected the suppression of microglial inflammation-related genes by SZR104 in our experiments [25]. The inhibition of microglia activation by SZR104 (see next paragraph) supports this assumption. The lack of significance can be explained on the basis of the low number of samples (four samples).

### 3.3. Postepileptic Transformation of Hippocampal Microglia

Microglia cells are activated rapidly following pathological changes in the brain [9]. The expression of neurotransmitter receptors on their surface renders them sensitive to neuronal hyperactivity [12–15]. The receptors initiate the transformation of microglia from resting to activated status by regulating their cytokine secretion [12–15,18]. This means that in the acute phase of the post-epileptic period, the secretion of IL-6, tumor necrosis factor  $\alpha$  (TNF $\alpha$ ), interleukin-12 and interleukin-1 $\beta$  will be boosted and the brain cytokines will be secreted primarily by the microglia cells [18]. The stimulation of proinflammatory IL-6 secretion by neuronal hyperactivity was proven in our experiments. Microglia can promote neurodegeneration [10,11,13] but can also be the protector of neurons [11,13]. It is an open question whether these epileptic microglia cells boosted or delayed the neurodegeneration caused by the PILO epilepsy [26]. Further in vivo experiments are necessary in order to determine the exact role of microglia in our epilepsy experiments.

### 3.4. Inhibition of Phagocytosis In Vitro by KYNA and SZR104

Cultured microglia cells stimulated with LPS displayed a large increase in phagocytosis of fluorescent microbeads. This observation is supported by previous data from our laboratory [20–22]. The number of internalized microbeads increased more than four-fold in the stimulated cells. The LPS probably stimulated Toll-like receptor 4 (TLR4) and transient receptor potential ankyrin 1, 4 receptors (TRPA1, TRPA4) [27]. These receptors mediated those membrane and cytoplasmic processes which lead to phagocytosis; they increase the  $Ca^{++}$  permeability of the membrane (TRPA effect), exert regulatory effects on gene expression (TLR4 effect) and increase the cytoplasmic cation concentrations (TRPA effect). Treatment of the cells with KYNA and SZR104 prevented the increase in phagocytotic activity by LPS. We think that during the in vitro exposure, KYNA and SZR104 were able to prevent the actions of LPS mainly through the repression of TLR4 by the deregulation of inflammation-related genes, consequently preventing phagocytosis [7,25]. It was proven in monocytic cell cultures that KYNA and SZR104 directly facilitated the expression of anti-inflammatory tumor necrosis factor-stimulated gene-6 (TSG-6) and, at the same time, attenuated the TNF $\alpha$  production of these cells [25]. These actions could have been exerted through the cytoplasmic aryl hydrocarbon receptor (AHR) [7,8,25]. Experimental evidence suggested that KYNA is an endogenous ligand of AHR [7,8,28–30] and inhibited phagocytosis in myeloid cells through AHR signaling [31].

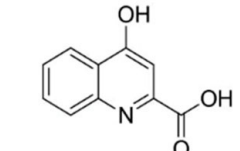
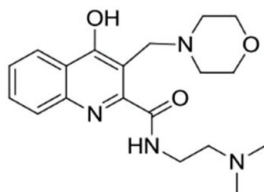
Literature data prove that other tryptophan derivatives and probably also the synthetic analogue SZR104 are ligands of the AHR [28]. The AHR is a cytoplasmic ligand-dependent transcription factor which was proven to exert immunosuppressive and anti-inflammatory effects [7,8,28–30]. The AHR complex is present in the mammalian hippocampus in neurons, astrocytes and microglia cells [29]. The AHR participates in several intracellular regulatory processes, from cell differentiation to apoptosis [7,8,28–30]. KYNA is known to be the endogenous modulator of the AHR [7,8], although the molecular details of this action are not clear [25,28]. On the basis of the literature [25,28], we think that SZR104 also acted on the AHR [25]. SZR104 was reportedly crossing the BBB [4] because it was applied successfully in PTZ seizures, in vivo [4]. During the 40-min pretreatment period, SZR104 crossed the BBB and acted on microglial AHRs, inhibiting the transformation of microglia into reactive forms and inhibiting the reentry of the cells into the cell cycle during and following the seizure [29,30]. This effect was the result of the genomic AHR pathway [28]. Since the effect of SZR104 was completely independent of the actions of extracellular glutamate on NMDA receptors, it did not influence the seizure symptoms and did not prevent the mortality of the animals. Similarly, in cell culture, KYNA and SZR104 supposedly acted through the AHR pathway and thereby suppressed phagocytosis through the decrease in the expression of TLR-4 on the cell surface because of the inhibition of inflammation-related gene expression [25]. The repression of some cytoskeletal proteins necessary for migration and phagocytosis was also reported [32]; these finally resulted in the strong decrease in phagocytotic activity of LPS-treated cells [31,32]. We certainly need further experiments to clear the possible role of AHRs in the pharmacological action of SZR104.

## 4. Materials and Methods

### 4.1. Kynurenes Used

The following kynurenes were investigated in our experiments [3,4,25] (Table 2).

**Table 2.** Molecular structure, chemical name, empirical formula and molecular weight of KYNA and its analogue SZR104.

Code	Molecular Structure	Chemical Name	Empirical Formula and Molecular Weight
KYNA		4-hydroxyquinolin-2-carboxylic acid	C <sub>10</sub> H <sub>7</sub> NO <sub>3</sub> 189.17
SZR104		N-(2-(dimethylamino)ethyl)-3-(morpholinomethyl)-4-hydroxyquinoline-2-carboxamide	C <sub>19</sub> H <sub>26</sub> N <sub>4</sub> O <sub>3</sub> 358.43

#### 4.2. In Vivo Experiments

Adult (30 g body weight), male NMRI strain mice were used. Animals were housed in standard conditions with dark/light cycle (12–12 h), room temperature 24 °C and humidity 22%, with food and water ad libitum. The animal experiments were approved first by the Faculty Ethical Committee on Animal Experiments (MÁB), University of Szeged (approval No.: 1-74-1/2017.MÁB), and the Government Office of Csongrád County (Department of Food and Animal Health; approval No.: CS/101/3347-2/2018). The animal experiments were conducted according to the European Union Directive 2010/63/EU of the European Parliament and of the Council of 22 September 2010 on the Protection of Animals Used for Scientific Purposes.

The experiments were performed in the morning. Epilepsy was triggered through intraperitoneal (i.p.) injection of 190 mg/kg pilocarpine hydrochloride (PILO). PILO (Sigma-Aldrich St.Louis, MO, USA) was dissolved in sterile physiological saline (supplied by the Central Pharmacy of the Medical Faculty, Szeged, Hungary). Control animals received i.p. physiological saline. SZR104 was dissolved in distilled water and i.p. administered at a dose of 358 mg/kg 40 min before the PILO injection, according to [4]. The groups of experimental animals are shown in Table 2.

Generalized tonic-clonic seizures developed in the PILO- and SZR104 + PILO-injected animals. At 90 min from the time of the PILO injection, the motor convulsions were stopped with 10 mg/kg diazepam (Seduxen® Richter, Budapest, Hungary) i.p., and the animals were treated with Ringer-lactate solution injected intradermally. The animals were observed for 3–4 h after the injections. Mortality was 30% in PILO- and 40% in PILO + SZR104-injected animals. One day (24 h) after the treatments, the surviving animals were anesthetized with halothane (Sigma-Aldrich, St. Louis, MO, USA), the left cardiac ventricle was cannulated and the animals were perfused through the heart and ascending aorta with 50 mL cold 4% paraformaldehyde in 0.1 M phosphate-buffered saline (PBS; pH 7.4). Brains were postfixed in the fixative for 24 h, at 4 °C, cryoprotected in 30% sucrose in PBS at room temperature and sectioned on a freezing microtome (Reichert-Jung, Cryocut 1800, Vienna, Austria) in coronal planes at 25-µm thickness between the coronal levels 67 and 79, according to Allen's Mouse Brain Atlas ([www.brain-map.org](http://www.brain-map.org)).

#### 4.3. Analysis of Blood Samples

Samples of blood (300–500 µL) were taken from the right ventricle of the heart of the halothane-anesthetized animals with a sterile tuberculin syringe. The blood samples were centrifuged at 3000×g for 10 min and then the serum layers were collected and stored at –20 °C until measurement. IL-6 concentrations were determined using the LEGEND MAX™ Elisa kit (BioLegend Inc., San Diego, CA, USA), according to the instructions of the manufacturer. The sensitivity of the assay was 2 pg/mL.

The intraassay coefficient of variation was <5.7%, and the interassay coefficient of variation was <10.7%. Statistical analysis of ELISA data was done using R Studio for Windows (version 1.3.1073). Data are expressed as mean  $\pm$  SEM, differences were calculated with an ANOVA and a post hoc Bonferroni's test was performed for significance.

#### 4.4. Iba1 Immunohistochemistry

The brain sections were processed free-floating, according to the following protocol. Endogenous peroxidase activity was blocked with 3% H<sub>2</sub>O<sub>2</sub> for 15 min. Non-specific binding sites were blocked with 20% normal pig serum (NPS; diluted: 1/10; Abcam, Cambridge, UK) and tissue permeability was enhanced by using 1% Triton X-100 in the blocking solution. The sections were incubated overnight at room temperature with the primary rabbit anti-Iba1 antibody (1/8000, Fujifilm Wako Chemicals Europe GmbH, Neuss, Germany). Biotinylated secondary antibodies (1:400, Jackson Immuno Research, West Grove, PA, USA) were used for 1 h at room temperature and the signal was detected with peroxidase-labeled streptavidin (1/6000, Rockland Immunochemicals Incorporation, Limerick, PA, USA). All incubations were done in plastic vials with continuous agitation. The sites of the immunoreaction were visualized with diaminobenzidine tetrahydrochloride (DAB) + H<sub>2</sub>O<sub>2</sub>. Sections were mounted on microscope slides, air-dried, dehydrated and coverslipped with DPX (Merck KGaA, Darmstadt, Germany). Chemicals other than antibodies were purchased from Sigma-Aldrich (St. Louis, MO, USA).

#### 4.5. Evaluation of the Immunohistochemical Data

The stained sections were scanned with a Slide scanner (Mirax Midi, 3DHistech Ltd., Budapest, Hungary) equipped with a Panoramic Viewer 1.15.4 program (3DHistech Ltd., Budapest, Hungary). The digitized sections were analyzed using Image Pro Plus 4.5 morphometry software (Media Cybernetics, Silver Spring, MD, USA). Four sections were analyzed from every animal. Using the digital image, the hippocampal formation (subiculum, hippocampus and dentate gyrus) was manually outlined as the area of interest (AOI). The threshold was determined in such a way that the counting program could equally recognize Iba1 immunoreactive microglial cells. The software counted the number of the immunostained cells in the entire AOI (i.e., in every layer of the hippocampal formation). The number of microglia cells in the AOI was normalized to one square millimeter. The surface area of the single microglia cells was also measured with the help of Image Pro Plus 4.5 software (Media Cybernetics, Silver Spring, MD, USA). Single microglia cells were selected from the digital images with 3000 $\times$  magnification, their contours were manually outlined and their area was measured. The selection and the measurements were relatively simple because of the low staining background and the strong Iba1 immunostaining of the microglial cells. Ten microglia cells were selected from the hippocampi of each experimental group. These cell area measurements were expressed as square micrometer values. Data are expressed as mean  $\pm$  SEM, differences were calculated with a one-way ANOVA and a post hoc Bonferroni's test was performed ( $p \leq 0.05$  was significant). GraphPad Prism8 (version 8.4.3) software (GraphPad Software, LLC, San Diego, CA, USA) was used to statistically analyze the results of the immunohistochemical measurements.

#### 4.6. Cell Culture Experiments

Microglial-enriched cell cultures were prepared from primary cortical cell cultures. Forebrain cerebrocortical tissue samples were obtained from newborn Sprague Dawley rats. The animals were decapitated, the cerebral cortex was removed, minced with scissors, incubated for 10 min at 37 °C in Dulbecco's Modified Eagle's Medium (DMEM; Invitrogen, Carlsbad, CA, USA, containing 1 g/L D-glucose, 110 mg/L Na-pyruvate, 4 mM L-glutamine, 3.7 g/L NaHCO<sub>3</sub>, 10,000 U/mL penicillin G, 10 mg/mL streptomycin sulfate and 25  $\mu$ g/mL amphotericin B) supplemented with 0.25% trypsin (Invitrogen, Carlsbad, CA, USA) and then centrifuged at 1000 $\times$  g for 10 min at room temperature (RT). The pellet was resuspended, washed twice in 5 mL DMEM containing 10% heat-inactivated

bovine serum (Invitrogen, Carlsbad, CA, USA) and centrifuged for 10 min at 1000× g at RT. The final pellet was resuspended in 2 mL of the same solution and passed through a sterile filter (100-µm pore size; Greiner Bio-One Hungary Kft., Mosonmagyaróvár, Hungary) to eliminate tissue fragments that resisted dissociation. The filtered suspension was resuspended in 2 mL of the same solution, after which the cells were counted and plated in the same medium either on poly-L-lysine-coated culture flasks (75 cm<sup>2</sup>, 10 × 10<sup>6</sup> cell/flask) or coverslips (2 × 10<sup>5</sup> cells/coverslip) and incubated at 37 °C in a humidified air atmosphere supplemented with 5% CO<sub>2</sub>. The DMEM containing 10% bovine serum (BSA) was changed the next day, and then, every 3 days. Secondary microglial cells were subcloned from mixed primary cultures maintained in a poly-L-lysine-coated culture flask by shaking the cultures at 120 rpm in a platform shaker for 20 min at 37 °C. Microglia from the supernatant were collected by centrifugation at 3000× g for 8 min at 4 °C and resuspended in 2 mL DMEM containing 10% bovine serum. The cells were seeded at a density of 10<sup>6</sup> cells/Petri dish for Western blots or 2 × 10<sup>5</sup> cells/coverslip/Petri dish for immunocytochemistry and phagocytosis assay and cultured in DMEM containing 10% BSA in a humidified atmosphere supplemented with 5% CO<sub>2</sub> at 37 °C for 7 days (subDIV7). The DMEM containing 10% BSA was changed the next day, and then, every 3 days. On the sixth day of subcloning (subDIV6), the medium was replaced and the microglial cells were treated for 24 h with either LPS (20 ng/mL final concentration, dissolved in DMEM), KYNA (1 µM) or SZR104 (1 µM final concentration) alone or with a combination of LPS + KYNA and LPS + SZR104 and the effects were compared in functional tests (phagocytosis, Iba1 protein synthesis). The LPS treatment served as an inflammation challenge [14]. For the measurement of phagocytic activity, phagocytosed microbeads were counted in the microglia of the secondary cultures. Cultures treated with fluorescently labeled microbeads were incubated for 60 min at 37 °C. The cells were fixed in 4% formaldehyde in 0.05 M PBS (pH 7.4, RT) for 5 min and rinsed in 0.05 M PBS for 3 × 5 min. The cells were first incubated with 0.05 M PBS containing 5% normal goat serum (Sigma-Aldrich, St. Louis, MO, USA) and 0.3% Triton X-100 for 30 min at 37 °C, then treated with mouse anti-CD11b/c antibody (1/200 Invitrogen Carlsbad, CA, USA) in 0.05 M PBS containing 1% BSA solution overnight at 4 °C. After washing at RT (3 × 5 min in 0.05 M PBS), cells were incubated with Alexa Fluor 568 goat anti-mouse immunoglobulin G (IgG; Invitrogen, Carlsbad, CA, USA) diluted (1/1000) in 1 mg/mL polyvinylpyrrolidone/0.05 M PBS containing 1 mg/mL polyvinylpyrrolidone in the dark for 2 h, at RT. The coverslips were then rinsed twice in 1 mg/mL polyvinylpyrrolidone/0.05 M PBS, then in distilled water, and were then dried and mounted on microscope slides covered with Prolong Diamond Antifade with 4',6-Diamine-2'-phenylindole dihydrochloride (DAPI; Thermo Fisher, Waltham, MA, USA).

#### 4.7. *In Vitro* Phagocytosis Assay

The fluid-phase phagocytotic capacity of the microglial cells was determined via the uptake of fluorescent microspheres (2-µm diameter; Sigma-Aldrich, St. Louis, MO, USA). The cells were plated on coverslips in Petri dishes at a density of 200,000 cells/coverslip in 2 mL DMEM containing 10% heat-inactivated bovine serum and cultured for 7 days (subDIV7); then, 2 µL 2.5% aqueous suspension of fluorescent microspheres was added and the secondary culture was incubated for 60 min at 37 °C. The cells were washed five times in 0.05 M PBS, fixed in 0.05 M PBS containing 4% formaldehyde, and CD11b/c-immunocytochemistry was performed. The coverslips were mounted in Prolong Diamond Antifade with DAPI (Thermo Fisher, Waltham, MA, USA) and the fluorescent microbeads were counted under the microscope with 20× and 40× objectives—100 random fields with a total of 1690 bead-labeled cells were counted and the number of phagocytosed microbeads (mean ± SEM) was analyzed. Statistical comparisons were made using SigmaPlot (v. 12.3, Systat Software Inc., Chicago, IL, USA) and data were analyzed with a Kruskal–Wallis one-way analysis of variance on ranks, followed by Dunn's method for pairwise multiple comparison procedures for statistically significant differences between the groups.

#### 4.8. Western Blot Analysis

Cultured cells were collected with a rubber policeman, homogenized in 50 mM TrisHCl (pH 7.5) containing 150 mM NaCl, 0.1% Nonidet P40, 0.1% cholic acid, 2 µg/mL leupeptin, 1 µg/mL pepstatin, 2 mM phenylmethylsulfonyl fluoride and 2 mM EDTA, incubated on ice for 30 min and centrifuged at 10,000× g for 10 min. The pellet was discarded, and the protein concentration of the supernatant was determined [33]. For the Western blot analysis of Iba1 immunoreactivity, 10 µg protein was separated on sodium dodecyl sulfate (SDS)-polyacrylamide gel, transferred onto Hybond-ECL nitrocellulose membrane (Amersham Biosciences, Little Chalfont, UK), blocked for 1 h in 5% non-fat dry milk in Tris-buffered saline (TBS) containing 0.1% Tween 20 and incubated with either a rabbit anti-Iba1 polyclonal antibody (dilution 1/1000; Fujifilm Wako GmbH, Neuss, Germany) or a mouse anti-glyceraldehyde-3-phosphate dehydrogenase (GAPDH) monoclonal antibody (clone GAPDH-71.1; 1/20,000 final dilution; Sigma-Aldrich, St. Louis, MO, USA). Non-specifically bound or excess antibody was removed with 5 × 5 min rinses in 0.1 M TBS containing 0.1% Tween 20. Membranes were then incubated for 1 h with either peroxidase-conjugated goat anti-rabbit or peroxidase-conjugated rabbit anti-mouse antibody (dilution 1/2000; Sigma-Aldrich, St. Louis, MO, USA) and washed five times in 0.1% TBS–Tween 20. The enhanced chemiluminescence method (ECL plus Western blotting detection reagents; Amersham Biosciences, Little Chalfont, UK) was used to reveal immunoreactive bands, according to the manufacturer's instructions.

#### 4.9. Image Analysis

Grayscale digital images of the Western blots were acquired by scanning the autoradiographic films with a desktop scanner (Epson Perfection V750 Pro; Seiko Epson Corp., Nagano, Japan). Images were scanned and processed at identical settings to allow comparisons of the blot results from different samples. The densities of immunoreactive lanes equally loaded with protein were quantified and presented as percent of controls. A one-way ANOVA (SigmaPlot, v.12.3, Systat Software Inc., Chicago, IL, USA) was used for statistical comparisons. Values as percent of controls are presented as the mean ± SEM from at least four immunoblots, each representing an independent experiment.

### 5. Conclusions

We investigated the possible pharmacological effects of the synthetic KYNA analogue SZR104. SZR104 crosses the BBB [4]. In the present experiments, SZR104 did not prevent behavioral convulsions and did not decrease the mortality of epileptic mice subjected to systemic pilocarpine treatment. On the other hand, SZR104 significantly decreased the number of microglia cells in the epileptic hippocampus and prevented microglia proliferation. Furthermore, SZR104 significantly decreased the size of individual microglia cells in the epileptic hippocampus and prevented microglia activation. Finally, SZR104 and KYNA significantly decreased microglial phagocytosis *in vitro*.

These experimental results were explained on the basis of data from the literature and the following hypothetical conclusions were drawn:

1. Although it was previously supposed that KYNA analogues act as iGluR antagonists [1–4,23], the present SZR104 action mechanism was not connected to NMDA receptors. SZR104 was acting through non-glutamatergic molecular mechanisms.
2. We supposed that SZR104 actions were exerted through the AHR complex [25]. KYNA and the synthetic analogue SZR104 are ligands of the AHR [28].
3. The action on AHRs could explain the inhibitory effect of SZR104 on microglia activation and proliferation. The phenotype change of the microglia could be the consequence of the genomic actions of the AHR complex [28], through a molecular scenario including the decrease in TNFα secretion and increasing tumor necrosis factor-stimulated gene-6 (*TSG-6*) expression [25]. The depletion of TNFα may affect multi-protein complex containing mammalian target of rapamycin (mTOR) protein (mTORC1) activity and the nuclear translocation of mTOR [34].

The depletion of TNF $\alpha$  and mTORC1 activation may arrest the cell cycle in the late G1 phase through metabolic checkpoints [35], thereby preventing microglia proliferation.

4. The inhibition of microglia phagocytosis by SZR104 and KYNA could also utilize AHR pathways, causing the decrease in TLR-4 expression on the cell surface [28], the induction of cytoskeletal changes [32] or the deregulation of the nuclear factor kappa-light-chain-enhancers of activated B cells (NF- $\kappa$ B) pathway [28].

**Author Contributions:** Conceptualization: L.V., K.G., I.F. and A.M. (András Mihály). Methodology, formal analysis, investigation, resources and data curation: N.L., D.K., M.S., K.D., A.M. (Adrienne Mátyás) and I.F. Synthesis of KYNA and SZR104: F.F. Original draft preparation and writing and editing: K.G. and A.M. (András Mihály). Supervision and project administration: K.G. and A.M. (András Mihály). Funding acquisition: L.V. All authors have read and agreed to the published version of the manuscript.

**Funding:** This research was funded by GINOP 2.3.2-2015-16-00034, TKP2020 Thematic Excellence Program 2020 and NKFIH-1279-2/2020 TKP 2020. During the preparation of the manuscript, András Mihály was funded by the Faculty of Medicine and Health Sciences of Carl von Ossietzky University, Oldenburg, Germany, as a Visiting Professor and by the Hanse-Wissenschaftskolleg (Institute for Advanced Study), Delmenhorst, Germany, by providing a Joint Fellowship for A.M. (András Mihály).

**Acknowledgments:** The technical help of Monica Kara (Department of Anatomy, University of Szeged, Szeged, Hungary) is greatly appreciated.

**Conflicts of Interest:** The authors declare no conflict of interest.

## Abbreviations

AHR	Aryl hydrocarbon receptor
AMPA	$\alpha$ -amino-3-hydroxy-5-methyl-4-isoxazole
ANOVA	Analysis of variance
AOI	Area of interest
BBB	Blood–brain barrier
CNS	Central nervous system
ELISA	Enzyme-linked immunosorbent assay
GAPDH	Glyceraldehyde-3-phosphate dehydrogenase
GYKI52466	a 2,3-benzodiazepine, which is non-competitive AMPA receptor antagonist
Iba1	Ionized calcium binding adaptor molecule 1
iGluR	Ionotropic glutamate receptor
IL-6	Interleukin-6
KYNA	Kynurenic acid
KP	Kynurenine pathway
LPS	Lipopolysaccharide, endotoxin
mTOR	Mammalian target of rapamycin
mTORC1	Multi-protein complex containing mTOR protein
NF- $\kappa$ B	Nuclear factor kappa-light-chain-enhancers of activated B cells; protein complex regulating cellular responses
NMDA	N-methyl-D-aspartic acid
PILO	Pilocarpine
RT-PCR	Reverse transcription polymerase chain reaction
QUIN	Quinolinic acid
SEM	Standard error of the mean
SZR104	N-(2-(dimethylamino)ethyl)-3-(morpholinomethyl)-4-hydroxyquinoline-2-carboxamide
TLR4	Toll-like receptor4
TNF $\alpha$	Tumor necrosis factor-alpha
TRPA1,4	Transient receptor potential ankyrin 1,4 receptors

## References

1. Biernacki, T.; Sandi, D.; Bencsik, K.; Vécsei, L. Kynurenines in the pathogenesis of multiple sclerosis: Therapeutic perspectives. *Cells* **2020**, *9*, 1564. [[CrossRef](#)] [[PubMed](#)]
2. Vécsei, L.; Szalárdy, L.; Fülöp, F.; Toldi, J. Kynurenines in the CNS: Recent advances and new questions. *Nat. Rev. Drug Discov.* **2013**, *12*, 64–82. [[CrossRef](#)] [[PubMed](#)]
3. Fülöp, F.; Szatmári, I.; Vámos, E.; Zádori, D.; Toldi, J.; Vécsei, L. Syntheses, transformations and pharmacological applications of kynurenic acid derivatives. *Curr. Med. Chem.* **2009**, *16*, 4828–4842. [[CrossRef](#)] [[PubMed](#)]
4. Demeter, I.; Nagy, K.; Gellért, L.; Vécsei, L.; Fülöp, F.; Toldi, J. A novel kynurenic acid analog (SZR104) inhibits pentylenetetrazole-induced epileptiform seizures. An electrophysiological study. *J. Neural Transm.* **2012**, *119*, 151–154. [[CrossRef](#)]
5. Kovács, A.; Mihály, A.; Komáromi, A.; Gyengési, E.; Szente, M.; Weiczner, R.; Krisztin-Péva, B.; Szabó, G.; Telegdy, G. Seizure, neurotransmitter release, and gene expression are closely related in the striatum of 4-aminopyridine-treated rats. *Epilepsy Res.* **2003**, *55*, 117–129. [[CrossRef](#)]
6. Weiczner, R.; Krisztin-Péva, B.; Mihály, A. Blockade of AMPA receptors attenuates 4-aminopyridine seizures, decreases the activation of inhibitory neurons but is ineffective against seizure-related astrocytic swelling. *Epilepsy Res.* **2008**, *78*, 22–32. [[CrossRef](#)]
7. Wirthgen, E.; Hoeflich, A.; Rebl, A.; Günther, J. Kynurenic acid: The Janus-faced role of an immunomodulatory tryptophan metabolite and its link to pathological conditions. *Front. Immunol.* **2017**, *8*, 1957. [[CrossRef](#)]
8. Routy, J.-P.; Routy, B.; Graziani, G.M.; Mehraj, V. The kynurenine pathway is a double-edged sword in immune-privileged sites and in cancer: Implications of immunotherapy. *Int. J. Tryptophan Res.* **2016**, *9*, 67–77. [[CrossRef](#)]
9. Kreutzberg, G.W. Microglia: A sensor for pathological events in the CNS. *Trends Neurosci.* **1996**, *19*, 312–318. [[CrossRef](#)]
10. Priller, J.; Prinz, M. Targeting microglia in brain disorders. *Science* **2019**, *365*, 32–33. [[CrossRef](#)]
11. Hickman, S.; Izzy, S.; Seu, P.; Morsett, L.; El Khoury, J. Microglia in neurodegeneration. *Nat. Neurosci.* **2018**, *21*, 1359–1369. [[CrossRef](#)]
12. Lee, M. Neurotransmitters and microglial-mediated neuroinflammation. *Curr. Protein Pept. Sci.* **2013**, *14*, 21–32. [[CrossRef](#)]
13. Deczkowska, A.; Keren-Shaul, H.; Weiner, A.; Colonna, M.; Schwartz, M.; Amit, I. Disease-associated microglia: A universal immune sensor of neurodegeneration. *Cell* **2018**, *173*, 1073–1081. [[CrossRef](#)] [[PubMed](#)]
14. Kirdajova, D.B.; Kriska, J.; Tureckova, J.; Anderova, M. Ischemia-triggered glutamate excitotoxicity from the perspective of glial cells. *Front. Cell. Neurosci.* **2020**, *14*. [[CrossRef](#)] [[PubMed](#)]
15. Pocock, J.M.; Kettenmann, H. Neurotransmitter receptors on microglia. *Trends Neurosci.* **2007**, *30*, 527–535. [[CrossRef](#)] [[PubMed](#)]
16. Sapp, E.; Kegel, K.B.; Aronin, N.; Hashikawa, T.; Uchiyama, Y.; Tohyama, K.; Bhide, P.G.; Vonsattel, J.P.; DiFiglia, M. Early and progressive accumulation of reactive microglia in the Huntington disease brain. *J. Neuropathol. Exp. Neurol.* **2001**, *60*, 161–172. [[CrossRef](#)]
17. Hovens, I.B.; Nyakas, C.; Shoemaker, R.G. A novel method for evaluating microglial activation using ionized calcium-binding adaptor protein-1 staining: Cell body to cell size ratio. *Neuroimmunol. Neuroinflamm.* **2014**, *1*, 82–88. [[CrossRef](#)]
18. Benson, M.J.; Manzanero, S.; Borges, K. Complex alterations in microglial M1/M2 markers during the development of epilepsy in two mouse models. *Epilepsia* **2015**, *56*, 895–905. [[CrossRef](#)]
19. Diaz-Aparicio, I.; Beccari, S.; Abiega, O.; Sierra, A. Clearing the corpses: Regulatory mechanisms, novel tool, and therapeutic potential of harnessing microglial phagocytosis in the diseased brain. *Neural Regen. Res.* **2016**, *11*, 1533–1539. [[CrossRef](#)]
20. Kata, D.; Földesi, I.; Fehér, Z.L.; Hackler, L., Jr.; Puskás, L.G.; Gulya, K. Rosuvastatin enhances anti-inflammatory and inhibits pro-inflammatory functions in cultured microglial cells. *Neuroscience* **2016**, *314*, 47–63. [[CrossRef](#)]
21. Szabó, M.; Gulya, K. Development of the microglial phenotype in culture. *Neuroscience* **2013**, *241*, 280–295. [[CrossRef](#)] [[PubMed](#)]

22. Kata, D.; Földesi, I.; Fehér, L.Z.; Hackler, L., Jr.; Puskás, L.G.; Gulya, K. A novel pleiotropic effect of aspirin: Beneficial regulation of pro- and anti-inflammatory mechanisms in microglial cells. *Brain Res. Bull.* **2017**, *132*, 61–74. [[CrossRef](#)] [[PubMed](#)]
23. Stone, T.W. Does kynurenic acid act on nicotinic receptors? An assessment of the evidence. *J. Neurochem.* **2020**, *152*, 627–649. [[CrossRef](#)]
24. Szakács, R.; Weiczner, R.; Mihály, A.; Krisztin-Péva, B.; Zádor, Z.; Zádor, E. Non-competitive NMDA receptor-antagonists moderate seizure-induced c-fos expression in the rat cerebral cortex. *Brain Res. Bull.* **2003**, *59*, 485–493. [[CrossRef](#)]
25. Mándi, Y.; Endrész, V.; Mosolygó, T.; Burián, K.; Lantos, I.; Fülöp, F.; Szatmári, I.; Lőrinczi, B.; Balog, A.; Vécsei, L. The opposite effect of kynurenic acid and different kynurenic acid analogs on tumor necrosis factor- $\alpha$  (TNF- $\alpha$ ) production and tumor necrosis factor-stimulated gene-6 (TSG-6) expression. *Front. Immunol.* **2019**, *10*, 1406. [[CrossRef](#)]
26. Curia, G.; Longo, D.; Biagini, G.; Jones, R.S.G.; Avoli, M. The pilocarpine model of temporal lobe epilepsy. *J. Neurosci. Methods* **2008**, *172*, 143–157. [[CrossRef](#)]
27. Startek, J.B.; Talavera, K.; Voets, T.; Alpizar, Y.A. Differential interactions of bacterial lipopolysaccharides with lipid membranes: Implications for TRPA1-mediated chemosensation. *Nat. Sci. Rep.* **2018**, *8*, 12010. [[CrossRef](#)]
28. Larigot, L.; Juricek, L.; Dairou, J.; Coumoul, X. AhR signaling pathways and regulatory functions. *Biochim. Open* **2018**, *7*, 1–9. [[CrossRef](#)]
29. Juricek, L.; Coumoul, X. The aryl hydrocarbon receptor and the nervous system. *Int. J. Mol. Sci.* **2018**, *19*, 2504. [[CrossRef](#)]
30. Mulero-Navarro, S.; Fernandez-Salguero, P.M. New trends in aryl hydrocarbon receptor biology. *Front. Cell Dev. Biol.* **2016**, *4*, 1–13. [[CrossRef](#)]
31. Kondrikov, D.; Elmansi, A.; Bragg, R.T.; Mobley, T.; Barrett, T.; Eisa, N.; Kondrikova, G.; Schoeinlein, P.; Aguilar-Perez, A.; Shi, X.-M.; et al. Kynurenine inhibits autophagy and promotes senescence in aged bone marrow mesenchymal stem cells through the arylhydrocarbon receptor pathway. *Exp. Gerontol.* **2020**, *130*, 110805. [[CrossRef](#)] [[PubMed](#)]
32. Zhao, L.; Shu, Q.; Sun, H.; Ma, Y.; Kang, D.; Zhao, Y.; Lu, J.; Gong, P.; Yang, F.; Wan, F. 1'H-indole-3'-carbonyl-thiazole-4-carboxylic acid methyl ester blocked human glioma cell invasion via aryl hydrocarbon receptors' regulation of cytoskeletal contraction. *Biomed Res. Int.* **2020**. [[CrossRef](#)]
33. Lowry, O.H.; Rosebrough, N.J.; Farr, A.L.; Randall, R.J. Protein measurement with the folin phenol reagent. *J. Biol. Chem.* **1951**, *193*, 265–275. [[PubMed](#)]
34. Laplante, M.; Sabatini, D.M. mTOR signaling at a glance. *J. Cell Sci.* **2009**, *122*, 3589–3594. [[CrossRef](#)] [[PubMed](#)]
35. Mukhopadhyay, S.; Saqena, M.; Foster, D.A. Synthetic lethality in KRas-driven cancer cells created by glutamine deprivation. *Oncoscience* **2015**, *2*, 807–808. [[CrossRef](#)]

**Publisher's Note:** MDPI stays neutral with regard to jurisdictional claims in published maps and institutional affiliations.



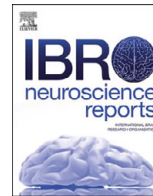
© 2020 by the authors. Licensee MDPI, Basel, Switzerland. This article is an open access article distributed under the terms and conditions of the Creative Commons Attribution (CC BY) license (<http://creativecommons.org/licenses/by/4.0/>).

## II)

Dulka K, Nacsa K, **Lajkó N**, Gulya K (2021) Quantitative morphometric and cell-type-specific population analysis of microglia-enriched cultures subcloned to high purity from newborn rat brains. **IBRO Neurosci Rep.** 10:119-129. doi: 10.1016/j.ibneur.2021.01.007

Open Access (freely available online):

<https://www.ncbi.nlm.nih.gov/pmc/articles/PMC8019997/pdf/main.pdf>



## Research Paper

# Quantitative morphometric and cell-type-specific population analysis of microglia-enriched cultures subcloned to high purity from newborn rat brains

Karolina Dulka, Kálmán Nacsa, Noémi Lajkó, Karoly Gulya\*

( ) - / 0 12 0 / 1 3 5 6 ( 78 - / 378 - / 392 - . .



## ARTICLE INFO

: . / 6  
 Cell yield  
 Differential adherence  
 Immunocytochemistry  
 Proliferation  
 Purity of culture  
 Secondary/tertiary culture

## ABSTRACT

Morphological and functional characterizations of cultured microglia are essential for the improved understanding of their roles in neuronal health and disease. Although some studies (phenotype analysis, phagocytosis) can be carried out in mixed or microglia-enriched cultures, in others (gene expression) pure microglia must be used. If the use of genetically modified microglial cells is not feasible, isolation of resident microglia from nervous tissue must be carried out. In this study, mixed primary cultures were established from the forebrains of newborn rats. Secondary microglia-enriched cultures were then prepared by shaking off these cells from the primary cultures, which were subsequently used to establish tertiary cultures by further shaking off the easily detachable microglia. The composition of these cultures was quantitatively analyzed by immunocytochemistry of microglia-, astrocyte-, oligodendrocyte- and neuron-specific markers to determine yield and purity. Microglia were quantitatively characterized regarding morphological and proliferation aspects. Secondary and tertiary cultures typically exhibited  $73.3\% \pm 17.8\%$  and  $93.1\% \pm 6.0\%$  purity for microglia, respectively, although the total number of microglia in the latter was much smaller. One in seven attempts of culturing the tertiary cultures had  $\sim 99\%$  purity for microglia. The overall yield from the number of cells plated at DIV0 to the Iba1-positive microglia in tertiary cultures was  $\sim 1\%$ . Astrocytic and neuronal contamination progressively decreased during subcloning, while oligodendrocytes were found sporadically throughout culturing. Although the tertiary microglia cultures had a low yield, they produced consistently high purity for microglia; after validation, such cultures are suitable for purity-sensitive functional screenings (gene/protein expression).

## 1. Introduction

Microglia, the resident immune cells of the central nervous system (CNS), are derived from macrophage-like cells of mesodermal origin and play important roles in both physiological and pathophysiological conditions (Kettenmann et al., 2011; Prinz and Priller, 2014). Microglia migrate to the CNS in the early stages of embryonic development as primitive myeloid progenitor cells and display a ramified morphology at rest (Ginhoux and Jung, 2014; Saijo and Glass, 2011). Inflammation or injury elicits a variety of structural and functional changes that morph

these cells from a ramified, resting form to an activated, ameboid type displaying lamellipodia, pseudopodia, filopodia and podosomes (Szabo et al., 2016); this form is also capable of antigen presentation and phagocytosis (Kreutzberg, 1996; Marín-Teva et al., 2004). Activated microglia can exert both beneficial and harmful effects on neurons (Tang and Le, 2016) and astrocytes (Liddelov et al., 2017), as they produce not only neurotrophic factors and anti-inflammatory cytokines, but also potentially neurotoxic mediators, such as neuroinflammatory cytokines, reactive oxygen radicals, nitric oxide and proteases, upon activation (Kraft and Harry, 2011). The amount and quality of such pro- and

5 ANOVA, One-way analysis of variance; CNPase, 2',3'-Cyclic nucleotide 3'-phosphodiesterase; CNS, Central nervous system; DIV, Day(s) in vitro; DMEM, Dulbecco's Modified Eagle's Medium; FBS, Fetal bovine serum; FITC, Fluorescein isothiocyanate; GFAP, Glial fibrillary acidic protein; Iba1, Ionized calcium-binding adapter molecule 1; Ki67, Proliferation marker antigen identified by the monoclonal antibody Ki67; PBS, Phosphate buffered saline; PI, Proliferation index; PVP, Polyvinylpyrrolidone; Rpm, Revolutions per minute; RT, Room temperature; S1, S2, Secondary subcultures; S.D., Standard deviation; subDIV, Subcloned day(s) in vitro; T1, T2, Tertiary subcultures; TI, Transformation index.

\* Correspondence to: Department of Cell Biology and Molecular Medicine, University of Szeged, Somogyi utca 4, Szeged H-6720, Hungary.

// 66 [dulka.karolina@med.u-szeged.hu](mailto:dulka.karolina@med.u-szeged.hu) (K. Dulka), [knacsa@bibl.u-szeged.hu](mailto:knacsa@bibl.u-szeged.hu) (K. Nacsa), [lajko.noemi@med.u-szeged.hu](mailto:lajko.noemi@med.u-szeged.hu) (N. Lajkó), [gulyak@bio.u-szeged.hu](mailto:gulyak@bio.u-szeged.hu) (K. Gulya).

<https://doi.org/10.1016/j.ibneur.2021.01.007>

Received 16 November 2020; Accepted 30 January 2021

Available online 6 February 2021

2667-2421/© 2021 The Author(s). Published by Elsevier Ltd on behalf of International Brain Research Organization. This is an open access article under the CC

BY license (<http://creativecommons.org/licenses/by/4.0/>).

anti-inflammatory mediators produced by microglia affect the development and progression of neuropathological conditions (Prinz and Priller, 2014; Yao et al., 2013; Liddel et al., 2017). The rapid response of microglia to inflammatory cues and injury can be studied in vitro and may provide important information regarding the mechanisms underlying neuroinflammation, oxidative stress and the development of neurodegenerative disorders, leading to more effective treatments using microglia as a novel and specific therapeutic target (Gresa-Arribas et al., 2012; Kata et al., 2016, 2017).

In addition to the recently developed protocols that use induced pluripotent stem cells to derivate microglial-like cells (Muffat et al., 2016; Speicher et al., 2019), many conventional cell culture techniques are still available for isolating and culturing microglia from several species (Olah et al., 2012; Szabo and Gulya, 2013; Yip et al., 2009). These cultures are mostly derived from embryonic (Hassan et al., 1991; Gingras et al., 2007; Szabo and Gulya, 2013), newborn or perinatal rodent brains (Ni and Aschner, 2010; Yao et al., 2013), while adult nervous tissues are used less frequently (Moussaud and Draheim, 2010; Pulido-Salgado et al., 2017; Rustenhoven et al., 2016). The methods used for isolating microglia from nervous tissues or for subculturing from a mixed neuronal/glia culture include differential adhesion (shaking) techniques, gradient density centrifugation (Gingras et al., 2007; Moussaud and Draheim, 2010; Jin and Kim, 2015), cell sorting (Ford et al., 1995; Marek et al., 2008) and harvesting microglia from a non-adherent floating cell layer without any shaking at all (Moussaud and Draheim, 2010).

As many of these often-controversial or not fully documented methodological studies used different separation techniques or were carried out without an extensive quantitative analysis of the contaminating cell types present in the cultures, we set out to analyze meticulously our differential adhesion culture method, emphasizing the critical steps that are necessary for the establishment of highly enriched microglial cultures; we also aimed to catalog all of the major contaminating cell types. Immunocytochemistry was applied to the characterization of secondary and tertiary cultures using specific antibodies for microglial, neuronal, astrocyte and oligodendrocyte markers. Morphometric characterization on binary (digital) silhouettes of the microglia collected from different subcultures was used to analyze their area, perimeter and transformation index. Cell proliferation was assessed using the anti-Ki67 antibody, which was raised against the proliferation marker antigen Ki67. Such detailed description of microglial cell cultures established from neonatal rats is unique in the literature.

## 2. Experimental procedures

### 2.1. Animals

All animal experiments were carried out in strict compliance with the European Council Directive (86/609/EEC) and EC regulations (O.J. of EC No. L 358/1, 18/12/1986) regarding the care and use of laboratory animals for experimental procedures, and followed the relevant

Hungarian and local legislation requirements. The experimental protocols were approved by the Institutional Animal Welfare Committee of the University of Szeged (II./1131/2018). The pregnant Sprague–Dawley rats (190–210 g) were kept under standard housing conditions and fed ad libitum. Seven breeding runs (with 8–10 pregnant rats in each) provided the litters (6–14 pups from each mother) from which independent cell culture experiments were run to establish the primary and derived cultures.

### 2.2. Antibodies

The antibodies used in our studies are listed in Table 1. For the characterization of the microglial cells, we used an antibody against the ionized calcium-binding adapter molecule 1 (Iba1) (Imai et al., 1996). The anti-glia fibrillary acidic protein (GFAP) antibody (Guillemin et al., 1997), the anti- $\beta$  tubulin III (Banerjee et al., 1990) antibody and the anti-2',3'-cyclic nucleotide 3'-phosphodiesterase (CNPase) antibody (Zhang et al., 2010) were used to detect astrocytes, neurons and oligodendrocytes, respectively. The anti-Ki67 antibody was used to detect proliferating cells (Szabo et al., 2016); the Ki67 nuclear protein is expressed in all active phases of the cell cycle, i.e., from the late G1 phase through the end of the M phase (Sobecki et al., 2016).

### 2.3. Preparation of primary mixed cultures from cerebral tissue

Mixed primary neuron/glia cultures were established from newborn rats. Briefly, animals of both sexes were decapitated and the cerebra were removed and cleared from the meninges. The forebrains were minced with scissors and incubated in 9 ml of Dulbecco's Modified Eagle's Medium (DMEM; Invitrogen, Carlsbad, CA, USA) containing 1 g/l of D-glucose, 110 mg/l of Na-pyruvate, 4 mM L-glutamine, 3.7 g/l of NaHCO<sub>3</sub>, 10,000 U/ml of penicillin G, 10 mg/ml of streptomycin sulfate and 25  $\mu$ g/ml of amphotericin B, and supplemented with 0.25% trypsin (Invitrogen) for 10 min at 37 °C, followed by centrifugation at 1000 $\times$ g for 10 min at room temperature (RT) (Szabo and Gulya, 2013). The pellet was resuspended in 10 ml DMEM containing 10% heat-inactivated fetal bovine serum (FBS; Invitrogen) and passed through a sterile filter (100  $\mu$ m pore size; Greiner Bio-One Hungary Kft., Mosonmagyaróvár, Hungary), to eliminate tissue fragments that resisted dissociation. The filtered cell suspension was centrifuged for 10 min at 1000 $\times$ g at RT and the pellet was resuspended in 5 ml DMEM/10% FBS, after which the primary mixed cells were seeded in the same medium (DIV0) either on poly-L-lysine-coated culture flasks (75 cm<sup>2</sup>; 10<sup>7</sup> cells/flask) or coverslips (15  $\times$  15 mm; 2  $\times$  10<sup>5</sup> cells/coverslip). Primary mixed cells seeded on coverslips were used for immunocytochemical comparisons with further subcultures. The cultures were maintained at 37 °C in a humidified air atmosphere supplemented with 5% CO<sub>2</sub>. The medium was changed the next day and then in every 3 days. Unless stated otherwise, the reagents were purchased from Sigma (St. Louis, MO, USA).

**Table 1**  
Primary and secondary antibodies used in immunocytochemistry.

Primary antibody, abbreviated name	Primary antibody, full name	Final dilution	Company	Secondary antibody with fluorochrome, full name	Final dilution	Company
Iba1	Rabbit anti-Iba1 polycl. ab.	1/500	Wako, Osaka, Japan	Alexa Fluor 488 or 568 goat anti-rabbit	1/1000	Invitrogen, Carlsbad, CA, USA
$\beta$ tubulin III	Mouse anti-tubulin, $\beta$ -III, monocl. ab., clone TU-20	1/200	Abcam, Cambridge, England	Alexa Fluor 568 goat anti-mouse	1/1000	Invitrogen, Carlsbad, CA, USA
GFAP	Chicken anti-GFAP	1/200	Abcam, Cambridge, England	FITC-rabbit anti-chicken/turkey	1/250	Invitrogen, Carlsbad, CA, USA
CNPase	Mouse anti-CNPase, monocl. ab., clone 11-5B	1/200	Abcam, Cambridge, England	Alexa Fluor 568 goat anti-mouse	1/1000	Invitrogen, Carlsbad, CA, USA
Ki67	Mouse anti-Ki67, monocl. ab., clone 8D5	1/50	Cell Signaling Technology, Leiden, NL	Alexa Fluor 488 goat anti-mouse	1/1000	Invitrogen, Carlsbad, CA, USA

## 2.4. Preparation of secondary and tertiary cell cultures

The preparation of secondary and tertiary cultures from mixed primary forebrain cultures is depicted in Fig. 1. After 10 and 17 days of culture (DIV10 and DIV17), microglial cells in the primary cultures were either visualized by immunocytochemistry or shaken off using a platform shaker (120 rpm for 20 min) at 37 °C. During the first and second shaking procedures, at DIV10 and DIV17, respectively, the microglia of the primary cultures were detached from the surface of the poly-L-lysine-coated culture flask. Microglia were collected from the supernatant by centrifugation (3000×g for 8 min at RT), resuspended in 4 ml of DMEM/10% FBS and seeded in the same medium on poly-L-lysine-coated culture flasks (75 cm<sup>2</sup>; 10<sup>7</sup> cells/flask) or coverslips (15 ×15 mm; 2 ×10<sup>5</sup> cells/coverslip). After the cells were allowed to adhere to the surface for 30 min, the supernatant containing any floating cells was carefully removed and cell culture medium (DMEM/10% FBS) was added to the cells. These cultures were designated as S1 and S2 subclones (from DIV10 and DIV17, respectively). On the fourth and twelfth day of subcloning (subDIV4 and subDIV12), the tertiary microglial cells were subcloned from the secondary cultures that were maintained in poly-L-lysine-coated culture flasks by shaking the cultures at 150 rpm in a platform shaker for 20 min at 37 °C. Microglia were collected from the supernatant by centrifugation at 3000×g for 8 min at RT. The pellet was resuspended in 2 ml of DMEM/10% FBS. The number of collected cells was determined in a Bürker chamber after trypan blue staining. The cells were then plated on poly-L-lysine-coated coverslips, for immunocytochemistry. These cultures were designated as T1 and T2 subclones (from subDIV4 and subDIV12, respectively). Primary mixed cells seeded on coverslips were fixed on DIV14, while secondary (S1, S2) and tertiary (T1, T2) cultures were fixed on the next day of subculture in 0.05 M PBS (pH 7.4 at RT) containing 4% formaldehyde for 10 min at RT and stored at –20 °C until use.

## 2.5. Immunocytochemistry

Multicolor immunofluorescence staining was performed as described (Kata et al., 2016; Szabo and Gulya, 2013). Fixed primary, secondary

and tertiary cultures on coverslips were rinsed three times for 5 min each in 0.05 M PBS. After permeabilization and blocking of the nonspecific sites for 30 min at 37 °C in 0.05 M PBS containing 5% normal goat serum (Sigma), 1% heat-inactivated bovine serum albumin (Sigma) and 0.05% Triton X-100, the cells on the coverslips were incubated overnight at 4 °C with the appropriate microglia-, neuron-, astrocyte- or oligodendrocyte-specific primary antibody, as well as with the proliferation-specific anti-Ki67 antibody (Table 1). The cultured cells were then washed four times for 10 min each at RT in 0.05 M PBS and incubated without Triton X-100 with the appropriate Alexa Fluor fluorochrome- or fluorescein isothiocyanate (FITC)-conjugated secondary antibody (Table 1) in the dark for 3 h at RT. The cells on the coverslip were washed four times for 10 min each in 0.05 M PBS at RT, and the cell nuclei were stained in a 0.05 M PBS solution containing 1 mg/ml polyvinylpyrrolidone (PBS-PVP) and 0.5 µl/ml Hoechst 33258 dye (Sigma). Finally, the coverslips were rinsed twice for 5 min each time in PBS-PVP, rinsed in distilled water for 5 min, air dried and mounted on microscope slides in Vectashield mounting medium (Vector Laboratories, Burlingame, CA, USA). To confirm the specificity of the secondary antibodies, omission control experiments (i.e., staining without the primary antibody) were performed. In these experiments, no immunocytochemical signals were observed.

## 2.6. Image analysis and statistics

Digital images were captured by a Leica DMLB epifluorescence microscope using a Leica DFC7000 T CCD camera (Leica Microsystems CMS GmbH, Wetzlar, Germany) and the LAS X Application Suite X (Leica). For the determination of the purity of the microglial cultures, the Hoechst 33258-labeled cell nuclei of Iba1-immunopositive cells were counted on coverslip-cultured samples. For each culture, 55–120 randomly selected microscope fields per coverslip from at least 10 coverslips were counted and analyzed using the computer program ImageJ (version 1.47; developed at the U.S. National Institutes of Health by W. Rasband, available at <https://imagej.net/Downloads>; Schneider et al., 2012). For the measurement of area (A, in µm<sup>2</sup>), perimeter (P, in µm) and transformation index (TI), Iba1-positive microglial images were

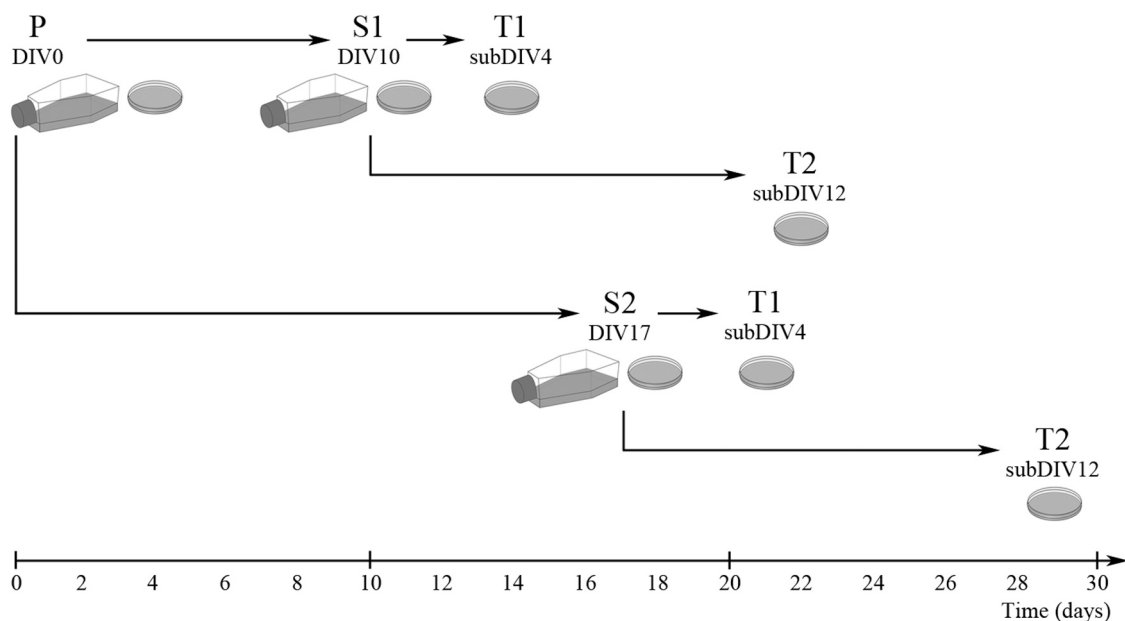


**Fig. 1.** Preparation of microglia-enriched secondary and tertiary cultures from mixed primary cultures. Mixed primary cultures (P, DIV0) were prepared as described in the Experimental procedures. After shaking the cultures, the supernatant was collected. The process was pre-experimentally optimized at 37 °C, 120 rpm for 20 min. Isolated cells were seeded either in Petri dishes or in culture flasks (S1, DIV10; S2, DIV17). Tertiary cultures were subcloned by further shaking the secondary cultures at 37 °C, 150 rpm for 20 min (T1, subDIV4; T2, subDIV12). The primary and secondary cultures were shaken twice. The composition of the secondary and tertiary cultures was then analyzed via quantitative immunocytochemistry using cell-specific markers.

converted into binary replicas using thresholding procedures implemented by the ImageJ and Adobe Photoshop CS5.1 software (Adobe Systems, Inc., San Jose, CA, USA), as described in detail by Szabo and Gulya (2013). The TI, which is a measure of differentiated cell morphology, was determined according to Fujita et al. (1996) using the following formula:  $[\text{perimeter of the cell } (\mu\text{m})]^2/4\pi [\text{cell area } (\mu\text{m}^2)]$ . Color correction of the images was occasionally performed when photomicrographs were prepared for publication. Morphometrical comparisons were made using SigmaPlot (v. 12.3, Systat Software Inc., Chicago, IL, USA) and data were analyzed via Kruskal–Wallis one-way analysis of variance (ANOVA) on ranks followed by Dunn’s method; for proliferation assays, via one-way ANOVA followed by Holm–Sidak’s method for pairwise multiple comparisons of differences between the groups; and for the yield data, via Kruskal–Wallis one way ANOVA on ranks, followed by Tukey’s test. Values were presented as the mean  $\pm$  S. D. and significance was set at  $p < 0.05$ .

### 3. Results

#### 3.1. Repeated shaking decreases the yield but increases the purity of microglia in cultures

Primary cultures were shaken twice at 120 rpm for 20 min, first on DIV10, then on DIV17, resulting in the S1 and S2 subcultures, respectively (Fig. 2A and B). These procedures yielded cells that amounted at first to  $12.5\% \pm 1.8\%$ , then  $6.3\% \pm 3.5\%$  of the total cell number of the original primary cultures (DIV0), respectively (Fig. 3). S1 cultures were also shaken twice at 150 rpm for 20 min, resulting in the T1 and T2 subcultures, respectively (Fig. 2C and D), with yields of  $5.1\% \pm 4.1\%$  on subDIV4 and  $2.4\% \pm 1.8\%$  on subDIV12 (calculated from the total cell number at the time of seeding on subDIV0; Fig. 3). In general, repeated shakings resulted in significantly fewer microglial cells that could be harvested (Fig. 3). The overall yield, which was calculated based on the ratio of the number of plated cells at DIV0 to the Iba1-positive microglia in T1 cultures, was  $\sim 1\%$ . In our study, secondary cultures resulted  $1.6 \times 10^6 \pm 1.5 \times 10^5$  cells/newborn rat, while tertiary cultures yielded  $8 \times 10^4 \pm 2 \times 10^4$  cells/newborn rat. It is important to emphasize that

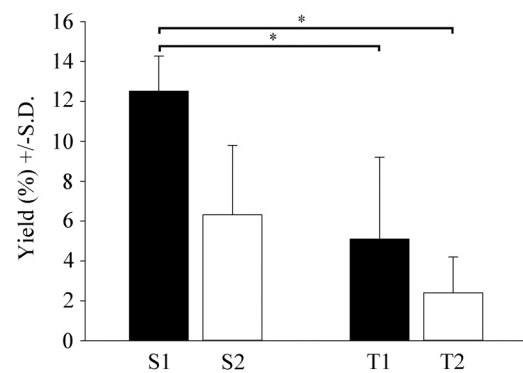


**Fig. 3.** Quantitative analysis of cultured cells in secondary and tertiary cultures. The percentage of the cells collected after shaking the primary and secondary cultures was determined by comparing with the initial number of cells (DIV0 and subDIV0). Despite the use of different (increasing) strengths of shaking of the primary and secondary cultures, we achieved decreasing cell yields in each case. The first shaking of the primary cultures yielded  $12.5\% \pm 1.8\%$  at DIV10 (S1), while the second shaking resulted in a lower yield of  $6.3\% \pm 3.5\%$  at DIV17 (S2). The first shaking of the microglial cells from the secondary cultures resulted in a yield of  $5.1\% \pm 4.1\%$  (T1), while the second shaking of these cells yielded a mere  $2.4\% \pm 1.8\%$  (T2). Newborn rats from seven breeding runs were used to generate seven independent culturing experiments ( $n = 7$ ). Data are the mean  $\pm$  S.D. Statistical comparisons were performed using SigmaPlot (v. 12.3, Systat Software Inc., Chicago, IL, USA) and data were analyzed via Kruskal–Wallis one-way analysis of variance on ranks, followed by Tukey’s test for statistically significant differences between the groups. \* denotes  $p < 0.001$ .

only one in seven independent cell culture experiments led to the generation of tertiary microglial cultures with a purity of 99% (Table 2).

#### 3.2. Multiple shaking affects microglial morphology

The morphological features of microglial cells (A, P and TI), were quantitatively analyzed using binary silhouettes on a total of 214 cells (Figs. 4 and 5). In the primary mixed neuron/glia cultures at DIV14,

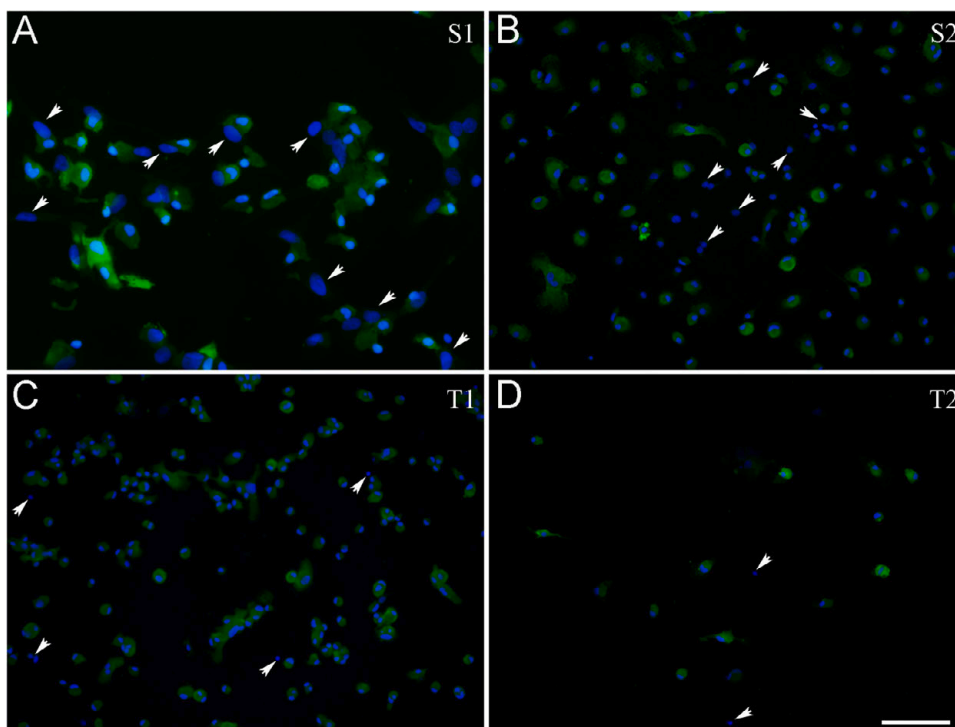


**Fig. 2.** Immunocytochemical localization of microglial cells in secondary and tertiary cultures. The number of Hoechst 33258-labeled cell nuclei (blue) and Iba1-positive (microglial) cells (green) was counted in cultures derived by shaking the primary cultures (S1; A), followed by a second shaking (S2; B); subsequently, the secondary cultures were also shaken twice (T1; C and T2; D). A total of 257,894 cells were counted under a fluorescence microscope using a  $20\times$  or  $40\times$  objective. Arrows point to cells that do not have Iba1-positive signals. Scale bar:  $75 \mu\text{m}$ .

**Table 2**

Yield and purity of the T1 subcultures in each independent cell culture experiment.

Independent cell culture experiment	Yield of cultured cells in T1 cultures (%)	Purity of T1 cultures for microglia (%)
1.	2.6	93.2
2.	3.2	99.0
3.	2.9	97.2
4.	1.5	80.7
5.	5.4	96.1
6.	6.8	93.9
7.	13.4	91.5
Mean $\pm$ S.D.	5.1 $\pm$ 4.1	93.1 $\pm$ 6.0

most of the microglial cells were ramified with an average area of  $601.1 \pm 192.2 \mu\text{m}^2$ , a perimeter of  $549.0 \pm 186.6 \mu\text{m}$  and a TI value of  $42.8 \pm 23.9$  (Figs. 4 and 5). Microglia in secondary (S1 and S2) and tertiary (T1 and T2) cultures displayed significant morphological differences, as secondary cultures had a larger cell size and shorter projections compared with those in tertiary cultures. The S1 subculture consisted mainly of larger amoeboid microglia with small pseudopodia ( $A = 186.6 \pm 66.7 \mu\text{m}^2$ ,  $P = 76.7 \pm 23.8 \mu\text{m}$ ,  $TI = 2.6 \pm 0.8$ ) (Figs. 4 and 5), while the S2 subculture microglia became more amoeboid, with a slightly smaller cell body and without pseudopodia ( $A = 181.0 \pm 145.8 \mu\text{m}^2$ ,  $P = 58.9 \pm 33.9 \mu\text{m}$ ,  $TI = 1.6 \pm 0.7$ ) (Figs. 4 and 5). Interestingly, while T1 subcultures consisted of microglia with a typical amoeboid morphology ( $A = 134.0 \pm 44.9 \mu\text{m}^2$ ,  $P = 48.4 \pm 11.4 \mu\text{m}$ ,  $TI = 1.4 \pm 0.3$ ), T2 subcultures contained microglia with shapes that varied from mostly small spherical to a few large flattened cells ( $A = 247.0 \pm 207.9 \mu\text{m}^2$ ,  $P = 77.4 \pm 46.4 \mu\text{m}$ ,  $TI = 2.1 \pm 1.1$ ) (Figs. 4 and 5). Damaged cells and cell debris were also found in T2 cultures, as multiple shakings reduced the survival of microglia because of mechanical stress.

### 3.3. Secondary and tertiary cultures have a different cell-type composition

Cell-specific markers were used to identify the cells in the cultures by immunocytochemistry (Fig. 6). Secondary cultures were enriched in microglia with a mean purity of  $73.3\% \pm 17.8\%$  (Fig. 7A). In addition to

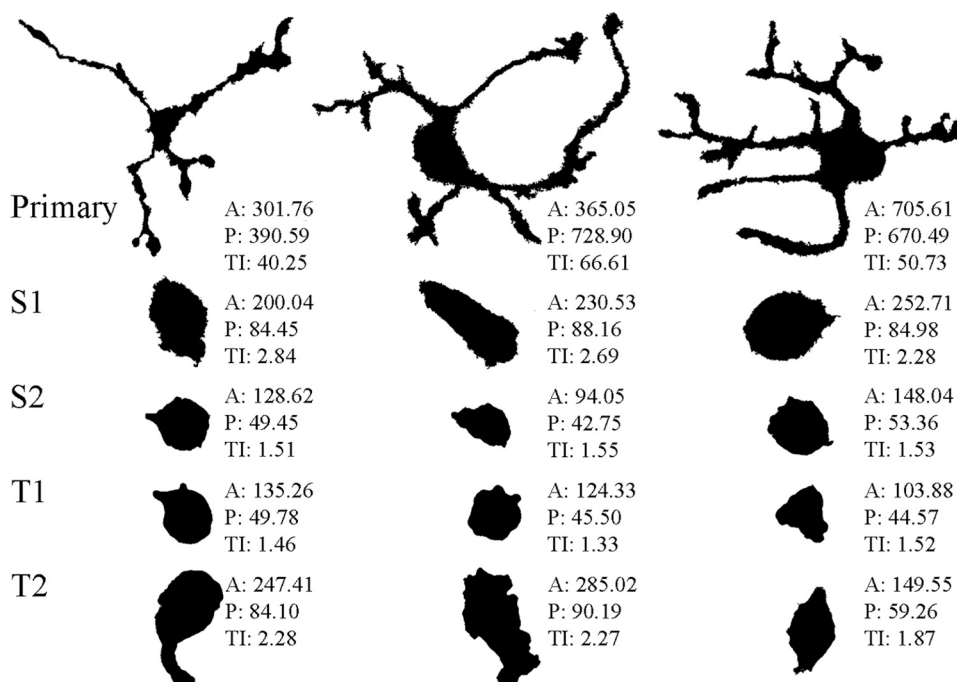


**Fig. 4.** Morphological heterogeneity of microglial cells in different cultures. Iba1-positive microglial cells from the different cultures were photographed, digitized and quantitatively analyzed according to their morphological characteristics. Area (A), perimeter (P) and transformation index (TI) are indicated for each digitized cell. Three representative cells are shown from different microglial cultures. S1: secondary culture established by the first shaking; S2: secondary culture established by the second shaking; T1: tertiary culture established by the first shaking; T2: tertiary culture established by the second shaking. Primary mixed cultures (Primary) were morphologically heterogeneous but exhibited predominantly ramified cell forms with large TI values. Subcultured microglia (S1, S2, T1 and T2) displayed an amoeboid form with  $TI < 3$ . Note that microglia in T2 cultures had increased cell-surface areas with a longer perimeter and larger TI values compared with secondary or T1 cultures. Scale bar for all silhouettes:  $50 \mu\text{m}$ .

microglia (Fig. 6A and E), a relatively large number of GFAP-immunoreactive astrocytes ( $19.0\% \pm 2.7\%$ ; Figs. 6I and 7A), a smaller number of  $\beta$ -tubulin III-positive neurons ( $3.1\% \pm 0.4\%$ ; Figs. 6B and 7A) and a few CNPase-positive oligodendrocytes ( $0.2\% \pm 0.1\%$ ; Figs. 6F and 7A) were found in these cultures. Approximately 4.4% of the cells in these cultures remained unidentified (Fig. 7A). The second shaking of the primary mixed neuron/glia cultures (S2) produced remarkably similar results: microglia, astrocytes, neurons and oligodendrocytes comprised  $74.1\% \pm 13.1\%$ ,  $12.3\% \pm 2.8\%$ ,  $2.5\% \pm 1.4\%$  and  $0.1\% \pm 0.1\%$  of the total number of cells, respectively. Unidentified cell types represented about 11% of the total cell population (Fig. 7C).

From the first shaking of the secondary culture, a high purity tertiary microglial culture was prepared, in which almost all cells were Iba1 immunoreactive. For example, T1 cultures contained  $93.1\% \pm 6.0\%$  microglia (with the highest purity being  $\sim 99.0\%$ ),  $6.8\% \pm 0.6\%$  astrocytes,  $1.1\% \pm 0.9\%$  neurons and  $0.2\% \pm 0.1\%$  oligodendrocytes (Fig. 7B). When secondary cultures were shaken for the second time, the purity of the cultures decreased as the amount of unidentified cell types rose to 14.1%. These T2 cultures contained  $79.2\% \pm 15.5\%$  microglia,  $2.4\% \pm 1.7\%$  astrocytes,  $1.1\% \pm 0.3\%$  neurons and  $3.2\% \pm 3.1\%$  oligodendrocytes (Fig. 7D). Although tertiary cultures produced a low cell yield, they had a consistently high purity, which rendered them suitable for purity-sensitive functional screenings, such as gene or protein expression analyses.

### 3.4. Quantitative analysis of proliferating microglia in secondary and tertiary cultures

To determine the rate of proliferating microglia, double-fluorescence immunocytochemistry was performed using the anti-Ki67 and anti-Iba1-antibodies (Fig. 8), and the proliferation index (PI) was determined (Fig. 9). The PI was defined as the ratio of Ki67-positive/Iba1-positive microglial cell nuclei per the total number of Iba1-positive cells  $\times 100$ . From a total of 18,000 analyzed cells, 14,634 were Iba1-positive and 411 were Ki67-positive/Iba1-positive microglia across 290 microscopic fields of view. In one experiment, for example, from a total of 2454 analyzed secondary cultured cells, 2149 were Iba1-positive ( $87.6\%$  purity) and 85 were Ki67-positive/Iba1-positive microglia ( $PI = 3.9\%$ ) across 30 microscopic fields of view. According to Ki67

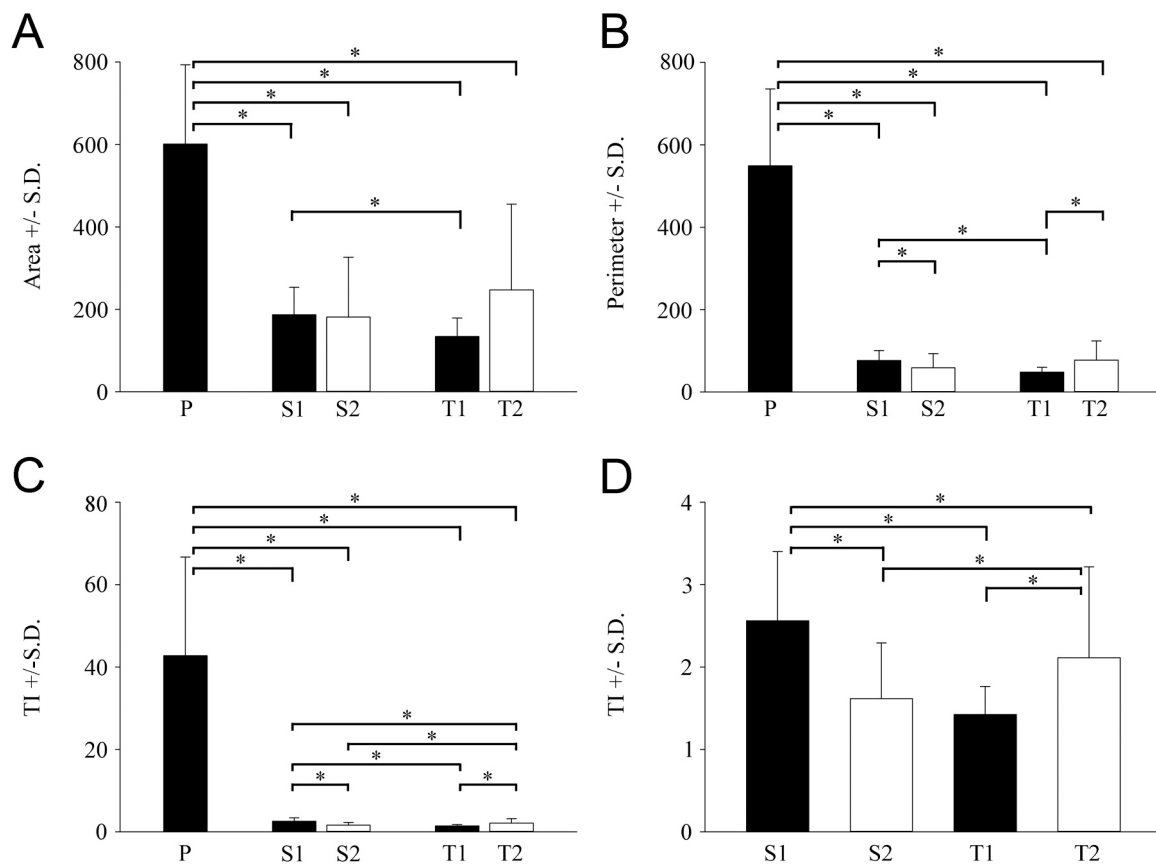


**Fig. 5.** Morphological parameters of microglia in different cultures. Iba1-positive microglia were photographed, digitized and quantitatively analyzed for (A) surface area ( $\mu\text{m}^2$ ), (B) perimeter ( $\mu\text{m}$ ) and TI value (C and D) from different microglial cultures. (C) and (D) are related. Statistical comparisons were performed using SigmaPlot (v. 12.3, Systat Software Inc., Chicago, IL, USA) and data were analyzed via Kruskal–Wallis one-way analysis of variance on ranks, followed by Dunn’s method for pairwise multiple comparison procedures for statistically significant differences between the groups. P: primary mixed neuron/glia culture; S1: secondary culture established by the first shaking; S2: secondary culture established by the second shaking; T1: tertiary culture established by the first shaking; T2: tertiary culture established by the second shaking. Values are presented as the mean  $\pm$  S.D. Significance was set at  $p < 0.05$ . \* denotes  $p < 0.05$ .

immunocytochemistry (Fig. 9), the number of proliferating microglia in the S1 cultures, on average, was about 3-fold larger ( $\text{PI} = 3.9\% \pm 0.3\%$ ) than those detected in the S2 ( $\text{PI} = 1.4\% \pm 0.9\%$ ) or the tertiary cultures ( $\text{PI} = 1.1\% \pm 0.1\%$ ;  $\text{PI} = 0.9\% \pm 0.4\%$  in T1 and T2, respectively), proving that the shakings affected cell composition and proliferation characteristics of the cultures. Both quantitative morphological and Ki67 immunocytochemical studies indicated that the derived microglia were amoeboid microglia capable of proliferation.

#### 4. Discussion

Microglial cultures derived from primary mixed neuronal/glia cultures are useful tools for studying fundamental morphological and functional characteristics of microglia, e.g., motility, secretory mechanisms, activation states, etc. (Stansley et al., 2012). Culturing microglia is a time-consuming and meticulous process that ultimately results in a low cellular yield with a variety of contaminating cell types (mainly astrocytes and oligodendrocytes, but also pericytes, fibroblasts, smooth muscle cells and endothelial cells) that degrade the purity of the culture (Saura, 2007).

Several studies exploited differential cellular adhesion to harvest microglia. Some used mild trypsinization (Saura et al., 2003), while others used a varied length and strength of shaking. In addition to shorter agitation times, e.g., 45 min or 3 h (Flode and Combs, 2007; Gingras et al., 2007), more vigorous methods such as 180 rpm for 15 h (Giulian and Baker, 1986) or 150 rpm for 16 h (Hassan et al., 1991) were also used. Other authors used gentle agitation, e.g., shaking the

flasks by hand and gently blowing with a pipette (Qin et al., 2012) or gently banging on the side and tapping the flasks at a speed of 45 rpm for about 9–12 min (Ni and Aschner, 2010). Typical protocols reported enzymatic digestion using differential adhesion steps with the shaking off of non-adherent cells after 2 or 24 h (Yip et al., 2009) or just 10 min (Gingras et al., 2007). While some researchers used a microglia enrichment step only once (Saura et al., 2003; Rustenhoven et al., 2016), others isolated microglia repeatedly from the same primary culture: 3 times after 7 days (Flode and Combs, 2007), 3 times after 8–10 days with passage (Qin et al., 2012), 2 times after 1 month (Gingras et al., 2007) and twice a week from the supernatant without shaking up to 32 days (Moussaud and Draheim, 2010). The purity of these microglia-enriched cultures was typically high and was accompanied by a low yield. Complex protocols with mechanical and enzymatic dissociation followed first by density separation, then immunomagnetic separation resulted in a low yield ( $7.5 \times 10^5$  cells/mouse) but high purity (98%) even from an adult brain (de Haas et al., 2007). Qin et al. (2012) reported one of the best yields, an average of  $7 \times 10^6$  cells/neonatal rat, after 3 shakings with passages, while Gordon et al. (2011) used a column-free magnetic separation technique with tetrameric antibody complexes to produce  $3 \times 10^6$  microglia/mouse pups with 97% of purity after only one shaking at 120 rpm for 2.5 h. Yield can be increased using GM-CSF treatment (Gingras et al., 2007; Moussaud and Draheim, 2010). Despite the low yield, the most popular and widely used methods are based on the differential adherence isolation of the different cell types, mainly because they offer simple techniques and low cost. In addition to the harvesting techniques, other factors (different donor species, age,

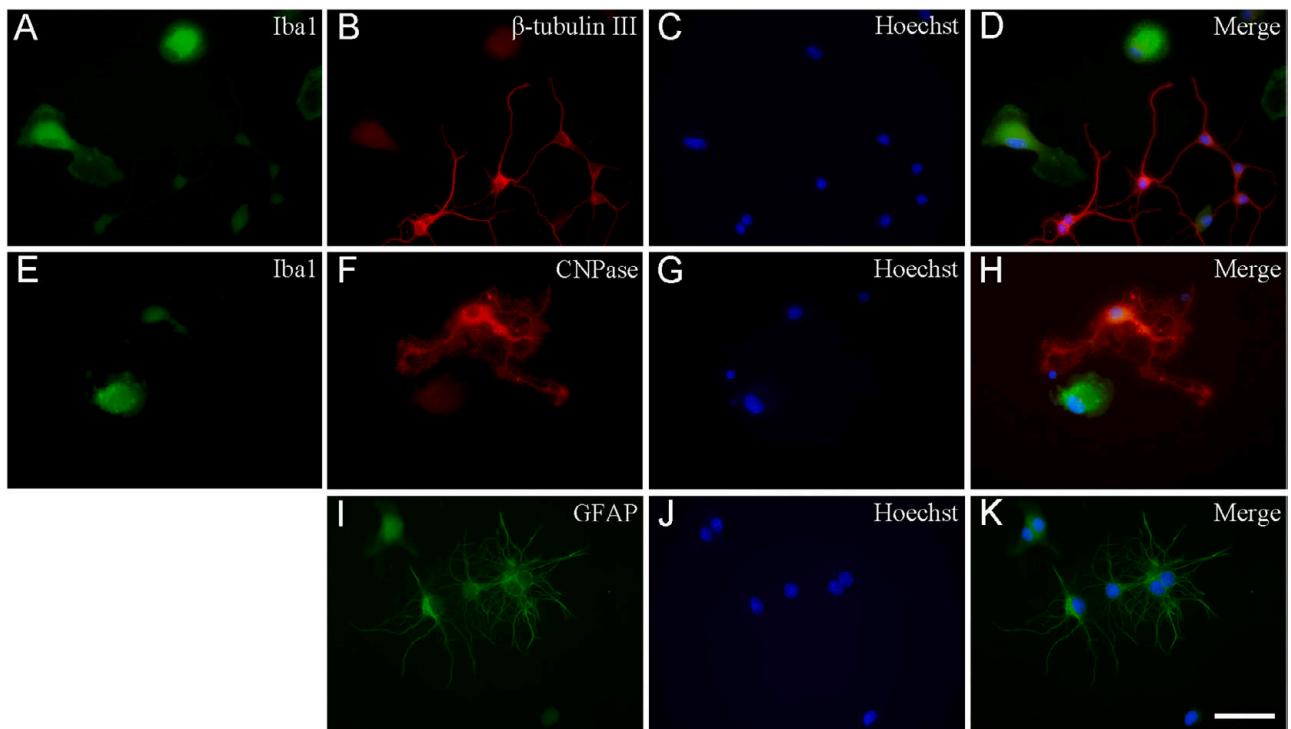


**Fig. 6.** Immunocytochemical localization of microglia, neurons, astrocytes and oligodendrocytes in secondary cell cultures. Different cell types were labeled by the corresponding marker proteins. An anti-Iba1 antibody was used to detect microglia (green in (A) and (E)), an anti- $\beta$  tubulin III antibody was used to detect neurons (red (B)), an anti-CNPase antibody was used to detect oligodendrocytes (red (F)) and an anti-GFAP antibody was used to detect astrocytes (green (I)). These primary antibodies were recognized by Alexa Fluor or FITC-conjugated secondary antibodies. The cell nuclei were stained with Hoechst 33258 (blue (C), (G), (J)). Merged images are also shown (D), (H), (K)). Scale bar: 50  $\mu$ m. (For interpretation of the references to colour in this figure legend, the reader is referred to the web version of this article.)

tissue type, coated or uncoated culture vessels, etc.) further contributed to the observed differences in yield and cell number.

Our previous studies demonstrated that the number of microglia constantly increased from immediately after seeding throughout the entire cell culture period (Szabo and Gulya, 2013), which allowed the shaking off of microglial cells more than once during culture. Therefore, we harvested microglia from two time points from the primary (DIV10 and DIV17) and secondary (subDIV4 and subDIV12) cultures, which resulted in the S1 and S2 and T1 and T2 subcultures, respectively. These cultures differed both in yield and morphological parameters, as evidenced by proliferation studies and quantitative morphological analyses of the binary silhouettes of the microglia. We found that secondary cultures were enriched (up to 73%) in microglia, and that repeated shaking of the same primary cultures decreased the yield and resulted in a lower microglial yield. Due to their low number, astrocytes will not form a confluent layer to which microglia could attach in secondary cultures, so microglia can easily be shaken off and seeded as a tertiary culture. Those microglia that attach directly to the plastic dish will most likely remain on the surface after shaking; we saw some of these remaining microglia cells under the microscope (data not shown). The low yield in tertiary cultures was probably due to this fact. Nevertheless, tertiary cultures had a consistently high purity. It is important to note that only one out of seven attempts of cell culture resulted in ~99% purity. Immunocytochemical validation of harvested samples using microglial markers allowed us to select cultures to be used in purity-sensitive functional screenings of gene or protein expression (Kata et al., 2016, 2017). Using a similar protocol, we previously provided evidence that microglia in secondary cultures could be immunochallenged by lipopolysaccharide and were shown to behave as expected in functional and gene expression studies (Kata et al., 2016, 2017; Szabo and Gulya, 2013; Szabo et al., 2016). In these studies, phagocytosis, proliferation and protein expression assays, pro- and

anti-inflammatory cytokine (IL-1 $\beta$ , tumor necrosis factor alpha, IL-10) production, as well as cytoskeleton reorganization studies and gene expression assays (testing 122 inflammation-related genes) were employed to test the functionality of in vitro cultured microglia. The present work focused on the purity/yield characteristics of the cultures and cataloged the cell types that make up these populations; we are aware that our method needs further functional studies to characterize microglia in these cultures.

Our secondary microglial cultures were contaminated mainly by astrocytes (12–19%) and, to a lesser degree, by neurons (2–3%) and oligodendrocytes (about 0.2%). Generation of the main cell types in the brain occurs in a temporally distinct yet overlapping pattern (Sauvageot and Stiles, 2002). In rats, neurogenesis peaks between E14 and E18, while astrocytogenesis at P2 (astrocytogenesis starts around E18 in mice) and oligodendrocytogenesis peaks at P14, although oligodendrocyte precursor cells appear earlier (Reemst et al., 2016; Sauvageot and Stiles, 2002). At the time of birth, non-neuronal cells comprise only about 6% of all brain cells in the rat (Bandeira et al., 2009), out of which perhaps 1–2% are microglia. Cellular abundances in newborn tissues are reflected in the composition of the primary cultures from which subsequent cultures are made. Astrocytes, the most contaminating cell type throughout culturing, attach to the surface strongly. Nevertheless, we were able to decrease their contamination in the secondary and tertiary cultures by shaking off the microglia from the astrocytic layer; in fact, this is the main reason we made tertiary cultures. It has to be taken into consideration that, although GFAP is a well-documented astrocyte marker, not all astrocyte subtypes express it at high levels, e.g., protoplasmic astrocytes of the gray matter (Emsley and Macklis, 2006; Miller and Raff, 1984; Reemst et al., 2016; Tabata, 2015). Approximately 4.4% of the cells in the secondary cultures remained unidentified, and some of them could be those protoplasmic astrocytes with low abundance of GFAP.

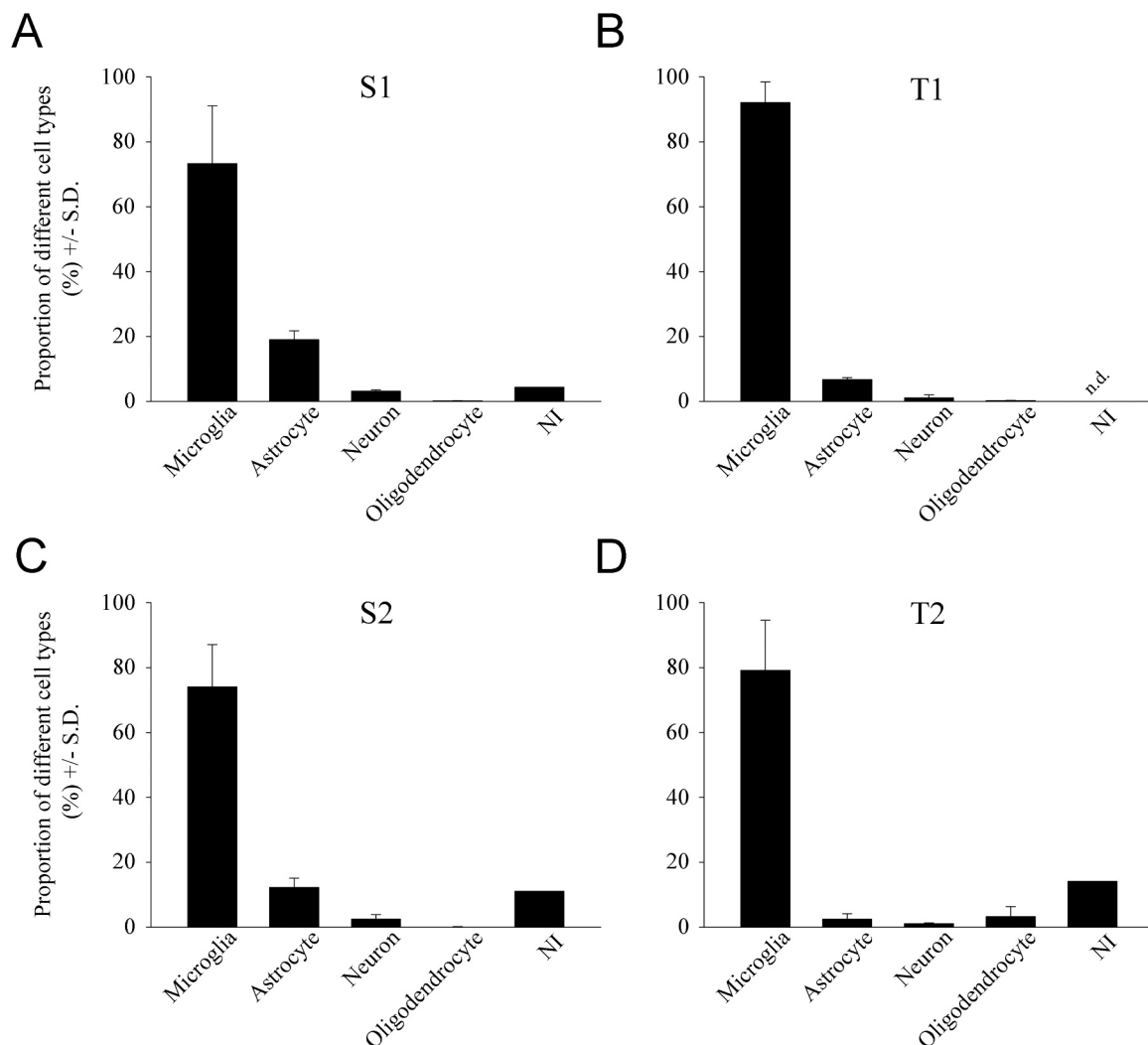


**Fig. 7.** Quantitative analysis of the distribution of different cell types in secondary and tertiary cultures. Microglia-enriched cultures were obtained after the shaking of the primary cultures (S1 = 73.3%, S2 = 74.1%; (A) and (C), respectively). Shaking of the secondary cultures led to tertiary cultures with higher purities (T1 = 93.1%, T2 = 79.3%; (B) and (D), respectively). The number of astrocytes and neurons progressively decreased throughout culturing. Occasionally, a few cells that were not identified (NI) immunocytochemically in this study were also observed in secondary cultures; such cells were exceptionally rare in T1, but were somewhat more numerous in T2 cultures. n.d.: not detected.

While the amounts of all contaminating cell types decreased considerably, the largest reduction in tertiary cultures was observed in the number of astrocytes (down to  $2.4\% \pm 1.7\%$  in T2). In fact, in similarly enriched microglial cultures, astrocytes were detected most often. For example, [Saura et al. \(2003\)](#) reported that, in such cultures, 0.2–0.5% of the cells were GFAP-positive astrocytes and that 0.8–1.7% of the cells expressed smooth muscle  $\alpha$  actin, which is a marker protein of both pericytes and astrocytes. A similar value (2.4%) was detected for pericytes by [Rustenhoven et al. \(2016\)](#) in highly enriched primary human microglial cultures.

The percentage of oligodendrocytes was typically around 0.5% ([Gingras et al. 2007](#); [Giulian and Baker, 1986](#); [Gordon et al. 2011](#); [Ni and Aschner, 2010](#); [Saura et al. 2003](#); [Yip et al. 2009](#)). Other much less frequent cell types are rarely counted. [Moussaud and Draheim \(2010\)](#) looked for the presence of neurons and fibroblasts in a culture containing 98% microglia, although they did not publish numerical data, merely figures derived from flow cytometry. Similarly, [Tamashiro et al. \(2012\)](#) noted only minimal contamination, without specifying the contaminating cell types.

Microglia become amoeboid after shaking the cultures. We demonstrated that the cells obtained from the second shaking were more

spherical than those obtained from the first shaking of primary cultures, as documented by their decreasing TI values. This morphological response could be attributed to the mechanical stress upon the more ramified microglia that remained attached to the surface in the primary culture. In tertiary cultures, microglia displayed increased TI values in T2 cultures compared with T1 cultures; however, these values remained lower than those detected in secondary cultures, probably as a consequence of the more varied cell sizes and shapes present in T2 cultures. One of the drawbacks of the differential cellular adherence method is that consecutive shaking acts as a mechanical stress that results in progressively fewer surviving cells. Because of such mechanical effects, which are mediated by contact-dependent structures via cytoskeletal remodeling ([Yan et al., 2012](#); [Vincent et al., 2012](#)), microglia easily detach from the surface of culture materials. Although many of these mechanisms depend on calmodulin-mediated phenomena ([Siddiqui et al., 2012](#); [Szabo et al., 2016](#)), the exact mechanisms underlying the manner in which the cytoskeleton adapts to the shearing forces of shaking and the changes in the expression of adhesion-promoting molecules remain largely unknown.

The establishment of immortalized microglial cell lines facilitated their culture in bulk. In these cultures, the cell population is

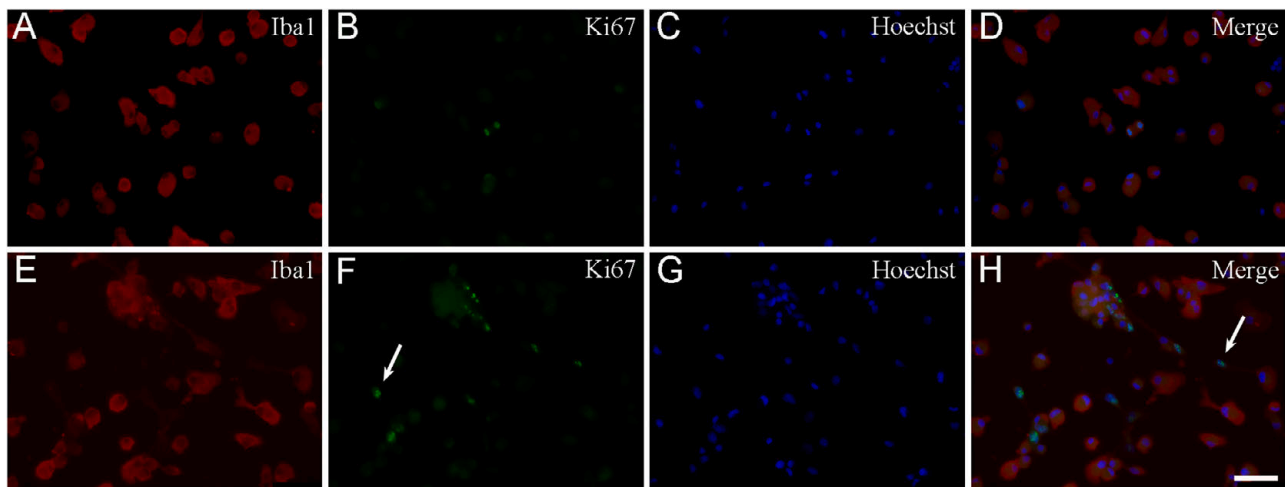


**Fig. 8.** Representative immunocytochemical images of Ki67-positive microglial and non-microglial cell types in secondary cultures. Cultured Iba1-positive microglia (red (A), (E)), proliferating Ki67-positive cells (green (B), (F)) and Hoechst 33258-labeled cell nuclei (blue (C) and (G)) were identified. Merged images are provided in panels (D) and (H). Note that some of the Ki67-positive cell nuclei (arrow in panel (F)) did not belong to Iba1-positive microglia. Scale bar: 75  $\mu$ m. (For interpretation of the references to colour in this figure legend, the reader is referred to the web version of this article.)

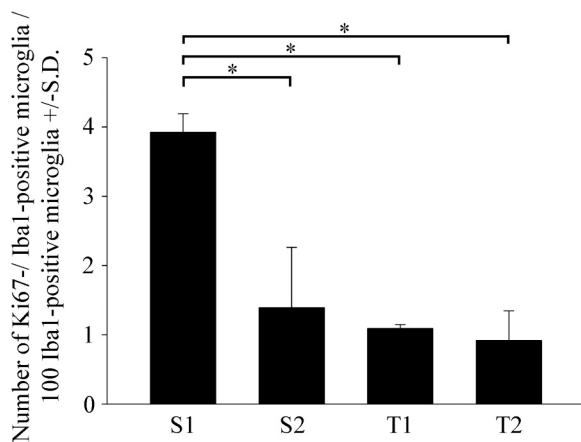


**Fig. 9.** Quantitative analysis of Ki67-positive microglia in secondary and tertiary cultures. Proliferation was measured as a function of Ki67 immunopositivity of the Iba1-immunopositive microglial cells in secondary (S1, S2) and tertiary (T1, T2) cultures, and calculated using the following equation:  $PI = \text{number of Ki67-positive microglia} / \text{total number of Iba1-positive microglia} \times 100$ . Ki67-positive microglia were counted in 290 microscopic fields of view from three separate cell culture experiments. Statistical comparisons were performed using SigmaPlot (v. 12.3, Systat Software Inc., Chicago, IL, USA) and analyses were carried out via one-way analysis of variance followed by pairwise multiple comparisons (Holm-Sidak method). The results are presented as the mean  $\pm$  S.D. Significance was set at  $p < 0.05$ .

homogeneous and a higher yield can be generated within a short period (Blasi et al., 1990; Nagai et al., 2005; Stansley et al., 2012). Undoubtedly, these cell lines are very similar both morphologically and functionally to microglia cultured from brain tissue, but the oncogene expressed by these cells could contribute to the altered morphological and functional characteristics (proliferation and adhesion capabilities, gene expression differences, etc.) of these microglia. However, altering the genetic parameters of these cells may not only provoke a non-physiological behavior in the cells or lead to genetic instability, but also potentially hamper the proper screening of these cells for therapeutic intervention. To avoid these complications, ex vivo microglia cultured to high purity (>98% with an acceptable yield) could be better suited for downstream applications that require high purity, such as gene or protein expression. Thus, there will always be reasons to culture

microglia from wild-type or genetically altered animals. The ex vivo culturing of microglial cells is also feasible if an analysis of in-house genomic modification of the animals is the goal of the experiment. The current technologies do not require high yield, as even single-cell-based gene expression analysis is widely available (Li et al., 2019; Matcovitch-Natan et al., 2016). Our protocol does not need expensive instrumentation and may abide the test of time especially when larger amount of cells or protein content are necessary for purity-sensitive functional screenings such as ELISA or Western analysis.

#### CRediT authorship contributions statement

Conceived and designed the experiments: KG. Performed the experiments: KD, KN, NL. Analyzed the data: KD, KN, NL. Contributed reagents/materials/analysis tools: KG. Wrote the paper: KD, KN, NL, KG. Edited the paper: KG. All authors have read and approved the final manuscript.

#### Conflict of Interest

The authors declare that they have no conflict of interest.

#### Acknowledgments

We thank Mrs. Edina Ratkai for excellent technical assistance.

#### Funding information

This work was supported by a grant from the Ministry of National Resources (GINOP 2.3.2-15-2016-00030 and 2.3.2-15-2016-00034) through the European Union Cohesion Fund. At the time of the experiments, KD and NL were PhD students, partly supported by the Theoretical Medicine Doctoral School, Faculty of Medicine, University of Szeged. The funders had no role in the study design, data collection and analysis, decision to publish or preparation of the manuscript.

#### Ethical approval

All applicable international, national and/or institutional guidelines for the care and use of animals were followed. Experimental procedures were carried out in strict compliance with the European Communities Council Directive (86/609/EEC) and followed Hungarian legislation

requirements (XXVIII/1998 and 243/1998) and university guidelines regarding the care and use of laboratory animals. All experimental protocols were approved by the Institutional Animal Welfare Committee of the University of Szeged (II./1131/2018).

## References

- Bandeira, F., Lent, R., Herculano-Houzel, S., 2009. Changing numbers of neuronal and non-neuronal cells underlie postnatal brain growth in the rat. *Proc. Natl. Acad. Sci. U. S. A.* 106 (33), 14108–14113. <https://doi.org/10.1073/pnas.0804650106>.
- Banerjee, A., Roach, M.C., Trcka, P., Ludueña, R.F., 1990. Increased microtubule assembly in bovine brain tubulin lacking the type III isotype of beta-tubulin. *J. Biol. Chem.* 265, 1794–1799.
- Blasi, E., Barluzzi, R., Bocchini, V., Mazolla, R., Bistoni, F., 1990. Immortalization of murine microglia cells by a v-rf/v-myc carrying retrovirus. *J. Neuroimmunol.* 27, 229–237. [https://doi.org/10.1016/0165-5728\(90\)90073-v](https://doi.org/10.1016/0165-5728(90)90073-v).
- Emsley, J.G., Macklis, J.D., 2006. Astroglial heterogeneity closely reflects the neuronal-defined anatomy of the adult murine CNS. *Neuron Glia Biol.* 2 (3), 175–186. <https://doi.org/10.1017/S1740925x06000202>.
- Flode, A.M., Combs, C.K., 2007. Microglia repetitively isolated from in vitro mixed glial cultures retain their initial phenotype. *J. Neurosci. Methods* 164, 218–224. <https://doi.org/10.1016/j.jneumeth.2007.04.018>.
- Ford, A.L., Goodall, A.L., Hickey, W.F., Sedgwick, J.D., 1995. Normal adult ramified microglia separated from other central nervous system macrophages by flow cytometric sorting. Phenotypic differences defined and direct ex vivo antigen presentation to myelin basic protein-reactive CD4+T cells compared. *J. Immunol.* 154, 4309–4321.
- Fujita, H., Tanaka, J., Toin, R., Tateishi, N., Suzug, Y., Matsuda, S., Sakanaka, M., Maedap, N., 1996. Effects of GM-CSF and ordinary supplements on the ramification of microglia in culture: a morphometrical study. *Glia* 18, 269–281. [https://doi.org/10.1002/\(sici\)1098-1136\(199612\)18:4<269::aid-glia2>3.0.co;2-t](https://doi.org/10.1002/(sici)1098-1136(199612)18:4<269::aid-glia2>3.0.co;2-t).
- Gingras, M., Gagnon, V., Minotti, S., Durham, H.D., Berthod, F., 2007. Optimized protocols for isolation of primary motor neurons, astrocytes and microglia from embryonic mouse spinal cord. *J. Neurosci. Methods* 163, 111–118. <https://doi.org/10.1016/j.jneumeth.2007.02.024>.
- Ginhoux, F., Jung, S., 2014. Monocytes and macrophages: developmental pathways and tissue homeostasis. *Nat. Rev. Immunol.* 14, 392–404. <https://doi.org/10.1038/nri3671>.
- Giulian, D., Baker, T.J., 1986. Characterization of amoeboid microglia isolated from developing mammalian brain. *J. Neurosci.* 6, 2163–2178. <https://doi.org/10.1523/JNEUROSCI.06-08-02163.1986>.
- Gordon, R., Hogan, C.E., Neal, M.L., Anantharam, V., Kanthasamy, A.G., Kanthasamy, A., 2011. A simple magnetic separation method for high-yield isolation of pure primary microglia. *J. Neurosci. Methods* 194 (2), 287–296. <https://doi.org/10.1016/j.jneumeth.2010.11.001>.
- Gresa-Arribas, N., Viéitez, C., Dentesano, G., Serratos, J., Saura, J., Solà, C., 2012. Modelling neuroinflammation in vitro: a tool to test the potential neuroprotective effect of anti-inflammatory agents. *PLoS One* 7 (9), e45227. <https://doi.org/10.1371/journal.pone.0045227>.
- Guillemín, G., Boussin, F.D., Croitoru, J., Franck-Duchenne, M., Le Grand, R., Lazarini, F., Dormont, D., 1997. Obtention and characterization of primary astrocyte and microglial cultures from adult monkey brains. *J. Neurosci. Res.* 49, 576–591. [https://doi.org/10.1002/\(SICI\)1097-4547\(19970901\)49:5<576::AID-JNR8>3.0.CO;2-8](https://doi.org/10.1002/(SICI)1097-4547(19970901)49:5<576::AID-JNR8>3.0.CO;2-8).
- de Haas, A.H., Boddeke, H.W., Brouwer, N., Biber, K., 2007. Optimized isolation enables ex vivo analysis of microglia from various central nervous system regions. *Glia* 55 (13), 1374–1384. <https://doi.org/10.1002/glia.20554>.
- Hassan, N.F., Campbell, D.E., Rifat, S., Douglas, S.D., 1991. Isolation and characterization of human fetal brain-derived microglia in in vitro culture. *Neuroscience* 41, 149–158. [https://doi.org/10.1016/0306-4522\(91\)90205-3](https://doi.org/10.1016/0306-4522(91)90205-3).
- Imai, Y., Iбата, I., Ito, D., Ohsawa, K., Kohsaka, S., 1996. A novel gene ibal in the major histocompatibility complex class III region encoding an EF hand protein expressed in a monocytic lineage. *Biophys. Biochem. Res. Commun.* 224, 855–862. <https://doi.org/10.1006/bbrc.1996.1112>.
- Jin, Y.H., Kim, B.S., 2015. Isolation of CNS-infiltrating and resident microglial cells. *Bio-Protoc.* 5 (2), e1385 <https://doi.org/10.21769/bioprotoc.1385>.
- Kata, D., Földesi, I., Feher, L.Z., Hackler Jr, L., Puskas, L.G., Gulya, K., 2016. Rosuvastatin enhances anti-inflammatory and inhibits pro-inflammatory functions in cultured microglial cells. *Neuroscience* 314, 47–63. <https://doi.org/10.1016/j.neuroscience.2015.11.053>.
- Kata, D., Földesi, I., Feher, L.Z., Hackler, L., Puskas, L.G., Gulya, K., 2017. A novel pleiotropic effect of aspirin: Beneficial regulation of pro- and anti-inflammatory mechanisms in microglial cells. *Brain Res. Bull.* 132, 61–74. <https://doi.org/10.1016/j.brainresbull.2017.05.009>.
- Kettenmann, H., Hanischuk Noda, M., Verkhratsky, A., 2011. Physiology of microglia. *Physiol. Rev.* 91, 461–553. <https://doi.org/10.1152/physrev.00011.2010>.
- Kraft, A.D., Harry, G.J., 2011. Features of microglia and neuroinflammation relevant to environmental exposure and neurotoxicity. *Int. J. Environ. Res. Public Health* 8, 2980–3018. <https://doi.org/10.3390/ijerph8072980>.
- Kreutzberg, G.W., 1996. Microglia: a sensor for pathological events in the CNS. *Trends Neurosci.* 19, 312–318. [https://doi.org/10.1016/0166-2236\(96\)10049-7](https://doi.org/10.1016/0166-2236(96)10049-7).
- Liddelow, S.A., Guttenplan, K.A., Clarke, L.E., Bennett, F.C., Bohlen, C.J., Schirmer, L., Bennett, M.L., Münch, A.E., Chung, W.S., Peterson, T.C., Wilton, D.K., Frouin, A., Napier, B.A., Panicker, N., Kumar, M., Buckwalter, M.S., Rowitch, D.H., Dawson, V.L., Dawson, T.M., Stevens, B., Barres, B.A., 2017. Neurotoxic reactive astrocytes are induced by activated microglia. *Nature* 541, 481–487. <https://doi.org/10.1038/nature21029>.
- Li, Q., Cheng, Z., Zhou, L., Darmanis, S., Neff, N.F., Okamoto, J., Gulati, G., Bennett, M.L., Sun, L.O., Clarke, L.E., Marschallinger, J., Yu, G., Quake, S.R., Wyss-Coray, T., Barres, B.A., 2019. Developmental heterogeneity of microglia and brain myeloid cells revealed by deep single-cell RNA sequencing. *Neuron* 101, 207–223. <https://doi.org/10.1016/j.neuron.2018.12.006>.
- Marek, R., Caruso, M., Rostami, A., Grinspan, J.B., Das, S.J., 2008. Magnetic cell sorting: a fast and effective method of concurrent isolation of high purity viable astrocytes and microglia from neonatal mouse brain tissue. *J. Neurosci. Methods* 175, 108–118. <https://doi.org/10.1016/j.jneumeth.2008.08.016>.
- Marín-Teva, J.L., Dusart, I., Colin, C., Gervais, A., van Rooijen, N., Mallat, M., 2004. Microglia promote the death of developing Purkinje cells. *Neuron* 41, 535–547. [https://doi.org/10.1016/s0896-6273\(04\)00069-8](https://doi.org/10.1016/s0896-6273(04)00069-8).
- Matcovitch-Natan, O., Winter, D.R., Giladi, A., Vargas Aguilar, S., Spinrad, A., Sarrazin, S., Ben-Yehuda, H., David, E., Zelada González, F., Perrin, P., Keren-Shaul, H., Gury, M., Lara-Astaiso, D., Thaiss, C.A., Cohen, M., Bahar Halpern, K., Baruch, K., Deczkowska, A., Lorenzo-Vivas, E., Itzkovitz, S., Elinav, E., Sieweke, M.H., Schwartz, M., Amit, I., 2016. Microglia development follows a stepwise program to regulate brain homeostasis. *Science* 353 (6301), aad8670. <https://doi.org/10.1126/science.aad8670>.
- Miller, R.H., Raff, M.C., 1984. Fibrous and protoplasmic astrocytes are biochemically and developmentally distinct. *J. Neurosci.* 4 (2), 585–592. <https://doi.org/10.1523/JNEUROSCI.04-02-00585.1984>.
- Moussaud, S., Draheim, H.J., 2010. A new method to isolate microglia from adult mice and culture them for an extended period of time. *J. Neurosci. Methods* 187, 243–253. <https://doi.org/10.1016/j.jneumeth.2010.01.017>.
- Muffat, J., Li, Y., Yuan, B., Mitalipova, M., Omer, A., Corcoran, S., Bakiasi, G., Tsai, L.H., Aubourg, P., Ransohoff, R.M., Jaenisch, R., 2016. Efficient derivation of microglia-like cells from human pluripotent stem cells. *Nat. Med.* 22, 1358–1367. <https://doi.org/10.1038/nm.4189>.
- Nagai, A., Mishima, S., Ishida, Y., Ishikura, H., Harada, T., Kobayashi, S., Kim, S.U., 2005. Immortalized human microglial cell line: phenotypic expression. *J. Neurosci. Res.* 81 (3), 342–348. <https://doi.org/10.1002/jnr.20478>.
- Ni, M., Aschner, M., 2010. Neonatal rat primary microglia: isolation, culturing and selected applications. *Curr. Protoc. Toxicol.* 43, 12.17.1–12.17.16. <https://doi.org/10.1002/0471140856.tx1217s43>.
- Olah, M., Raj, D., Brouwer, N., De Haas, A.H., Eggen, B.J., Den Dunnen, W.F., Biber, K.P., Boddeke, H.W., 2012. An optimized protocol for the acute isolation of human microglia from autopsy brain samples. *Glia* 60 (1), 96–111. <https://doi.org/10.1002/glia.21251>.
- Prinz, M., Priller, J., 2014. Microglia and brain macrophages in the molecular age: from origin to neuropsychiatric disease. *Nat. Rev. Neurosci.* 15, 300–312. <https://doi.org/10.1038/nrn3722>.
- Pulido-Salgado, M., Vidal-Taboada, J.M., García Diaz-Barriga, G., Serratos, J., Valente, T., Castillo, P., Matalonga, J., Straccia, M., Canals, J.M., Vallerod, A., Solà, C., Saura, J., 2017. Myeloid C/EBPβ deficiency reshapes microglial gene expression and is protective in experimental autoimmune encephalomyelitis. *J. Neuroinflammation* 14 (1), 54. <https://doi.org/10.1186/s12974-017-0834-5>.
- Qin, K., Li, Y.H., Tian, G., Xu, W.W., Li, P., Zhang, R., Li, Z.Y., Jiang, X.D., 2012. A much convenient and economical method to harvest a great number of microglia. *Cell. Mol. Neurobiol.* 32, 67–75. <https://doi.org/10.1007/s10571-011-9735-9>.
- Reemst, K., Noctor, S.C., Lucassen, P.J., Hol, E.M., 2016. The indispensable roles of microglia and astrocytes during brain development. *Front. Hum. Neurosci.* 10, 566. <https://doi.org/10.3389/fnhum.2016.00566>.
- Rustenhoven, J., Park, I.-H.T., Schweder, P., Scotter, J., Correia, J., Smith, M.A., Gibbons, M.H., Oldfield, L.R., Bergin, S.P., Mee, E.W., LMR, Faull, Curtis, A.M., Graham, S. E., Dragunow, M., 2016. Isolation of highly enriched primary human microglia for functional studies. *Sci. Rep.* 6, 19371. <https://doi.org/10.1038/srep19371>.
- Saijo, K., Glass, C.K., 2011. Microglial cell origin and phenotypes in health and disease. *Nat. Rev. Immunol.* 11, 775–787. <https://doi.org/10.1038/nri3086>.
- Saura, J., 2007. Microglial cells in astroglial cultures: a cautionary note. *J. Neuroinflammation* 4, 26. <https://doi.org/10.1186/1742-2094-4-26>.
- Saura, J., Tusell, J.M., Serratos, J., 2003. High-yield isolation of murine microglia by mild trypsinization. *Glia* 44, 183–189. <https://doi.org/10.1002/glia.10274>.
- Sauvageot, C.M., Stiles, C.D., 2002. Molecular mechanisms controlling cortical gliogenesis. *Curr. Opin. Neurobiol.* 12 (3), 244–249. [https://doi.org/10.1016/s0959-4388\(02\)00322-7](https://doi.org/10.1016/s0959-4388(02)00322-7).
- Schneider, C.A., Rasband, W.S., Eliceiri, K.W., 2012. NIH image to ImageJ: 25 years of image analysis. *Nat. Methods* 9, 671–675. <https://doi.org/10.1038/nmeth.2089>.
- Siddiqui, T.A., Lively, S., Vincent, C., Schlichter, L.C., 2012. Regulation of podosome formation, microglial migration and invasion by Ca<sup>2+</sup>-signaling molecules expressed in podosomes. *J. Neuroinflammation* 9, 770. <https://doi.org/10.1186/1742-2094-9-250>.
- Sobecki, M., Mrouj, K., Camasses, A., Parisis, N., Nicolas, E., Llères, D., Gerbe, F., Prieto, S., Krasinska, L., David, A., Eguren, M., Birling, M.C., Urbach, S., Hem, S., Déjardin, J., Malumbres, M., Jay, P., Dulic, V., Lafontaine, D.L.J., Feil, R., Fisher, D., 2016. The cell proliferation antigen Ki-67 organises heterochromatin. *eLife* 5, e13722. <https://doi.org/10.7554/eLife.13722>.
- Speicher, A.M., Wiendl, H., Meuth, S.G., Pawlowski, M., 2019. Generating microglia from human pluripotent stem cells: novel in vitro models for the study of neurodegeneration. *Mol. Neurodegener.* 14, 46. <https://doi.org/10.1186/s13024-019-0347-z>.

- Stansley, B., Post, J., Hensley, K., 2012. A comparative review of cell culture systems for the study of microglial biology in Alzheimer's disease. *J. Neuroinflammation* 9, 577. <https://doi.org/10.1186/1742-2094-9-115>.
- Szabo, M., Dulka, K., Gulya, K., 2016. Calmodulin inhibition regulates morphological and functional changes related to the actin cytoskeleton in pure microglial cells. *Brain Res. Bull.* 120, 41–57. <https://doi.org/10.1016/j.brainresbull.2015.11.003>.
- Szabo, M., Gulya, K., 2013. Development of the microglial phenotype in culture. *Neuroscience* 241, 280–295. <https://doi.org/10.1016/j.neuroscience.2013.03.033>.
- Tabata, H., 2015. Diverse subtypes of astrocytes and their development during corticogenesis. *Front. Neurosci.* 9, 114. <https://doi.org/10.3389/fnins.2015.00114>.
- Tamashiro, T.T., Dalgard, C.F., Byrnes, K.R., 2012. Primary microglia isolation from mixed glial cell cultures of neonatal rat brain tissue. *J. Vis. Exp.* 66, e3814 <https://doi.org/10.3791/3814>.
- Tang, Y., Le, W., 2016. Differential roles of M1 and M2 microglia in neurodegenerative diseases. *Mol. Neurobiol.* 53, 1181–1194. <https://doi.org/10.1007/s12035-014-9070-5>.
- Vincent, C., Siddiqui, T.A., Schlichter, L.C., 2012. Podosomes in migrating microglia: components and matrix degradation. *J. Neuroinflammation* 9, 659. <https://doi.org/10.1186/1742-2094-9-190>.
- Yan, J., Zhou, X., Guo, J.J., Mao, L., Wang, Y.J., Sun, J., Sun, L.X., Zhang, L.Y., Zhou, X. F., Liao, H., 2012. Nogo-66 inhibits adhesion and migration of microglia via GTPase Rho pathway in vitro. *J. Neurochem.* 120, 721–731. <https://doi.org/10.1111/j.1471-4159.2011.07619.x>.
- Yao, L., Kan, E.M., Lu, J., Hao, A., Dheen, S.T., Kaur, C., Ling, E.A., 2013. Toll-like receptor 4 mediates microglial activation and production of inflammatory mediators in neonatal rat brain following hypoxia: role of TLR4 in hypoxic microglia. *J. Neuroinflammation* 10, 785. <https://doi.org/10.1186/1742-2094-10-23>.
- Yip, P.K., Kaan, T.K.Y., Fenesan, D., Malcangio, M., 2009. Rapid isolation and culture of primary microglia from adult mouse spinal cord. *J. Neurosci. Methods* 183, 223–237. <https://doi.org/10.1016/j.jneumeth.2009.07.002>.
- Zhang, L., Chopp, M., Zhang, R.L., Wang, L., Zhang, J., Wang, Y., Toh, Y., Santra, M., Lu, M., Zhang, Z.G., 2010. Erythropoietin amplifies stroke-induced oligodendrogenesis in the rat. *PLoS One* 5, e11016. <https://doi.org/10.1371/journal.pone.0011016>.

## III)

Szabo\* M, **Lajkó\* N**, Dulka K, Szatmári I, Fülöp F, Mihály A, Vécsei L, Gulya K  
(2022) Kynurenic acid and its analog SZR104 exhibit strong antiinflammatory effects  
and alter the intracellular distribution and methylation patterns of H3 histones in  
immunochallenged microglia-enriched cultures of newborn rat brains. **Int. J. Mol. Sci.**  
23(1079) doi: 10.3390/ijms23031079 (**IF 5.923**) (Q1) (*\*These authors contributed  
equally to this work and should be considered joint first authors.*)

Open Access (freely available online):

<https://www.mdpi.com/1422-0067/23/3/1079/htm>



Article

# Kynurenic Acid and Its Analog SZR104 Exhibit Strong Antiinflammatory Effects and Alter the Intracellular Distribution and Methylation Patterns of H3 Histones in Immunochallenged Microglia-Enriched Cultures of Newborn Rat Brains

Melinda Szabo <sup>1,†</sup>, Noémi Lajkó <sup>1,†</sup>, Karolina Dulka <sup>1</sup>, István Szatmári <sup>2,3</sup> , Ferenc Fülöp <sup>2,3</sup>, András Mihály <sup>4</sup>, László Vécsei <sup>5</sup> and Karoly Gulya <sup>1,\*</sup>

- <sup>1</sup> Department of Cell Biology and Molecular Medicine, University of Szeged, 6720 Szeged, Hungary; szabo.melinda.1@med.u-szeged.hu (M.S.); lajko.noemi@med.u-szeged.hu (N.L.); dulka.karolina@med.u-szeged.hu (K.D.)
- <sup>2</sup> ELKH-SZTE Stereochemistry Research Group, Institute of Pharmaceutical Chemistry, University of Szeged, 6720 Szeged, Hungary; szatmari.istvan@szte.hu (I.S.); fulop.ferenc@szte.hu (F.F.)
- <sup>3</sup> Interdisciplinary Excellence Center, Institute of Pharmaceutical Chemistry, University of Szeged, 6720 Szeged, Hungary
- <sup>4</sup> Department of Anatomy, University of Szeged, 6720 Szeged, Hungary; mihaly.andras@med.u-szeged.hu
- <sup>5</sup> ELKH-SZTE Neuroscience Research Group, Department of Neurology, Interdisciplinary Excellence Center, University of Szeged, 6720 Szeged, Hungary; vecsei.laszlo@med.u-szeged.hu
- \* Correspondence: gulyak@bio.u-szeged.hu
- † These authors contributed equally to this work and should be considered joint first authors.



**Citation:** Szabo, M.; Lajkó, N.; Dulka, K.; Szatmári, I.; Fülöp, F.; Mihály, A.; Vécsei, L.; Gulya, K. Kynurenic Acid and Its Analog SZR104 Exhibit Strong Antiinflammatory Effects and Alter the Intracellular Distribution and Methylation Patterns of H3 Histones in Immunochallenged Microglia-Enriched Cultures of Newborn Rat Brains. *Int. J. Mol. Sci.* **2022**, *23*, 1079. <https://doi.org/10.3390/ijms23031079>

Academic Editors: Csaba Hetényi and Uko Maran

Received: 18 December 2021

Accepted: 17 January 2022

Published: 19 January 2022

**Publisher's Note:** MDPI stays neutral with regard to jurisdictional claims in published maps and institutional affiliations.



**Copyright:** © 2022 by the authors. Licensee MDPI, Basel, Switzerland. This article is an open access article distributed under the terms and conditions of the Creative Commons Attribution (CC BY) license (<https://creativecommons.org/licenses/by/4.0/>).

**Abstract:** Kynurenic acid (KYNA) is implicated in antiinflammatory processes in the brain through several cellular and molecular targets, among which microglia-related mechanisms are of paramount importance. In this study, we describe the effects of KYNA and one of its analogs, the brain-penetrable SZR104 (N-(2-(dimethylamino)ethyl)-3-(morpholinomethyl)-4-hydroxyquinoline-2-carboxamide), on the intracellular distribution and methylation patterns of histone H3 in immunochallenged microglia cultures. Microglia-enriched secondary cultures made from newborn rat forebrains were immunochallenged with lipopolysaccharide (LPS). The protein levels of selected inflammatory markers C-X-C motif chemokine ligand 10 (CXCL10) and C-C motif chemokine receptor 1 (CCR1), histone H3, and posttranslational modifications of histone H3 lys methylation sites (H3K9me3 and H3K36me2, marks typically associated with opposite effects on gene expression) were analyzed using quantitative fluorescent immunocytochemistry and western blots in control or LPS-treated cultures with or without KYNA or SZR104. KYNA and SZR104 reduced levels of the inflammatory marker proteins CXCL10 and CCR1 after LPS-treatment. Moreover, KYNA and SZR104 favorably affected histone methylation patterns as H3K9me3 and H3K36me2 immunoreactivities, and histone H3 protein levels returned toward control values after LPS treatment. The cytoplasmic translocation of H3K9me3 from the nucleus indicated inflammatory distress, a process that could be inhibited by KYNA and SZR104. Thus, KYNA signaling and metabolism, and especially brain-penetrable KYNA analogs such as SZR104, could be key targets in the pathway that connects chromatin structure and epigenetic mechanisms with functional consequences that affect neuroinflammation and perhaps neurodegeneration.

**Keywords:** antiinflammation; CCR1; CXCL10; cytoplasmic histone; H3K9me3; H3K36me2; kynurenic acid; SZR104

## 1. Introduction

Several recent experimental and clinical studies have found that endogenous tryptophan metabolites, including kynurenic acid (KYNA), are involved in several neurophysiological and neuropathophysiological mechanisms [1–3]. The biological significance of the

kynurenine pathway; KYNA synthesis, degradation, and excretion; and the kynurenine pathway's immunomodulatory properties in vertebrates are all well established [2–5]. In fact, KYNA exerts modulatory effects on the immune system through the regulation of T cells, natural killer cells [4], and microglial cells [5]. The neuroprotective role of KYNA in different inflammatory/neurodegenerative central nervous system disorders is of particular interest. However, since KYNA does not pass the blood–brain barrier, researchers are attempting to synthesize KYNA analogs that can penetrate this barrier [6] and hence to provide possible treatments for neurodegenerative or neuroinflammatory disorders [7,8]. One such analog, N-(2-(dimethylamino)ethyl)-3-(morpholinomethyl)-4-hydroxyquinoline-2-carboxamide (SZR104; Table S1), was recently synthesized [9,10] and applied successfully against pentylenetetrazole-induced seizures, and in doing so significantly it decreased the seizure-evoked field potentials [11]. Moreover, KYNA and SZR104 exhibit antiinflammatory properties both in vitro and in vivo; they markedly inhibit the lipopolysaccharide (LPS)-stimulated phagocytotic activity of cultured microglial cells and thus display potent immunosuppressive capabilities in an animal model of epilepsy [5].

Microglial cells are the intrinsic immune cells of the central nervous system, and they possess complex cellular and molecular mechanisms that detect deviations from homeostasis in nervous tissue. Under physiological conditions, microglia are mostly ramified and survey the parenchymal integrity of the central nervous system [12]. At the site of damage or inflammation, activated microglia change their morphology, express increased levels of major histocompatibility antigens, and become phagocytic [13]. They also release inflammatory cytokines and other potentially cytotoxic substances that can amplify inflammatory responses by activating and recruiting other cells to a lesion or infection [14,15]. For example, inflammation can be exacerbated by the secretion of the C–X–C motif chemokine ligand 10 (CXCL10) from microglia [16,17] or other cell types [18–20]. CXCL10 induces chemotaxis, apoptosis, the inhibition of cell growth, and angiostasis [21]. Both CXCL10 and its receptor (the C–X–C motif chemokine receptor 3) are crucial for leukocyte trafficking and homing to inflamed tissues, as well as for the perpetuation of inflammation that leads to tissue damage [22]. Previous studies have reported that CXCL10 is involved in the pathophysiology of multiple sclerosis [1,23]. Similarly, the C–C motif chemokine receptor 1 (CCR1) and its ligands may play a role in the pathogenesis of multiple sclerosis [24].

DNA in the nucleus is wrapped around proteins known as histones, which form the chromatin structure. The capability of eukaryotic cells to maintain their diverse phenotypes is ensured by the chemical modifications of the DNA molecule, the activities of chromatin-associated proteins, and numerous posttranslational modifications of the histone proteins [25–27]. Although histones are typically located inside the nucleus, where they regulate transcription, they are known to have a wide range of functions in various cellular and extracellular locations as well [25–27]. When they are in the extracellular milieu, they become damage-associated molecular patterns that promote inflammation, cytotoxicity, coagulation, and apoptosis [28–31]. Cytoplasmic functions of histone proteins include participation in cell signaling pathways related to the mediation of immunological functions such as innate immunity [28]. The cytoplasmic accumulation of histones and nucleosomes precedes the externalization of phagocytosis signals on the outer membrane surface of apoptotically dying lymphoblasts [32–34]. For instance, the translocation of a specific histone H1 subtype from the nucleus into the cytoplasm triggers the release of cytochrome C from the mitochondria and thus leads to apoptosis [35].

Histone modifications (acetylations, methylations, phosphorylations, ubiquitinations, etc.) are posttranslational modifications made in the nucleus by the appropriate enzymes [25,32,36]. As a consequence, transcription often becomes altered because modified histones and the DNA will interact differently. The cytoplasmic accumulation of such modified histones might indicate that they were released/transported from the nucleus, perhaps as a consequence of distress [29–31]. Histone modifications are key epigenetic

regulatory features that govern many cellular functions. Specific histone posttranslational modifications can direct site-specific activation or the silencing of transcription [36]; hence, they are the principal players that regulate gene expression. Histone methylations at lysine (lys (K)) and arginine (arg (R)) residues are relatively stable and considered potential marks for carrying the epigenetic information present in specific regions of the genome. For example, several monomethylations (i.e., H3K9me1, H3K27me1, and H3K79me1) and some dimethylations of histone H3 proteins (H3K36me2) are linked to active transcription, while other dimethylations (H3K9me2) and most trimethylations of this core histone (i.e., H3K9me3, H3K27me3, and H3K79me3) are linked to gene repression [37,38].

In this study, we investigated the relationships among (a) KYNA and its analog SZR104, (b) the inflammatory mechanisms that gives rise to epigenetic changes via histone methylations, and (c) the intracellular localizations of unmethylated and methylated histones in microglial cells. Besides the inflammatory markers CXCL10 and CCR1, we quantitatively analyzed the levels of unmodified core histone H3 and histone H3 lys methylations at the H3K9me3 and H3K36me2 sites (Table S2), marks that are considered contrary in regulating gene expression [37,38] and also involved in immunomodulation [39–42], using western blots and multicolor light microscopic immunofluorescence. As far as we know, our approach for studying KYNA and its brain-penetrable analog SZR104, with regard to epigenetics and neuroinflammation, is unique in the literature. Our results shed light on the indicator roles that these histones, translocated to the cytoplasm, might play in neuroinflammation; furthermore, our findings highlight the beneficial role that the endogenous kynurenine system could play in antiinflammatory mechanisms.

## 2. Results

### 2.1. KYNA and SZR104 Downregulate LPS-Induced CXCL10 Levels While Differentially Altering CCR1 Levels

In CD11b/c-labeled microglial cells taken from unchallenged (control) and treated microglia-enriched secondary cell cultures (subDIV7), there was a robust increase in the amount of immunoreactivity of the inflammation marker CXCL10 in LPS-treated microglia (Figure 1). Following an LPS immunochallenge, typical amoeboid morphology was observed (Figure 1F) with CXCL10 immunoreactivity localized in the cytoplasm (Figure 1G).

Treatments with KYNA or SZR104 (a brain-penetrable KYNA analog), either alone or in combination with LPS, reduced CXCL10 immunoreactivity to unchallenged levels (Figure 1K,O,S,W). Moreover, quantitative light microscopic microdensitometric analysis of CXCL10 protein expression revealed that LPS challenge significantly elevated CXCL10 immunoreactivity (approximately fourfold) in microglial cells, whereas KYNA alone, SZR104 alone, or either combined with LPS significantly depleted the CXCL10 immunoreactive signal to control (unchallenged) levels (Figure 2). A similar but weaker response was recorded when the immunoreactivity of CCR1, another inflammation marker, was tested in control and treated cells. A localization analysis in CD11b/c-labeled microglial cells revealed slightly increased CCR1 immunoreactivity in LPS-challenged cultures (Figure 3G) relative to that observed in the control (Figure 3C). A quantitative light microscopic microdensitometric analysis of the cellular CCR1 levels of the cultures showed that an LPS challenge significantly elevated CCR1 immunoreactivity by 48%, whereas KYNA or SZR104 alone, or the combined treatment with LPS + KYNA, proved ineffective (Figure 4A). Interestingly, the combined treatment of LPS + SZR104 significantly lowered CCR1 immunoreactivity as compared to LPS-treated cultures, and it reverted to a level observed in unchallenged (control) cultures. A quantitative western blot analysis revealed that cytoplasmic CCR1 immunoreactivity was significantly increased after LPS treatment (Figure 4B). KYNA or SZR104, either alone or in combination with LPS, did not noticeably affect CCR1 levels.

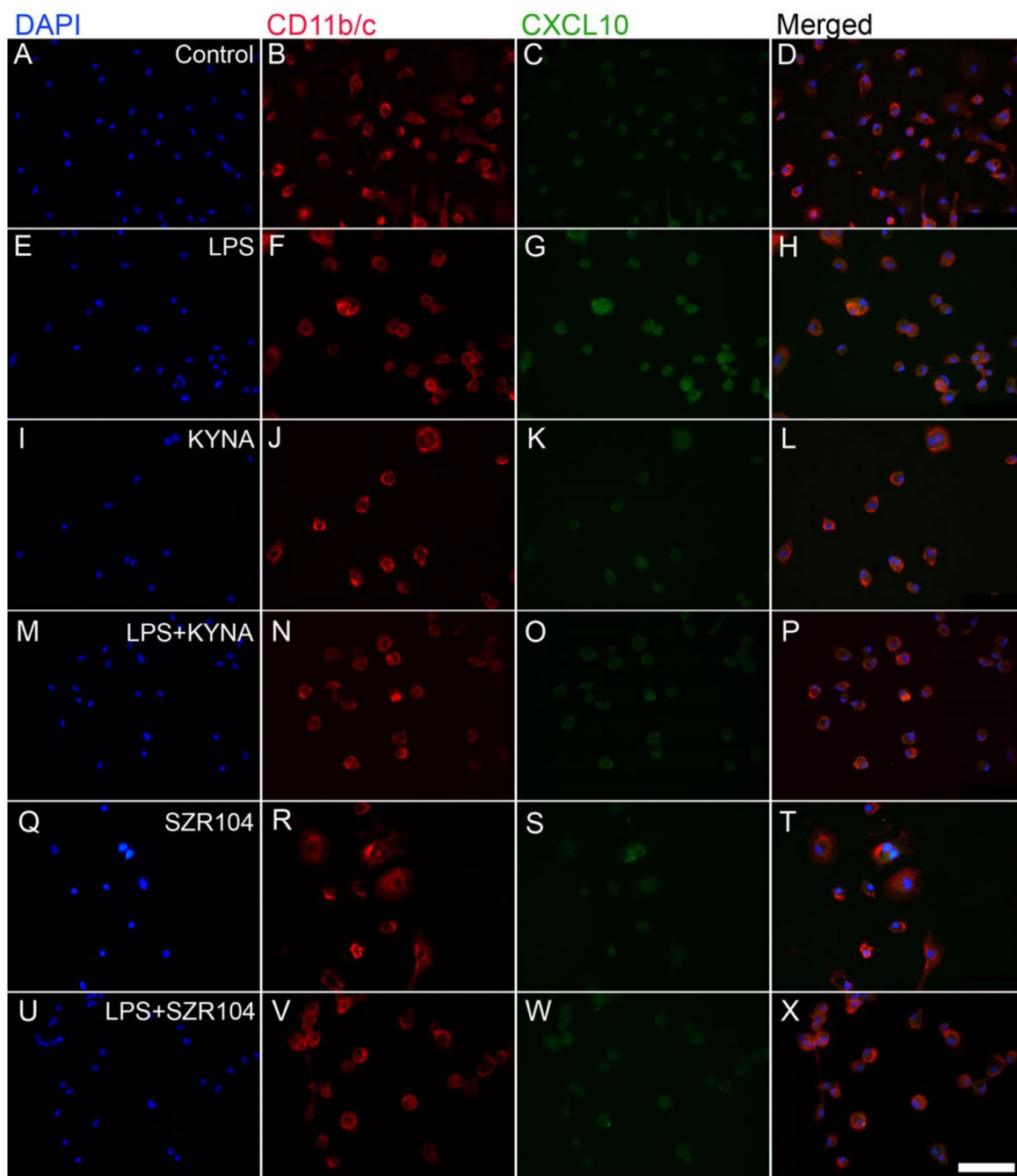


**Figure 1.** Localization of CXCL10 immunoreactivity in CD11b/c-labeled microglial cells in unchallenged and treated microglia-enriched cultures. The distribution of CD11b/c (red) and CXCL10 (green) immunoreactivities and their colocalizations is shown. The anti-CD11b/c antibody was used to highlight microglial cells. Note the very high purity of the microglial cultures (DAPI vs. CD11b/c labels). The following cultures (subDIV7) were used: (A–D) unstimulated (control), (E–H) LPS-challenged, (I–L) KYNA-treated, (M–P) LPS + KYNA-treated, (Q–T) SZR104-treated, and (U–X) LPS + SZR104-treated cultures. Cell nuclei are labeled with DAPI (blue). CXCL10 immunoreactivity was more intensive after LPS treatment in microglia; KYNA and SZR104 decreased the amount of CXCL10 in these cells. No visible cell loss was observed after the treatments were applied. This is in agreement with the findings of Steiner et al. [43], who found there was no effect on cell viability when microglial cells were treated with KYNA. LPS: 20 ng/mL; KYNA: 1  $\mu$ M; and SZR104: 1  $\mu$ M. Scale bar: 75  $\mu$ m.

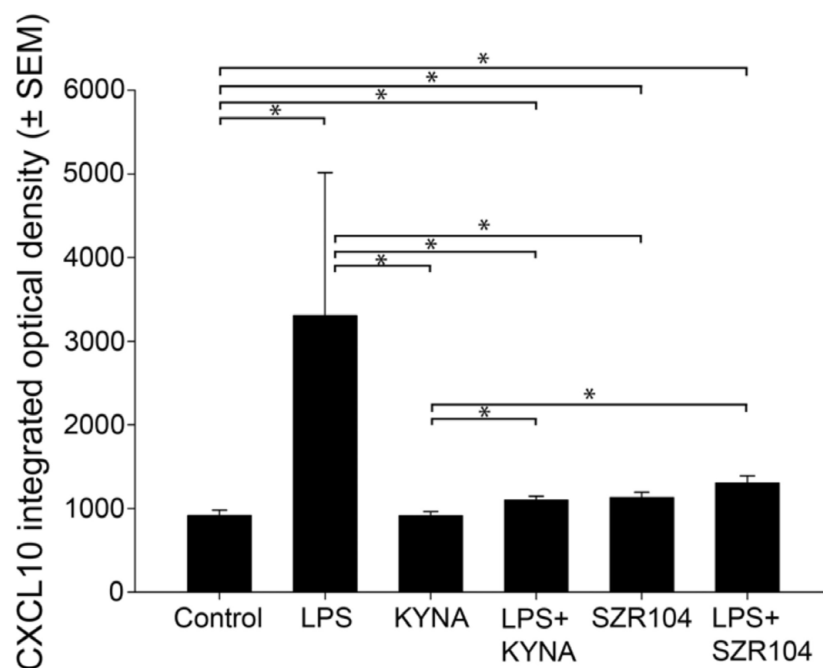


**Figure 2.** Quantitative light microscopic microdensitometric analysis of CXCL10 protein expression in unchallenged and treated microglia-enriched cultures. The LPS challenge significantly elevated cytoplasmic CXCL10 immunoreactivity (approximately fourfold) in microglial cells, whereas KYNA alone, SZR104 alone, or the combined treatments significantly weakened the CXCL10 immunoreactive signal to levels observed in unchallenged (control) cells. LPS: 20 ng/mL; KYNA: 1  $\mu$ M; and SZR104: 1  $\mu$ M. Data (presented as means  $\pm$  SEMs) were analyzed using Kruskal–Wallis one-way ANOVA on ranks: \*  $p < 0.05$ .

## 2.2. KYNA and SZR104 Alter the Intracellular Histone H3 Distribution and H3 lys Methylation Patterns

Unmodified histone H3 levels were monitored because they form a pool for further posttranslational modifications. H3 immunoreactivity was detected in both the cytoplasm and nucleus of unchallenged microglia; that is, after nuclear import, histone H3 mostly accumulated in the nucleus (Figure 5A–D). We also did not detect any extracellular histone signal in these studies. Interestingly, every experimental manipulation of the cells, except for the LPS + SZR104 treatments, resulted in the increased accumulation of histone H3 in both the nuclear and the cytoplasmic compartments, indicating that both elevated *de novo* synthesis and increased nuclear import occurred as outcome of the treatments (Figures 5E–X and 6F). Of these treatments, KYNA produced the strongest nuclear accumulation of unmodified H3 immunoreactivity (Figure 5J). When LPS and SZR104 treatments were combined, however, neither the nuclear nor the cytoplasmic H3 immunoreactivities were different from the controls (Figure 6). Quantitative microdensitometry of H3 immunosignals on cultured microglia corroborated these findings (Figure 7A). The CTCF values for nuclear localization increased significantly only after LPS or KYNA treatments, compared to controls, but decreased significantly after the combined treatments of LPS + KYNA and LPS + SZR104, as compared to LPS-challenged cultures (Figure 7A). In contrast, CTCF values for cytoplasmic localization were higher in all experimental groups except for the LPS + SZR104 treatment case (Figure 7B). Moreover, cytoplasmic H3 levels were affected differently by the combined treatments, i.e., LPS + KYNA increased, while LPS + SZR104 returned cytoplasmic H3 levels to controls (Figures 6J and 7B). The nuclear and cytoplasmic histone H3 distributions elicited by the LPS + SZR104 treatment were rather like those of unchallenged microglia.

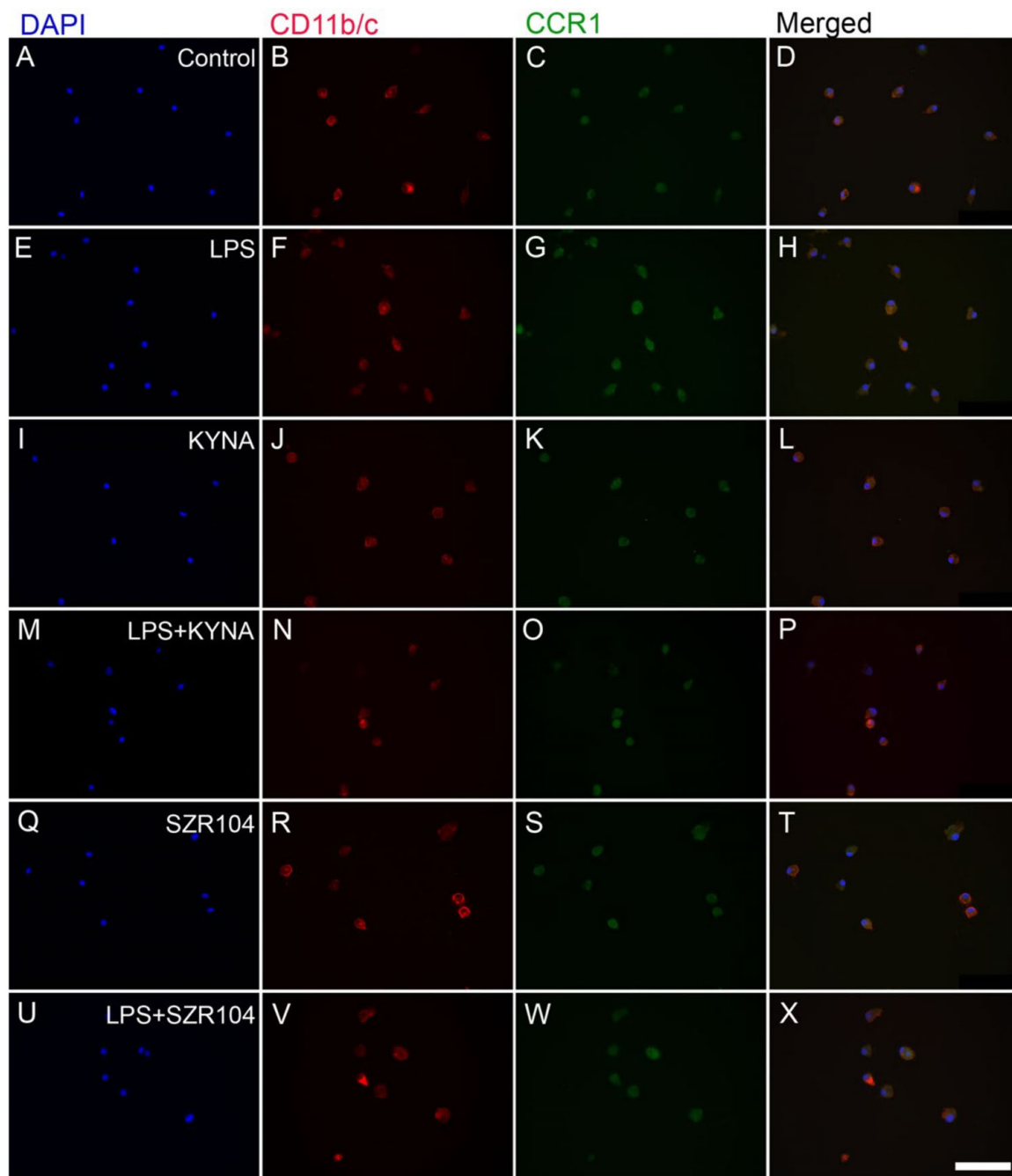


**Figure 3.** Localization of CCR1 immunoreactivity in CD11b/c-labeled microglial cells in unchallenged and treated microglia-enriched cultures. The distribution of CD11b/c (red) and CCR1 (green) immunoreactivities, as well as their colocalizations, is shown. The anti-CD11b/c antibody was used to highlight microglial cells. Note the very high purity of the microglial cultures (DAPI vs. CD11b/c labels). The following cultures (subDIV7) were used: (A–D) unstimulated (control), (E–H) LPS-challenged, (I–L) KYNA-treated, (M–P) LPS + KYNA-treated, (Q–T) SZR104-treated, and (U–X) LPS + SZR104-treated cultures. Representative immunocytochemical images confirm that the LPS challenge (G) slightly increased CCR1 immunoreactivity in microglial cells compared with that in unchallenged (control) cells (C), but the level of the immunoreactive signal returned to control levels with KYNA (K), SZR104 (S), or combined treatments (O,W). LPS: 20 ng/mL; KYNA: 1  $\mu$ M; and SZR104: 1  $\mu$ M. Scale bar: 75  $\mu$ m.

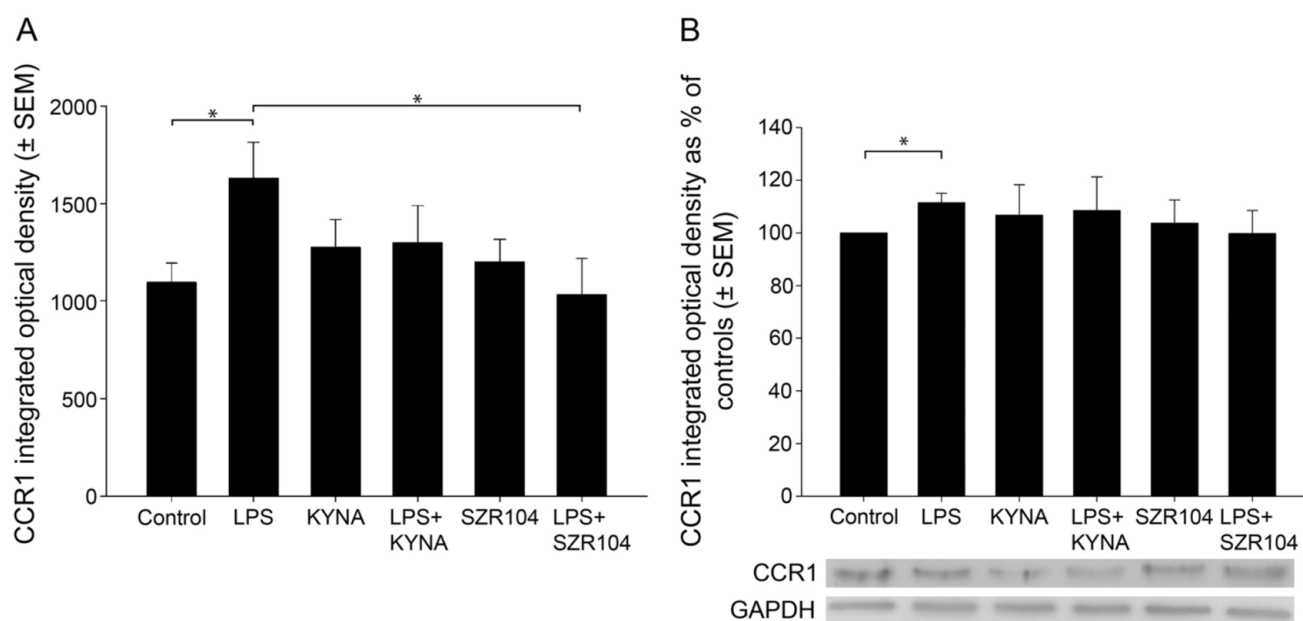


**Figure 4.** Quantitative analysis of CCR1 protein expression in unchallenged and treated microglia-enriched cultures. **(A)** A quantitative light microscopic microdensitometric analysis of CCR1 protein expression. The LPS challenge significantly elevated CCR1 immunoreactivity to approximately 148% of the control value in microglial cells, whereas KYNA or SZR104 alone, or the combined treatment of LPS + KYNA, did not significantly alter the amount of CCR1 immunoreactive signal compared to controls. However, LPS + SZR104-treated cultures displayed significantly lowered CCR1 levels compared to LPS-treated cultures, and they returned to levels seen in unchallenged (control) cells. Data (presented as means  $\pm$  SEMs) were analyzed with the Mann–Whitney rank sum test: \*  $p < 0.05$ . **(B)** A quantitative western blot analysis of cytoplasmic CCR1 immunoreactivity. Representative images of western blots are shown below the graph, together with the GAPDH immunoreactive bands that served as protein load control. Protein samples were collected from at least five separate cultures, electrophoresed, and then quantitatively analyzed, as described in the Materials and Methods section. CCR1 immunoreactivity significantly increased after the LPS treatment. It did not change when the cultures were treated with LPS + KYNA or LPS + SZR104. Error bars indicate integrated optical density values with the data values for each group expressed as a percentage of the control values. LPS: 20 ng/mL; KYNA: 1  $\mu$ M; and SZR104: 1  $\mu$ M. Integrated optical density data (presented as means  $\pm$  SEMs) were analyzed with the Mann–Whitney rank sum test: \*  $p < 0.02$ .

However, when the amount of unmodified cytoplasmic histone H3 was quantitatively analyzed via western blots, only the LPS + KYNA treatment showed a significant increase (Figure 8). This might be due to denaturing conditions in detecting histone H3 proteins in westerns that concealed the changes observed in multicolor immunocytochemistry when individually identified microglia were analyzed.

Our analysis of the intracellular localization of H3K9me3 immunoreactivity in CD11b/c-labeled microglia in unchallenged (control) and variably treated microglia-enriched secondary cell cultures (subDIV7) demonstrated that LPS challenge (Figures 9E–H and 10F) increased H3K9me3 immunopositivity relative to that observed in the unchallenged control (Figures 9A–D and 10B) or other treatments (Figure 9I–X). Strong histone H3K9me3 immunoreactivity was detected in both the nucleus and cytoplasm after the LPS challenge (Figures 9F and 10F), but decreased when LPS treatment was combined with KYNA or SZR104 (Figure 10J). Quantitative fluorescent microdensitometry revealed that the nuclear accumulation of H3K9me3 protein increased significantly after LPS treatment but that the LPS + KYNA or LPS + SZR104 treatments reduced this accumulation (Figures 10J and 11A). However, the effect of KYNA alone did not differ significantly from that of the control. By contrast, SZR104 had a greater inhibiting effect on the extranuclear translocation of

H3K9me3. Similar values and tendencies were noted when cytoplasmic H3K9me3 was analyzed (Figure 11B): KYNA or SZR104, either alone or in combination with LPS, was able to recover LPS-induced cytoplasmic accumulation of H3K9me3 protein. However, SZR104 was found to be more potent than KYNA in inhibiting H3K9me3 translocation to the cytoplasm (Figure 11B).

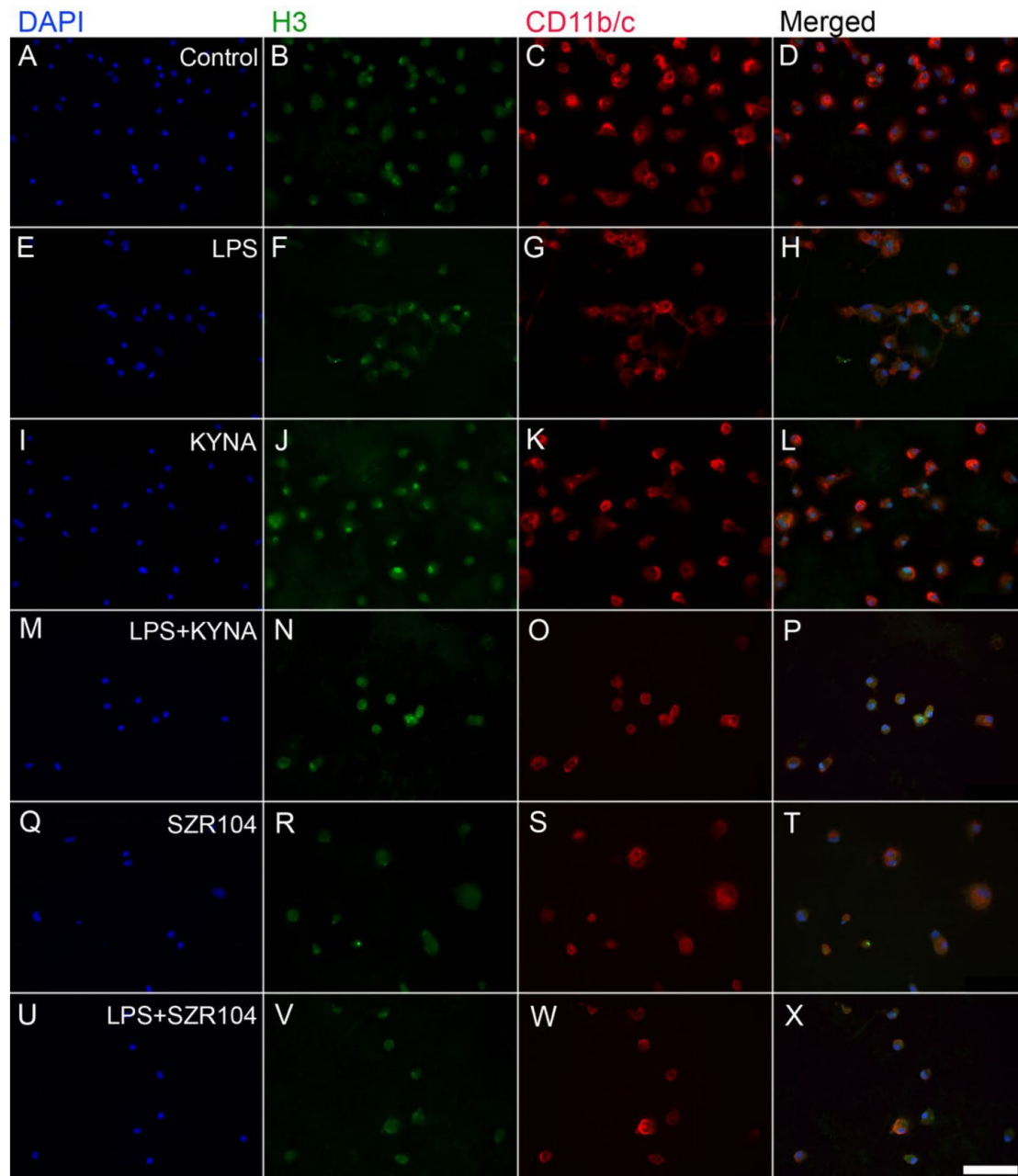


**Figure 5.** Localization of histone H3 protein immunoreactivity in unchallenged and treated microglia-enriched cultures. Representative immunocytochemical images demonstrate the intracellular distribution of histone H3 protein immunopositivity (green) in unstimulated (control) (A–D), LPS-challenged (E–H), KYNA-treated (I–L), LPS + KYNA-treated (M–P), SZR104-treated (Q–T), and LPS + SZR104-treated (U–X) CD11b/c-immunopositive microglial cells (red). The anti-CD11b/c antibody was used to highlight microglial cells. Note the very high purity of the microglial cultures (DAPI vs. CD11b/c labels). Histone H3 was detected in both the nucleus and cytoplasm of microglia. Cell nuclei are labeled with DAPI (blue). LPS: 20 ng/mL; KYNA: 1  $\mu$ M; and SZR104: 1  $\mu$ M. Scale bar: 75  $\mu$ m.

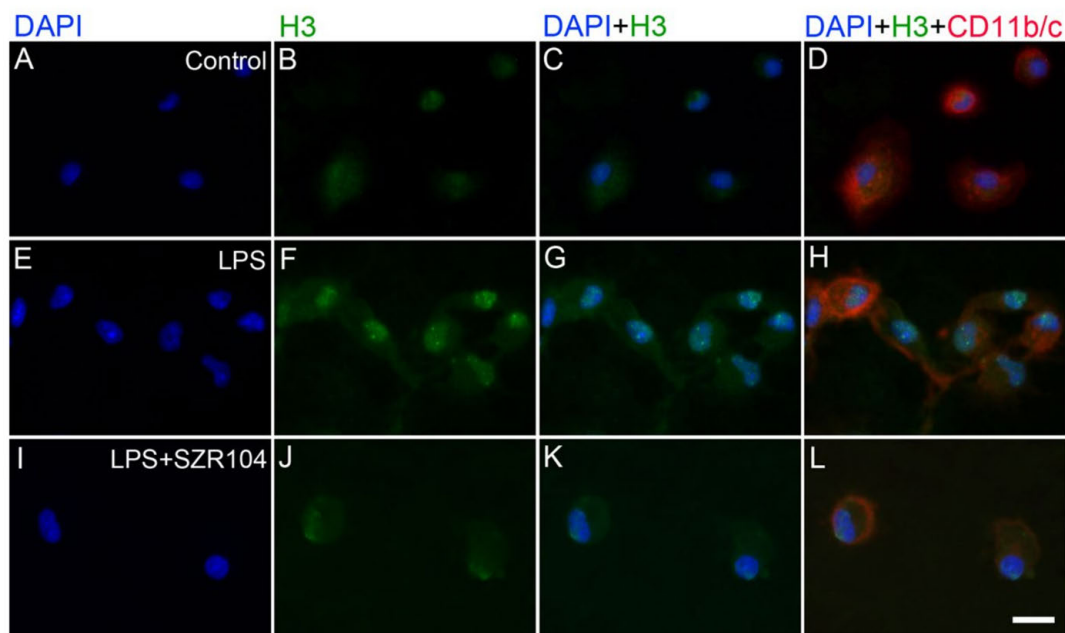


**Figure 6.** Intracellular localization of histone H3 protein immunoreactivity in unchallenged and treated microglia-enriched cultures. Representative enlarged immunocytochemical images showing a subset of microglial cells from Figure 5 demonstrate the intracellular distribution of histone H3 immunopositivity (green) in unstimulated (control) (A–D), LPS-challenged (E–H), and LPS + SZR104-treated (I–L) CD11b/c-immunopositive microglial cells (red). The anti-CD11b/c antibody was used to highlight microglial cells. After LPS treatment (F), unmodified histone H3 was detected in both the nucleus and cytoplasm of microglia. LPS + SZR104 treatments lowered both nuclear and cytoplasmic H3 immunosignal. Cell nuclei are labeled with DAPI (blue). Scale bar: 15  $\mu$ m.

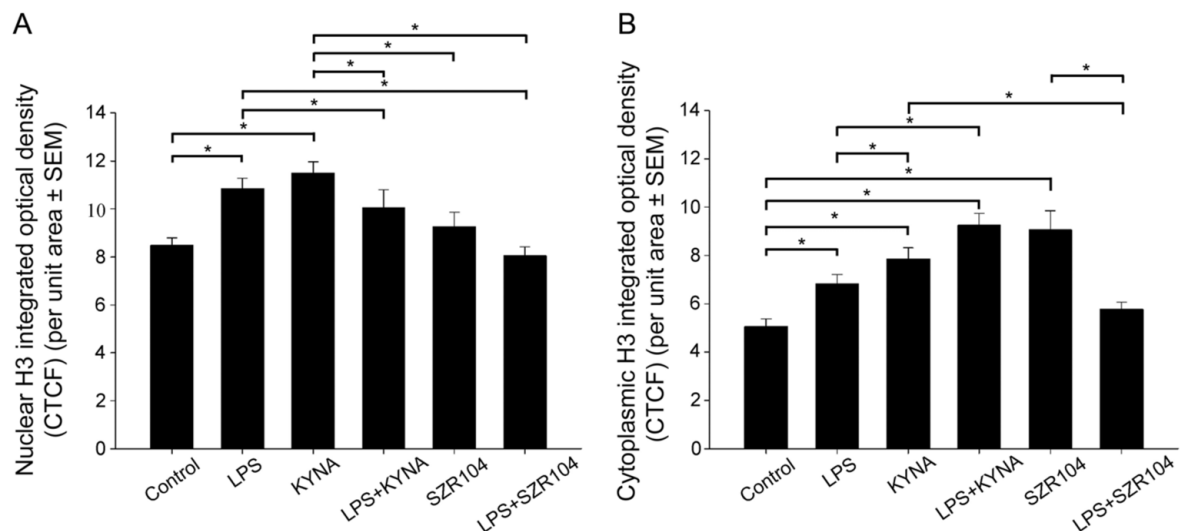


**Figure 7.** Intracellular distribution of unmodified histone H3 protein immunoreactivity in the nucleus and cytoplasm of microglia in unchallenged and treated microglia-enriched cultures. Corrected total cell fluorescence (CTCF) values for the whole cell, nucleus, and cytoplasm were calculated as described in the Materials and Methods section. (A) The amount of H3 immunoreactivity rose significantly in the nucleus of LPS- and KYNA-treated microglia. SZR104 effectively decreased the amount of histone H3 after LPS treatment. (B) Except for the LPS + SZR104 treatment, all the treatments increased the amount of unmodified cytoplasmic histone H3. LPS: 20 ng/mL; KYNA: 1  $\mu$ M; and SZR104: 1  $\mu$ M. Data (presented as means  $\pm$  SEMs) were analyzed with Kruskal–Wallis one-way ANOVA on ranks: \*  $p < 0.05$ .

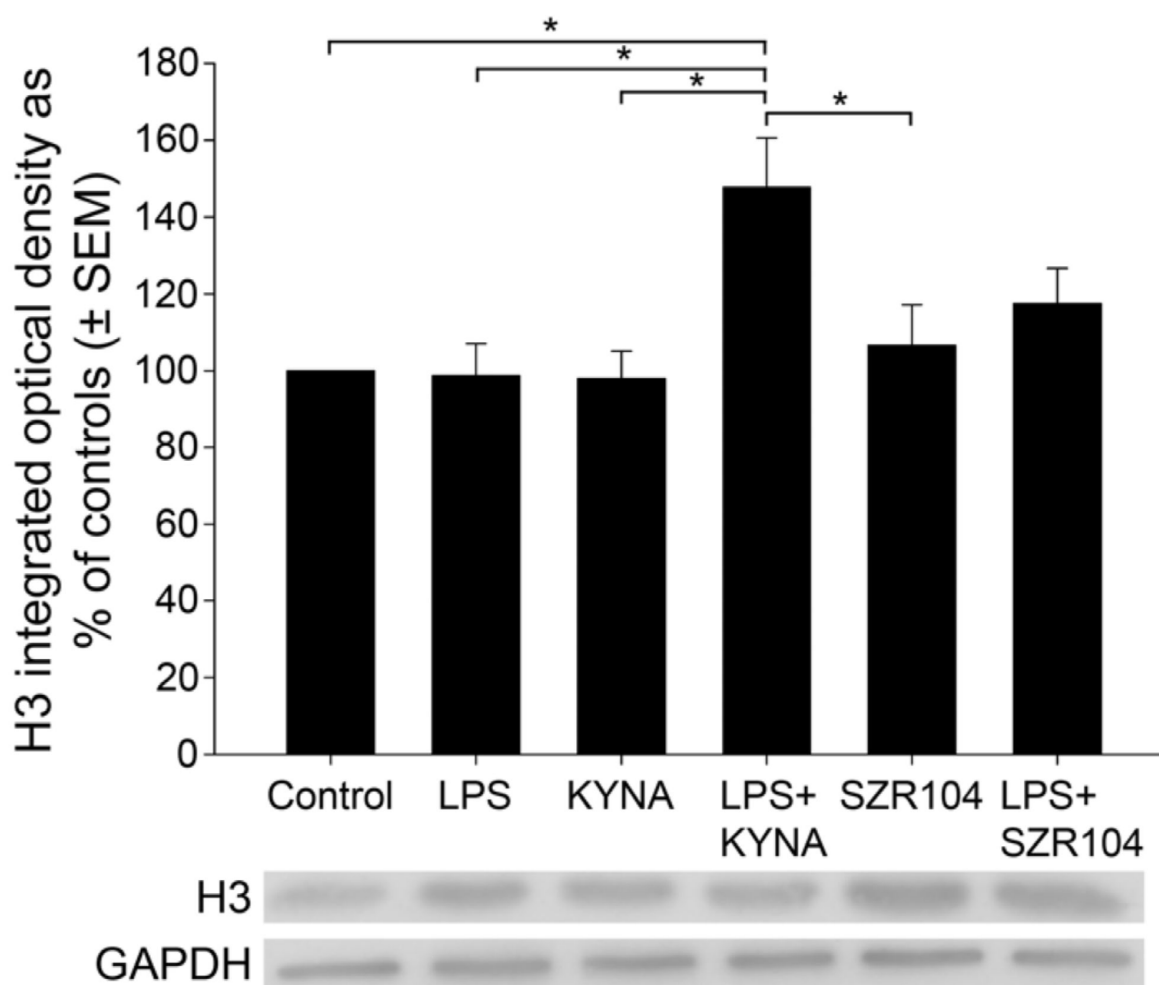


**Figure 8.** Quantitative western blot analysis of the cytoplasmic histone H3 protein level in microglia-enriched cultures. Representative images of western blots are shown below the graph, together with the GAPDH immunoreactive bands that served as inner standards. Protein samples were collected from at least five separate cultures (subDIV7), electrophoresed, and quantitatively analyzed as described in the Materials and Methods section. The combined LPS + KYNA treatment induced a significant increase in histone H3 immunoreactivity when compared with that in control (unchallenged) and other treated cultures. The error bars indicate integrated optical density values with data expressed as a percentage of the control values. LPS: 20 ng/mL; KYNA: 1  $\mu$ M; and SZR104: 1  $\mu$ M. Data values (presented as means  $\pm$  SEMs) were analyzed using ANOVA followed by pairwise multiple comparisons (Holm–Sidak method): \*  $p < 0.05$ .

When the intracellular distribution of H3K36me2 immunoreactivity in CD11b/c-labeled microglia was measured, a marked increase, relative to unchallenged control levels (Figure 12A–D), was seen exclusively within the nuclei of the microglia after LPS challenge (Figures 12E–H and 13F). By contrast, the other treatments did not affect H3K36me2 immunoreactivity appreciably (Figure 12I–X). For example, LPS + SZR104 treatments returned the nuclear levels of H3K36me2 to the control levels (Figure 13J). A quantitative microdensitometric analysis of H3K36me2-immunopositive signals revealed that LPS treatment dramatically increased the amount of H3K36me2 signal in the nuclei of CD11b/c-labeled microglial cells, whereas the other treatments had only a minor effect. Moreover, KYNA or SZR104 alone, or the combination treatments, had significantly lower H3K36me2 signals compared to LPS-challenged levels (Figure 14).

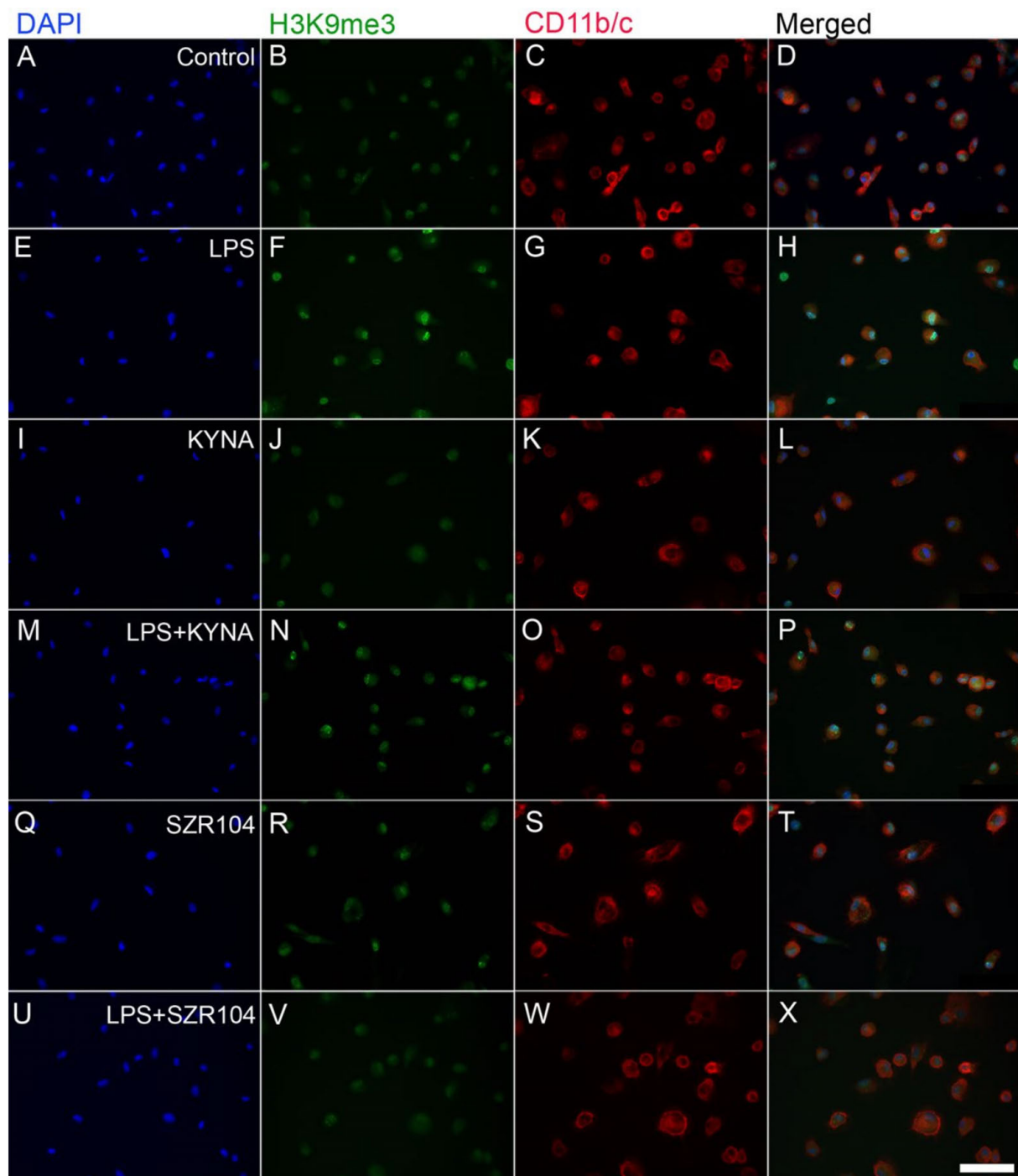


**Figure 9.** Localization of H3K9me3 immunoreactivity in CD11b/c-labeled microglia in unchallenged and treated microglia-enriched cultures. Representative immunocytochemical images showing the intracellular distribution of histone H3K9me3 protein immunopositivity (green) in unstimulated (control) (A–D), LPS-challenged (E–H), KYNA-treated (I–L), LPS + KYNA-treated (M–P), SZR104-treated (Q–T), and LPS + SZR104-treated (U–X) CD11b/c-immunopositive microglial cells (red). The anti-CD11b/c antibody was used to highlight microglial cells. The very high purity of the microglial cultures is evident (DAPI vs. CD11b/c labels). Note that LPS challenge (F) increased the H3K9me3 immunopositivity relative to that in unchallenged controls (B) or other treatments. Histone H3K9me3 was detected in both the nucleus and cytoplasm. LPS: 20 ng/mL; KYNA: 1  $\mu$ M; and SZR104: 1  $\mu$ M. Scale bar: 75  $\mu$ m.

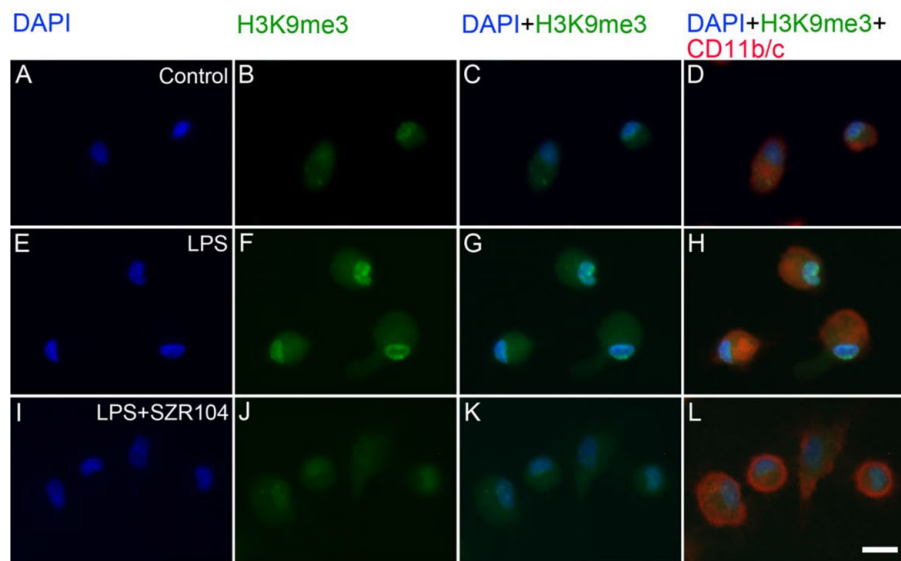


**Figure 10.** Intracellular localization of H3K9me3 immunoreactivity in CD11b/c-labeled microglia in unchallenged and treated microglia-enriched cultures. Representative enlarged immunocytochemical images showing a subset of microglial cells from Figure 9 demonstrate the intracellular distribution of histone H3K9me3 immunopositivity (green) in unstimulated (control) (A–D), LPS-challenged (E–H), and LPS + SZR104-treated (I–L) CD11b/c-immunopositive microglial cells (red). The anti-CD11b/c antibody was used to highlight microglial cells. After LPS treatment (F), increased amounts of H3K9me3 immunolabel were detected in both the nucleus and cytoplasm of microglia, although the nuclear component was more pronounced. LPS + SZR104 treatments lowered the amounts of both nuclear and cytoplasmic H3K9me3 immunosignal. Cell nuclei are labeled with DAPI (blue). Scale bar: 15  $\mu$ m.

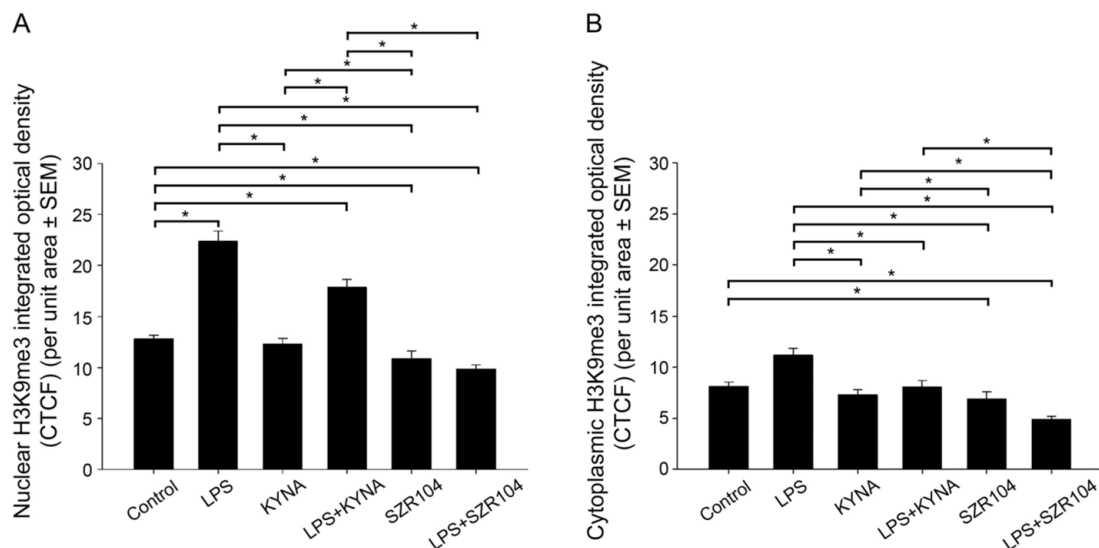


**Figure 11.** Intracellular distribution of histone H3K9me3 protein immunoreactivity in the nucleus and cytoplasm of microglia in unchallenged and treated microglia-enriched cultures. A quantitative microdensitometric analysis of H3K9me3-immunopositive signals in the nucleus (A) and cytoplasm (B) was performed, as described in the Materials and Methods section. (A) LPS treatment increased the amount of H3K9me3 signal in the nucleus, whereas KYNA and SZR104 treatment did not alter the signal compared to the control level. (B) Cytoplasmic H3K9me3 was reduced uniformly when cells were treated with KYNA, SZR104, or with a combination of treatments. LPS: 20 ng/mL; KYNA: 1  $\mu$ M; and SZR104: 1  $\mu$ M. Integrated density data values (presented as means  $\pm$  SEMs) were analyzed with Kruskal–Wallis one-way ANOVA: \*  $p < 0.05$ .

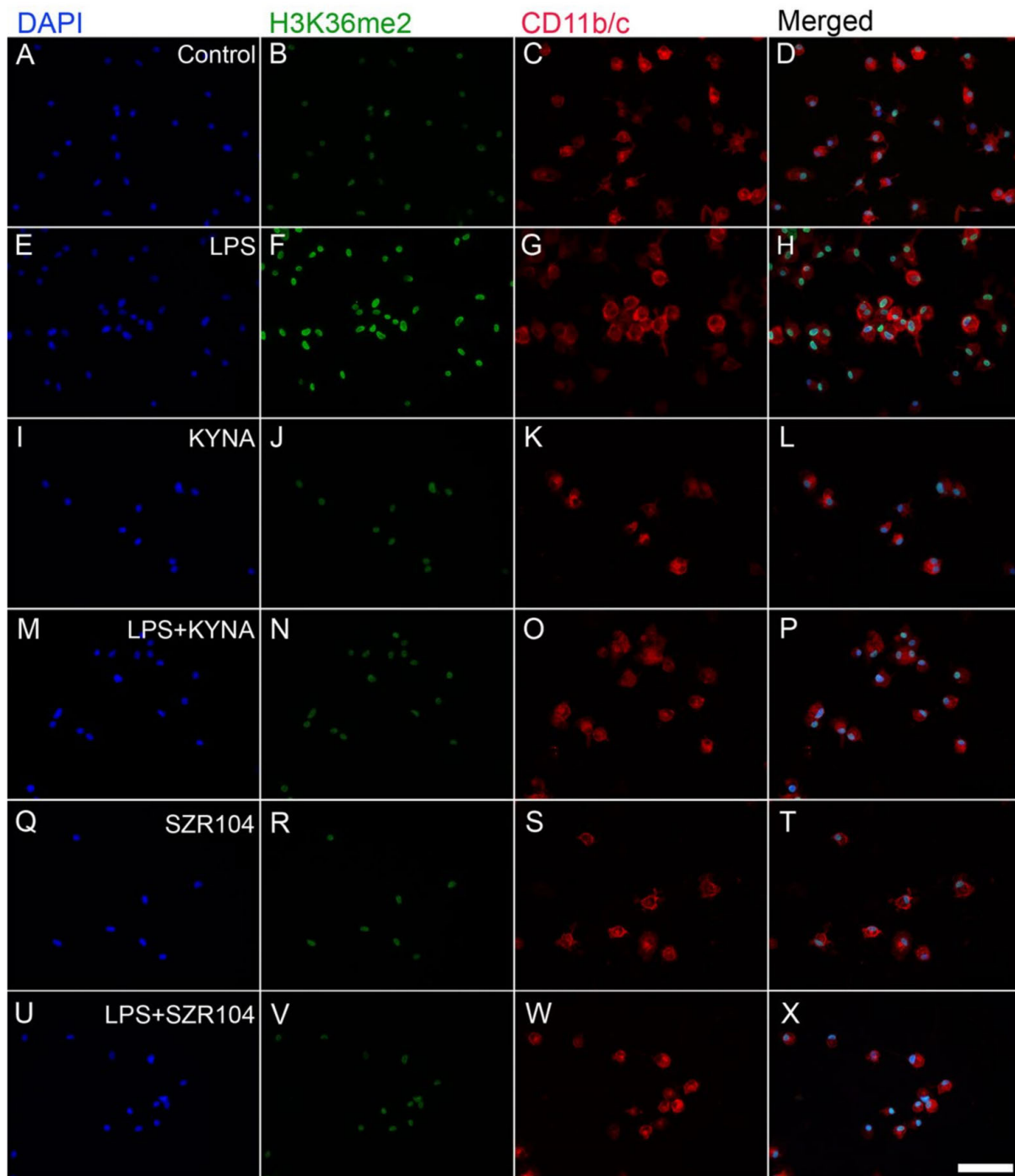


**Figure 12.** Localization of H3K36me2 immunoreactivity in CD11b/c-labeled microglia in unchallenged and treated microglia-enriched cultures. Representative immunocytochemical images showing the intracellular distribution of histone H3K36me2 protein immunopositivity (green) in unstimulated (control) (A–D), LPS-challenged (E–H), KYNA-treated (I–L), LPS + KYNA-treated (M–P), SZR104-treated (Q–T), and LPS + SZR104-treated (U–X) CD11b/c-immunopositive microglial cells (red). The anti-CD11b/c antibody was used to highlight microglial cells. The very high purity of the microglial cultures is evident (DAPI vs. CD11b/c labels). Note that the LPS challenge (E–H) markedly increased H3K36me2 immunopositivity relative to that of the unchallenged control (A–D) or any other treatment (I–X). Histone H3K36me2 was detected in the nucleus. LPS: 20 ng/mL; KYNA: 1  $\mu$ M; and SZR104: 1  $\mu$ M. Scale bar: 75  $\mu$ m.

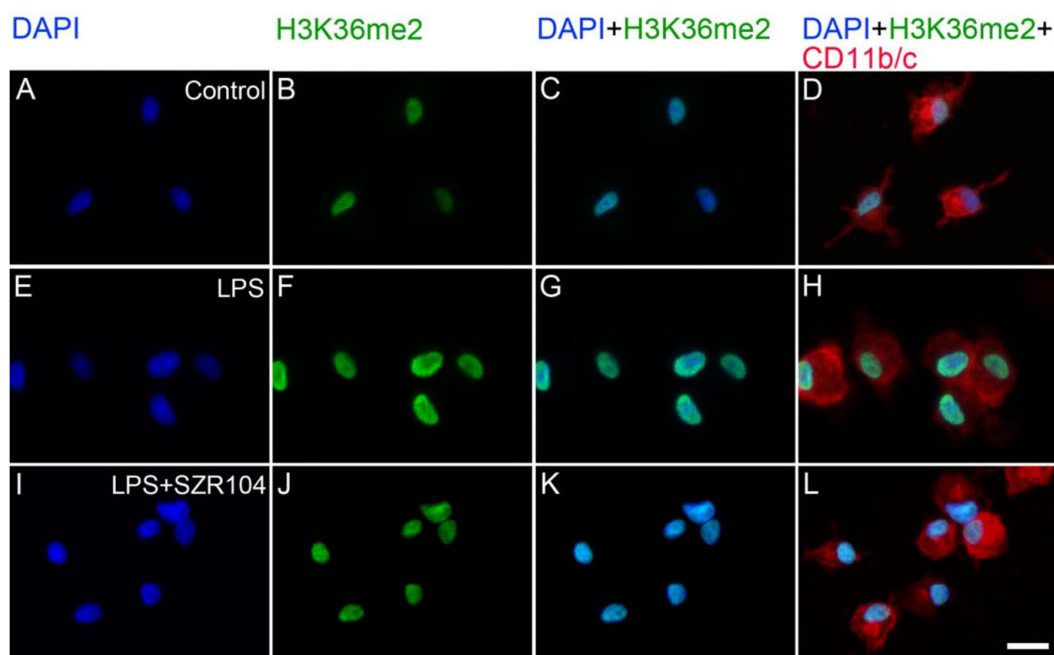


**Figure 13.** Intracellular localization of H3K36me2 immunoreactivity in CD11b/c-labeled microglia in unchallenged and treated microglia-enriched cultures. Representative enlarged immunocytochemical images showing a subset of microglial cells from Figure 12 demonstrate the intracellular distribution of histone H3K36me2 immunopositivity (green) in unstimulated (control) (A–D), LPS-challenged (E–H), and LPS + SZR104-treated (I–L) CD11b/c-immunopositive microglial cells (red). The anti-CD11b/c antibody was used to highlight microglial cells. After LPS treatment (F), increased amounts of H3K36me2 immunolabel were detected in the nucleus of microglia. There was no signal in the cytoplasm. LPS + SZR104 treatments lowered the amounts of nuclear H3K36me2 immunosignal (J). Cell nuclei are labeled with DAPI (blue). Scale bar: 15  $\mu$ m.

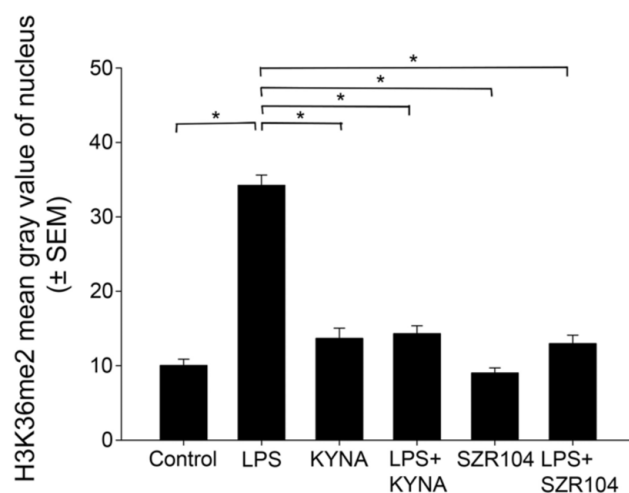


**Figure 14.** Intracellular distribution of histone H3K36me2 protein immunoreactivity in the nucleus of microglia in unchallenged and treated microglia-enriched cultures. A quantitative microdensitometric analysis of H3K36me2-immunopositive signals in the nucleus was performed as described in the Materials and Methods section. The LPS treatment dramatically increased the amount of the H3K36me2 signal in the nucleus, whereas KYNA, SZR104, or a combination of treatments decreased it toward the unchallenged control levels. LPS: 20 ng/mL; KYNA: 1  $\mu$ M; and SZR104: 1  $\mu$ M. The integrated density data values (presented as means  $\pm$  SEMs) were analyzed with Kruskal–Wallis one-way ANOVA on ranks: \*  $p < 0.05$ .

### 3. Discussion

In the functioning of the immune system, endogenous kynurenine metabolism is implicated. Recent studies showed that the amounts of several inflammation-related marker proteins decreased after treatments with KYNA or its analogs. For example, it was demonstrated by Mándi et al. [8] and Lajkó et al. [5] that KYNA and several KYNA analogs, including SZR104, interfered with immune functions *in vivo* and *in vitro*. KYNA and SZR104 not only attenuated tumor necrosis factor- $\alpha$  (TNF- $\alpha$ ) production and increased tumor necrosis factor-stimulated gene-6 mRNA expression in U-937 cells stimulated with heat-inactivated *Staphylococcus aureus* [8] but they also inhibited the LPS-stimulated phagocytotic activity of microglial cells *in vitro* while suppressing microglial activity in an *in vivo* model of epilepsy [5]. Another potent proinflammatory cytokine, interleukin-1 $\beta$ , was elevated in sepsis but was ameliorated by KYNA and its synthetic analogues SZR72 and SZR104 [44]. Furthermore, SZR72 inhibited the production of the inflammatory mediators TNF- $\alpha$ , calprotectin, S100A12, and HNP1-3 in blood cultures of rheumatoid arthritis patients [45]. Interestingly, a possible role for indoleamine 2,3-dioxygenase, a key kynurenine pathway enzyme, in immunity has recently emerged [46], further emphasizing the crucial role this system plays in immunomodulatory functions. As KYNA is a metabolite of the endogenous kynurenine system, with proven antiinflammatory properties, we wanted to know whether its effect went beyond conventional targets in the intermediary metabolic or intracellular signaling pathways and perhaps had effects on phenomena such as epigenetics elicited through histone metabolism/transport. In particular, we sought to investigate (a) how SZR104, a brain-penetrable analog of KYNA, behaves in our systems; (b) how inflammatory signals affect histone methylations and, consequently, epigenetic changes; and (c) how the intracellular localization of unmodified and methylated histones change during inflammation or amelioration of inflammation.

In the present study, KYNA and SZR104 exhibited strong antiinflammatory properties, as demonstrated by their effective amelioration of LPS-challenged CXCL10 and CCR1 production in microglial cultures. This *in vitro* functional study shows for the first time that KYNA and SZR104 effectively ameliorate the production of two proinflammatory signal molecules, CXCL10 and CCR1, in LPS-challenged microglia. Our results are in agreement with those of other studies that found similar CXCL10 reduction in activated microglia after treatment with antiinflammatory drugs [47,48]. Earlier, we previously reported a similar downregulation of CCR1 after aspirin treatment in LPS-challenged microglial-enriched cultures [49]. Structural differences between KYNA and SZR104 might be the reason these compounds produced somewhat different responses in immunocytochemical and western blot analyses. While KYNA and SZR104 were both effective in ameliorating the LPS-induced elevation of CXCL10 immunoreactivity, only the combined treatment with LPS + SZR104 was effective in significantly inhibiting CCR1 immunoreactivity in these tests. As we used high-purity microglia, this was also the first time that we could identify microglia-specific immune responses to these compounds.

The strong antiinflammatory action of KYNA and SZR104 on inflammatory marker proteins was accompanied by a similarly favorable regulation of histone methylation marks in microglia-enriched cultures. We demonstrated that KYNA and SZR104 reverted the H3K9me3 and H3K36me2 immunoreactivities toward levels observed in the control, i.e., unchallenged values, after immunochallenge by LPS treatment. Our findings also indicated that the cytoplasmic translocation of methylated H3K9 proteins from the nucleus after the LPS challenge was a cellular response to immunological distress. Cytoplasmic translocation from the nucleus of these methylated histones could be ameliorated or inhibited by KYNA and SZR104, which confirms the antiinflammatory nature of these drugs in the present experimental setup. We also observed differential effects of KYNA and SZR104 on the cytoplasmic H3 localization; that is, LPS + KYNA increased, while LPS + SZR104 returned cytoplasmic H3 levels to control values. The detailed mechanisms behind these differential effects of KYNA and SZR104 are not yet understood.

Histones are essential structural and functional components of chromatin. Histone proteins are typically located in the nucleus, but they have functions at extranuclear or even extracellular sites. For instance, extracellular histones released in response to a bacterial challenge contribute to endothelial dysfunction, renal failure and death during sepsis [50]. Patients with sepsis have increased levels of extracellular histones that are correlated with a poor prognosis and the development of sepsis-related consequences such as end-organ damage. These histones originate in megakaryocytes that contain cytoplasmic histones and transfer the proteins to their platelet progeny [31]. Observations on cytoplasmic accumulation of histones have been made in certain pathologic states. For example, altered and differential intracellular histone distribution were detected by Wu et al. [51]. They showed that not all cell lines released histones from nucleosomes during DNA fragmentation and apoptosis, while Gabler et al. [32] demonstrated that the cytoplasmic accumulation of histones and nucleosomes in physiological cells was a precursor to apoptosis, occurring in parallel with the initial phagocytosis signals. During microglia activation by LPS, for instance, DNA damage and genome instability were observed [52,53]. Unmodified H2B in the cytoplasm acts as a sensor that detects double-stranded DNA fragments derived from infectious agents or damaged cells and as a consequence activates innate and acquired immune responses in various cell types [54,55]. Therefore, the cytoplasmic localization of histones is also of pathophysiological importance. For example, the translocation of nuclear histone H1 to the cytoplasm in cultured pulmonary arterial smooth muscle cells is associated with pathologic states such as idiopathic pulmonary hypertension [56]. The cytoplasmic accumulation of the unmodified nucleosomal histones H1, H2A, H2B, H3, and H4 in cell lysates was observed very early on in the process of apoptosis [32,34]. When the effects of doxorubicin, an anthracycline widely used in anticancer therapy, were tested on the aggregation and intracellular distribution of both partners of the H2A-H2B dimer, marked differences between the two histones were found [57]. For H2A, aggregation retention was observed; for H2B, a massive accumulation in the cytoplasm of Jurkat leukemia cells was observed concomitant with its disappearance from the nuclei.

Alterations in histone posttranslational modifications are viewed as an important process by which various cellular functions, including transcription [25,58], gene silencing [59], and immunity [60], are regulated. For example, methylation sites can influence the binding of epigenetic factors to histone tails, which alters the extent to which DNA is wrapped around histone proteins and the availability of genes in the DNA to be activated [38,61,62]. In neuronal cultures, Hayakawa et al. [63] found three metabolites (kynurenine, 3-OH-kynurenine, and anthranilate) from the tryptophan pathways that increase H3K4 trimethylation, resulting in upregulated gene expression at hippocampal-linked loci (except those encoding pan-neural markers). Dimethylated and trimethylated H3K9 sites, i.e., transcriptionally repressive marks, are both found more often at silenced genes [37] and are typical of heterochromatic regions [64]. For instance, H3K9me2 is important in the regulation of inflammatory responses because it suppresses interferon and interferon-inducible antiviral gene expression [65] and epigenetically attenuates target gene-induction by inflammatory signaling in vascular smooth muscle cells [66]. H3K9me3 has been implicated in the opening of chromatin on inflammatory gene promoters, and it is seen at significantly increased levels in treatment-resistant tumors [67]. Additionally, macrophages cultured in high-glucose conditions display increased expressions of cytokine genes and decreased H3K9me3 levels when compared with cells incubated in a normal glucose culture [68]. Methylation of H3K36 has also been found to be related to inflammatory functions and transcription of proinflammatory genes [39–41]. Our data suggest that while the expressions of unmodified histone H3 proteins and inflammatory marker proteins such as CXCL10 and CCR1 are probably regulated independently from each other by pro- and antiinflammatory agents, the subcellular localization of this protein and its methylated forms could be affected by both pro- and antiinflammatory agents through yet unidentified mechanisms.

In summary, methylations of the histone H3 lys sites seem to be essential epigenetic marks for inflammation. Interestingly, KYNA and its analog SZR104 might act on KYNA signaling pathways that potentially ameliorate neuroinflammation through the elicitation of antiinflammatory actions. Our findings corroborate previous studies on the antiinflammatory properties of endogenous KYNA and raise the possibility that some of the newly designed KYNA analogs that can penetrate the blood–brain barrier may alter gene expression epigenetically to activate antiinflammatory mechanisms. Hence, our findings may lead to the development of antiinflammatory medications targeting the central nervous system.

#### 4. Materials and Methods

##### 4.1. Animals

All our animal experiments were conducted in strict compliance with the European Council Directive (86/609/EEC) and EC regulations (O.J. of EC No. L 358/1, 18/12/1986), related to the care and use of laboratory animals for experimental procedures, and the relevant Hungarian and local legislation requirements were followed. Experimental protocols were approved by the Institutional Animal Welfare Committee of the University of Szeged (II./1131/2018; date of approval: 30 May 2018). The pregnant Sprague–Dawley rats (190–210 g) used in this study were maintained under standard housing conditions and fed ad libitum. A total of five breeding runs (with 5–7 pregnant rats each) provided the litters (6–12 pups from each mother), from which independent culturing experiments were performed.

##### 4.2. Reagents and Antibodies

KYNA (mol. weight: 189.17 g) was purchased from Sigma-Aldrich (Budapest, Hungary), and SZR104 (mol. weight: 358.43 g; Table S1) was synthesized in-house as described in previous studies by our laboratories [9,10,69]. KYNA and SZR104 were dissolved in Dulbecco's Modified Eagle's Medium (DMEM; Invitrogen, Carlsbad, CA, USA) and added at the appropriate concentration to the cultures. Bacterial lipopolysaccharide (LPS; Sigma-Aldrich) was used to elicit immunochallenge. The primary and secondary antibodies used in our study are listed in Table S2. For the characterization of microglial cells, we used an antibody against the CD11b/c, clone OX-42 [70]. We also used antibodies against the secreted ligand CXCL10 and the receptor CCR1 as inflammation markers [21,71]. In addition, we used antibodies against the unmodified core histone H3 protein and its posttranslational modifications at lys sites, H3K9me3, and H3K36me2, to detect the cytoplasmic and nuclear localizations of these proteins. An anti-glyceraldehyde 3-phosphate dehydrogenase (GAPDH) antibody was used as an internal control in western blot experiments [72].

##### 4.3. Cell Culture

Forebrain tissue samples taken from newborn Sprague–Dawley rats of both sexes were removed; cleared from the meninges; minced with scissors; and homogenized for 10 min at 37 °C in DMEM containing 1 g/L D-glucose, 110 mg/L Na-pyruvate, 4 mM L-glutamine, 3.7 g/L NaHCO<sub>3</sub>, 10,000 U/mL penicillin G, 10 mg/mL streptomycin sulfate, and 25 µg/mL amphotericin B supplemented with 0.25% trypsin (Invitrogen). After centrifugation at 1000 g and room temperature (RT) for 10 min, the pellet was resuspended, washed in 10 mL of DMEM containing 10% heat-inactivated fetal bovine serum (FBS; Invitrogen), and again centrifuged for 10 min at 1000 g and RT. The final pellet was filtered through a sterile filter (100 µm pore size; Greiner Bio-One Hungary Kft., Mosonmagyaróvár, Hungary) to eliminate tissue fragments that had resisted dissociation. The cells were resuspended in 2 mL of the same solution and then seeded on poly-L-lysine-coated culture flasks (75 cm<sup>2</sup>; 10<sup>7</sup> cells/flask) and cultured at 37 °C in a humidified air atmosphere supplemented with 5% CO<sub>2</sub>. The medium was changed the next day and then every 3 days. After 7 days of culture, microglial cells in the primary cultures were shaken off using a platform shaker (120 rpm for 20 min) at 37 °C as we described earlier [73]. Microglia were collected from the supernatant by centrifugation (3000 g for 8 min at RT), resuspended in 4 mL of

DMEM/10% FBS, and seeded in the same medium either on poly-L-lysine-coated coverslips ( $15 \times 15$  mm;  $2 \times 10^5$  cells/coverslip) for immunocytochemistry or in poly-L-lysine-coated Petri dishes ( $10^6$  cells/Petri dish) for western blot analysis. The number of cells collected was determined in a Bürker chamber after trypan blue staining. DMEM/10% FBS was replaced the next day and then on the third and sixth days of subcloning (subDIV6). These cultures were used in previous studies [5,73], and  $73.3\% \pm 17.8\%$  purity was routinely achieved for microglia in secondary cultures [73]. In this latter study, we demonstrated that the main contaminating cell types were glial fibrillary acidic protein-immunoreactive astrocytes ( $19.0\% \pm 2.7\%$ ),  $\beta$ -tubulin III-positive neurons ( $3.1\% \pm 0.4\%$ ), and 2',3'-cyclic nucleotide 3'-phosphodiesterase-positive oligodendrocytes ( $0.2\% \pm 0.1\%$ ). In the present study, only samples of harvested cultures from different breeding runs with the highest microglia purity (typically around 98%) were selected through immunocytochemical validation as reported earlier [73].

On subDIV6, the expanded microglia-enriched cultures were treated for 24 h with LPS alone (20 ng/mL final conc., dissolved in DMEM; Sigma-Aldrich), KYNA alone (1  $\mu$ M final conc., dissolved in DMEM), SZR104 alone (1  $\mu$ M final conc., dissolved in DMEM), or with a combination LPS + KYNA or LPS + SZR104. LPS treatment served as an immunochallenge. The following six culture types were used: (a) control (unchallenged and untreated) cultures, (b) 20 ng/mL LPS-stimulated cultures, (c) 1  $\mu$ M KYNA-treated cultures, (d) 1  $\mu$ M SZR104-treated cultures, (e) LPS-challenged + KYNA-treated cultures (at indicated doses), and (f) LPS-challenged + SZR104-treated cultures (at indicated doses).

#### 4.4. Immunocytochemistry

The microglia-enriched secondary cultures were assessed using antibodies against a microglia-specific antigen, two inflammation markers, an unmodified core histone H3, and two antigens that recognize specific histone H3 lys modifications (Table S2). Immunocytochemistry was performed according to our previously used protocols [5,73]. Briefly, the cells were fixed in 4% formaldehyde in 0.05 M phosphate-buffered saline (pH 7.4) at RT for 5 min and then rinsed in 0.05 M phosphate-buffered saline for  $3 \times 5$  min. After permeabilization and blocking of the nonspecific sites for 30 min at 37 °C in 0.05 M phosphate-buffered saline containing 5% normal goat serum and 0.3% Triton X-100, the cells on the coverslips were incubated overnight at 4 °C with the appropriate primary antibody diluted in 0.05% phosphate-buffered saline containing 1% bovine serum albumin and 0.3% Triton X-100 solution. The cells were then washed in 0.05 M phosphate-buffered saline for  $3 \times 5$  min at RT before being incubated without Triton X-100 but with the appropriate Alexa Fluor fluorochrome-conjugated secondary antibody in the dark for 2 h at RT. Afterwards, the cells were washed in 0.05 M phosphate-buffered saline for  $3 \times 5$  min and then in distilled water once for 5 min at RT. Lastly, the prepared coverslips were mounted on microscope slides in Prolong Diamond Antifade with 4',6-diamidino-2-phenylindole dye (DAPI; Thermo Fisher, Waltham, MA, USA). To confirm the specificity of the secondary antibodies, omission control experiments (i.e., staining without the primary antibody) were also carried out. In these experiments, immunocytochemical signals were not observed.

#### 4.5. Western Blot Analysis

Cultured cells were collected with a rubber policeman; homogenized in 50 mM Tris-HCl (pH 7.5) containing 150 mM NaCl, 0.1% Nonidet P40, 0.1% cholic acid, 2  $\mu$ g/mL leupeptin, 1  $\mu$ g/mL pepstatin, 2 mM phenylmethylsulfonyl fluoride, and 2 mM ethylenediaminetetraacetic acid; and then centrifuged at 10,000 g for 10 min. The pellet was discarded, and the protein concentration of the supernatant was determined [74]. Due to the high purity and low yield of the cultures, the protein concentration was typically low (about 0.5  $\mu$ g/ $\mu$ L). Western blot analysis was performed as previously described [72] with the exception of the occasional use of large, five-well combs to make wells with 50  $\mu$ L capacity (Mini-Protean Tetra Cell module; Bio-Rad Hungary Ltd., Budapest, Hungary) to accommodate larger volumes in order to compensate for lower protein content; consequently, such

sample sets (control and 5 treatments) were often run in two gels. Briefly, equal amounts of proteins in the linear range of detection were loaded onto a polyacrylamide gel. For the quantitative assessment of protein expression on western blots, 10 µg of protein was denatured at 100 °C for 5 min, loaded into wells, and separated on 12% sodium dodecyl sulfate–polyacrylamide gel before being transferred onto a Hybond-ECL nitrocellulose membrane (Amersham Biosciences, Little Chalfont, Buckinghamshire, England), blocked for 1 h in 5% nonfat dry milk in 0.1 M Tris-buffered saline containing 0.1% Tween 20, and finally incubated overnight with the appropriate antibody (Table S2). Nonspecifically bound or excess antibody was removed with 5 × 5 min rinses in 0.1 M Tris-buffered saline containing 0.1% Tween 20. The membranes were then incubated for 1 h with the appropriate peroxidase-conjugated secondary antibody. The enhanced chemiluminescence method (Amersham Biosciences) was used according to the manufacturer's instructions to reveal immunoreactive bands. Proper dilutions and exposure times for each antibody were tested before performing the actual experiments. GAPDH detection was used as a control for equal protein load.

Grayscale digital images of the blots were acquired by scanning the autoradiographic films with a desktop scanner (Epson Perfection V750 Pro; Seiko Epson Corp., Nagano, Japan). Images were scanned and processed at identical settings to allow comparisons to be made of the blot results obtained from different samples. The densities of immunoreactive lanes equally loaded with protein aliquots were quantified, and data values were presented as a percentage of the control. For statistical comparisons, a one-way ANOVA or Mann–Whitney rank sum test was used and a *p* value of < 0.05 was considered significant. Values are presented as the mean ± standard error of the mean (SEM) from at least five immunoblots, one from each independent experiment.

#### 4.6. Image Analysis and Statistics

Digital images were captured using a Leica DMLB epifluorescence microscope equipped with a Leica DFC7000 T CCD camera (Leica Microsystems CMS GmbH, Wetzlar, Germany) and via the LAS X Application Suite X (Leica). For the intracellular (nuclear and cytoplasmic) localization and quantitative analyses of the levels of unmodified core histone H3 and the methylated histone H3 proteins H3K9me3 and H3K36me2, the DAPI-labeled cell nuclei of anti-CD11b/c-labeled cells were identified on coverslip-cultured samples.

For the quantitation of immunofluorescent images, 65–180 randomly selected CD11b/c-positive microglia were analyzed from three separate experiments. A quantitative microscopic analysis of histone immunofluorescence was conducted in ImageJ (version 1.47; originally developed by W. Rasband at the U.S. National Institutes of Health, Bethesda, MD, USA) [75], available at <https://imagej.net/Downloads>, accessed on 10 July 2013). Briefly, the densities of the whole cell and nuclei (mean gray values), the areas, and their integrated optical densities (fluorescence per area) were calculated. The corrected total cell fluorescence (CTCF) values (CTCF<sub>whole cell</sub> and CTCF<sub>nucleus</sub>) were then computed as described in the method developed by L. Hammond (Queensland Brain Institute, The University of Queensland, Australia), available at <https://theolb.readthedocs.io/en/latest/imaging/measuring-cell-fluorescence-using-imagej.html>, accessed on 30 October 2020, as follows: CTCF = integrated density – (area of selected cell × mean fluorescence of background readings). Lastly, cytoplasmic CTCF values were calculated using the following formula: CTCF<sub>cytoplasm</sub> = CTCF<sub>whole cell</sub> – CTCF<sub>nucleus</sub>. Identical microscopic and software parameter settings were then applied for each color channel. The color correction of images was occasionally performed when photomicrographs were prepared for publication. Statistical comparisons were made using SigmaPlot, and the data values were analyzed using Kruskal–Wallis one-way ANOVA on ranks followed by Dunn's method for pairwise multiple comparisons of differences between groups; the significance was set at *p* < 0.05. Data values are presented as the mean ± SEM.

**Supplementary Materials:** The following are available online at <https://www.mdpi.com/article/10.3390/ijms23031079/s1>.

**Author Contributions:** Conceptualization, K.G.; Funding acquisition, F.F., A.M., L.V. and K.G.; Investigation, M.S., N.L. and K.D.; Methodology, M.S., N.L., K.D. and K.G.; Resources, I.S., F.F., A.M., L.V. and K.G.; Writing—original draft, M.S., N.L., K.D. and K.G.; Writing—review and editing, K.G. All authors have read and agreed to the published version of the manuscript.

**Funding:** This work was supported by a grant from the Ministry of National Resources (GINOP 2.3.2-15-2016-00030 and 2.3.2-15-2016-00034) through the European Union Cohesion Fund. At the time of the experiments, NL and KD were PhD students, partly supported by the Theoretical Medicine Doctoral School, Albert Szent-Györgyi School of Medicine, University of Szeged. The funders had no role in the study design, data collection and analysis, decision to publish, or preparation of the manuscript.

**Institutional Review Board Statement:** All applicable international, national, and/or institutional guidelines for the care and use of animals were followed. Experimental procedures were carried out in strict compliance with the European Communities Council Directive (86/609/EEC) and followed Hungarian and local legislation requirements (XXVIII/1998 and 243/1998) and university guidelines regarding the care and use of laboratory animals. The experimental protocols were approved by the Institutional Animal Welfare Committee of the University of Szeged (II./1131/2018; date of approval: 30 May 2018).

**Informed Consent Statement:** Not applicable.

**Data Availability Statement:** Data is contained within the article.

**Conflicts of Interest:** The authors declare no conflict of interest. The funders had no role in the design of the study; in the collection, analyses, or interpretation of data; in the writing of the manuscript; or in the decision to publish the results.

## Abbreviations

ANOVA	one-way analysis of variance
CCR1	C-C motif chemokine receptor 1 (also known as chemokine receptor 1)
CD11b/c	cluster of differentiation 11b/c, the rat CR3 complement receptor
CTCF	corrected total cell fluorescence, an area-dependent value
CXCL10	C-X-C motif chemokine ligand 10 (also known as interferon-inducible cytokine IP-10)
DAPI	2-[4-(aminoiminomethyl)phenyl]-1H-indole-6-carboximidamide hydrochloride
DIV	day(s) in vitro
DMEM	Dulbecco's Modified Eagle's Medium
FBS	fetal bovine serum
GAPDH	glyceraldehyde 3-phosphate dehydrogenase (EC 1.2.1.12)
H	histone
H3K	histone H3 lys modification
Iba1	ionized calcium-binding adaptor molecule 1
IgG	immunoglobulin G
ICC	immunocytochemistry
KYNA	kynurenic acid
PBS	phosphate-buffered saline
rpm	revolutions per minute
RT	room temperature
SEM	standard error of the mean
subDIV	subcloned day(s) in vitro
SZR104	N-(2-(dimethylamino)ethyl)-3-(morpholinomethyl)-4-hydroxyquinoline-2-carboxamide
TBS	Tris-buffered saline
WB	western blot

## References

1. Vazirinejad, R.; Ahmadi, Z.; Kazemi Arababadi, M.; Hassanshahi, G.; Kennedy, D. The biological functions, structure and sources of CXCL10 and its outstanding part in the pathophysiology of multiple sclerosis. *Neuroimmunomodulation* **2014**, *21*, 322–330. [CrossRef] [PubMed]
2. Vécsei, L.; Szalárdy, L.; Fülöp, F.; Toldi, J. Kynurenines in the CNS: Recent advances and new questions. *Nat. Rev. Drug Discov.* **2013**, *12*, 64–82. [CrossRef]
3. Wirthgen, E.; Hoeflich, A.; Rebl, A.; Günther, J. Kynurenic acid: The janus-faced role of an immunomodulatory tryptophan metabolite and its link to pathological conditions. *Front. Immunol.* **2017**, *8*, 1957. [CrossRef]
4. Routy, J.P.; Routy, B.; Graziani, G.M.; Mehraj, V. The kynurenine pathway is a double-edged sword in immune-privileged sites and in cancer: Implications for immunotherapy. *Int. J. Tryptophan Res.* **2016**, *9*, 67–77. [CrossRef] [PubMed]
5. Lajkó, N.; Kata, D.; Szabó, M.; Mátyás, A.; Dulka, K.; Földesi, I.; Fülöp, F.; Gulya, K.; Vécsei, L.; Mihály, A. Sensitivity of rodent microglia to kynurenines in models of epilepsy and inflammation in vivo and in vitro: Microglia activation is inhibited by kynurenic acid and the synthetic analogue SZR104. *Int. J. Mol. Sci.* **2020**, *21*, 9333. [CrossRef] [PubMed]
6. Molnár, K.; Lőrinczi, B.; Fazakas, C.; Szatmári, I.; Fülöp, F.; Kmetykó, N.; Berkecz, R.; Ilisz, I.; Krizbai, I.A.; Wilhelm, I.; et al. SZR-104, a Novel Kynurenic Acid Analogue with High Permeability through the Blood-Brain Barrier. *Pharmaceutics* **2021**, *13*, 61. [CrossRef]
7. Biernacki, T.; Sandi, D.; Bencsik, K.; Vecsei, L. Kynurenines in the pathogenesis of multiple sclerosis: Therapeutic perspectives. *Cells* **2020**, *9*, 1564. [CrossRef]
8. Mándi, Y.; Endrész, V.; Mosolygó, T.; Burián, K.; Lantos, I.; Fülöp, F.; Szatmári, I.; Lőrinczi, B.; Balog, A.; Vécsei, L. The opposite effects of kynurenic acid and different kynurenic acid analogs on tumor necrosis factor- $\alpha$  (TNF- $\alpha$ ) production and tumor necrosis factor-stimulated gene-6 (TSG-6) expression. *Front. Immunol.* **2019**, *10*, 1406. [CrossRef] [PubMed]
9. Fülöp, F.; Szatmári, I.; Toldi, J.; Vécsei, L. Modifications on the carboxylic function of kynurenic acid. *J. Neural Transm.* **2012**, *119*, 109–114. [CrossRef] [PubMed]
10. Fülöp, F.; Szatmári, I.; Toldi, J.; Vécsei, L. Novel Types of c-3 Substituted Kinurenic Acid Derivatives with Improved Neuroprotective Activity. Patent No: WO2017149333A1, 8 September 2017. Available online: <https://patents.google.com/patent/WO2017149333A1/en> (accessed on 2 June 2021).
11. Demeter, I.; Nagy, K.; Gellért, L.; Vécsei, L.; Fülöp, F.; Toldi, J. A novel kynurenic acid analog (SZR104) inhibits pentylenetetrazole-induced epileptiform seizures. An electrophysiological study. *J. Neural Transm.* **2012**, *119*, 151–154. [CrossRef]
12. Ginhoux, F.; Jung, S. Monocytes and macrophages: Developmental pathways and tissue homeostasis. *Nat. Rev. Immunol.* **2014**, *14*, 392–404. [CrossRef]
13. Kettenmann, H.; Hanisch, U.-K.; Noda, M.; Verkhratsky, A. Physiology of microglia. *Physiol. Rev.* **2011**, *91*, 461–553. [CrossRef] [PubMed]
14. Kreutzberg, G.W. Microglia: A sensor for pathological events in the CNS. *Trends Neurosci.* **1996**, *19*, 312–318. [CrossRef]
15. Ubogu, E.E.; Cossoy, M.B.; Ransohoff, R.M. The expression and function of chemokines involved in CNS inflammation. *Trends Pharmacol. Sci.* **2006**, *27*, 48–55. [CrossRef] [PubMed]
16. Cheeran, M.C.-J.; Hu, S.; Sheng, W.S.; Peterson, P.K.; Lokensgard, J.R. CXCL10 production from cytomegalovirus-stimulated microglia is regulated by both human and viral interleukin-10. *J. Virol.* **2003**, *77*, 4502–4515. [CrossRef]
17. Nakamichi, K.; Saiki, M.; Sawada, M.; Takayama-Ito, M.; Yamamuro, Y.; Morimoto, K.; Kurane, I. Rabies virus-induced activation of mitogen-activated protein kinase and NF-kappaB signaling pathways regulates expression of CXC and CC chemokine ligands in microglia. *J. Virol.* **2005**, *79*, 11801–11812. [CrossRef] [PubMed]
18. Dyer, K.D.; Percopo, C.M.; Fischer, E.R.; Gabryszewski, S.J.; Rosenberg, H.F. Pneumoviruses infect eosinophils and elicit MyD88-dependent release of chemoattractant cytokines and interleukin-6. *Blood* **2009**, *114*, 2649–2656. [CrossRef]
19. Lo, B.K.K.; Yu, M.; Zloty, D.; Cowan, B.; Shapiro, J.; McElwee, K.J. CXCR3/ligands are significantly involved in the tumorigenesis of basal cell carcinomas. *Am. J. Pathol.* **2010**, *176*, 2435–2446. [CrossRef] [PubMed]
20. Wilson, N.O.; Huang, M.B.; Anderson, W.; Bond, V.; Powell, M.; Thompson, W.E.; Armah, H.B.; Adjei, A.A.; Gyasi, R.; Tettey, Y.; et al. Soluble factors from Plasmodium falciparum-infected erythrocytes induce apoptosis in human brain vascular endothelial and neuroglia cells. *Mol. Biochem. Parasitol.* **2008**, *162*, 172–176. [CrossRef]
21. Liu, M.; Guo, S.; Hibbert, J.M.; Jain, V.; Singh, N.; Wilson, N.O.; Stiles, J.K. CXCL10/IP-10 in infectious diseases pathogenesis and potential therapeutic implications. *Cytokine Growth Factor Rev.* **2011**, *22*, 121–130. [CrossRef]
22. Klein, R.S. Regulation of neuroinflammation: The role of CXCL10 in lymphocyte infiltration during autoimmune encephalomyelitis. *J. Cell Biochem.* **2004**, *92*, 213–222. [CrossRef] [PubMed]
23. Tomioka, R.; Matsui, M. Biomarkers for multiple sclerosis. *Intern. Med.* **2014**, *53*, 361–365. [CrossRef] [PubMed]
24. Szczuciński, A.; Losy, J. Chemokines and chemokine receptors in multiple sclerosis. Potential targets for new therapies. *Acta Neurol. Scand.* **2007**, *115*, 137–146. [CrossRef] [PubMed]
25. Kouzarides, T. Chromatin modifications and their function. *Cell* **2007**, *128*, 693–705. [CrossRef]
26. Lawrence, M.; Daujat, S.; Schneider, R. Lateral thinking: How histone modifications regulate gene expression. *Trends Genet.* **2016**, *32*, 42–56. [CrossRef] [PubMed]
27. Zlatanova, J.S.; Srebrevna, L.N.; Banchev, T.B.; Tasheva, B.T.; Tsanev, R.G. Cytoplasmic pool of histone H1 in mammalian cells. *J. Cell Sci.* **1990**, *96 Pt 3*, 461–468. [CrossRef] [PubMed]

28. Parseghian, M.H.; Luhrs, K.A. Beyond the walls of the nucleus: The role of histones in cellular signaling and innate immunity. *Biochem. Cell Biol.* **2006**, *84*, 589–604. [[CrossRef](#)]
29. Chen, R.; Kang, R.; Fan, X.G.; Tang, D. Release and activity of histone in diseases. *Cell Death Dis.* **2014**, *5*, e1370. [[CrossRef](#)] [[PubMed](#)]
30. Ekaney, M.L.; Otto, G.P.; Sossdorf, M.; Sponholz, C.; Boehringer, M.; Loesche, W.; Rittirsch, D.; Wilharm, A.; Kurzai, O.; Bauer, M.; et al. Impact of plasma histones in human sepsis and their contribution to cellular injury and inflammation. *Crit. Care* **2014**, *18*, 543. [[CrossRef](#)]
31. Frydman, G.H.; Tessier, S.N.; Wong, K.H.K.; Vanderburg, C.R.; Fox, J.G.; Toner, M.; Tompkins, R.G.; Irimia, D. Megakaryocytes contain extranuclear histones and may be a source of platelet-associated histones during sepsis. *Sci. Rep.* **2020**, *10*, 4621. [[CrossRef](#)]
32. Gabler, C.; Blank, N.; Hieronymus, T.; Schiller, M.; Berden, J.H.M.; Kalden, J.R.; Lorenz, H.M. Extranuclear detection of histones and nucleosomes in activated human lymphoblasts as an early event in apoptosis. *Ann. Rheum. Dis.* **2004**, *63*, 1135–1144. [[CrossRef](#)] [[PubMed](#)]
33. Gabler, C.; Kalden, J.R.; Lorenz, H.M. The putative role of apoptosis-modified histones for the induction of autoimmunity in systemic lupus erythematosus. *Biochem. Pharmacol.* **2003**, *66*, 1441–1446. [[CrossRef](#)]
34. Gabler, C.; Blank, N.; Winkler, S.; Kalden, J.R.; Lorenz, H.M. Accumulation of histones in cell lysates precedes expression of apoptosis-related phagocytosis signals in human lymphoblasts. *Ann. N. Y. Acad. Sci.* **2003**, *1010*, 221–224. [[CrossRef](#)] [[PubMed](#)]
35. Konishi, A.; Shimizu, S.; Hirota, J.; Takao, T.; Fan, Y.; Matsuoka, Y.; Zhang, L.; Yoneda, Y.; Fujii, Y.; Skoultchi, A.I.; et al. Involvement of histone H1.2 in apoptosis induced by DNA double-strand breaks. *Cell* **2003**, *114*, 673–688. [[CrossRef](#)]
36. Venkatesh, S.; Workman, J.L. Histone exchange, chromatin structure and the regulation of transcription. *Nat. Rev. Mol. Cell Biol.* **2015**, *16*, 178–189. [[CrossRef](#)] [[PubMed](#)]
37. Barski, A.; Cuddapah, S.; Cui, K.; Roh, T.Y.; Schones, D.E.; Wang, Z.; Wei, G.; Chepelev, I.; Zhao, K. High-resolution profiling of histone methylations in the human genome. *Cell* **2007**, *129*, 823–837. [[CrossRef](#)]
38. Hyun, K.; Jeon, J.; Park, K.; Kim, J. Writing, erasing and reading histone lysine methylations. *Exp. Mol. Med.* **2017**, *49*, e324. [[CrossRef](#)]
39. Honma, K.; Machida, C.; Mochizuki, K.; Goda, T. Glucose and TNF enhance expression of TNF and IL1B, and histone H3 acetylation and K4/K36 methylation, in juvenile macrophage cells. *Gene* **2020**, *763S*, 100034. [[CrossRef](#)] [[PubMed](#)]
40. Jain, N.; Vogel, V. Spatial confinement downsizes the inflammatory response of macrophages. *Nat. Mater.* **2018**, *17*, 1134–1144. [[CrossRef](#)] [[PubMed](#)]
41. Zhuang, L.; Jang, Y.; Park, Y.K.; Lee, J.E.; Jain, S.; Froimchuk, E.; Broun, A.; Liu, C.; Gavrilova, O.; Ge, K. Depletion of Nsd2-mediated histone H3K36 methylation impairs adipose tissue development and function. *Nat. Commun.* **2018**, *9*, 1796. [[CrossRef](#)] [[PubMed](#)]
42. Sacconi, S.; Natoli, G. Dynamic changes in histone H3 Lys 9 methylation occurring at tightly regulated inducible inflammatory genes. *Genes Dev.* **2002**, *16*, 2219–2224. [[CrossRef](#)] [[PubMed](#)]
43. Steiner, L.; Gold, M.; Mengel, D.; Dodel, R.; Bach, J.P. The endogenous  $\alpha 7$  nicotinic acetylcholine receptor antagonist kynurenic acid modulates amyloid- $\beta$ -induced inflammation in BV-2 microglial cells. *J. Neurol. Sci.* **2014**, *344*, 94–99. [[CrossRef](#)]
44. Poles, M.Z.; Nászai, A.; Gulácsi, L.; Czákó, B.L.; Gál, K.G.; Glenz, R.J.; Dookhun, D.; Rutai, A.; Tallósy, S.P.; Szabó, A.; et al. Kynurenic acid and its synthetic derivatives protect against sepsis-associated neutrophil activation and brain mitochondrial dysfunction in rats. *Front. Immunol.* **2021**, *12*, 717157. [[CrossRef](#)]
45. Balog, A.; Varga, B.; Fülöp, F.; Lantos, I.; Toldi, G.; Vécsei, L.; Mándi, Y. Kynurenic acid analog attenuates the production of tumor necrosis factor- $\alpha$ , calgranulins (S100A 8/9 and S100A 12), and the secretion of HNP1-3 and stimulates the production of tumor necrosis factor-stimulated gene-6 in whole blood cultures of patients with rheumatoid arthritis. *Front. Immunol.* **2021**, *12*, 632513. [[CrossRef](#)]
46. Boros, F.A.; Vécsei, L. Immunomodulatory effects of genetic alterations affecting the kynurenine pathway. *Front. Immunol.* **2019**, *10*, 2570. [[CrossRef](#)] [[PubMed](#)]
47. Hankittichai, P.; Lou, H.J.; Wikan, N.; Smith, D.R.; Potikanond, S.; Nimlamool, W. Oxyresveratrol inhibits IL-1 $\beta$ -induced inflammation via suppressing AKT and ERK1/2 activation in human microglia, HMC3. *Int. J. Mol. Sci.* **2020**, *21*, 6054. [[CrossRef](#)] [[PubMed](#)]
48. Liu, W.; Ye, J.; Yan, H. Investigation of key genes and pathways in inhibition of oxycodone on vincristine-induced microglia activation by using bioinformatics analysis. *Dis. Markers* **2019**, *2019*, 3521746. [[CrossRef](#)] [[PubMed](#)]
49. Kata, D.; Földesi, I.; Feher, L.Z.; Hackler, L.; Puskas, L.G.; Gulya, K. A novel pleiotropic effect of aspirin: Beneficial regulation of pro- and anti-inflammatory mechanisms in microglial cells. *Brain Res. Bull.* **2017**, *132*, 61–74. [[CrossRef](#)]
50. Xu, J.; Zhang, X.; Pelayo, R.; Monestier, M.; Ammollo, C.T.; Semeraro, F.; Taylor, F.B.; Esmon, N.L.; Lupu, F.; Esmon, C.T. Extracellular histones are major mediators of death in sepsis. *Nat. Med.* **2009**, *15*, 1318–1321. [[CrossRef](#)]
51. Wu, D.; Ingram, A.; Lahti, J.H.; Mazza, B.; Grenet, J.; Kapoor, A.; Liu, L.; Kidd, V.J.; Tang, D. Apoptotic release of histones from nucleosomes. *J. Biol. Chem.* **2002**, *277*, 12001–12008. [[CrossRef](#)] [[PubMed](#)]
52. Jaiswal, Y.K.; Jaiswal, M.K.; Agrawal, V.; Chaturvedi, M.M. Bacterial endotoxin (LPS)-induced DNA damage in preimplanting embryonic and uterine cells inhibits implantation. *Fertil. Steril.* **2009**, *91* (Suppl. 5), 2095–2103. [[CrossRef](#)] [[PubMed](#)]
53. Kovalchuk, I.; Walz, P.; Thomas, J.; Kovalchuk, O. Genomic instability in liver cells caused by an LPS-induced bystander-like effect. *PLoS ONE* **2013**, *8*, e67342. [[CrossRef](#)]

54. Kobiyama, K.; Kawashima, A.; Jounai, N.; Takeshita, F.; Ishii, K.J.; Ito, T.; Suzuki, K. Role of extrachromosomal histone H2B on recognition of DNA viruses and cell damage. *Front. Genet.* **2013**, *4*, 91. [[CrossRef](#)] [[PubMed](#)]
55. Kobiyama, K.; Takeshita, F.; Jounai, N.; Sakaue-Sawano, A.; Miyawaki, A.; Ishii, K.J.; Kawai, T.; Sasaki, S.; Hirano, H.; Ishii, N.; et al. Extrachromosomal histone H2B mediates innate antiviral immune responses induced by intracellular double-stranded DNA. *J. Virol.* **2010**, *84*, 822–832. [[CrossRef](#)]
56. Talati, M.; Seeley, E.; Ihida-Stansbury, K.; Delisser, H.; McDonald, H.; Ye, F.; Zhang, X.; Shyr, Y.; Caprioli, R.; Meyrick, B. Altered expression of nuclear and cytoplasmic histone H1 in pulmonary artery and pulmonary artery smooth muscle cells in patients with IPAH. *Pulm. Circ.* **2012**, *2*, 340–351. [[CrossRef](#)] [[PubMed](#)]
57. Nánási, P., Jr.; Imre, L.; Firouzi Niaki, E.; Bosire, R.; Mocsár, G.; Türk-Mázló, A.; Ausio, J.; Szabó, G. Doxorubicin induces large-scale and differential H2A and H2B redistribution in live cells. *PLoS ONE* **2020**, *15*, e0231223. [[CrossRef](#)] [[PubMed](#)]
58. Tran, T.Q.; Lowman, X.H.; Kong, M. Molecular Pathways: Metabolic control of histone methylation and gene expression in cancer. *Clin. Cancer Res.* **2017**, *23*, 4004–4009. [[CrossRef](#)] [[PubMed](#)]
59. Wiles, E.T.; Selker, E.U. H3K27 methylation: A promiscuous repressive chromatin mark. *Curr. Opin. Genet. Dev.* **2017**, *43*, 31–37. [[CrossRef](#)]
60. Meng, M.; Liu, H.; Chen, S.; Zhao, H.; Gao, X.; Zhang, J.; Chen, D. Methylation of H3K27 and H3K4 in key gene promoter regions of thymus in RA mice is involved in the abnormal development and differentiation of iNKT cells. *Immunogenetics* **2019**, *71*, 489–499. [[CrossRef](#)] [[PubMed](#)]
61. Kumar, A.; Kumari, N.; Sharma, U.; Ram, S.; Singh, S.K.; Kakkar, N.; Kaushal, K.; Prasad, R. Reduction in H3K4me patterns due to aberrant expression of methyltransferases and demethylases in renal cell carcinoma: Prognostic and therapeutic implications. *Sci. Rep.* **2019**, *9*, 8189. [[CrossRef](#)]
62. Zhao, Q.; Zhang, J.; Chen, R.; Wang, L.; Li, B.; Cheng, H.; Duan, X.; Zhu, H.; Wei, W.; Li, J.; et al. Dissecting the precise role of H3K9 methylation in crosstalk with DNA maintenance methylation in mammals. *Nat. Commun.* **2016**, *7*, 12464. [[CrossRef](#)] [[PubMed](#)]
63. Hayakawa, K.; Nishitani, K.; Tanaka, S. Kynurenine, 3-OH-kynurenine, and anthranilate are nutrient metabolites that alter H3K4 trimethylation and H2AS40 O-GlcNAcylation at hypothalamus-related loci. *Sci. Rep.* **2019**, *9*, 19768. [[CrossRef](#)] [[PubMed](#)]
64. Rosenfeld, J.A.; Wang, Z.; Schones, D.E.; Zhao, K.; DeSalle, R.; Zhang, M.Q. Determination of enriched histone modifications in non-genic portions of the human genome. *BMC Genom.* **2009**, *10*, 143. [[CrossRef](#)] [[PubMed](#)]
65. Fang, T.C.; Schaefer, U.; Mecklenbrauker, I.; Stienen, A.; Dewell, S.; Chen, M.S.; Rioja, I.; Parravicini, V.; Prinjha, R.K.; Chandwani, R.; et al. Histone H3 lysine 9 di-methylation as an epigenetic signature of the interferon response. *J. Exp. Med.* **2012**, *209*, 661–669. [[CrossRef](#)]
66. Harman, J.L.; Dobnikar, L.; Chappell, J.; Stokell, B.G.; Dalby, A.; Foote, K.; Finigan, A.; Freire-Pritchett, P.; Taylor, A.L.; Worssam, M.D.; et al. Epigenetic regulation of vascular smooth muscle cells by histone H3 lysine 9 dimethylation attenuates target gene-induction by inflammatory signaling. *Arterioscler. Thromb. Vasc. Biol.* **2019**, *39*, 2289–2302. [[CrossRef](#)]
67. Torrano, J.; Al Emran, A.; Hammerlindl, H.; Schaidler, H. Emerging roles of H3K9me3, SETDB1 and SETDB2 in therapy-induced cellular reprogramming. *Clin. Epigenetics* **2019**, *11*, 43. [[CrossRef](#)]
68. Li, M.F.; Zhang, R.; Li, T.T.; Chen, M.Y.; Li, L.X.; Lu, J.X.; Jia, W.P. High glucose increases the expression of inflammatory cytokine genes in macrophages through H3K9 methyltransferase mechanism. *J. Interferon Cytokine Res.* **2016**, *36*, 48–61. [[CrossRef](#)] [[PubMed](#)]
69. Fülöp, F.; Szatmári, I.; Vámos, E.; Zádori, D.; Toldi, J.; Vécsei, L. Syntheses, transformations and pharmaceutical applications of kynurenic acid derivatives. *Curr. Med. Chem.* **2009**, *16*, 4828–4842. [[CrossRef](#)] [[PubMed](#)]
70. Szabo, M.; Gulya, K. Development of the microglial phenotype in culture. *Neuroscience* **2013**, *241*, 280–295. [[CrossRef](#)]
71. Neote, K.; DiGregorio, D.; Mak, J.Y.; Horuk, R.; Schall, T.J. Molecular cloning, functional expression, and signaling characteristics of a C-C chemokine receptor. *Cell* **1993**, *72*, 415–425. [[CrossRef](#)]
72. Dulka, K.; Szabo, M.; Lajkó, N.; Belec, I.; Hoyk, Z.; Gulya, K. Epigenetic consequences of in utero exposure to rosuvastatin: Alteration of histone methylation patterns in newborn rat brains. *Int. J. Mol. Sci.* **2021**, *22*, 3412. [[CrossRef](#)] [[PubMed](#)]
73. Dulka, K.; Nacs, K.; Lajkó, N.; Gulya, K. Quantitative morphometric and cell-type-specific population analysis of microglia-enriched cultures subcloned to high purity from newborn rat brains. *IBRO Neurosci. Rep.* **2021**, *10*, 119–129. [[CrossRef](#)] [[PubMed](#)]
74. Lowry, O.H.; Rosebrough, N.J.; Farr, A.L.; Randall, R.J. Protein measurement with the Folin phenol reagent. *J. Biol. Chem.* **1951**, *193*, 265–275. [[CrossRef](#)] [[PubMed](#)]
75. Schneider, C.A.; Rasband, W.S.; Eliceiri, K.W. NIH Image to ImageJ: 25 years of image analysis. *Nat. Methods* **2012**, *9*, 671–675. [[CrossRef](#)] [[PubMed](#)]